Doctoral Thesis
Ingeniería Industrial

Microstructural analysis of heated ultra-high-performance fibre-reinforced-concrete under cyclic loading

PhD. Candidate:
José David Ríos Jiménez

PhD. Advisor:
Héctor Cifuentes Bulté

Departamento de Mecánica de Medios Continuos y Teoría de Estructuras
Escuela Técnica Superior de Ingeniería
Universidad de Sevilla

Seville, January 2019

A thesis submitted to Universidad de Sevilla for the degree

of

Doctor of Philosophy

Microstructural analysis of heated ultra-high-performance fibre-reinforced-concrete under cyclic loading

Thesis by:

José David Ríos Jiménez

M.Sc. Ingeniero Industrial

Advisor:

Héctor Cifuentes Bulté

Prof. Dr. Ingeniero Industrial

Departamento de Mecánica de Medios Continuos y Teoría de Estructuras

Escuela Técnica Superior de Ingeniería

Universidad de Sevilla

January 2019

Tesis: Microstructural analysis of heated ultra-high-performance fibre-reinforced-concrete under cyclic loading

Autor: José David Ríos Jiménez

Director: Héctor Cifuentes Bulté

El tribunal nombrado para juzgar la Tesis arriba indicada, compuesto por los siguientes doctores:

Presidente:

Vocales:

Secretario:

acuerdan otorgarle la calificación de:

El Secretario del Tribunal

Fecha:

This doctoral thesis has been funded from the Ministry of Finance and Competitiveness of Spain (Ministerio de Economía y Competitividad) through the projects BIA2013-48352-P and BIA2016-75431-R.

A mi familia, por su apoyo
A Alicia, por su alentadora sonrisa

A la memoria
de mi abuela

Acknowledgements

It has been by sitting down to write these words, the last steps of this rough journey, when the awareness of its impact on my life, professional and personal, has been deeply perceived. Having reached the epilogue of this enriching and satisfying stage, I think that it is undoubtedly just and meritorious to recognize that I have not walked alone, and therefore, that it is time to ask for the account.

Whether there is a person responsible that I have performed this thesis, it is Prof. Héctor Cifuentes Bulté, with whom my debt can never be paid. Thank you for your lessons, for your advice and support during all these years, but especially for your friendship. I have no doubt that it is impossible to have found a better person than you.

My special mention to Prof. Fernando Medina Encina for teaching me to take my first steps with reinforced concrete structures and be the maker of awakening my interest in them. I will never forget your classes.

To Prof. Pilar Ariza Moreno for believing in me. Your interest in my training and work have been a motivation and a constant challenge. Thank you.

My thanks to Emilio Gómez Álvarez for his advice and tireless help, especially when the laboratory tasks were insisting on contravening the end of this thesis, but above all for their friendship.

During the course of this doctoral thesis, I have been fortunate to make different stays that have allowed me to collaborate with several research groups, which undoubtedly have all contributed to complement my training and analyse my research from other point of views, but especially thank you for your consideration and always warm welcome. My sincere thanks to the research group of Prof. Gonzalo Ruiz and Rena C. Yu, of the Universidad de Castilla-La

Mancha (Spain); to Prof. Stanislav Seitl of the Academy of Sciences of the Czech Republic; to that of Prof. Alfonso Fernández-Canteli, of the Universidad de Oviedo (Spain) and to the group of Prof. Surendra Shah of Northwestern University (USA).

I could not finish without remembering those people who have been accompanying me on the road since the beginning, or that I feel like they have been doing it, without which nothing could have been possible. To my father, for inculcating me that effort and sacrifice at work are not an option. To my mother, for the education transmitted, but especially for the life given from her infinite love. To my brother, for the revision of the text, the advices, but above all for being always I need you. To Alicia, for her supporting me and understanding me when discouragement overshadowed everything. Your smile was the light that guided me when the clarity was vanished.

José David

Seville, January 2019

Agradecimientos

Ha sido al sentarme a escribir estas palabras, los últimos pasos de esta escabrosa travesía, cuando la consciencia de su repercusión en mi vida, profesional y personal, se ha percibido profundamente. Habiendo llegado al epílogo de esta enriquecedora y satisfactoria etapa, creo que es sin duda justo y meritorio reconocer que no he caminado solo, y así por tanto, que es la hora de rendir cuentas.

Si hay una persona responsable de que haya realizado esta tesis ese es el Prof. Héctor Cifuentes Bulté, con quién mi deuda nunca podrá estar saldada. Gracias por tus lecciones, por tus consejos y apoyo durante todos estos años, pero especialemente por tu amistad. No tengo dudas de que es imposible haber encontrado mejor persona que tú.

Mi especial mención al Prof. Fernando Medina Encina por enseñarme a dar mis primeros pasos con las estructuras de hormigón armado y ser el artifice de despertar mi interés en ellas. Nunca olvidaré sus clases.

A la Prof. Pilar Ariza Moreno por creer en mí. Su interés en mi formación y trabajo han sido una motivación y un reto constante. Gracias.

Mi agradecimiento a Emilio Gómez Álvarez por sus consejos e incansable ayuda, especialemte cuando las tareas de laboratorio se empeñaban en contravenir el final de esta tesis, pero sobre todo por su amistad.

Durante el transcurso de esta tesis doctoral he tenido la suerte de realizar diferentes estancias que me han permitido la colaboración con diversos grupos de investigación, los cuáles, sin duda, todos han contribuido a complementar mi formación y a analizar mis investigaciones desde otras perspectivas, pero especialmente gracias por su consideración y siempre calurosa acogida. Mi sincero agradecimiento al grupo de investigación de los Prof. Gonzalo Ruiz

y Rena C. Yu, de la Universidad de Castilla-La Mancha (España); al del Prof. Stanislav Seitl de la Academia de Ciencias de la República Checa; al del Prof. Alfonso Fernández Canteli, de la Universidad de Oviedo (España) y al grupo del Prof. Surendra Shah de Northwestern University (EEUU).

No podría terminar sin acordarme de aquellas personas que llevan acompañándome en el camino desde el comienzo, o que así siento que lo llevan haciendo, sin el apoyo de los cuáles no podría haber sido posible. A mi padre, por inculcarme que el esfuerzo y el sacrificio en el trabajo no son una opción. A mi madre, por la educación transmitida, pero especialmente por la vida entregada desde su infinito amor. A mi hermano, por la revisión del texto, los consejos, pero sobretodo por estar siempre que lo necesito. A Alicia, por su apoyo y comprensión cuando el desánimo todo lo ensombrecía. Tú sonrisa era la luz que me guiaba cuando la claridad se desvanecía.

José David

Sevilla, Enero 2019

Abstract

Concrete is currently the structural material more used in civil engineering and building construction. Nowadays, the application of the technological advances of the chemical industry in the processes of concrete manufacture, as well as the addition of fibres as reinforcement of the cementitious matrix, has meant a significant improvement in the mechanical and fracture behaviour of these materials. High performance and especially, ultra-high-performance concretes are examples of such advances.

One of the advantages of the use of concrete as structural material is its high resistance in fire situations compared to other types of materials, like steel. However, the maximum service temperature of structural concrete is essentially limited by the internal damage caused by them. This thermal damage is evidenced by the generation of cracks on the border of the pore matrix, as a consequence of the pressure inferred by the evaporation of the free water and dehydration of the compounds arisen from the cement hydration.

One of the alternatives to mitigate the thermal damage of the cementitious matrix is the addition of polymer fibres, which are melted at relatively low temperatures (approximately 160 °C). The melting of the fibres generates a network of micro-channels that allow the evacuation of the evaporated water more efficiently, so that the pressure inside the pores of the matrix is reduced and consequently the thermal damage. Another alternative is the use of steel fibres as reinforcement of the concrete matrix. The presence of steel fibres, well-distributed and in the right amount, hinders the free crack propagation because they act as barriers. Nevertheless, the addition of fibres generates a greater heterogeneity of the matrix that can induce the alteration of its microstructure and affect the mechanical and fracture properties of concrete. This effect,

together with the high packing density of high-performance concrete and, more significantly in ultra-high-performance concrete, leads to the thermal damage produced in the matrix of the material must be conveniently analysed using the appropriate techniques, like the computed tomography.

In some applications, the concrete elements must bear thermal and mechanical loads simultaneously at moderately temperatures, but for long periods of time. In these cases, the microstructure of the matrix, as well as its degradation by thermal damage, is closely related to the mechanical strength and fracture behaviour of the material. In other applications, concretes are subjected to cyclic thermo-mechanical loads that entail the generation and propagation of cracks as a result of thermo-mechanical fatigue. The reinforcement of concretes with a high number of steel fibres, as in the case of ultra-high-performance concretes, allows to reach very high values of the tensile and flexural strength. Thus, it is possible to reduce or dispense the use of prestressed reinforcement in those applications where it is necessary that the material resists high tensile stress without cracking. In all these cases, the analysis of the macro-mechanical behaviour (mechanical and fracture properties) and its time evolution is closely related to the microstructure of the material and the mechanisms produced in the micro-scale by the addition of fibres, the thermal degradation and the crack growth by cyclic loading.

This thesis begins with the study of the microstructural behaviour and its effect on the macroscopic properties of high-strength concrete reinforced with polypropylene fibres of different length and subjected to high temperatures (Chapter 2). The discussion focuses on the connection between the microstructure and the mechanical and fracture properties of the different concretes. In the Chapter 3, it is analysed the effect that the addition of different steel fibres has in the microstructure of an ultra-high-performance concrete and to determine its influence on the microstructure and the mechanical and fracture properties. In the next chapter, it is analysed the effect of temperature on the internal structure of the ultra-high-performance concrete of Chapter 3, as well as the influence of thermal damage on its mechanical and fracture properties. Chapter 5 focuses on the validation of a fatigue failure probability model in compression, developed by Saucedo et al., for its application in flexural fatigue tests on high and ultra-high performance fibre-reinforced concrete and the evaluation of the effect of fibres on the model parameters. Finally, in Chapter 6, the fatigue behaviour of an ultra-high-performance concrete subjected to different temperatures is analysed by determining the Wöhler curves through a fatigue failure probability model developed by Castillo and Fernández-Canteli. All the analysis carried

out have focused on relating the effect of thermal damage and the influence of fibres on the microstructure, with the obtained macro-mechanical properties.

Resumen

El hormigón es en la actualidad el material estructural más empleado en ingeniería civil y en edificación. Actualmente, la aplicación de los avances tecnológicos de la industria química en los procesos de fabricación de los hormigones, así como la adición de fibras como refuerzo de su matriz cementicia, supone una mejora significativa en el comportamiento mecánico y en fractura de estos materiales. Una muestra de ello son los hormigones de altas prestaciones y los hormigones de ultra-altas prestaciones.

Una de las ventajas de la utilización del hormigón como material estructural es su resistencia en situaciones de incendio frente otro tipo de materiales, como el acero. Sin embargo, la máxima temperatura de servicio del hormigón estructural está limitada fundamentalmente por el daño que ésta causa en el material. Este daño térmico se manifiesta mediante la generación de fisuras en el borde de los poros de la matriz como consecuencia de la presión inferida por la evaporación del agua libre y la deshidratación de los compuestos resultantes de la hidratación del cemento.

Una de las alternativas para paliar el daño térmico de la matriz cementicia es la adición de fibras poliméricas que se funden a temperaturas relativamente reducidas (aproximadamente 160 °C). La fusión de las fibras genera una red de microcanales que permiten la evacuación del vapor de agua al exterior de manera más eficiente, de modo que la presión en los poros de la matriz se reduce y en consecuencia el daño térmico. Otra alternativa es el uso de fibras de acero como refuerzo de la matriz. La presencia de las fibras de acero, bien distribuidas y en cantidades adecuadas, dificulta la propagación libre de fisuras en la matriz debido a que actúan como barreras. Sin embargo, la adición de fibras genera una mayor heterogeneidad de la matriz que puede inducir a la alteración de la

estructura interna del hormigón y repercutir en sus propiedades mecánicas y de fractura. Este efecto, unido a la elevada densidad de empaquetamiento de los hormigones de altas prestaciones y, más significativamente en los hormigones de ultra-altas prestaciones, hacen que el daño térmico producido en la matriz del material deba analizarse convenientemente mediante las técnicas oportunas, como la tomografía computarizada.

En algunas aplicaciones, los elementos de hormigón deben soportar cargas térmicas y mecánicas acopladas, a temperaturas no muy elevadas, durante periodos prolongados de tiempo. En estos casos, la microestructura de la matriz, así como su degradación producida por el daño térmico, está íntimamente relacionada con las propiedades mecánicas y en fractura del material. En otras aplicaciones, los hormigones están sometidos a cargas cíclicas termo-mecánicas que conllevan la generación y propagación de fisuras por el efecto de fatiga termo-mecánica. El refuerzo de hormigones con un alto número de fibras de acero, como en el caso de los hormigones de ultra-altas prestaciones, permite alcanzar valores de resistencia a la tracción y flexotracción muy elevados, de manera que se pueda reducir o prescindir de la utilización de armaduras activas en aquellas aplicaciones donde sea necesario que el material soporte altas tensiones sin fisurarse. En todos estos casos, el estudio del comportamiento macromecánico y su evolución con el tiempo está estrechamente relacionado con la estructura interna del material y los mecanismos generados en la microescala por la adición de fibras, la degradación térmica y el crecimiento de fisuras por cargas cíclicas.

Esta tesis comienza estudiando el comportamiento microestructural y su efecto sobre las propiedades macroscópicas de hormigones de altas prestaciones reforzados con fibras de polipropileno de diferente longitud y sometidos a altas temperaturas (Capítulo 2). La discusión se centra en la conexión existente entre la estructura porosa de la matriz y las propiedades mecánicas y en fractura de los diferentes hormigones. En el Capítulo 3, se analiza el efecto que la adición de diferentes fibras de acero tiene sobre la microestructura de un hormigón de ultra-altas prestaciones y se determina la influencia de las mismas sobre la estructura interna del material y sus propiedades mecánicas y de fractura. En el siguiente capítulo, se estudia el efecto de la temperatura sobre la estructura interna de los hormigones de ultra-altas prestaciones del Capítulo 3, así como la influencia del daño térmico sobre sus propiedades mecánicas y de fractura. El Capítulo 5 se centra en la validación de un modelo de probabilidad de fallo por fatiga a compresión, desarrollado por Saucedo et al., para su aplicación en ensayos de fatiga a flexotracción sobre hormigones de altas y ultra-altas prestaciones y una posterior evaluación del efecto de la adición de fibras sobre los parámetros del

modelo. Finalmente, en el Capítulo 6 se estudia el comportamiento en fatiga de los hormigones de ultra-altas prestaciones, sometidos a diferentes temperaturas, mediante la determinación de las curvas de Wöhler a través de un modelo de probabilidad de fallo por fatiga desarrollado por Castillo y Fernández-Canteli. Todos los estudios realizados se han centrado en relacionar el efecto del daño térmico y la influencia de las fibras sobre la microestructura, con las propiedades macromecánicas obtenidas.

Co-Authorship Statement

Refereed Journal Papers:

- Ríos, José D.; Cifuentes, Héctor; Leiva, Carlos; Seitl, Stanislav. (2019) "Analysis of the mechanical and fracture behavior of heated ultra-high-performance fiber-reinforced concrete by X-ray computed tomography". *Cement and Concrete Research*. In press.

- Ríos, José D.; Leiva, Carlos; Ariza, M. Pilar; Seitl, Stanislav; Cifuentes, Héctor. (2019) "Analysis of the tensile fracture properties of ultra-high-strength fiber-reinforced concrete with different types of steel fibers by X-ray tomography". *Materials and Design*. Vol 165. 10.1016/j.matdes.2019.107582.

- Ríos, José D.; Cifuentes, Héctor; Leiva, Carlos; García, Celia; Alba, Maria D. (2018) "Behavior of high-strength polypropylene fiber-reinforced self-compacting concrete exposed to high temperatures". *Journal of Materials in Civil Engineering. ASCE*. Vol. 30. No. 11. 10.1061/(ASCE) MT.1943-5533.0002491.

- Cifuentes, Héctor; Ríos, José D.; Gómez, Emilio (2018) "Effect of mix design on the size-independent fracture energy of normal- and high-strength self-compacting concrete". *Materiales de Construccion*. Vol. 68. No. 329. 10.3989/mc.2018.00717.

- Ríos, José D.; Cifuentes, Héctor; Yu, Rena C.; Ruiz, Gonzalo (2017), " Probabilistic flexural fatigue in plain and fiber-reinforced concrete". *Materials*. Vol. 10. No. 7-767. Pag. 1-25. 10.3390/ma10070767.

Refereed Journal Papers under review:

- Ríos, José D.; Cifuentes, Héctor; Blasón, Sergio; López-Aenlle, Manuel. "Fatigue behavior of an ultra-high-performance fibre-reinforced concrete heated up to 300 °C". *International Journal of Fatigue.*

- Ríos, José D.; Cifuentes, Héctor. "Microstructural analysis of the effect of steel fibres on the fracture behaviour of heated ultra-high-performance fibre-reinforced concrete". *Cement and Concrete Composites.*

Conference contributions:

- Ríos, José D.; Cifuentes, Héctor. "Probabilistic fatigue analysis of ultra-high-performance fibre-reinforced concrete under thermal effects". *12th International Fatigue Congress*. Poitiers, France. 27th May-1st June 2018.

- Ríos, José D.; Cifuentes, Héctor. "Análisis del comportamiento en fractura de un hormigón de muy alta resistencia sometido a temperaturas de 300 °C mediante tomografía computarizada". *35 Encuentro del Grupo Español de Fractura*. Málaga, Spain. 14-16th March 2018.

- Ríos, José D.; Cifuentes, Héctor; Medina, Fernando. "Determinación de las curvas de Wöhler en fatiga a flexotracción de un hormigón de muy alta resistencia sometido a temperatura elevada". *V Congreso Iberoamericano de Hormigón Autocompactante y Hormigones Especiales*. Valencia, Spain. 5-6th March 2018.

- Ríos, José D.; Cifuentes, Héctor. "Comportamiento en fractura de un hormigón de muy altas prestaciones frente a la adición de fibras metálicas". *34 Encuentro del Grupo Español de Fractura*. Santander, Spain. 29th-31st March 2017.

- Ríos, José D.; Cifuentes, Héctor, Leiva, Carlos, Medina, Fernando. "Influencia del tiempo de exposición de temperaturas en el comportamiento en fractura de hormigones autocompactantes reforzados con fibras de polipropileno. Comunicación en congreso". *VII Congreso Internacional de Estructuras de ACHE*. La Coruña, Spain. 20th-22nd June 2017.

- Ríos, José D.; Cifuentes, Héctor, Medina, Fernando. "Propiedades mecánicas en fatiga de un hormigón de muy altas prestaciones mediante ensayos de flexión en tres puntos. Comunicación en congreso. Comunicación en congreso". *VII Congreso Internacional de Estructuras de ACHE*. La Coruña, Spain. 20th-22nd June 2017.

- Ríos, José D.; Cifuentes, Héctor, Gomez, Emilio, Ariza, M.P. "Influence of fibres on the tensile fracture behaviour of the matrix of ultra-high strength fibre-reinforced concrete". *14th International Conference on Fracture*. Rhodes, Greece. 18th-23rd June 2017.

- Cifuentes, Héctor, Ríos, José D., Leiva, Carlos; Medina, Fernando. "Influencia del Tiempo de Exposición a Altas Temperaturas en el Comportamiento en Fractura de Hormigones Autocompactantes Reforzados con Fibras". *33 Encuentro del Grupo Español de Fractura*. San Sebastián, Spain. 9-11th March 2016.

- Ríos, José D., Cifuentes, Héctor; Yu, Rena C.; Ruiz, Gonzalo. "Aplicación de un Modelo Probabilístico al Comportamiento en Fatiga Por Flexotracción de Hormigones Reforzados con Fibras de Acero". *33 Encuentro del Grupo Español de Fractura*. San Sebastián, Spain. 9-11th March 2016.

Table of Contents

Notations

α	Exponent that describes the material's hardening under cyclic loading
α_0	Relative notch depth
α_t	Normalised parameter of the inverse analysis [110], $\alpha_t = \frac{\varepsilon_{t.u}}{\varepsilon_{t.el}}$
β_t	Normalised parameter of the inverse analysis [110], $\beta_t = \frac{\varepsilon_{t.d}}{\varepsilon_{t.el}}$
γ_t	Normalised parameter of the inverse analysis [110],$\gamma = \frac{f_{tu}}{f_t}$
δ	Deflection at midspan
δ_{loc}	Deflection corresponding to σ_{loc} [110]
δ_u	Ultimate deflection at midspan
$\Delta\sigma$	Stress range, σ_{max}-σ_{min}
ΔS	Stress level range, S_{max}-S_{min}
δ_{75}	Displacement corresponding to σ_{75} [110]
δ_{40}	Displacement corresponding to σ_{40} [110]
δ_{80u}	Displacement in the post-peak branch corresponding to σ_{80u} [110]
δ_{30u}	Displacement in the post-peak branch corresponding to σ_{30u} [110]
ε	Strain
ε_t	Strain corresponding to tensile stress
$\varepsilon_{t,el}$	Strain at first cracking tensile strength defines as $\frac{f_t}{E_c}$ [110]
$\varepsilon_{t.d}$	Strain at the intersection of the softening lines

$\varepsilon_{t.max}$	Strain at zero stress [110]
$\varepsilon_{t.u}$	Strain at ultimate stress [110]
ν	Location parameter in Weibull distribution according to [33]
λ	Scale parameter in Weibull distribution function
σ	Stress
$\dot{\sigma}_0$	Loading rate employed in a static test
σ_c	Compressive stress
σ_c^d	Dynamic material strength
$\dot{\sigma}_d$	Loading rate employed in a dynamic test
σ_{cmax}	Maximum compressive stress
σ_{cmin}	Minimum compressive stress
σ_{f_0}	Static failure stress (material strength)
σ_{fl}	Flexural stress defined as $\frac{P}{W_{el}}$
σ_{fail}	Failure stress for a certain fatigue life
σ_{loc}	Secant stiffness of 97‰σ_{max} according to [110]
σ_{max}	Maximum stress
σ_{max_0}	Equivalent static stress for σ_{max}
σ_{min}	Minimum stress
σ_{min_0}	Horizontal asymptote which determines the lower stress value
$\sigma_{min_{2m}}$	Two-million-cycle endurance limit
σ_t	Tensile stress
σ_{75}	Secant stiffness of 75% according to [110]
σ_{40}	Secant stiffness of 40% according to [110]
σ_{80u}	Softening stresses of 80‰σ_{loc} according to [110]
σ_{30u}	Softening stresses of 30‰σ_{loc} according to [110]
ν	Poisson's coefficient
χ_f	Fibre volume factor
Φ_{xr}	Total porosity
Ψ	Sphericity of pore
$\overline{\Psi}$	Average sphericity of pores
Ω	Deflection-actuator displacement ratio defined as $\frac{X_i^{def}}{X_i^{pos}}$

a	A material parameter defined by Suacedo et al. [154]
a_0	Depth of notch

A	Parabolic parameter in accordance to RILEM modifications proposed by Guinea et al. [53, 68, 140]
A_{lig}	Ligament area of a notched specimen
A_{pore}	Surface area of a pore
B	Threshold value of the fatigue life time
B_s	Width of the prismatic specimen
C	Endurance limit
C_f	
C_i	Initial compliance of P-CMOD according to [157]
d_{eq}	Equivalent diameter of pore
$\overline{d_{eq}}$	Average equivalent diameter of pores
d_f	Fibre diameter
D	Depth of the prismatic specimen
D_f	Fibre diameter
E_c	Young's modulus
f	Loading frequency of a fatigue test
f_0	Reference loading frequency
f_1	stress at the intersection point of the bilinear tension softening diagram of plain concretes
f_c	Compressive strength
f_{fl}	Monotonic flexural strength
f_{tu}	Tensile strength
f_t	First cracking strength
f_{ti}	Splitting tensile strength
f_r	Cyclic flexural loading applied
G_F	Independent-size fracture energy
GP	Generalized parameter of fatigue according to [33]
k	Shape parameter of a Weibull distribution
l_{ch}	Characteristic length
L	Length of the prismatic specimen
L_f	Fibre length
n_f	Number of fibres
N	Number of cycles to failure (fatigue life)
N_f	Mean fatigue life (P_{fail}=50%)
N_{ini}	Fatigue life to crack initiation
P	Load
P_{fail}	Probability of failure
R	Stress ratio defined as $\sigma_{min}/\sigma_{max}$

S	Stress level defined as f_r/f_{fl}
S_0	Initial stiffness of $\sigma_{fl} - \delta$ curve according to [110]
S_{max}	Maximum stress level
S_{min}	Minimum stress level
S_p	Span of the prismatic specimen
V	Normalized parameter of Weibull distribution according to [33]
V_f	Fibre volume fraction
V_{fibre}	Volume of a fibre
V_{pore}	Volume of a pore
V_{total}	Total volume of a sample
w	Water
w	Crack mouth opening displacement
w_1	CMOD at the intersection of the softening lines on plain concrete
w_d	CMOD at the intersection of the softening lines on fibre-reinforced concrete according to [110]
w_{max}	Maximum crack mouth opening displacement
W_{el}	Elastic modulus
W_F	Total fracture work
W_m	Measured fracture work
W_{nm}	Non-measured fracture work
X_i^{def}	Deflection data recorded by experimental test at room temperature
X_i^{pos}	Actuator displacement data recorded by experimental test at room temperature
${X_i^{'def}}_{300}$	Estimated deflection at 300 °C
${X_i^{pos}}_{300}$	Actuator displacement data recorded by experimental test at 300 °C

Abbreviations

BFUP	Béton fibré ultra performant
CA	Coarse aggregate
CDF	Cumulative distribution function
CMOD	Crack mouth opening displacement
CRM	Cement replacement material
CT	Computed tomography
D0	Plain concrete of HPFRC from Chapter 2
D1	HSC reinforced with short PP fibres
D2	HSC reinforced with long PP fibres
DL	UHPFRC reinforced only with macro-fibres
DS	UHPFRC reinforced only micro-fibres
DSC	Differential scanning calorimetry
DSL	UHPFRC reinforced with micro and macro-fibres in 50% ratio
DSLPP	DSL concrete reinforced additionally with PP fibres
DTA	Differential thermal analysis
EFNARC	European Federation of National Associations Representing for Concrete
ETSI	Escuela Técnica Superior de Ingeniería
FA	Fine aggregate
FAS	Fly ash
FPB	Four-point bending
FPZ	Fracture process zone
GGBS	Granulated blast-furnace slag

HPFRC	High-performance fibre-reinforced concrete
HPSCC	High-performance self-compacting concrete
HSC	High-strength concrete
HW	Hard-drawn wire fibre
LA	Limestone aggregate
LOI	Lost of ignition
LVDT	Linear voltage displacement transducer
ME	Melt extract fibre
NF	Non-fibre reinforced
NSC	Normal-strength concrete
PC	Portland cement
PFA	Powder fly ash
PP	Polypropylene
PPF	Polypropylene fibre
RC	Plain concrete of UHPFRC
RT	Room temperature
SCC	Self-compacting concrete
SDW	Surface-deformed wire fibre
SETRA	Road and traffic governmental agency
SF	Silica fume
SP	Superplasticizer
SS	Slit sheet fibre
SW	Smooth wire fibre
TG	Thermogravimetry
TPB	Three-point bending
UHPC	Ultra-high-performance concrete
UHPFRC	Ultra-high-performance fibre-reinforced concrete
UHPSCC	Ultra-high-performance self-compacting concrete
VTXRD	Variable temperature X-ray diffractometry

1 Introduction

Although concrete has been used for more than a hundred years, it has been a material on continuous evolution that has led to being the most employed construction material today [119]. The use of concrete on diverse types of applications, such as buildings or civil structures and infrastructures (e.g., pavements, bridge slabs, dams, railroad ties, precasted elements, containment vessels, retrofitting material, etc.), shows its great versatility. The main advantages, which have made possible the wide use of concrete, are essentially its good mechanical properties, durability, fire-resistance, on-site workability, easy handling, worldwide availability and relatively low cost versus efficiency. Nevertheless, concrete, as stony material, has a brittle matrix that result in low tensile strength and strain capacity, so that it has traditionally required the reinforcement in the form of continuous steel bars placed in the appropriate position inside the concrete element to withstand the imposed tensile stresses [48].

The appearance of steel fibres as reinforcement in concrete materials, in 1960s [150], together with the grand progress of additives by chemical industry, really conducted to a substantial evolution on performance of concrete, resulting in high-performance fibre-reinforced concrete concrete (HPFRC) and ultra-high-performance fibre-reinforced concrete (UHPFRC) in mid 1990s [169, 197]. Fibre-reinforced concrete is defined by ACI 544.1R-96 [4] as a composite material where an elevated number of fibres, commonly steel fibres for a better structural performance, are randomly dispersed on a cementitious matrix [48]. The inclusion of steel fibres has led to important changes in the concrete behaviour, essentially after cracking. When the cracking appears, the steel fibres stitch crack front delaying the crack opening by providing stress transfer along the crack and allowing a higher energy absorption capacity [7, 200, 209]. Thus,

the fracture properties have been significantly improved on HPFRC and UHPFRC. Nevertheless, the structural performance of fibre-reinforced concrete is strongly affected by the matrix-fibre properties [48, 162, 210]. Depending on fibres (i.e., strength, stiffness, length, shape, volume fraction) and matrix (i.e., microstructure, stiffness, defects, constituents) the concrete properties change.

1.1 Motivation

1.1.1 Fatigue on HPFRC and UHPFRC

The enhancement in concrete strength by its continuous development has made possible to use concrete in structural applications with higher requirements. Slenderer designs and more complex structures are more widely used and even new applications, where concrete never would had been applied, are considered (e.g., concrete wind turbine towers or energy storage systems in solid medium). The use of slenderer elements has reduced the weight of structures while the loads are maintained. As result, the permanent loads decrease and consequently, the live loads (i.e. wind, earthquake, sea waves, etc.) represent a higher percentage of the total loads [131, 181]. Thus, such structures are more sensitive to fatigue failure than conventional concrete [131]. On the other hand, these enhanced concrete (i.e., HSC and UHPFRC) are mostly used in infrastructures where the time-variable loads are predominant (e.g., bridge decks, pavements, high-speed railways, high rise buildings, off-shore structures, etc.) [64, 167]. This fact has led to the most common failure of concrete structures is due to cyclic loading [12]. Thus, in recent years, the research interest has been focused on the developments of fatigue performance of concrete [12, 20, 64, 84, 111, 166].

The fatigue strength (i.e., endurance limit) of concrete is defined as the fraction of the static strength that it can support repeatedly for a given number of cycles [2]. The fatigue damage inferred by cyclic loading in concrete materials can be stated from two point of views, macroscopic or microscopic level. In the macroscopic level, the cyclic loads results in a reduction of the strength and stiffness of the material, as well as an increase of the strains. The progressive growth of this damage leads to fatigue failure. In the microscopic level, the damage leads to birth and growth of micro-defects (mainly microcracks) that results in a progressive degradation of the matrix [181]. There are researches that suggested that crack propagation connect pores of the specimen, following the path of minimal energy [30]. It is worth mentioning that in concrete, as pores are randomly distributed throughout the matrix, damage is randomly

distributed throughout concrete. That represents a significant difference with metallic materials where defects are concentrated [181].

As shown, the heterogeneity and internal structure of concrete, a material with inherent flaws, are two important factors in those cases where cyclic loads are predominant and fatigue design criteria must be taken into account. The inclusion of fibres in the concrete matrix (e.g., HPFRC or UHPFRC) has beneficial effects in the fatigue behaviour. The fibre reinforcement increases the fatigue life of concrete by bridging cracks and thus retarding their growth but might increase the heterogeneity of matrix and become the source of additional defects (e.g., micro-cracks generation or pore structure alteration [60, 124, 125]. As observed, it is required a multiscale analysis of the fatigue life of HPFRC and UHPFRC considering the macroscopic level, (i.e., the mechanical and fracture properties, as well as fibre influence) and the microscopic level (i.e., pore structure of concrete).

1.1.2 Thermal degradation of concrete

During the second half of 19th century, the use of concrete in buildings and civil infrastructures significantly increased due to the fact that its low thermal conductivity conferred it a good behaviour against accidental fires, in comparison with other usual construction materials [180]. However, the progressive improvement of concrete properties has led to use this material in new situations, in which the material must be capable of bearing thermal and mechanical loads [132, 211].

By contrast, the maximum serviceability temperature of structural concrete is normally limited by the potential damage caused by high temperatures in concrete, resulting in explosive failure, (i.e., spalling) [85, 136]. Spalling is one of the greatest concerns when dealing with concrete structures subjected to high temperatures. The temperature affects of several ways, by means of the generation of thermal gradients which infer internal stresses and by the high pore pressure derived of water evaporation and dehydration of C-S-H gel and portlandite [147, 180]. The stresses generated by both effects can reach the tensile strength of concrete and cause the birth and growth of microcracks leading to the spalling of the material at high temperatures [97].

As observed, the thermal damage in concrete depends on its thermal conductivity of concrete and the matrix composition, which varies with different components [10, 174]. The thermal conductivity strongly depends on the pore density of matrix. Additionally, a more dense structure (i.e., HPFRC and UHPFRC) improves the concrete strength but leads to a more difficult pore pressure attenuation and as a consequence, the thermal damage in cementitious matrix

is higher [23, 87]. Thus, whether the concrete has a high matrix porosity, as happens in the case of normal strength concrete, the steam can flow outside the concrete through the pore connection of the matrix. This effect, combined with medium-high temperatures, causes small effects of the pore pressure and thus, results in negligible damage to the concrete matrix.

In the last two decades, research interest has been focused on the influence of the addition of fibres in the concrete to reduce crack propagation at high temperatures. Polypropylene fibres, which melt at approximately 160 °C, have been proven adequate to control the spalling of concrete; their melting creates an additional capillary pore network inside the concrete, which allows the release of the water steam generated by dehydration reactions [137, 179]. Thus, the main objective of polypropylene fibres is not the structural reinforcement but the improvement of the fire resistance of concrete. Instead, steel fibres can be used in order to increase the residual strength of concrete after exposure to elevated temperatures [39, 103]. However, some researches [49] argued that the benefit of adding steel fibres may not be so obvious, since they contribute to speeding up the heating of the concrete and may be prone to producing internal flaws because of thermal incompatibility with the concrete matrix. Additionally, the modification of the internal structure of concrete matrix by the addition of fibres [12, 141, 142] conducts to the alteration of thermal conductivity of concrete and as a consequence, affects on the generation of thermal gradients in the matrix at high temperatures [10, 174]. As observed, the pore structure of concrete matrix is an important factor also in structures subjected to high temperatures because influence on the generation and progression of the thermal damage in the concrete when the temperature is risen.

1.1.3 Analysis of microstructure

As mentioned, the porosity of concrete matrix is highly important since not only has influence on the mechanical and fracture properties under monotonic loading, but also has influence on concrete structures exposed to high temperatures and the fatigue failure under cyclic loading [12, 43, 181, 205]. Nowadays, the application of micro X-ray computed tomography (CT) to characterise engineered materials becomes more and more widespread because of the availability of the X-ray CT equipments in the laboratories. By means of this technique, the internal structure of those materials can be characterised at several scales (from micro to macro-scale), with a clear representation of the internal distribution of the components of the material, especially those with different densities. Several applications can be found to characterise metals and alloys [59, 114], porous

materials [91], composites [191] and fibre-reinforced composites [155], asphalt mixtures [80]. In case of concrete, due to its inherent porosity, the X-ray technique has been successfully applied for the study of plain concrete [50, 60, 196], as well as fibre-reinforced concrete [19, 26, 141], especially where steel fibres were used due to the well differentiated densities of voids, fibres, aggregates and the cementitious matrix. In case of UHPFRC the utilization of X-ray CT to characterise them is scarcer [143] and not exempt from added difficulties due to the large amount of steel fibres present in these mixes [192]. However, since in this kind of concretes the coarse aggregates can be avoid in order to improve the packing of their matrix, the efforts can be focused only in the study of the air voids, the fibres and the cementitious matrix and do not distinguish between the cement paste and aggregates.

1.2 Research background

Although fatigue behaviour of concrete has been studied since the beginning of the last century, mainly from the development of reinforced concrete bridges, such subject has not been tackled systematically by the scientific community up to the early 1950 [154, 172]. Later, the appearance of steel fibre-reinforced concrete in 1960s led to enhance the concrete performance (i.e., tensile and flexural strength, energy absorption capacity, etc.) and conducted to slenderer and more complex infrastructures [131, 204], some of which are applications where time-variable loads are predominant (e.g., high-speed railway sleepers, high-rise buildings, slender bridge decks, wind turbine tower, etc.). This has led to an increasingly research interest on fatigue behaviour of fibre-reinforced concrete structures during the last decades [20, 78, 79, 181].

Despite the large number of research focused on fatigue behaviour of concrete, there is no an accepted strategy in the scientific community to achieve an efficiently and reliably designing concrete structures against fatigue failure. [133, 172]. Briefly, the fatigue damage criteria might be addressed from two points of view, the deterministic and probabilistic approach. The former is a simple but not very efficient way of designing since the fatigue concern is inherently a probabilistic matter. In the deterministic criteria, for a specific maximum stress, a theoretical mean value of fatigue life is given. Furthermore, in order to consider the possibility of an early failure, partial safety factors are commonly used over concrete strength and applied loads, resulting in conservative designs [133]. Anyway, currently design codes, such as Eurocode 2 [58] and Model Code 2010 [1], adopt a deterministic design criteria mainly because

of simplicity of use.

By contrast, the most research has been focused on the probabilistic approach of fatigue behaviour [31, 33, 46, 118, 148, 154, 165, 167]. The main problem when testing concrete specimens under fatigue is the wide scatter of cycles to failure under the same loading conditions. In fact, the scatter might vary from 100 to 100,000 cycles [133]. The probabilistic approach had led to consider different distributions, such as log-normal or Birnbaum-Saunders [133]. Nevertheless, the most of researcher agree that the fatigue failure follows a Weibull distribution. Castillo and Fernández-Canteli [33] carried out a comprehensive study of fatigue failure and demonstrated that Weibull and Gumbel are the only family distributions applicable to fatigue. Indeed, numerous fatigue models have been developed based on one of these distributions [33, 78, 154, 167].

Despite the advances, there is a lack of consensus in the methodology to address the analysis of fatigue in concrete. Hence, most of recent research on fibre-reinforced concrete has been focused basically on the development of probabilistic predictions of fatigue damage [25, 34, 78, 113, 154], as well as the fatigue strength (i.e., endurance limit) in compression [154, 193], in tension [82, 111] or flexion [12, 168]. The tensile and flexural fatigue strength have focused more the research attention due to its significant enhancement on the fibre-reinforced concrete. Some studies have mentioned the remarkable influence of fibre-reinforcement on the fatigue performance [12, 142]. Al-Azzawi and Karihaloo [12] stood out that well-dispersed fibre-distribution improved significantly the fatigue behaviour. Singh et al. [164] and Goel et al. [65] mentioned as the amount of fibres increased the scatter of fatigue results but also the flexural fatigue life for a certain fibre content. By contrast, few researches have studied the influence of microstructure on the fatigue degradation of concrete. Vicente et al. [181] studied the influence of pore morphology in compressive fatigue loading of high-strength concrete with different air-entrant agent but it is scarce no similar works under tension or flexion [117] and with other types of concrete, such as UHPFRC, in which the microstructure is sustainable different than normal or high-strength concrete.

In the case of UHPFRC, the few available results are essentially focused on the fatigue strength prediction of UHPFRC under flexural [12, 125] or tensile [111, 112] cyclic loading. Other researches have studied the fatigue performance in particular applications, such as the use of thin strips of UHPFRC as retrofitted material on reinforced concrete beams under cyclic loading [122] or the study of UHPFRC fatigue behaviour combined with steel rebars R-UHPFRC [112]. In all those works, they have not established a connection

between the fibre-reinforcement or concrete matrix with the fatigue behaviour beyond the comments by Al-Azzawi and Karihaloo [12], in which highlighted the benefit of a well-dispersed fibre distribution in the fatigue life. Despite the important role that fibre-reinforcement and microstructure play on the fatigue performance [12, 105, 142], there is a lack of comprehensive studies of UHPFRC mainly focused on establish a relationship among the internal microstructure of the matrix, the fibre reinforcement and the macroscopic fatigue behaviour of the composite concrete.

The low thermal conductivity of concrete increased the interest of application of concrete in buildings and civil infrastructures during 1960s, due to its excellent behaviour when exposed to fire conditions in comparison with the rest of construction materials (i.e., steel) [180]. The great fire resistance of concrete has led it to go on being one of the first options when good fire performance is required. Then, numerous fire resistance researches for all types of concrete (i.e., plain, fibre-reinforced, high-strength and ultra-high-performance concrete) have been carried out [24, 36, 52, 72, 73, 85, 107, 108, 127, 174, 180].

The application of concrete in the construction of pressure vessels in nuclear power plants since 1970s conducted to focus the thermal studies on the structural behaviour of concrete under high temperatures [6, 37, 101, 195]. From 1980s, the focus was shifted towards high strength concrete. The higher packing density of this concrete leads to be more sensitive to concrete explosion (i.e., spalling) than normal strength concrete under high temperatures [32, 35, 98, 153].

One of the main causes of spalling is the thermal gradients inside the matrix and the thermal incompatibility of the different components of concrete (i.e., cement paste, aggregates, steel rebars, fibres, etc.), which have different coefficients of thermal expansion. Additionally, the dehydration of concrete constituents (i.e., C-S-H gel and portlandite) and the evaporation of free water generate high pore pressures inside matrix which might results in spalling failure [97, 180].

One of the studied solutions to reduce the spalling is the addition of polypropylene fibres to concrete matrix, not as structural reinforcement but as improvement of fire resistance, creating a network of channels when fibres are melted (around 160 °C) to evacuate steam vapour more easily [24, 108, 147, 205]. Steel fibres have also been taken into account to increase the cracking strength of concrete during the material thermal degradation [103, 161]. However, some works have exposed that the presence of steel fibres might become harmful because they contribute to speeding up the heating of the concrete and prone micro-cracks [49].

The interest on the enhancement of concrete performance have conducted to employ several active constituents, which partially substitute the cement and modifie the hydration reactions and as a consequence, reduces shrinkage effects [27, 198, 202]. One of the subjects more studied in the literature is the influence of curing temperature on the concrete behaviour [86, 97, 158, 178]. The puzzolanic active components reacts faster on hot-cured than cold-cured, leading to a more dense matrix which enhance concrete properties. That has led to numerous works, which analyse different active components (i.e., silica fume, fly ash, ground granulated furnace slag, etc.) and even recycled materials (i.e., rice husk) [43, 121, 182]. The hot-curing is more effective in UHPFRC since it contains components with finer particle size [86]. In fact, there are also studies focused on effects of re-curing on residual properties of concrete [8–10].

The significant enhancement of UHPFRC performance has led to new possibilities of applications for this type of concrete. Some of these applications are the use of UHPFRC in liquefied natural gas (LNG) tanks subjected to cryogenic conditions (approximately -162 °C) [94–96] or the construction of steam or molten salts containment vessels, in which the concrete must be capable of bearing medium-high temperatures (i.e., commonly between 300-500 °C) for long periods of time. Other novel application is the manufacturing of concrete energy storage systems in solid medium [16, 83, 132, 194]. In this case, concrete is used as a heat battery to supply thermal energy in solar power plants in periods of absent of solar light. The researches performed so far have positioned very well concrete with respect to other materials (i.e., silicon carbide, quartzite rock, alumina ceramics), due to its great thermal and mechanical properties, as well as its availability and relative low production-expenses. In aforementioned applications, the UHPFRC must support high thermal gradients, coupled cycles of thermal and mechanical loading for long periods of time. However, the studies relative to applications subjected to those testing conditions in UHPFRC are limited. UHPFRC might become a reliable alternative but it is needed to study properly the thermal degradation by reactions during heating at high-medium temperatures, the damage of thermal cyclic loading and the variation of mechanical properties with age.

1.3 Aims and objectives of the thesis

Once have been exposed the most critical aspects concerning the fatigue performance and temperature exposure of high-strength concrete and ultra-high-performance fibre reinforced concrete, the global objectives of this thesis are

presented:

1. Deepen the understanding of the effects of a temperature increase in the concrete matrix (i.e., phase changes and microstructure) of high-strength concrete and ultra-high-performance fibre-reinforced concrete subjected to long periods of time. Subsequently to establish a connection between phase changes and pore structure of concrete depending on the temperature reached.
2. To study the influence of fibre-reinforcement on the microstructure of the concrete matrix by X-ray computed tomography scan and mercury intrusion porosimetry at diverse temperatures and thus, to analyse the temperature and fibre influence on the microstructure.
3. To determine the effect of fibre reinforcement, by using of different fibres, on the mechanical and fracture properties of high-strength concrete and ultra-high-performance fibre-reinforced concrete. Additionally, to study the degradation of mechanical and fracture properties caused by thermal damage when concrete are subjected to different temperatures.
4. To establish a connection among the different types of fibres used as reinforcement, the modification of matrix due to temperature and the mechanical and fracture properties measured for high-strength concrete and ultra-high-performance concrete.
5. Deepen of the knowledge of the influence of the type of fibre reinforcement on the fatigue life of high-strength concrete and ultra-high-performance concrete by the use of a probabilistic fatigue model.
6. To determine the influence of diverse increasing temperatures on the fatigue life of a ultra-high-performance fibre-reinforced. To establish a connection among the fatigue behaviour, the influence of fibre addition, the degradation of the microstructure by thermal damage and the static loading behaviour of UHPFRC.

1.4 Outline of the thesis

With the intention of a clear and concise setting out of the main concerns exposed, above the present document is organized in seven chapters, which are further divided into sections and sub-sections as follows:

In Chapter 2 it has been analysed the use of high-strength concrete reinforced with polypropylene fibres at long exposure times to high temperatures. It was analysed the concrete behaviour in hot tests: 100, 300, 500 and 700 °C and cooled-down states at different exposure times (6, 24 and 48 h). It was also experimentally determined the thermogravimetric analysis, fracture behaviour, compressive strength, Young's modulus and tensile strength of concrete. Subsequently, it was performed a comprehensive analysis of the thermal and mechanical behaviour of high-strength concrete under different thermal conditions.

Chapter 3 has been focused on the study of mechanical and fracture properties of an UHPFRC fabricated with different steel fibres (short and long fibres). For the analysis, different techniques have been employed, from mechanical tests to X-ray computed tomography, in order to connect the observed variations of the mechanical properties of the mixes with its microstructure. In such a way, a comprehensive study of the pore structure distribution from X-ray computed tomography image analysis and mercury intrusion porosimetry have been carried out, highlighting the influence of the kind of fibres employed as reinforcement on the pore size and distribution of the concrete matrix and subsequently, on its mechanical and fracture properties.

In Chapter 4, the effects of temperature on mechanical and fracture behaviour of an UHPFRC are studied. Fibre-reinforced concrete mixes and its matrix without any type of reinforcement were studied in order to compare the influence of steel fibres. To this end, X-ray CT technique was used to analyse the deterioration of the microstructure due to the thermal damage evolution of each concrete at room temperature and heated to 300 °C. Complementary, a thermogravimetric analysis of the concrete matrix was performed in order to relate the observed phase changes, due to dehydration and decomposition, with the deterioration of microstructure. On the other hand, an analysis of the mechanical and fracture properties of materials were also carried out at room temperature and 300 °C. Finally, it was established a connection between the thermal damage within the concrete matrix and its corresponding mechanical and fracture behaviour.

In Chapter 5, experimental data sets available in the literature on the flexural fatigue of plain and fibre-reinforced concrete were fitted with a probabilistic model developed by Saucedo et al. With these tests, this model was validated for flexural fatigue at various loading frequencies. More than 100 series of flexural fatigue tests in the literature are fit with excellent results. Since the distribution of monotonic tests was not available in the majority of cases, a

two-step procedure is established to estimate the model parameters based solely on fatigue tests.

In Chapter 6 the influence of the microstructure in the fatigue behaviour of UHPFRC subjected to diverse temperatures (i.e., room temperature, 100, 200 and 300 °C) is analysed. A comprehensive experimental program is carried out in order to determine the fatigue strength (i.e., endurance limit) of a UHPFRC and its corresponding unreinforced concrete matrix through three-point bending fatigue tests on notched specimens for the determination of the S-N field at room temperature, 100, 200 and 300 °C. A probabilistic fatigue model based on Weibull distribution functions developed by Castillo and Fernández-Canteli was used to determine the S-N field. Finally, it was established a connection among the results from X-ray CT scan, thermoanalytic analysis, the mechanical and fracture properties and the fatigue behaviour at the different temperatures tested.

Finally in Chapter 7 the main conclusions of the work performed in this thesis are discussed and the future developments are exposed.

2 Fracture behaviour of high-strength PP fibre-reinforced SCC at high temperatures

2.1 Polypropylene fibre reinforcement of concrete subjected to high temperatures

The interest on the energy generation by renewable energy sources is being of great interest for those countries committed to the reduction of CO_2 emissions [17]. Solar energy is one of the most widespread renewable technology used worldwide [16] and also the only one that allows for its storage. One of the uses of concrete, different to the traditional structural applications, is thermal storage systems in steam collectors or, the emerging option, as thermal energy storage system in solid media due to its mechanical properties and heat storage capabilities [16]. In both cases, the material must not only be capable of bearing loads, but also, they must withstand the effect of high temperatures for long exposure times.

In this chapter it is experimentally analysed the use of a high-strength PP fibre-reinforced self-compacting concrete in applications on which the concrete is subjected to high temperatures for long time. For that, it is analysed the behaviour of concrete at different temperatures (100, 300, 500 and 700 °C,

designed as hot tests), cooled-down states (designed as cold tests) and different exposure times (6, 24 and 48 h). Experimental thermogravimetric analysis, fracture energy, compressive strength, Young's modulus and tensile strength tests are performed. Afterwards, a comprehensive analysis was done to establish a connection between the thermal and mechanical behaviour under the aforementioned diverse conditions.

2.2 Description of the polypropylene fibre reinforced mixes

The materials used in this study were: as binder, portland cement type II 32.5 B-L, in accordance with the EN 197-1 standard [57]. Silica fume (SF) manufactured by Sika, model S-92-D, with 90% of particles under 0.1 μm and a SiO_2 content above 90%. Their chemical compositions are specified in Table 2.1. As aggregates, fine aggregate (FA) with a maximum size of 2 mm. Its grading distribution is presented in Table 2.2. Its chemical composition is shown in Table 2.1. FA was essentially SiO_2 and Al_2O_3. Coarse aggregate (CA) had a maximum size of 10 mm (Table 2.2). It was chemically composed essentially of SiO_2 and Al_2O_3 (Table 2.1). Limestone aggregate (LA) with a maximum size of 4 mm (Table 2.2). It was composed essentially of SiO_2 and Al_2O_3, and showed a chemical composition very similar to FA.

Table 2.2 presents the grading distribution of FA, CA and LA. As observed in this table, FA was the finest, with an average particle size of 0.48 mm; LA presented an average particle size of 0.66 mm, and CA had an average particle size of 6.72 mm.

In this study, three mixtures of high-strength PP fibre-reinforced concrete were casted. All mixtures had a matrix with the same components and mix proportions, differentiated only by their respective sort of PP fibre. The first mix, called D0, was considered as the control concrete mix and was not reinforced with PP fibres. The second and third concrete mixes, designated as D1 and D2, respectively, had a PP fibre content of 1.2 kg/m^3. Fibre length was 6 mm in the D1 concrete and 24 mm in the D2 concrete. The materials and concrete mix proportions are presented in Table 2.3.

The concrete mixes were prepared with a laboratory mixer. All dry constituents were poured into the mixer and rotated for 5 min. Next, the PP fibres and the superplasticizer were added to the water and then poured into the mixer. Finally, the mixer was left to rotate for a further 15 min until a fluid and

Table 2.1 Chemical compositions of the constituents of HSC.

	% mass				
compound	cement[a]	SF	FA	CA	LA
SiO_2	20.69	95.63	86.50	83.35	86.97
Al_2O_3	5.24	0.43	5.83	4.50	5.56
Fe_2O_3	2.46	0.10	1.33	2.26	1.39
MnO	0.10	0.02	0.03	0.05	0.02
MgO	1.50	0.39	0.13	0.36	0.19
CaO	61.89	0.21	0.59	3.42	0.51
Na_2O	0.36	0.20	0.87	0.09	0.95
K_2O	0.73	0.79	2.37	1.04	1.97
TiO_2	0.28	<0.01	0.13	0.23	0.15
P_2O_5	0.17	0.08	0.07	0.05	0.02
SO_3	1.11	0.04	0.04	0.03	0.03
LOI	4.76	1.84	1.34	3.59	1.51

[a] Type II cement 32.5 B-L

Table 2.2 Grading distribution of aggregates.

Sieve size (mm)						
Material	>16	10	8	4	2	1
FA	0.00	0.00	0.00	0.00	0.00	22.20
CA	0.00	19.30	40.13	38.31	2.26	0.00
LA	0.00	0.00	0.00	0.00	11.50	26.50
Material	0.5	0.25	0.125	0.063	<0.063	
FA	35.82	26.15	10.33	3.74	1.10	
CA	0.00	0.00	0.00	0.00	0.00	
LA	21.00	17.33	12.00	9.17	2.33	

homogeneous mix was observed. Slump flow tests were carried out on the self-compacting concrete (SCC) mixes in accordance with EFNARC guidelines [51], with satisfactory results. The specimens were immediately cast, subsequently unmolded, and after 24 h cured in a water bath at 20 °C for 28 days.

Table 2.3 Constituents and mix proportions.

Quantity (kg/m^3)								
Type	cement	FA	LA	CA	SF	SP	PPF	w/c
D0	657	867	139	1301	99	23	0	0.20
D1	657	867	139	1301	99	23	1.2 (6 mm)	0.20
D2	657	867	139	1301	99	23	1.2 (24 mm)	0.20

2.3 Heating of high-strength PP fibre-reinforced SCC

2.3.1 Heating procedure

Experimental tests were conducted on specimens at high temperatures (hot tests) and also after cooling them down (cold tests) to determine the influence of temperature on the fracture behaviour. Furthermore, a first batch of specimens of each mix (D0, D1 and D2) was tested at room temperature, without undergoing any heating, to serve as control results. In the so-called hot tests, the second batch of specimens was heated at a rate of 10 °C/min until reaching five different temperatures (100, 300, 500, and 700 °C), subjected to three different exposure times (6, 24, and 48 h) at each of these temperatures, and immediately tested. In the so-called cold tests, the third batch of specimens was heated at the same rate and the same temperatures for 48 h and then cooled for 24 h at room temperature, after which they were tested. The testing equipment used was specifically designed to perform high-temperature tests, and made it possible to insert the framework and the specimen into the furnace.

2.3.2 Mass loss and thermal tests

The effect of temperature on the concrete was monitored by thermal analysis and variable temperature X-ray powder diffractometry (VTXRD) analysis. VTXRD tests were performed at the X-ray laboratory (University of Seville, Spain) by a Bruker D8 Advance diffractometer (Bruker, Germany) fitted with a high-temperature camera (Anton Paar XRK 900, Austria) and a position-sensitive detector (Bruker Vantec PSD, Germany) in the 25 °C to 900 °C temperature range at a heating rate of 10 °C/min (target: Cu; voltage: 40 kV; current: 40 mA; geometry combining divergent Göbel mirror configurations; detector: radial Soller slits; time scans: 5 min).

Simultaneous thermal tests (TG/DTA) were performed at the Functional Characterization Service (University of Seville, Spain) on a TA (model STD-Q600) instrument, using alumina as a reference. The specimens were put into platinum crucibles in a chamber containing air during the entire heating period. The temperature was increased at a constant rate of 10 °C/min. A differential scanning calorimetric analysis (DSC) was carried out. The specimens, 5 mm in diameter and 3 mm thick, were placed in nonhermetic aluminum containers and subjected to a heating program of 2 °C/min in a TA Instruments 2920 DSC from 40 °C up to 300 °C, using nitrogen as a purge gas [183].

2.3.3 Pore size distribution

Pore size distribution was determined by mercury intrusion porosimeter tests. Three samples of each of the mixtures (D0, D1 and D2) were tested and an average value was considered. The tests were conducted on a measuring pressure range of 1.02×10^{-2} to 2.04×10^{2} MPa. The selected contact angle was 141°, so the measurable pore size ranged from 0.007 to 144 pm. Pellet-shaped specimens about 5 mm in size were used. All specimens were previously heated to 105 °C until no moisture was left.

2.4 Mechanical and fracture test procedure

2.4.1 Compressive strength

The compressive strength tests of the control concrete mix and the hot and cold specimens were carried out in accordance with the EN12390-3 standard [55] in $50\times50\times50$ mm^3 cubes. These cubes were obtained by sawing off the $100\times100\times440$ mm^3 cast prisms. The specimens of each batch were all simultaneously heated in the same furnace to ensure that they were all subjected to the same heating process. Four cube specimens were tested in each case.

2.4.2 Tensile strength

Splitting tensile tests were carried out to determine the tensile strength of concrete because of the complexity of direct-tension testing in concrete [139]. Cylindrical specimens 100×200 mm in size (diameter $\times$ height) were manufactured with each concrete mix. The experimental tests were performed on specimens at room temperature (i.e., control concrete and cold specimens).

In the hot tests, due to limitations of the testing machine, tensile strength evolution was estimated from the maximum load value of three-point bending tests. It is noted that the right determination of the tensile strength from three-point bending tests requires a more sophisticated procedure [67, 77, 189]; nevertheless, as the main objective is the analysis of the evolution of the tensile strength with temperature, a direct relationship between f_{tu} and the peak load of the three-point bending (TPB) tests was assumed. This simplified procedure was verified by using specimens at room temperature (i.e., control concrete and cold specimens) and obtaining tensile strength values in agreement with their corresponding experimental results. The procedure proved to be a reasonable way to estimate this material property in hot tests, given the difficulty of experimental testing.

The splitting tensile tests were conducted on the 100×200 mm cylinders according to the EN 12390-6 standard [56]. Plywood strips 15 mm wide $\times$ 4 mm thick were placed between the specimens and the actuator. Four specimens were tested in each case.

2.4.3 Fracture energy

The fracture energy was determined by means of three-point bending tests on $50\times50\times220$ mm^3 following the RILEM work-of-fracture method [146]. The recommendations proposed by Guinea et al. [53, 68, 140] were considered to obtain a size-independent value. Four specimens were tested in each case. The influence of the span/depth ratio [89] was avoided because the specimen length was L =220 mm, so specimen span length was S_p =200 mm (Fig. 2.1). It was equal to four times the depth of the cross section. Initial notch depth was a_0=25 mm, so relative notch depth was $\alpha_0 = 0.5$ in all cases. The notches were prepared with a diamond saw prior to the heating process. The TPB tests were carried out in a 200 kN dynamic machine. The vertical displacement at the midpoint in specimens at room temperature (i.e., control concrete and cold specimens) was measured with a linear voltage displacement transducer (LVDT) mounted on a rigid frame fixed to the specimen. In hot specimens, this measurement was estimated from the actuator position recording, because the high temperatures made it impossible to use any measuring instrument. Loading was conducted using an actuator, at a rate of 0.01 mm/min until the peak load was reached; after this, the velocity was increased to 0.05 mm/min during the postpeak branch of the load-displacement (P-δ) curve. From the P-δ curve, the fracture energy of concrete was determined using Eq. (2.1) specified in the RILEM [146], applying the corrections corresponding to the adjustment of the

tail of the load displacement curve proposed by Guinea et al. [44, 68].

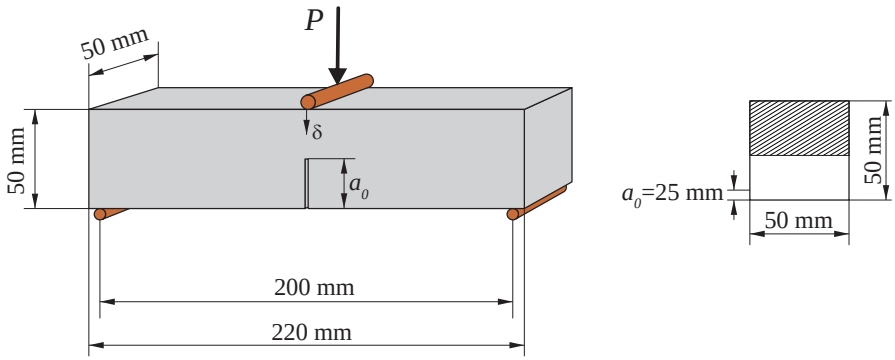

Figure 2.1 Drawing of the TPB test of a notched specimen.

$$G_F = \frac{W_F}{B_s(D-a_0)}, \tag{2.1}$$

where G_F is the fracture energy, W_F is the total work of fracture and $B_s(D-a_0)$ is the ligament area. The total work of fracture is given by:

$$W_F = W_m + W_{nm}, \tag{2.2}$$

W_m is the measured work of fracture corresponding to the total area below the P-δ curve recorded until the end of the test at δ_u. W_{nm} is the nonmeasured work of fracture, obtained by means of the remote tail constant, A, taking into account the influence of cutting the P-δ curve [53].

$$W_{nm} = \frac{2A}{\delta}, \tag{2.3}$$

2.4.4 Young's modulus

The Young's modulus of the specimens tested at room temperature (i.e., control concrete and cold specimens) was determined in accordance with the EN 12390-13 standard [54]. This was done by gradually loading a cylindrical specimen in compression to approximately a third of its failure load and measuring the

corresponding strain with 30 mm strain gauges. In the hot tests, it was impossible to use measuring instruments, so the Young's modulus was determined based on the compliance method proposed by Jenq and Shah [157]. This method requires previous knowledge of the initial slope of the load-crack mouth opening displacement curve (P-CMOD), which cannot be measured in the hot specimens. The initial slope of the P-CMOD curve is related to the Young's modulus, as shown in Eq. (2.6). Consequently, the initial slope of the load displacement curve (P-δ) is also related to material stiffness, so it is possible to obtain an initial slope of the P-CMOD curves and establish their relationship with the P-δ curves. In the hot tests, the P-CMOD curve was estimated from load-actuator-position curves, applying the aforementioned rate. The estimated P-CMOD was used to determine the Young's modulus by means of Jenq and Shah's compliance method [157].

According to these indications, after obtaining the initial compliance (C_i) of the P-CMOD curves for all hot specimens, the Young's modulus of concrete was obtained using the following expression:

$$E_c = \frac{6S_p a_0 V_1(\alpha_0^{'})}{C_i B_s D^2}, \tag{2.4}$$

where $V_1(\alpha_0^{'})$ is the geometric function given by Eq. (2.5)

$$V_1(\alpha_0^{'}) = 0.8 - 1.7\alpha_0^{'} + 2.4\alpha_0^{'2} + \frac{0.66}{(1-\alpha_0^{'})^2}, \tag{2.5}$$
$$+\tfrac{4D}{S_p}(-0.04 - 0.58\alpha_0^{'} + 1.47\alpha_0^{'2} - 2.04\alpha_0^{'3})$$

$$\alpha_0^{'} = \frac{a_0 + HO}{D + HO}, \tag{2.6}$$

and HO is the clip gauge holder thickness. In this case, HO was 1 mm and there was no accuracy loss if $\alpha_0^{'} \approx \alpha_0$. According to Eq. (2.4), materials with higher initial P-CMOD compliance curves have lower Young's modulus values.

2.5 Results and discussion

2.5.1 Mass loss

The thermogravimetric analysis of D0 (plain concrete) from room temperature to 1,000 °C after 28 cured days is presented in Fig. 2.2. As shown, D0 exhibited three different weight losses. The first was observed at 100 °C, represented a mass loss of 4.2% wt and was caused by the moisture present in concrete matrix. The second, observed between 200 and 500 °C, represented a mass loss of only 1.5% wt. It was caused by the dehydration of chemically bound water in several hydrates of the concrete (i.e., calcium silicate, carboaluminates, ettringite), although primarily to the dehydration of calcium silicate hydrates at 450 °C. The third was observed between 650 and 750 °C, represented a mass loss of 3.5% wt and was due to the decarbonation of calcium carbonate from the clinker and the filler [13].

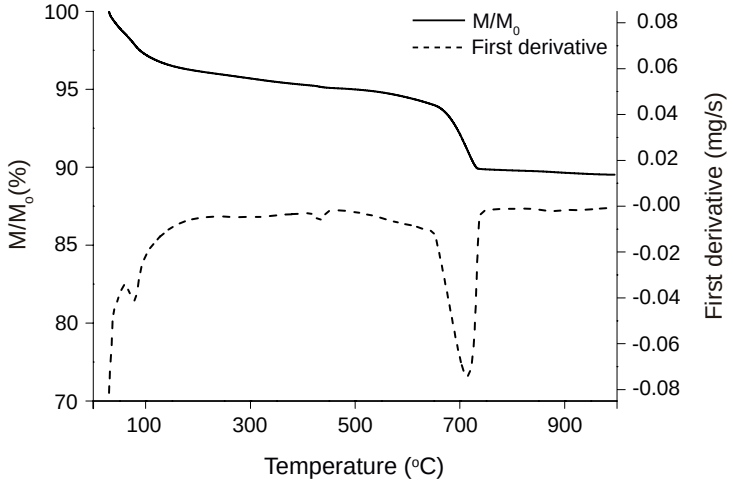

Figure 2.2 TG of concrete: D0 mix (without PP fibres).

Fig. 2.3 presents the mineral composition of a D0 mix at diverse temperatures (i.e., from room temperature to 900 °C) after 28 cured days. The main mineral compounds at room temperature were quartz (q); calcite: $CaCO_3$ (c); C_3S: Ca_3SiO_5 (s) and albite: $NaAlSi_3O_8$, (a). When the temperature of D0 sample reached 700 °C, the calcite disappeared, because it decomposed into CO_2 and CaO, as shown in Fig. 2.2.

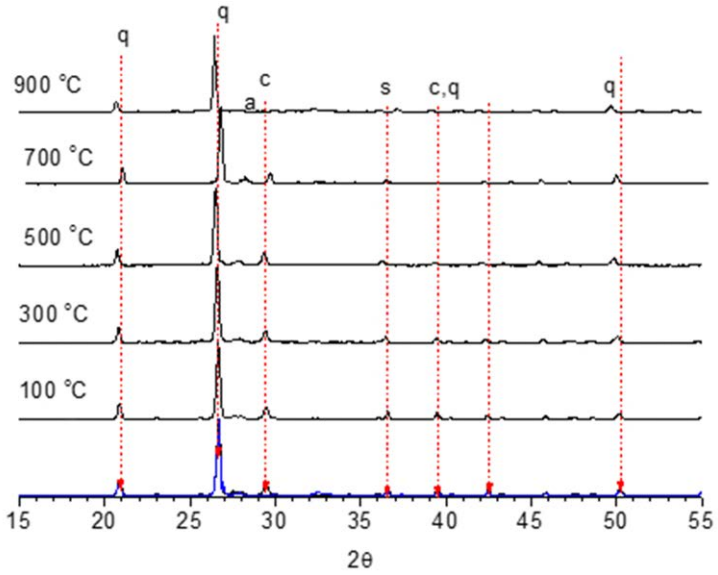

Figure 2.3 Mineral composition of D0.

The DSC analysis of the polypropylene fibres is presented in Fig. 2.4. The melting process occurred over a range of temperatures between 145 and 180 °C, as observed from the width of the melting endotherm. The melting point, that is, the peak of the melting endothermic, was 165 °C.

As shown in Fig. 2.4, the fibres presented only one mass loss at 460 °C, because at that point they were transformed into water and CO_2.

2.5.2 Fracture energy

The fracture energy results determined in each hot and cold test at the diverse exposure times are shown in Fig. 2.5. In D0 hot tests (Fig. 2.5.a), the fracture energy showed a decreasing trend at 100 °C. At that point, the concrete matrix still did not show any significant microcracking, so the vapour could not be freely evacuated. This led to high moisture gradients in the matrix, entailing a reduction in the fracture energy [205]. Above 100 °C, the fracture energy rose until a temperature of 500 °C was reached, as shown by the increased area under the load-deflection curves (work-of-fracture) (Fig. 2.6.b and c) [45], which increased along with the temperature. Although the maximum load decreased due to microcracking by spalling, deflection increased [205]. At 700 °C, a remarkable amount of microcracking occurred due to the decarbonation of the

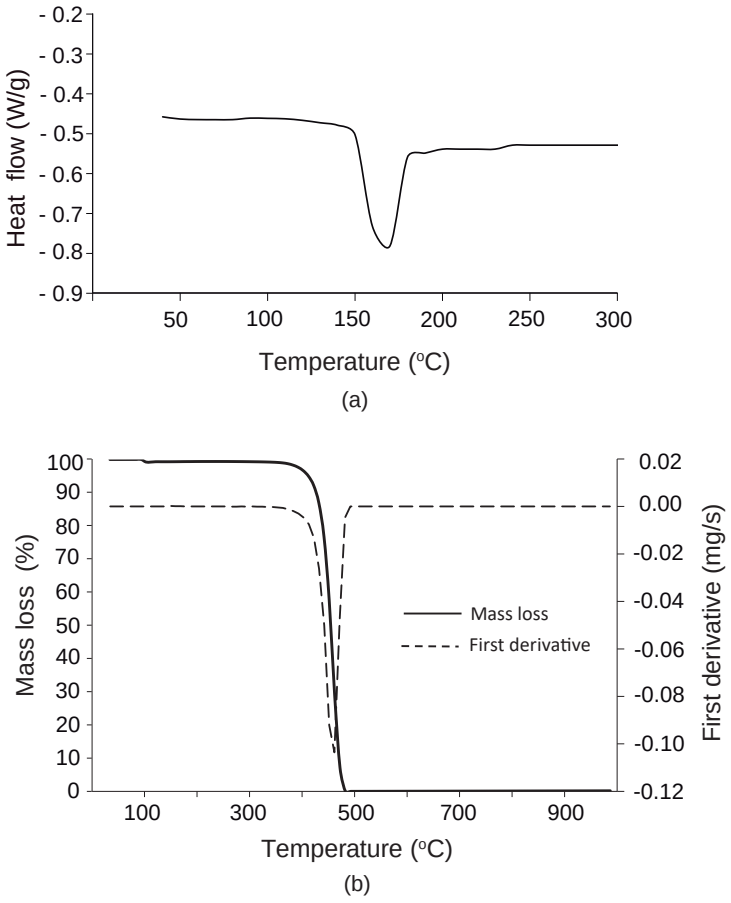

Figure 2.4 (a) DSC and (b) TGA of the PP fibres.

calcium carbonate (Fig. 2.2, Fig. 2.3), significantly reducing the resistance of the material [43, 177] and the fracture energy.

In the D1 and D2 hot tests carried out on the PP fibre-reinforced mixes (Fig. 2.5.a and b, respectively), the fracture energy was slightly higher at 25 and 100 °C because the fibres compensated the harmful effects of the high pressure and moisture gradients within the concrete [40, 43]. At low temperatures such as 25 and 100 °C, the PP fibres were not affected by temperature (Fig. 2.4), and their main role was the stitching of eventual cracks. At the aforementioned temperatures, the fibres gave the concrete higher ductility, as inferred from the higher fracture energy values (Fig. 2.5.b and c).

In the D1 and D2 hot tests at 300 °C, the fracture energy values rise because

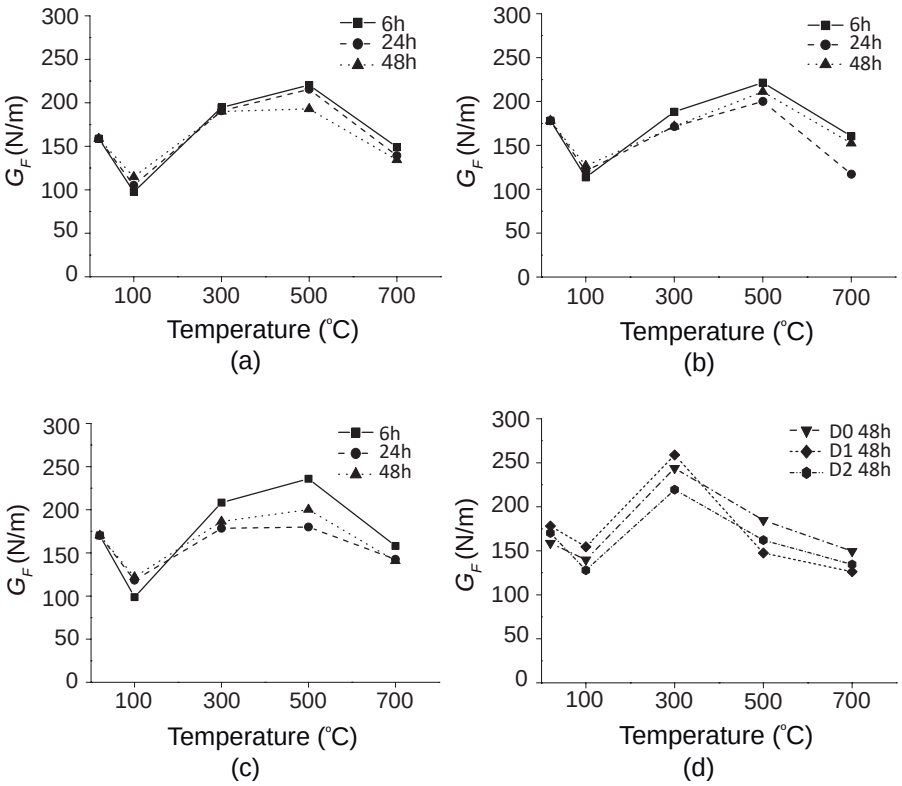

Figure 2.5 Evolution of the fracture energy with temperature for each exposure time: (a) D0 hot tests; (b) D1 hot tests; (c) D2 hot tests; and (d) cold tests.

the PP fibres had partially melted at this point (Fig. 2.4). Consequently, internal vapour was evacuated more easily, and the area under the load-deflection curves risen. Due to the reproducibility of results, only the load-deflection curves for D0 tests have been shown. In the D1 and D2 cases, the load-deflection curves are shown in Appendix A. At 500 °C, the fracture energy was still high for the same reasons that affected D0. At 700 °C, in addition to the decarbonation process, the PP fibres were completely transformed into gaseous water and CO_2, and the pore level in the concrete matrix significantly increased around 33 μm (the diameter of the fibres), as demonstrated in Fig. 2.9. The use of longer fibres increased the ductility of the material, as inferred from the higher fracture energy values in Fig. 2.5.c when compared with Fig. 2.5.b. Furthermore, the longer

fibres created a greater network of channels through which vapour could be more efficiently evacuated, reducing damage to the concrete matrix and increasing the fracture energy [43].

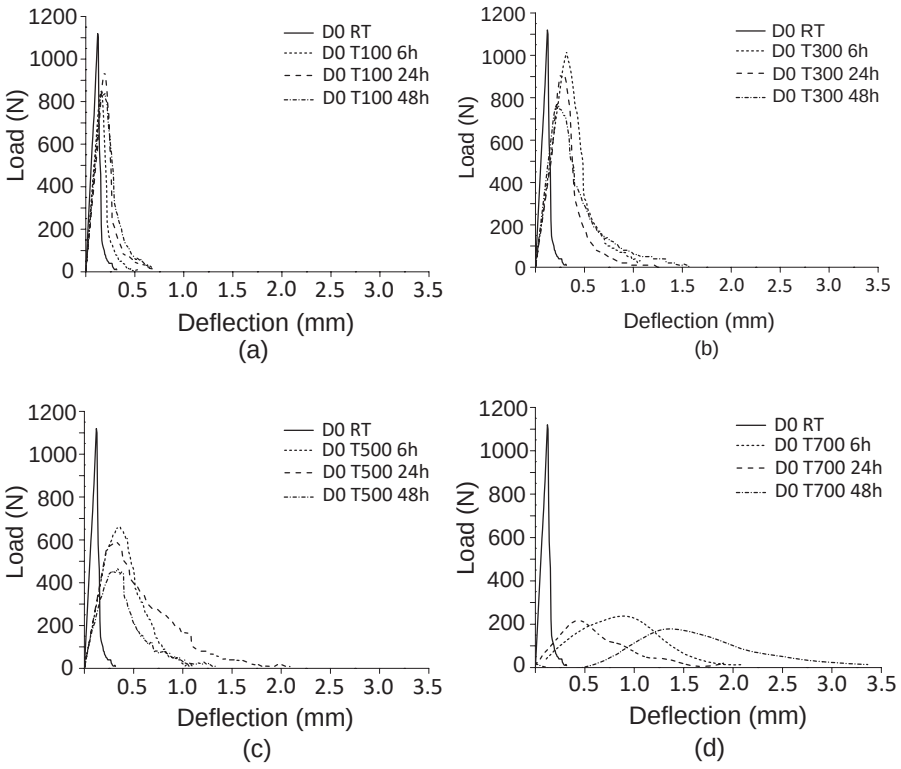

Figure 2.6 Load-deflection curves in D0 hot tests: (a) 100 °C; (b) 300 °C; (c) 500 °C; and (d) 700 °C.

Regarding the D0 cold test, the trend was similar to that of D0 hot tests, with a difference: additional microcracking occurred due to the cooling process, resulting in an earlier damage to the matrix (Fig. 2.5.d) [43,205]. Comparing the D1 and D0 cold tests, at 100 °C the addition of PP fibres increased the ductility of the material, as shown by the growing deflection in Fig. 2.8. The D1 and D2 load-deflection curves of cold tests have been represented in Appendix A due to the reproducibility of results. It is worth noting that they showed qualitatively a similar trend with a more pronounced deflection. At 300 °C, the maximum load noticeably decreased as the PP fibres partially melted (Fig. 2.4). The deflection

increased because the matrix had more pores due to the melting of the fibres, which, in turn, led to higher ductility (Fig. 2.7) [43]. Both effects (i.e., a light decrease in maximum load and an increase in deflection) led to higher fracture energy (Fig. 2.5.d). At 500 and 700 °C, the trend of the load-deflection curves was the same as at 300 °C (Fig. 2.8). The main difference was that the fibres were completely melted at that temperature, so the damage level was higher (Fig. 2.4).

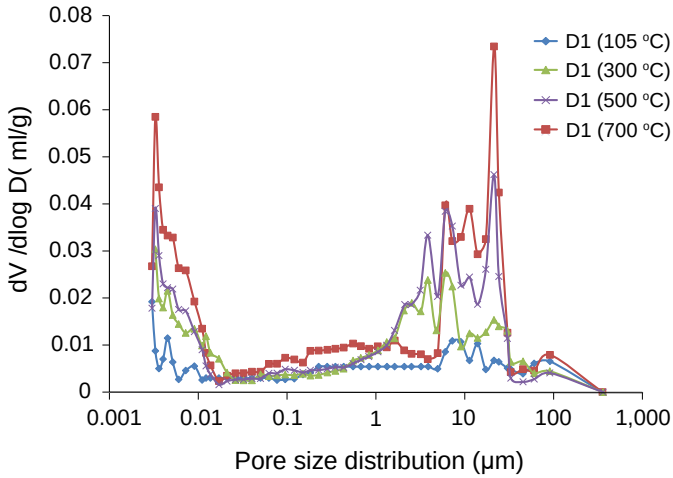

Figure 2.7 Pore size distribution of D1 concrete.

Regarding the D1 cold test (Fig. 2.5.d) in comparison with the D1 hot test, the maximum load increased at 100 °C, as two effects happened simultaneously: the effect of temperature on the cement paste, improving its hydration [43, 205], and the reduction in internal pressure because there was more time for it to be released during the cooling process [205]. As a result, the fracture energy was higher in the D1 cold test (Fig. 2.5.b). At higher temperatures (300, 500 and 700 °C), the pore level and microcracking in the cement paste increased, owing to the heating process and the additional effect of the thermal gradient during cooling [43,177,205]. A similar effect was observed by Tufail et al. [177] through the compressive stress-strain curves after high temperature exposition. The addition of longer fibres weakened the bearing capacity of the material at room temperature and 100 °C, as seen from the comparison between D1 and D2 in hot and cold tests (Fig. 2.5.b-d, respectively). At 300 °C, when the fibres were partially melted, the network of channels in the matrix was larger, which entailed a significant reduction in spalling. As a result, the peak loads in the

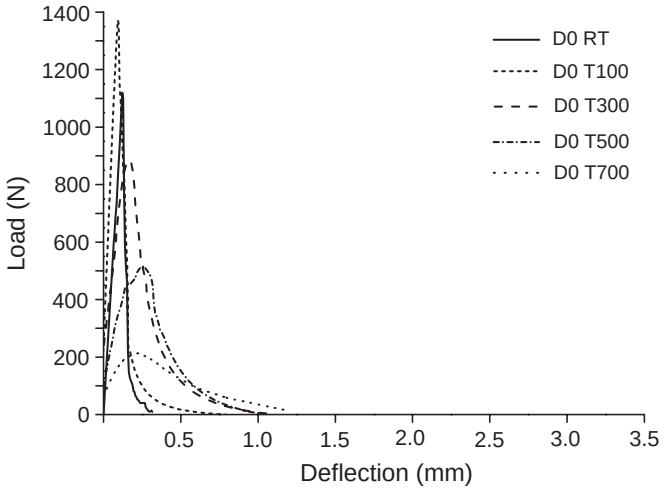

Figure 2.8 Load-deflection curves in D0 cold tests.

load-deflection curves were higher. At 500 and 700 °C, when the fibres had completely melted, the damage level was similar in D1 and D2.

Exposure time to a given temperature had no influence on the fracture energy, because the core of the specimens reached the target temperature in less than 6 h; hence, the thermal effects were similar at the different exposure times (6, 24, and 48 h).

2.5.3 Compressive strength

The compressive strength of all the mixes is presented in Fig. 2.9. As observed in Fig. 2.9.(a–c) (hot tests), a decrease-increase-decrease trend was seen in all three concrete mixes (D0, D1, and D2) at the three exposure times (6, 24, and 48 h). This behaviour was similar to that reported in previous studies by Zhang and Bicanic [205]. As regards D0 hot tests (Fig. 2.9.a), when the specimens were heated to 100 °C the compressive strength decreased, due to vapour pressure in the concrete matrix [43, 205]. Between 100 and 300 °C, the temperature affected the cement paste by improving its hydration, thus leading to an increase in the compressive strength. At temperatures above 300 °C, the matrix showed considerable microcracking; as a result, the compressive strength decreased with the increase in temperature. In the D1 and D2 hot tests (Fig. 2.9.b and c), in which the specimens were reinforced with PP fibres, the results were qualitatively and quantitatively similar to those obtained by the D0 (Fig. 2.9.a). The fibres

did not improve the compressive mechanical properties [145]. Furthermore, the inclusion of fibres in the matrix reduced the compressive strength at 700 °C, when they were completely melted.

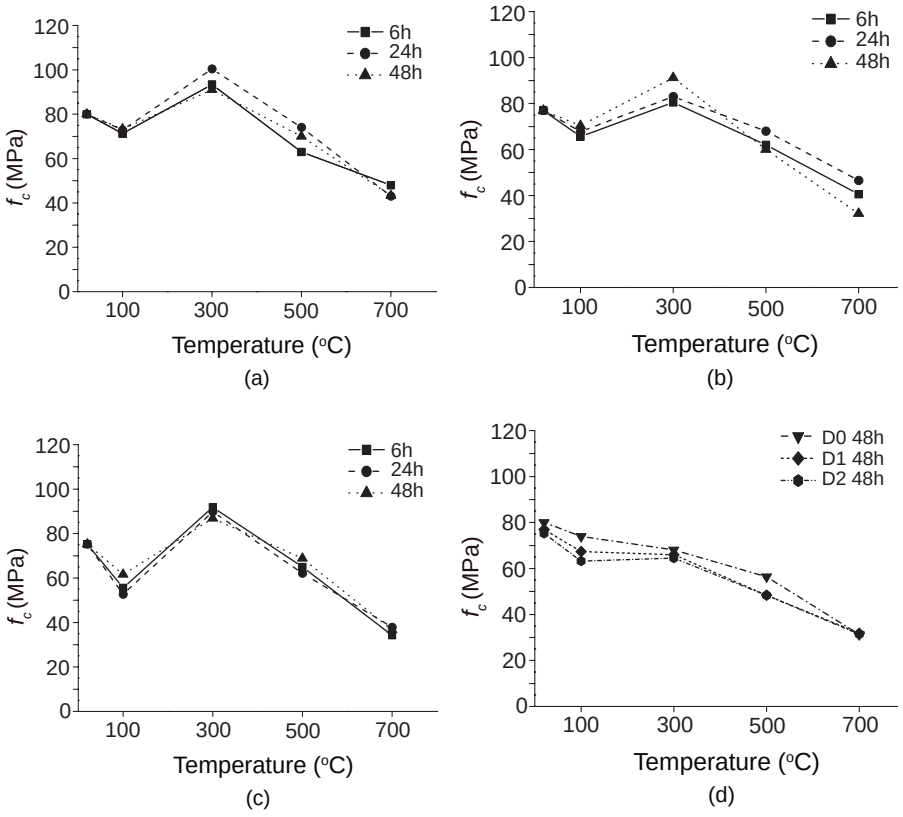

Figure 2.9 Evolution of compressive strength with temperature at each exposure time: (a) D0 hot tests; (b) D1 hot tests; (c) D2 hot tests; and (d) cold tests.

Regarding the D0 cold tests (Fig. 2.9.d), the evolution of the results represented a decrease-increase-decrease trend, in keeping with the findings of previous studies [205]. At 100 °C, the compressive strength was slightly greater than in the hot tests because this temperature did not generate high vapour pressure. At 300 °C, the microcracking caused by the heating and cooling processes prevented any increase in resistance, as was the case in the hot tests (Fig. 2.9.a), leading to a decrease in the compressive strength [126]. At 500 °C, the com-

pressive strength decreased because the damage sustained during the heating and cooling processes was more significant, due to the higher temperature reached [205]. At 700 °C, the very high temperature caused the decomposition process of the cement paste [43, 205] along with microcracking during the cooling process. As for the PP fibre-reinforced specimens, that is, D1 and D2 (Fig. 2.9.d), the compressive strength was similar to that of D0 at 100 °C, although it decreased in some cases when the proportion of fibres was very high, as shown in Fig. 2.9.d, due to the worm effect of fibres, leading to more pores in the concrete matrix [145]. At 300 °C, the fibres were partially melted, the fibre channels were not completely free, and vapour discharge was consequently more difficult, generating spalling. Because of this, the concrete matrix sustained further damage, in comparison with room temperature and the same mixes in hot tests. At 500 and 700 °C, the fibres were melted, and the behaviour was similar to that observed in the D0 cold tests. Exposure time to a given temperature had no influence on the compressive strength, because the core of the specimens reached the target temperature in less than 6 h; hence, the thermal effects were similar at the different exposure times (6, 24, and 48 h).

2.5.4 Young's modulus

The hot and cold tests showed a decreasing trend from 25 to 700 °C, so rigidity always decreased. The decrease in E_c with temperature in all mixes was due to the microcracking of the cement paste caused by the heating procedure (in hot tests, Fig. 2.10.(a–c)) and the additional effect of the cooling process (in cold tests, Fig. 2.10.d) [43]. Compared with the hot tests, the Young's modulus of the material at 25 °C [40, 63] was improved by adding PP fibres (Fig. 2.10.b and c). Nevertheless, there was a sharp drop of approximately 50% at 100 °C, which shows how the vapour pressure quickly affected this property. However, from 100 to 700 °C the evolution of E_c was less marked and almost linear [43, 177, 205]. As the temperature rose, thermal microcracking took place, which entailed a reduction in the rigidity of the concrete [43]. The effect of the fibres was barely noticeable at temperatures below 500 °C. The highest values were obtained by the PP fibre-reinforced concrete. The effect of the PP fibres was only slightly noticeable, but it is worth noting that both the D2 mixes (reinforced with long fibres) and D1 mixes (reinforced with short fibres) achieved better results. The reason for this is that the addition of PP fibres increases the ductility of the material, and this effect is more noticeable when the PP fibres are longer [63]. At higher temperatures, internal vapour pressure is reduced by means of the canal connections generated by the melting PP fibres, so that vapour pressure

can be more efficiently evacuated [43].

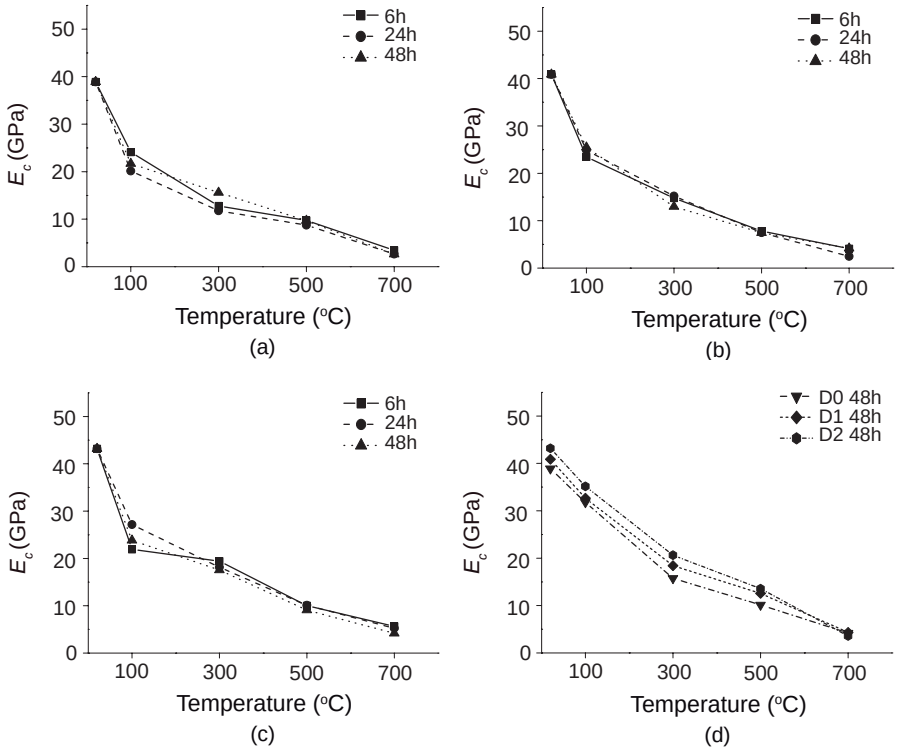

Figure 2.10 Evolution of Young's modulus with temperature at each exposure time: (a) D0 hot tests; (b) D1 hot tests; (c) D2 hot tests; and (d) cold tests.

2.5.5 Tensile strength

The trend observed in the hot tests (Fig. 2.11.a–c) responds to a three-stage decrease-increase-decrease pattern, in accordance with that proposed by Zhang and Bicanic [205]. The effect of the PP fibres was not very noticeable on the splitting tensile strength (Fig. 2.11.b and c) in the tests conducted at 25 °C [145]. For all mixes in hot tests (D0, D1, and D2), the tensile strength decreased when the mixes reached 100 °C, in keeping with the trend shown by the compressive strength [43, 205]. When the temperature rose above 100 °C, the tensile strength of concrete increased because of the hydration effect caused by the temperature on the cement paste. In fibre-reinforced mixes, a more noticeable decrease took

place between 500 and 700 °C due to dehydration, the decomposition of the cement paste [43, 205], and the melting of the fibres, which created more voids in the concrete matrix than in the D0 mix [23, 43, 160].

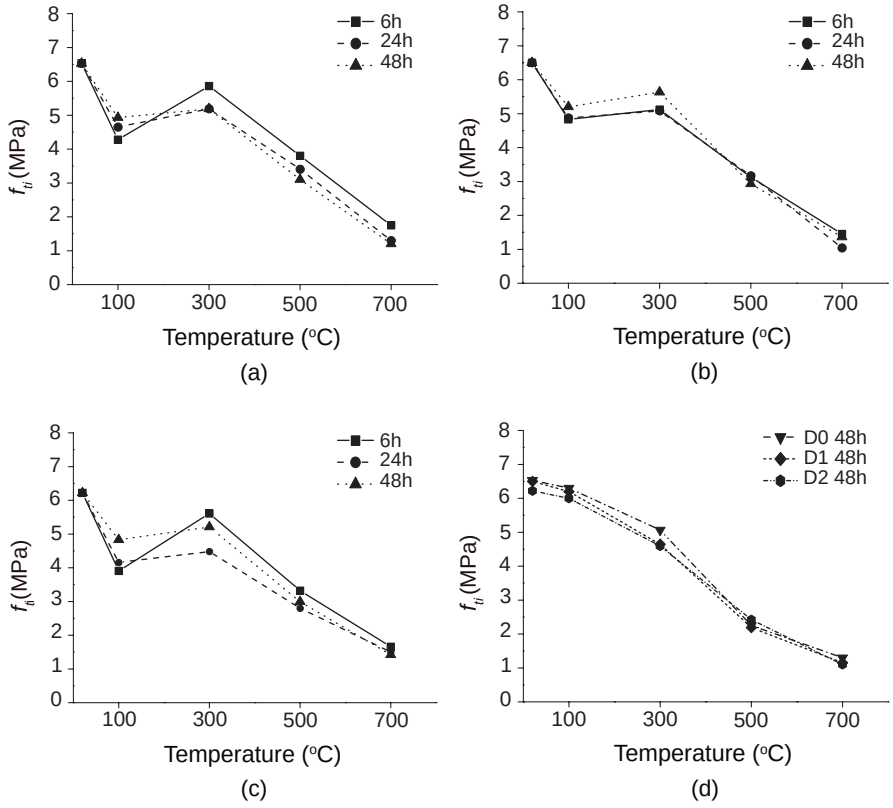

Figure 2.11 Evolution of splitting tensile strength with temperature at each exposure time: (a) D0 hot tests; (b) D1 hot tests; (c) D2 hot tests; and (d) cold tests.

The evolution of the results in the cold tests (Fig. 2.11.d) presented a decreasing trend, as in previous studies [43,205]. The splitting tensile strength results at 100 °C were better than in the hot tests because vapour pressure had more time to be evacuated during the cooling process. At temperatures above 100 °C, the concrete matrix, which was already damaged by the previous heating process, showed a further increase in internal damage due to the cooling process, which generated more microcracks and propagated already existing ones [205]. The

effect of the PP fibres on the splitting tensile strength was more remarkable than their effect on the residual compressive strength, but the behaviour was similar. The addition of PP fibres to the concrete matrix created a worm effect that increased the number of pores. This effect was more remarkable when the amount of fibres and their length increased. When concrete mixes reached temperatures above 300 °C, the fibres were partially or completely melted, and the proportion of voids in the concrete matrix significantly rose. As a result, the splitting tensile strength decreased. This effect was more remarkable in mixes reinforced with longer fibres (D2, Fig. 2.11.d).

2.5.6 Characteristic length

Characteristic length, l_{ch}, was assessed in both the hot and cold mixes. This fracture parameter provides information about the intrinsic brittleness of the cohesive material [75, 151]. It is also directly related to the fracture process zone (FPZ), although it does not indicate its exact length [3]. Therefore, a material with higher characteristic length will also have a greater FPZ length and thus a higher ductility [22]. Because all specimens were of the same size, there was no size effect, and it was consequently possible to directly analyse the ductility of the mixes by means of the characteristic length values. The characteristic length is defined as:

$$l_{ch} = \frac{E_c G_F}{f_{tu}^2}, \tag{2.7}$$

where f_{tu} is the tensile strength and was, in this case, considered equal to the splitting tensile strength f_{ti}. The hot tests (Fig. 2.12.a–c) showed a decrease-increase trend, in which the lowest point was reached at 300 °C. If the temperature rose to 300 °C, this affected the cement paste, improving its hydration and leading to an increase in the splitting tensile strength (Fig. 2.11.a–c) [43, 205] and a decrease in the characteristic length. From 500 to 700 °C, the porosity level increased significantly, softening the material and increasing its ductility. Postpeak softening significantly increased, as shown in (Fig. 2.6.c and d), which led to higher characteristic length and FPZ values.

In the PP fibre-reinforced hot mixes (Fig. 2.12.b and c), the characteristic length was higher than in nonreinforced specimens (Fig. 2.12.a), as this increased when the PP fibres were partially or completely melted, resulting in a softer concrete matrix with higher ductility. However, this effect became more

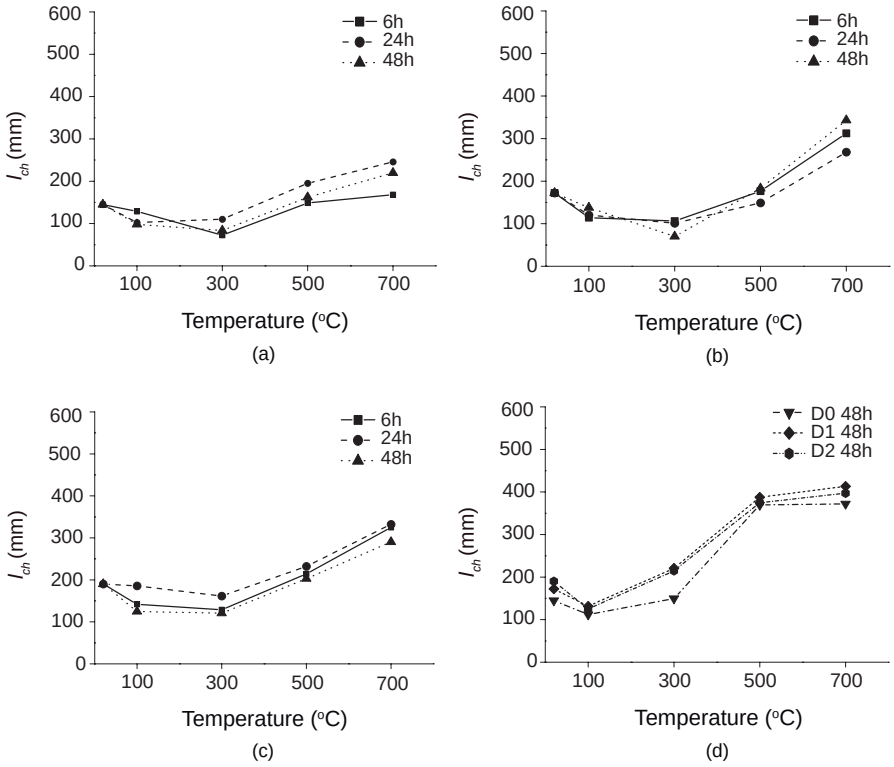

Figure 2.12 Evolution of the characteristic length with temperature for each exposure time: (a) D0 hot tests; (b) D1 hot tests; (c) D2 hot tests; and (d) cold tests.

noticeable at temperatures above 500 °C, because the porosity level was higher (Fig. 2.7).

In the cold tests (Fig. 2.12.d), at 100 °C the trend was similar to that of the hot tests, but the lowest characteristic length values were reached because the damage was sustained during the cooling process. At 300 °C, the matrix of cold mixes was more damaged than that of hot tests at the same temperature. This led to a more ductile material with a higher characteristic length. At temperatures above 300 °C, the level of damage in the matrix increased (Fig. 2.7), and the PP fibres melted. The addition of fibres increased ductility at any temperature, as in the hot tests; this effect was more noticeable when longer fibres were used.

2.6 Concluding remarks

In this chapter, the effects of temperature on the fracture behaviour and other mechanical properties of high-strength polypropylene fibre-reinforced self-compacting concrete were analysed, at a range of temperatures until 700 °C and after cooling at three different exposure times (6, 24 and 48 h).

The effect of temperature in concrete mixes led to an irreversible and increasing process of weight loss with higher temperatures. This process involved dehydration of residual moisture at low temperatures, dehydration of chemically bound water at medium-high temperatures, and decarbonation of calcium carbonate at higher temperatures. The addition of PP fibres created a network of channels in the matrix that reduced internal pressure damage and spalling effects. Nonetheless, it also reduced material strength at room temperature due to the higher number of pores generated by the major trapped air and the presence of PP material. As long as they are not degraded, the fibres have a light bridge effect on the crack front that stitches any eventual microcracking. This improves the strength properties and ductility of the concrete in both hot and cold conditions. Longer fibres reduced the effects of spalling and create a greater network of channels for the evaporation of internal pressure. Yet, they also increased the number of voids in the matrix, which in turn reduced its mechanical properties and causes a softening of the material.

Regarding the cooling process, this generated additional microcracking due to the thermal gradient that is more significant from medium-high temperatures, where this thermal gradient is more abrupt, and the fibres are partially melted. These harmful effects add to those sustained during the heating process. When the thermal gradient is more gradual, the cooling process does not cause significant damage, and the fibres help to stitch any microcracking. This leads to higher mechanical properties.

It was observed as exposure time had no effect when the temperature is uniformly reached in the entire matrix. From that point, the behaviour of concrete is the same regardless of the length of time the specimens are exposed to the temperature.

3 Effect of microstructure and steel fibres on the fracture behaviour of UHPFRC

3.1 Ultra-high-performance steel fibre-reinforced concrete

The addition of steel fibres in concrete materials significantly enhances the mechanical and fracture properties as well as the durability and the deformation at failure [60, 200]. Nevertheless, a high content of fibres can alters the microstructure and infers internal flaws in the matrix [102, 141]. In the case of ultra-high-performance fibre-reinforced concrete, where a large amount of fibres are added, the mechanical and fracture behaviour is remarkably dependent on the type of fibres used (i.e., geometry, length, etc.) as well as its distribution and orientation in the concrete matrix. Although many researches have studied the mechanical [66, 156, 190, 199, 203] and fracture properties [92, 170, 176, 185, 186] of UHPFRC, there are scarce studies which establish a connection among the influence of the distribution and orientation of different types of steel fibres in the microstructure with the mechanical and fracture behaviour.

In this chapter, a comprehensive experimental study about the influence of the type of steel fibres employed as reinforcement of UHPFRC on the mechanical

and fracture properties as well as its relationship with the distortion of the microstructure through X-ray computed tomography scan and mercury intrusion porosimetry has been carried out. Concrete reinforced with different steel fibres in length and diameter has been tested to determine its tensile properties and to relate the cracking and post-cracking strength of the mix with the fibres employed in their reinforcement as well as with the pore structure of the matrix.

3.2 Description of the UHPFRC mixes

3.2.1 Mix proportions and specimen preparation

Four different mixes of ultra-high-performance fibre-reinforced concrete were prepared. The mixes only differed in the kind of steel fibres used as reinforcement. The constituents of the matrix were the same for all mixes and are specified in Table 3.1. The UHPFRC mixes were designed and manufactured following the recommendations given by Deeb and Karihaloo [47]. The binder materials were Type I Portland cement 52.5 R/SR produced by the Portland Valderribas cement factory, silica fume (SF) manufactured by SIKA and ground-granulated blast-furnace slag (GGBS) provided by Arcelor. The aggregates were two types of quartz sand with different maximum aggregate size. The finest sand had a maximum particle size of 0.315 mm while the coarsest one was below 0.800 mm. A third-generation polycarboxylic ether-based superplasticizer (MasterGlenium ACE 325) with a specific gravity of 1.04 manufactured by BASF was used.

Table 3.1 Components and mix proportions of UHPFRC mixes.

Constituent	kg/m^3
cement (c)	544
silica fume	214
GGBS	312
water (w)	188
fine sand ($< 315\ \mu$m)	470
coarse sand ($< 800\ \mu$m)	470
superplasticizer (SP)	42
w/c	0.34
w/binder	0.17

Two different steel fibres were used in the study. Both were supplied by Bekaert and called as micro- and macro-fibres in this study. The micro-fibres

were straight OL 13/.20 model, 13 mm in length and 0.20 mm in diameter. The macro-fibres were hooked-end RC80/30CP model, 30 mm in length and 0.38 mm in diameter. The length of macro-fibres was limited in order to obtain good self-compactability of the mix reinforced with the longest fibres, DL (Table 3.2).

The four UHPFRC mixes used in this study were labelled as RC, DS, DL and DSL with the type of fibres and dosage specified in Table 3.2. The RC mix without fibres (plain concrete) was considered as the reference concrete matrix used as control. The remaining mixes were fibre-reinforced and contained the same fibre content (2.5% in volume fraction). Therefore, the difference between the fibre-reinforced mixes was only the type of fibre used as reinforcement. Specifically, the DS mix was reinforced only with micro-fibres, the DL mix with macro-fibres, and the DSL mix was a hybrid reinforced concrete with both types of fibres, combined at 50% (i.e., 98 kg/m^3 of micro-fibres and 98 kg/m^3 of macro-fibres).

Table 3.2 UHPFRC mixes and fibre proportions.

Mix	Fibre type	Fibre dosage (kg/m^3)
RC	no fibres	0
DS	micro-fibres	196
DL	macro-fibres	196
DSL	micro-fibres (50%) and macro-fibres (50%)	196

Each of the fibre-reinforced mixes (i.e., DS, DL and DSL) were used to cast 4 beams ($100 \times 100 \times 440$ mm^3), four cubes ($100 \times 100 \times 100$ mm^3) and four cylinders (100×200 mm^2). The concrete specimens were manufactured in a vertical mixer. The coarsest constituent (i.e., coarse sand) and the finest one (i.e., SF or GGBS) were mixed first, followed by the next coarsest constituent (i.e., fine sand) and next finest constituent (i.e., cement), and so on. Before each addition, the constituents were mixed for at least 2 min. The superplasticizer was added to the water in order to fluidize the dry mix. Afterwards, the water-SP mixture was poured in the mixer. All constituents were mixed for at least 30 min to obtain the right consistency. After 24 hours, the specimens were unmolded and cured in water at ambient temperature for 28 days.

3.3 Experimental program

3.3.1 Compression and Young's modulus tests

The compressive strength of all mixes (i.e., RC, DS, DL and DSL) was determined following the indications of EN12390-3:2009 [55] from the cubic specimens. According to this standard, the loading rate was established as 0.5 MPa/s. The tests were performed in a servo-hydraulic testing machine equipped with a load capacity of 3,000 kN. The Young's modulus of mixes was determined in accordance to EN12390-13:2014 [54] by gradually loading a cylindrical specimen in compression to approximately one third of its failure load in the same servo-hydraulic machine. Two linear variable differential transformers (LVDTs) at 180° were used to measure the shortening of the distance between the machine platens and thus obtain the average strain undergone by the cylinders.

3.3.2 Tensile and fracture behaviour tests

Steel fibre-reinforced concrete (DS, DL and DSL mixes)

In fibre-reinforced concrete, a distinction must be made between its cracking strength (related to the tensile strength of the matrix) and the ultimate tensile strength of the fibre-reinforced composite material (i.e., cementitious matrix + fibres), considering that the addition of fibres influences both strengths. For this reason, it is necessary to carry out an experimental study to determine these strengths separately. In a recent paper, López et al. [110] proposed a simplified inverse analysis method to determine the tensile properties of UHPFRC using unnotched four-point bending tests, distinguishing between first-cracking and tensile strength. In that study, the authors proposed a simplified method to obtain not only the tensile stress-strain ($\sigma - \varepsilon$) behaviour prior to crack localisation (Fig. 3.1.a), but also the stress-crack opening ($\sigma - w$) relationship after that point (Fig. 3.1.b). This type of analysis provides a wealth of experimental information, so it was selected to determine the tensile properties of the fibre-reinforced mixes (i.e., DS, DL and DSL). Table 3.3 summarizes the formulation proposed in [110].

where σ_{75} and σ_{40} are the stresses corresponding to the points of intersection between the experimental $\sigma_{fl} - \delta$ curve, with $\sigma_{fl} = \frac{P}{W_{el}}$ (flexural strength), and the straight line that represents a secant stiffness of 75% and 40% of the initial stiffness (S_0), $\sigma_{loc} = 97\%\sigma_{max}$ (with σ_{max} as the peak flexural strength) is the cracking location point, δ_{75} and δ_{loc} are the experimental midspan vertical displacements corresponding to the points of σ_{75} and σ_{loc} respectively, and

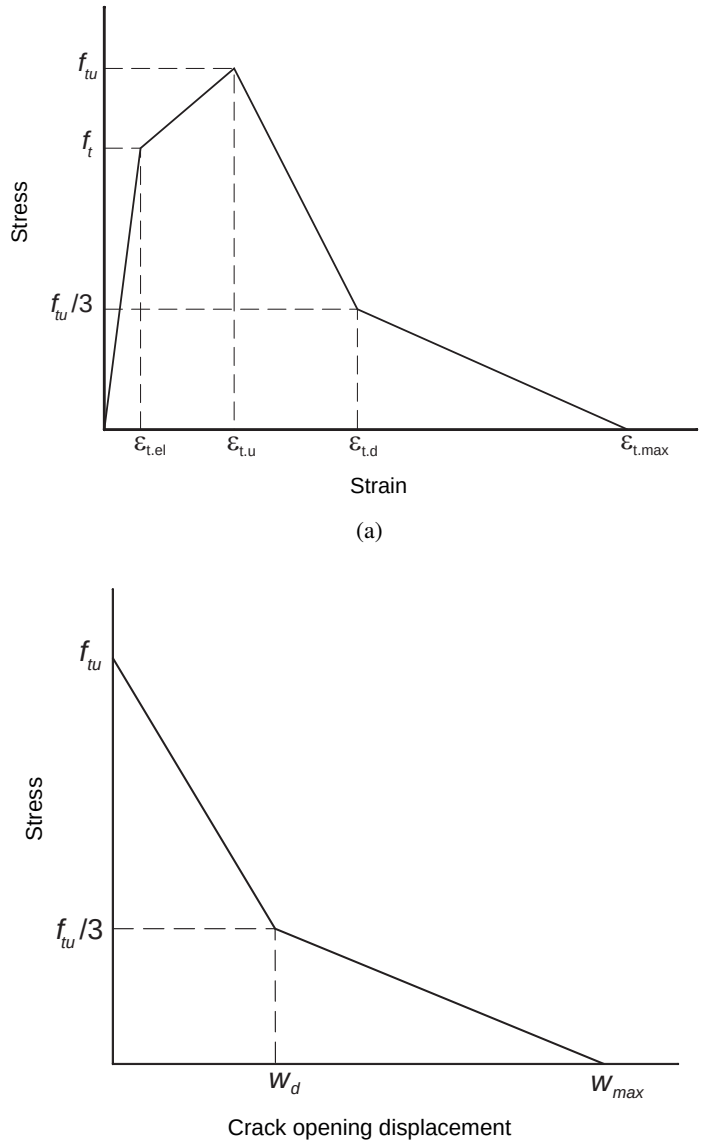

Figure 3.1 Constitutive laws obtained from inverse analysis [110]: (a) $\sigma - \varepsilon$ law and (b) cohesive $\sigma - w$ law.

Table 3.3 Formulation of the inverse analysis procedure developed by López et al. [110].

Parameter	$S_p/D = 3$	$S_p/D = 4.5$
f_t	$\frac{\sigma_{75}}{1.63}(\frac{\sigma_{75}}{\sigma_{45}})^{0.19}$	$\frac{\sigma_{75}}{1.59}(\frac{\sigma_{75}}{\sigma_{45}})^{0.21}$
$\varepsilon_{t.u}$	$\frac{f_t}{E_c}(7.65\frac{\delta_{loc}}{\delta_{75}} - 10.53)$	$\frac{f_t}{E_c}(6.65\frac{\delta_{loc}}{\delta_{75}} - 9.40)$
f_{tu}	$\alpha_t^{-0.18}(2.46\frac{\sigma_{loc}}{\sigma_{75}} - 1.76)f_t$	$\alpha_t^{-0.17}(2.24\frac{\sigma_{loc}}{\sigma_{75}} - 1.55)f_t$
$\varepsilon_{t.d}$	$\gamma_t^{-0.37}\alpha_t^{-0.88}(3.00\frac{\delta_{80u}}{\delta_{loc}} - 1.80)\frac{f_t}{E_c}$	$\gamma_t^{-0.38}\alpha_t^{-0.89}(2.82\frac{\delta_{80u}}{\delta_{loc}} - 1.68)\frac{f_t}{E_c}$
$\varepsilon_{t.max}$	$2.81\beta_t^{-0.76}\gamma_t^{-0.19}\alpha_t^{1.42}(\frac{\delta_{30u}}{\delta_{loc}})^{1.85}\frac{f_t}{E_c}$	$2.17\beta_t^{-0.76}\gamma_t^{-0.26}\alpha_t^{1.48}(\frac{\delta_{30u}}{\delta_{loc}})^{1.86}\frac{f_t}{E_c}$
w_d	$w_0 + (\varepsilon_{t.d} - \varepsilon_{t.u} - \frac{2f_{tu}}{3E_c})\frac{S_p}{3}$	
w_{max}	$w_0 + (\varepsilon_{t.max} - \varepsilon_{t.u} - \frac{f_{tu}}{E_c})\frac{S_p}{3}$	

δ_{80u} and δ_{30u} are the experimental displacements in the post-peak branch of the $\sigma_{fl} - \delta$ curve corresponding to the softening stresses of $\sigma_{80u} = 80\%\sigma_{loc}$ and $\sigma_{30u} = 30\%\sigma_{loc}$ respectively, $\varepsilon_{t.el} = \frac{f_t}{E_c}$, $\alpha_t = \frac{\varepsilon_{t.u}}{\varepsilon_{t.el}}$, $\beta_t = \frac{\varepsilon_{t.d}}{\varepsilon_{t.el}}$ and $\gamma_t = \frac{f_{tu}}{f_t}$. For a more detailed explanation see [109, 110].

Fig. 3.2.a shows a drawing of the four-point bending tests carried out in this study with an indication of the main dimensions of the specimens. Fig. 3.2.b illustrates a photograph taken during testing of one of the unnotched specimens. The tests were carried out under displacement control at a loading rate of 0.5 mm/min in a closed-loop dynamic universal testing machine with a maximum load capacity of 200 kN. The vertical midspan deflection (δ) was measured by using a 50 mm LVDT transducer mounted on a rigid frame. The use of a transducer with these characteristics makes it possible to record the full load-displacement curve until the specimen is broken into two halves. As shown, the S_p/D ratio was equal to 4; subsequently, following the inverse procedure proposed by López et al. [110], the values of the five key points to obtain the $\sigma - \varepsilon$ curves had to be obtained by linear interpolation between the values provided in Table 3.3.

Plain concrete (RC mix)

The reference concrete (RC mix) was subjected to two different tests. To compare the value of the flexural strength of the plain concrete with that of the fibre-reinforced mixes, four-point bending tests were performed on unnotched RC specimens. In this case, it was not possible to obtain a softening post-peak branch of the $\sigma_{fl} - \delta$ curve; nevertheless, the flexural strength (i.e., modulus of rupture) was determined with the four point-bending tests.

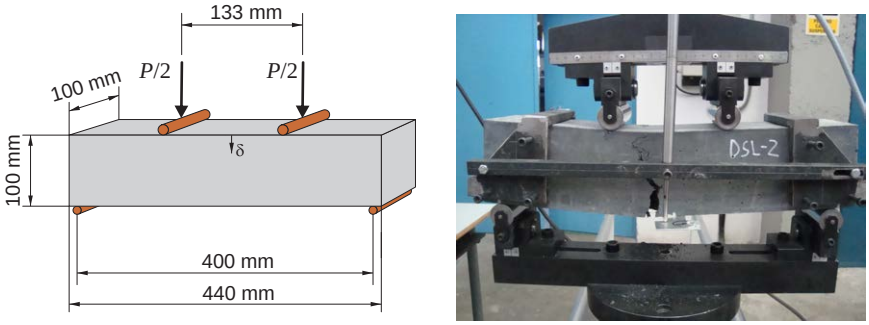

(a) (b)

Figure 3.2 Four-point bending test: (a) drawing of the test with dimensions and (b) photograph of one of the unnotched specimens during the test.

Three-point bending tests were also performed on notched specimens to determine the tensile and fracture properties of this type of concrete by means of flexural tests (Fig. 3.3.a). This provided data on the fracture energy and bilinear tension softening law ($\sigma - w_n$) for plain concrete. These tests were performed in accordance to the RILEM work-of-fracture method [146] applying the corrections proposed by Guinea et al. [53,68,140]. The tests were conducted controlling the crack mouth opening displacement (CMOD) with a clip gauge transducer. The midspan deflection was measured simultaneously with a LVDT transducer mounted on a rigid frame (Fig. 3.3.b), as in the case of the four-point bending tests. All tests were performed with the same dynamic machine.

The fracture properties were determined with an inverse analysis based on the non-linear hinge model to obtain the key points of the bilinear tension softening diagram. The procedure is described in [5]. It should be noted that a value of the direct tensile strength of concrete (f_t) is obtained from the bilinear approximation of the tension softening diagram (Fig. 3.4).

3.3.3 Microstructural analysis by X-ray CT and MIP

X-ray computed tomography: experimental tests and procedure of analysis

Various prismatic core samples ($100 \times 25 \times 25$ mm^3) were subjected to X-ray CT scans with the equipment of the X-ray laboratory of the University of Seville, Spain. The equipment consists on a Yxlon/Y Cougar Smt. system with a voltage

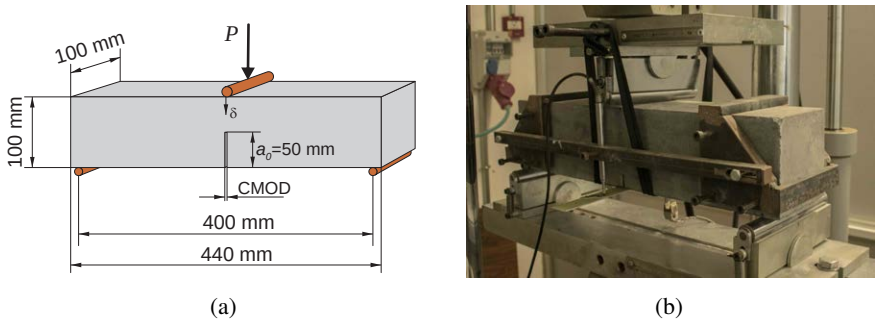

Figure 3.3 Three-point bending test: (a) drawing of the test with its dimensions and (b) photograph of one of the notched RC specimens during the test.

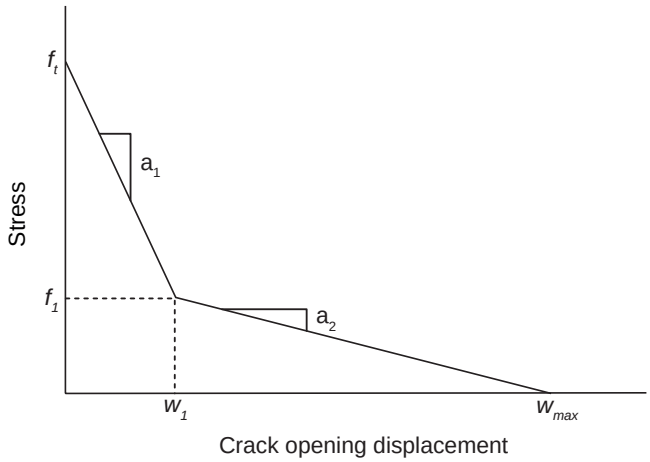

Figure 3.4 Bilinear tension softening diagram.

range of 25-160 kV and a current range of 0.01-1.0 mA. The equipment can generate 2D and 3D images with a maximum geometric magnification of 2,000x.

The core specimens were obtained from sawing the $100 \times 100 \times 440$ mm^3 beams used on the four-point bending tests. To avoid location effects on the porosity measurements (due to the concrete pouring into the molds), all the core specimens were obtained from the same part of the beam and four samples of each mix was scanned. Fig. 3.5 provides a diagram indicating the part from where the core specimens were taken.

The commercial software package VGStudioMax 2.2 was used for the 3D

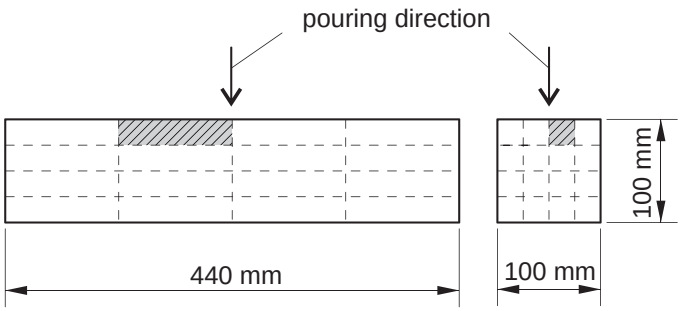

Figure 3.5 Extraction of the core specimens from notched beams.

reconstruction of the images from the multiple 2D X-ray scanned radiographs, with a scanning resolution of 1,024×1,024 pixels. The beam hardening and ring effects [143,173] were minimized by post-processing of the images. Specifically, a smoothing filter was applied to the data before the image analysis. One of the multiple 2D slices is shown in Fig. 3.6, where three main diverse shades of grey are distinguished in the grey-scale image. These shades are related to the different materials, depending on their density. The darkest shade corresponds to the lightest material (i.e., air voids or pores), the lightest shade shows the densest material (i.e., steel fibres) and the intermediate shade is that of the concrete matrix (with intermediate density).

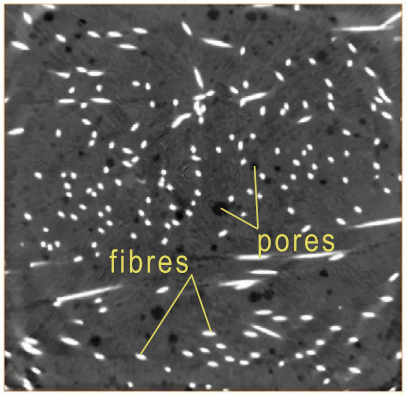

Figure 3.6 Pore and fibre areas in a grey-scale CT scanned slice.

To correctly identify the three main areas of interest (i.e., pores, steel fibres and matrix), it is necessary to determine the adequate grey-scale threshold

[143]. This segmentation into different phases according to grey-scale thresholds and the post-data analysis were conducted using AVIZO commercial software. Fig. 3.7 shows the results obtained from the sensitivity analysis of the pore volume fraction according to the grey-scale threshold, as proposed by Qsymah et al. [143]. As observed by the figure, the relationship between the selected pore volume and the grey-scale threshold is linear for lower threshold values. The optimum value of the grey-scale threshold is that where the relationship starts to be non-linear, determined as the point where the difference with the linear regression trend is 5% (the grey-scale threshold is 12,000 in this example). Since scanning conditions can affect the absorption density and also the threshold values quantitatively, a sensitivity analysis was conducted for each sample to determine the optimum threshold in order to ensure the reliability of the results.

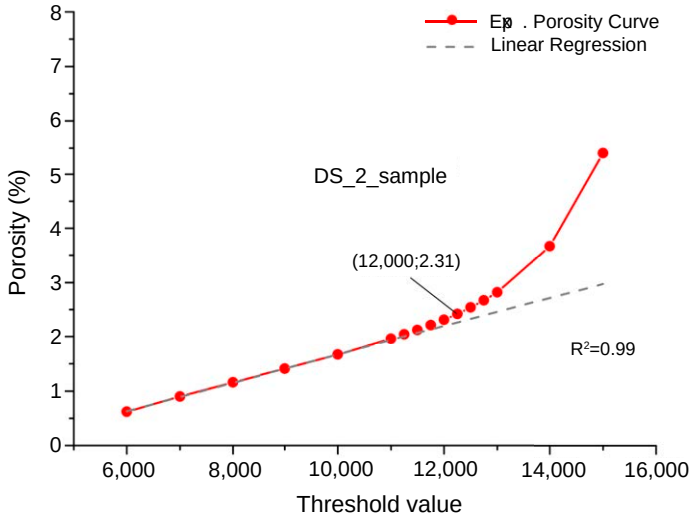

Figure 3.7 Sensitivity analysis to determine which threshold value yielded a realistic volume fraction.

If the same procedure were followed to determine the optimal threshold of the pores for the steel fibres, there would be a severe overlapping between nearby fibres, leading to errors (Fig. 3.8). For this reason, it is proposed a new procedure to determine the optimum grey-scale threshold enabling the correct identification of the fibres. This procedure introduces the fibre content as a new variable and the optimum threshold for the fibre segmentation is that where the volume of fibres obtained from AVIZO matches that calculated as the number

of fibres (not affected by the chosen threshold) multiplied by the unit volume provided by the fibre manufacturer. Following this procedure, a 3D sensitivity diagram (Fig. 3.9.a) can be drawn for each segmented sample.

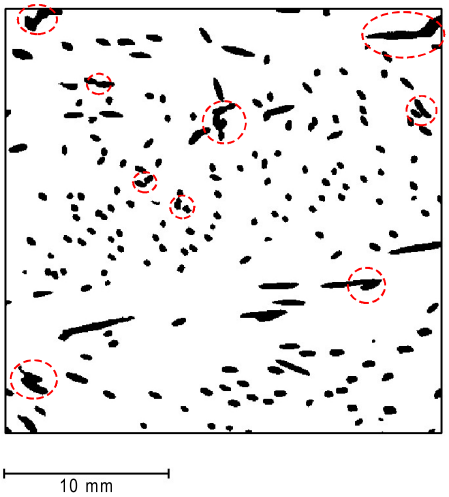

Figure 3.8 Fibre overlapping due to an excessively high grey-scale threshold value.

Fig. 3.9.a illustrates three clearly identified stages. Stage 1 (A-B) corresponds to the start of the graph (at the end of the whitest tones) where the range of the grey-value threshold follows a linear trend. At this stage, the fibre volume increases while the fibre content decreases due to the merging of pixels inside each fibre area. Stage 2 (B-C) follows a 3D curvilinear progression with a lighter decrement of the number of fibres. This effect is produced because the fibre regions are almost completely selected and thus pixel merging is significantly reduced. However, there is a new effect – fibre overlapping – that reduces the number of fibres more slowly. Fibre overlapping occurs when some fibres are very close to each other and for a certain range of the grey-value threshold the fibres start to overlap. Finally, Stage 3 (C-D) follows a 2D curvilinear progression where the number of fibres detected is stabilized because the overlapping effect disappears and only the fibre volume (i.e., fibre thickness) increases because of a slight thickness increment. The 2D orthogonal projection (Fibre Content-Porosity) shown in Fig. 3.9.b demonstrates that the optimum threshold value (1,570;2.02) is close to the loss of linearity (according to the end of Stage 1 and beginning of Stage 2). This point is obtained as the point where a deviation

of the linear regression is below 0.1. This definition of the optimum threshold value was consistent in all the cases analysed (either pore or fibre segmentation), providing strong consistency and reliability to the proposed methodology.

Mercury intrusion porosimetry

High-pressure mercury intrusion porosimetry technique was employed to determine the porosity and pore size distribution in the range between 1 and 10,000 nm. For each mix (RC, DS, DL, and DSL), three samples of 8 mm in diameter and 25 mm in length were tested. The maximum applied pressure was 413 MPa; the contact angle was 140° and the surface tension was 480 mN/m. The samples for the MIP tests were also extracted from the upper part of the three-point bending specimens, from a nearby area to that where the samples for the X-ray CT analysis were taken.

3.4 Results and discussion

3.4.1 Influence of steel fibres in the microstructure

One of the main objectives of this study is to analyse the tensile fracture behaviour of UHPFRC reinforced with different types of steel fibres and provide evidence of how such fibres have influence on the behaviour of the matrix through the porosity generated at different scales. The results of the porosity analysis are shown first so that the mechanical behaviour obtained for the different mixes can be related to the effect of the steel fibres on the pore structure of the matrix.

Mercury intrusion porosimetry

The porosity in concrete consists of four sort of pores: (a) gel pores, which are micropores whose characteristic dimensions are 0.5–10 nm; (b) capillary pores, which are mesopores with an average radius ranging from 5 to 5,000 nm and correspond to the water-filled space between the original cement grains; (c) macropores due to deliberately entrained air; and (d) macropores due to inadequate compaction [99]. Gel pores do not adversely influence the strength of concrete [99]. By contrast, capillary pores and other larger pores are responsible for a reduction in strength and elasticity. In order to analyse the different pore sizes, larger pores are studied using X-ray computed tomography and capillary pores were explored with mercury intrusion porosimetry.

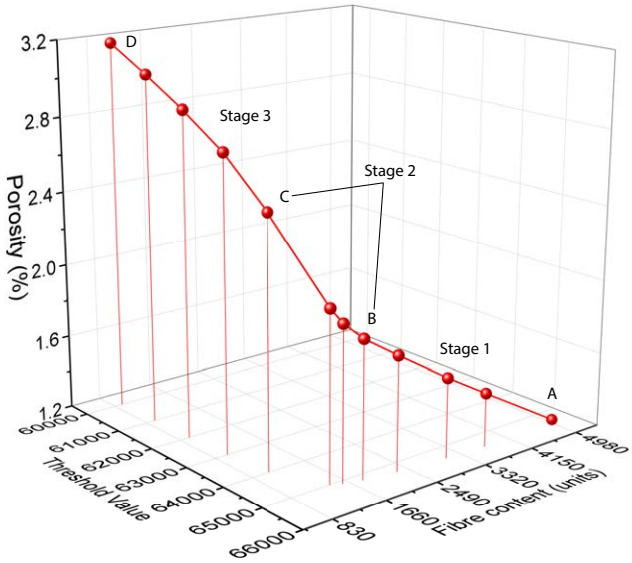

(a)

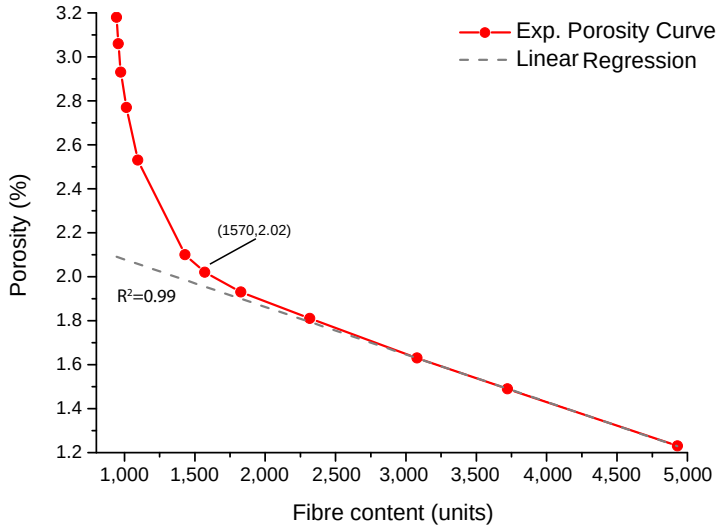

(b)

Figure 3.9 Fibre sensitivity analysis proposed: (a) 3D graph with the new parameter (i.e, fibre content); (b) orthogonal projection of Fibre Content-Porosity.

X-ray CT analysis

A comprehensive X-ray CT analysis of all mixes (i.e., RC, DS, DL and DSL) was performed, making it possible to explore the porosity of a large volume of material (Fig. 3.5) at a scale of pore sizes ranging from 0.3 mm to several mm and providing detailed information about key factors of the pore distribution inside the matrix (e.g., pore size, location, sphericity). Fig. 3.10 shows some images obtained with the X-ray computed tomography for each mix. The red spherical shaped volumes represent the pores and the golden lines represent the steel fibres.

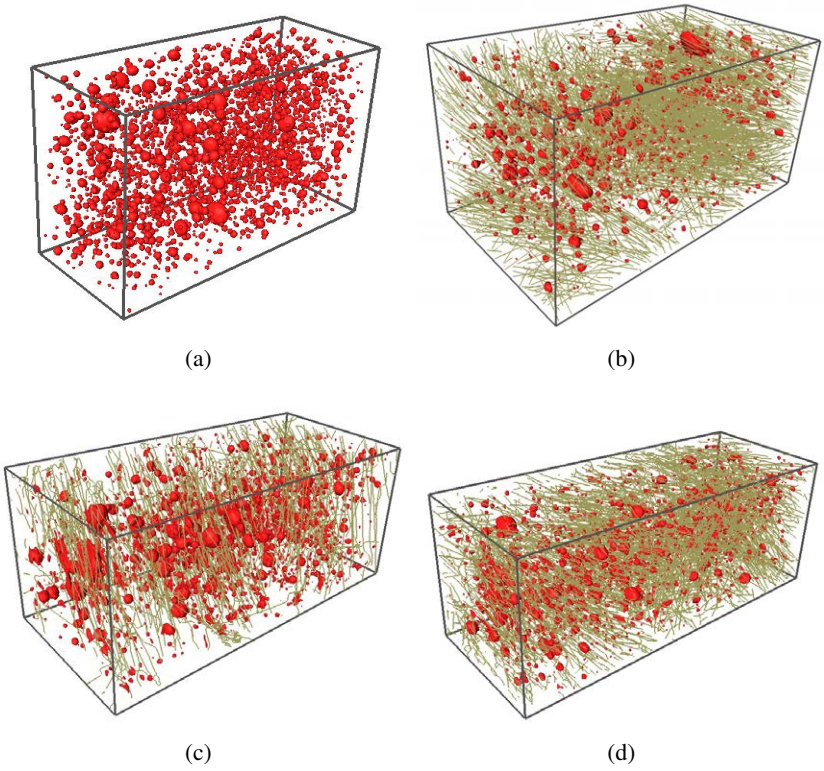

Figure 3.10 X-ray CT reconstruction of the RC (a), DS (b), DL (c) and DSL (d) mixes.

As mentioned above, this technique enables an in-depth analysis of the large pores of the matrix (between 0.3 and 4.6 mm). Fig. 3.11 shows the cumulative and differential pore volume versus the equivalent diameter (Eq. diameter). The

equivalent diameter is defined as:

$$d_{eq} = \sqrt[3]{6V_{pore}/\pi}, \tag{3.1}$$

where V_{pore} is the volume of a pore.

Fig. 3.11.a shows that porosity was highest in the RC mix and decreased when different types of steel fibres were added, especially when DS and DSL fibres were used. RC had a predominant equivalent diameter, d_{eq}, in the range of 0.5-1.3 mm; the distribution was much more uniform when the different types of steel fibres were used, although the number of larger pores was higher. Thus, the presence of fibres induced pore concentration and thus increased pore size [81].

Additionally, Table 3.4 reveals the most relevant parameters regarding the pore distribution analysis of the mixes, such as the average equivalent diameter, $\overline{d_{eq}}$, the total relative porosity, ($\phi_{xr} = \frac{\sum V_{pore}}{V_{total} - \sum V_{fibre}}$) and the average sphericity ($\overline{\Psi}$) obtained from X-ray image analysis and defined as:

$$\Psi = \frac{\pi^{1/3}(6V_{pore})^{2/3}}{A_{pore}}, \tag{3.2}$$

where A_{pore} is the surface area of a pore. Sphericity represents the diameter of a sphere with the same volume of the pore and how closely the shape of the pore is to a mathematically perfect sphere.

Table 3.4 Porosity parameters obtained for each mix.

Property	RC	DS	DL	DSL
$\overline{d_{eq}}$ (mm)	0.28 ± 0.03	0.33 ± 0.01	0.44 ± 0.03	0.34 ± 0.02
$\overline{\Psi}$	0.93 ± 0.02	0.91 ± 0.01	0.84 ± 0.01	0.88 ± 0.01
ϕ_{xr} (%)	4.0 ± 0.9	1.9 ± 0.3	3.4 ± 0.8	2.2 ± 0.5

One of the most relevant effects observed in the analysis was the size of the pores, which increased with the presence of fibres. As observed in Fig. 3.11.b, small-sized pores were more predominant in the unreinforced RC mix than in the fibre-reinforced mixes. The average equivalent diameter (Table 3.4) increased with the presence of fibres, particularly in DL reinforced with the longest macro-fibres.

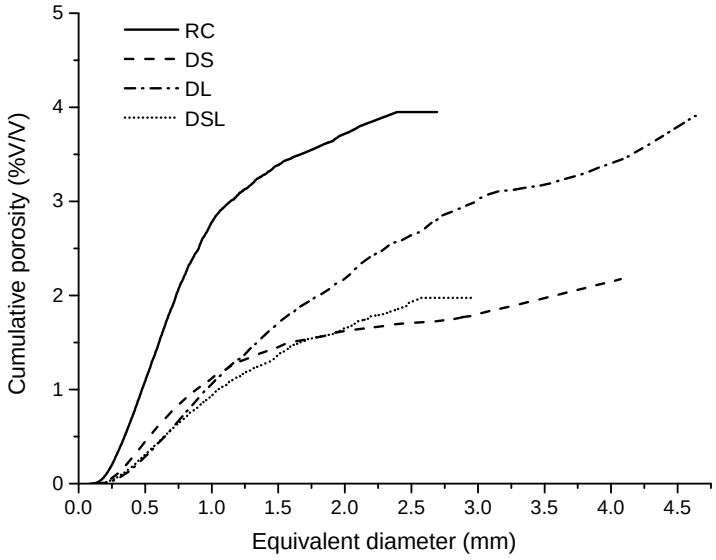

(a)

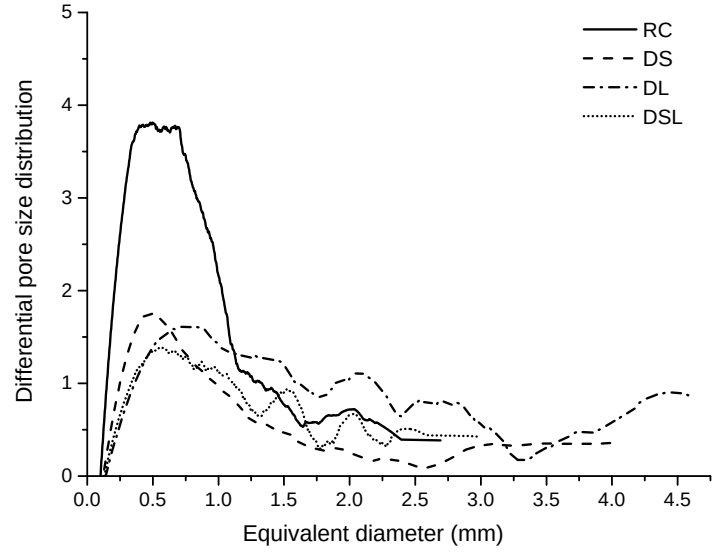

(b)

Figure 3.11 Pore size distribution of mixes determined by X-ray CT. Cumulative (a) and (b) differential porosity curves.

Most pores were clearly spherical, with values between 0.9 and 1. However, it was observed that the presence of fibres modified the shape of pores and reduced their sphericity. The greatest influence was produced by macro-fibres (DL mix) while micro-fibres reinforced mixes (i.e., DS and DSL) showed an intermediate effect. As shown in Fig. 3.10, the pores in the fibre-reinforced mixes had a more marked oval shape. The lower sphericity of the pores was produced by the distortion of the matrix due to the fibres and related with the concentration of pores around the steel fibres, as reported by Hwang et al. [81], and confirmed by the X-ray image analysis conducted in this thesis.

Fig. 3.12 presents the X-ray CT image analysis of a transversal cross section of the DL specimens. As observed, there was a concentration of pores under the steel fibres with a lower sphericity factor. Furthermore, the addition of fibres influenced the volume of pores generated in the matrix. The total porosity (ϕ_{xr}) was lower in the fibre-reinforced mixes. This means that the presence of fibres inside the cementitious matrix reduced its porosity: the fibres acted like tiny shovels helping to mix the concrete during its manufacturing inside the mixer, especially with the addition of micro-fibres. This effect was previously observed by Ponikiewski et al. [141], who reported a decrease in the porosity of the matrix in steel fibre-reinforced concrete with a high dosage of fibres. Simoes et al. [163] also obtained a slight decrease in the porosity of the matrix in some fibre-reinforced concrete mixes compared to the reference unreinforced matrix, especially in those with high fibre content. Nonetheless, it should be noted that there is a lack of information in the literature regarding the analysis of the porosity of steel fibre-reinforced concrete mixes compared to their equivalent unreinforced mix, particularly in ultra-high-performance concrete.

3.4.2 Analysis of the orientation and distribution of fibres

The distribution and orientation of steel fibres inside the matrix were also analysed using X-ray CT data. Fig. 3.13 shows the histograms of the fibre orientation, θ and φ (see the reference coordinate system provided in Fig. 3.13.c) obtained for each fibre-reinforced mix (DS, DL and DSL), where a predominant orientation of 0°, 90° and 180° was observed. Table 3.5 shows the average value of the orientation factors of the fibres, $\overline{\theta}$ and $\overline{\varphi}$, indicating the mean value and the coefficient of variation. Additionally, in order to study the fibre distribution inside the matrix, it was counted the number of fibres observed in a transversal section of each scanned specimen. In this regard, Table 3.5 also shows the number of fibres per unit area of transversal cross section, n_f, obtained from X-ray CT image analysis. At least four transversal cross sections were analysed

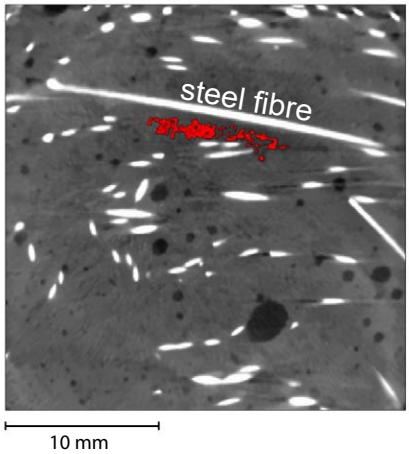

Figure 3.12 X-ray image of a cross section of a DL specimen. Red pores have a sphericity factor lower than 0.3.

for each sample. The n_f data shown in Table 3.5 were obtained as the average value of all sections analysed and specimens for each mix.

Table 3.5 Mean value of the average orientation factors of fibres and number of fibres per unit area of transversal cross section.

Mix	DS	DL	DSL
$\overline{\theta}(^\circ)$	37 ± 6	19 ± 4	29 ± 10
$\overline{\varphi}(^\circ)$	70 ± 1	72 ± 8	75 ± 4
$\frac{n_f}{cm^2}$	30 ± 5	7 ± 3	18 ± 7

A clear alignment effect was found in the macro-fibres [74], which were oriented parallel to the longest sides of the metal moulds. By contrast, the orientation of the micro-fibres inside the matrix was more random but a slight alignment effect was still observed. These effects are shown by the orientation angles of the fibres θ and φ (Fig. 3.13). A greater alignment effect was considered for values of $\overline{\theta}$ closest to zero and values of $\overline{\varphi}$ closest to 90°. An intermediate behaviour was observed in the blend of micro- and macro-fibres (i.e., the DSL mix). As expected, a greater number of fibres was observed in the transversal cross sections of the specimens made with the micro-fibre reinforced mix (DS). The lowest fibre values were found in the macro-fibre reinforced concrete (DL); an intermediate value of n_f was obtained in the DSL mix.

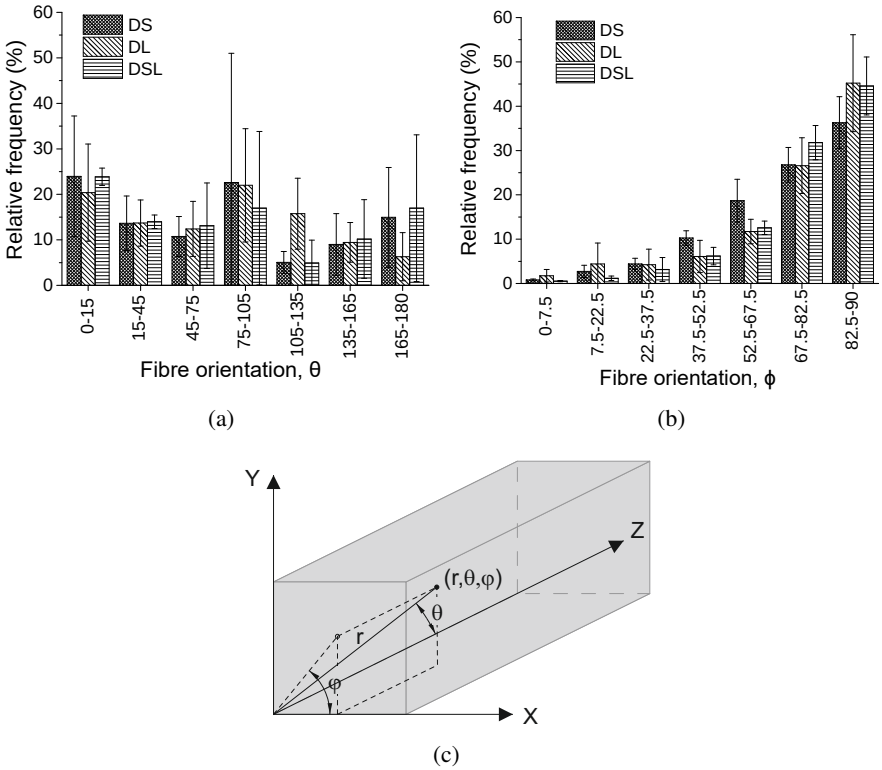

Figure 3.13 Histogram of the fibre orientation for theta (a) and phi (b) according to the reference coordinate system indicated in (c).

3.4.3 Mechanical properties

Compressive strength and Young's modulus

Fig. 3.14 shows the mechanical properties corresponding to well-established standarized tests, such as the compressive strength and Young's modulus obtained for the various UHPFRC mixes studied (i.e., RC, DS, DL and DSL).

As observed, the presence of fibres led to a significant improvement in the compressive strength of the mixes, with an average increase of 17% of f_c (similar to that reported by other authors under similar conditions [185]). This improvement was due to the positive sewing effect of the steel fibres against the tensile strains generated during the compression test in the concrete matrix [123]. As shown in Table 3.4, the compressive strength of each mix was inversely proportional to the porosity values (Table 3.4). With regard to the Young's

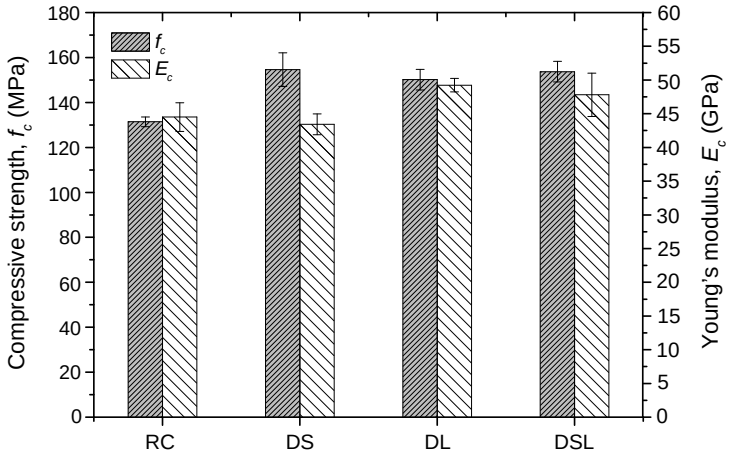

Figure 3.14 Compressive strength and Young's modulus of UHPFRC mixes.

modulus, no clear influence of fibres was observed, as reported by other authors [201]. In this study, a similar value of E_c was obtained for all mixes, even for the unreinforced mix (RC).

Flexural strength

The flexural strength, f_{fl}, (also known as modulus of rupture) of each concrete mix was obtained from the four-point bending tests. Fig. 3.15 shows the mean values and the deviation obtained for each mix.

As expected, a clear influence of the fibres was found regarding the flexural behaviour of the mixes. Mixes reinforced only with micro-fibres (DS) and those reinforced only with macro-fibres (DL) exhibited the best behaviour, with a similar maximum value above 20 MPa. Even in the blend of micro- and macro-fibres (DSL mix), where the lowest value was obtained, the flexural strength was more than three times that obtained for the unreinforced mix (RC).

3.4.4 Fracture properties

Constitutive $\sigma - \varepsilon$ law of fibre-reinforced mixes

The tensile stress-strain ($\sigma - \varepsilon$) curves for each of the fibre-reinforced mixes were obtained according to the inverse method proposed by López et al. [110] (Fig. 3.16.a). With the aim of facilitating the comparison of the tensile behaviour between the different mixes, Fig. 3.16.b shows the first-cracking strength (f_t) and tensile strength (f_{tu}) values of all mixes.

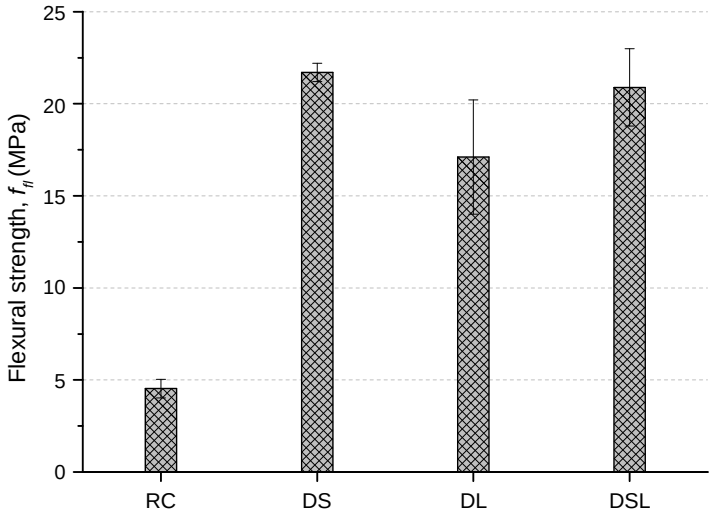

Figure 3.15 Flexural strength of UHPFRC mixes.

As expected, the tensile strength, f_{tu}, of the fibre-reinforced mixes increased with flexural strength. The highest strength value was obtained for the DS mix, reinforced only with micro-fibres. The values were quite similar in the DL and DSL mixes. Considerable differences were found between mixes in first-cracking strength. The highest value of f_t was obtained for the DS mix, reinforced with micro-fibres; it amounted to 1.96 times the value obtained for the RC mix. Nonetheless, the poorest value for the fibre-reinforced mixes was obtained for the DL mix, reinforced with only macro-fibres, and amounted to 1.45 times the value obtained for RC. In the DSL mix, results were intermediate between those of the DS and DL mixes. As observed, the presence of fibres improved the first-cracking strength, f_t, of the matrix and the tensile strength, f_{tu}, of the composite concrete (cementitious matrix + fibres) with two effects. The first effect was due to the well-known mechanisms of crack trapping and bridging [28] of fibres; the second effect was related to the influence of fibres on the porosity of the matrix. Overall, as shown by the X-ray CT analysis, fibre addition was associated with a decrease in the porosity of the cementitious matrix and a distortion in pore size and shape (i.e., the average equivalent diameter increased and the sphericity factor decreased). This explains the drop in the first-cracking strength observed in the DL mix compared to the other fibre-reinforced mixes. In this mix, porosity was greater than in mixes with micro-fibres, pore size was larger and the sphericity factor was lower (Table

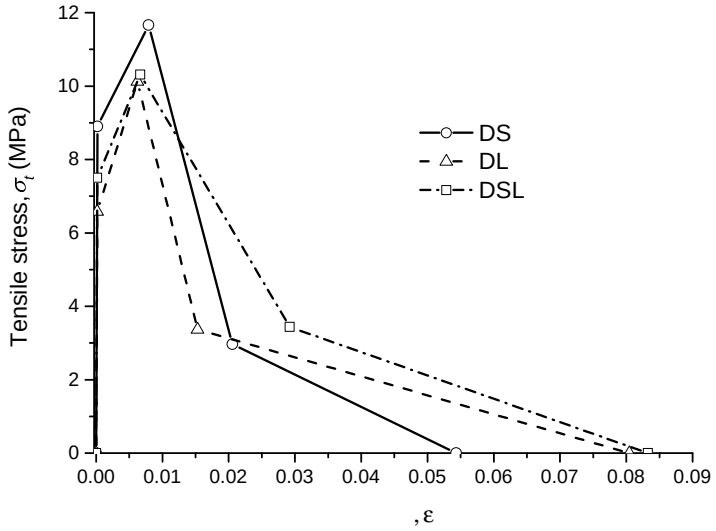

(a)

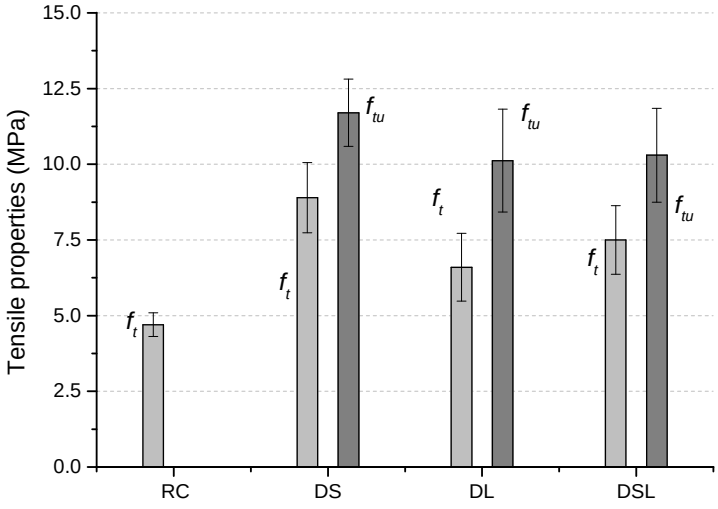

(b)

Figure 3.16 $\sigma - \varepsilon$ constitutive laws obtained for the fibre-reinforced mixes DS, DL and DSL (a) and tensile properties f_t and f_{tu} for all mixes (b).

3.4). This means that this type of macro-fibres distorts the matrix more than micro-fibres. Specifically, the mix reinforced with only macro-fibres exhibited a worse cracking behaviour. The first-cracking strength of the DL mix was still higher than that of the reference RC mix because of the positive effect of fibres explained above. The best cracking behaviour was obtained in the DS mix because of the very low porosity of the cementitious matrix and the larger number of fibres per area of the transversal cross-section in this mix (Table 3.5). The porosity obtained for this mix was even lower than that of the RC reference mix. It seems that steel fibres contribute to the mixing of concrete, acting as small micro-blades that help to beat the concrete matrix during the mixing, especially in the case of micro-fibres.

Fracture energy and characteristic length

In the plain concrete (RC), its size-independent fracture energy was determined according to the RILEM work-of-fracture method and with the corrections proposed by Guinea et al. [53, 68, 140].

According to this method, the specific fracture energy of the plain concrete mix was determined as follows:

$$G_F = \frac{W_m + W_{nm}}{A_{lig}} \tag{3.3}$$

where W_m is the measured work-of-fracture (area under the measured load-displacement curve) after the corrections of the initial part of the $P-\delta$ curve, W_{nm} is the non-measured work-of-fracture, determined by adjusting the tail of the softening branch of the curve and $A_{lig} = B_s(D-a_0)$ is the ligament area.

Additionally, the bilinear tension softening diagram ($\sigma - w$) for the unreinforced RC mix was also obtained according to the hinge model described in [5] and shown in Fig. 3.17.a.

In the fibre-reinforced mixes (DS, DL and DSL), the specific fracture energy was determined as the area under the cohesive $\sigma - w$ laws [88]. These laws were obtained in accordance to the procedure proposed by López et al. [109] (summarized in Table 3.3) and shown in Fig. 3.17.b for comparison (the axis scales are not the same in both figures because of the large difference between the values of the displacements of the plain concrete and the fibre-reinforced mixes).

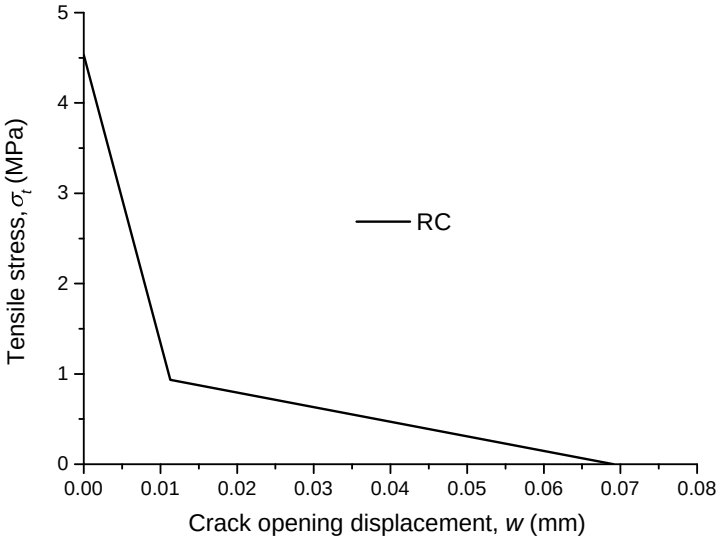

(a)

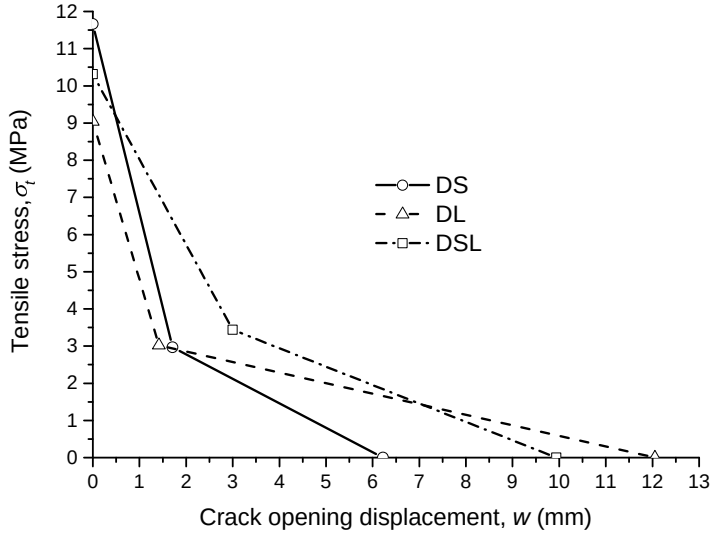

(b)

Figure 3.17 Bilinear tension softening diagram for (a) plain concrete RC and (b) fibre-reinforced DS, DL and DSL mixes.

Another important fracture parameter was the characteristic length, defined by Hillerborg [75] and given by:

$$l_{ch} = \frac{G_F E_c}{f_{tu}^2} \tag{3.4}$$

Table 3.6 shows the values of the specific fracture energy and characteristic length obtained for each mix.

Table 3.6 Fracture energy and characteristic length.

Mix	G_F (N/m)	l_{ch} (mm)
RC	$64 \pm 8\%$	128
DS	$19204 \pm 13\%$	6093
DL	$24614 \pm 17\%$	11832
DSL	$32552 \pm 15\%$	14667

As expected, the crack bridging effect of fibres [106] greatly increased the value of G_F [185] compared to that of the RC unreinforced mix, particularly the DL reinforced with the longest macro-fibres. The lowest value of the fibre-reinforced concrete mixes was obtained for DS, reinforced with micro-fibres due to its lower length and diameter and consequently its lowest interfacial bond with the cementitious matrix [201].

As the size of all specimens was the same, it was possible to conduct a ductility analysis directly based on the results of the characteristic length [41], so that the greater l_{ch}, the greater the ductility of the mix. The highest ductile behaviour was obtained for DL mix, with the highest specific fracture energy value and the lowest tensile strength value of the fibre-reinforced mixes. By contrast, the most brittle behaviour was shown by the unreinforced concrete, as its G_F value was much lower.

3.5 Concluding remarks

In the UHPFRC explored in this study, with a particular content of steel fibres, it was observed a reduction in the porosity of the cementitious matrix produced by fibres. The tensile properties of the UHPFRC mixes analysed depended on the type of fibres used as reinforcement. Although this concept may seem obvious, a distinction should be made between the first-cracking strength and the ultimate tensile strength. Fibres act as tiny shovels that help to mix the concrete during its manufacturing and reduce its porosity. This effect also led

to an increase of the first-cracking strength, f_t, of the reinforced mix, especially in the DS mix, reinforced only with micro-fibres and because additionally, there are a greater number of fibres crossing a unit sectional area of the matrix. The maximum tensile strength of the mixes, f_{tu}, was quite similar regardless of whether the fibres used to reinforce them were macro- (35/.55) or micro-fibres (13/.2). An enhanced ductile behaviour was obtained for the mixes reinforced with the longest macro-fibres due to the increase of the deformations before the debonding of the fibres. From a mechanical point of view, the best behaviour was obtained by the mix reinforced only with micro-fibres. Nonetheless, the higher price of this type of fibres can make it interesting to use a hybrid reinforced mix (50% of micro- and 50% of macro-fibres), which exhibited a better behaviour than the mix reinforced only with macro- fibres but whose price is lower than that of mixes with micro-fibres only.

4 Thermal effect on microstructure and fracture behaviour of UHPFRC

4.1 Thermal effect on ultra-high-performance concretes

The presence of steel fibres as reinforcement in concrete matrix not only hinders the propagation of cracks by bridging effect but also alters the microstructure of matrix inferring internal flaws, as observed in Chapter 3 and postulated by other authors [60, 200]. As analysed in Chapter 3, the pore morphology depends on the type of fibre added as well as its geometry and distribution. The pore morphology is an important factor on thermal conductivity of concrete, and as a consequence, on generation of the thermal gradients in the concrete matrix at temperature exposure. The internal stresses generated by the thermal gradients combined with the pore pressure from the water evaporation might reach the tensile strength of concrete and produce explosive spalling [10, 11, 87, 207]. In some applications, the UHPFRC must be capable of bearing thermal and mechanical loads simultaneously for long periods of time, like in structures for molten salt or steam storage tanks in solar power plants, as well as in energy storage systems by solid medium, in which, the

concrete material directly stores the thermal energy. This kind of study, relating the mechanical and fracture properties with the porosity evolution inside the UHPFRC at room and moderately elevated temperature, are really scarce in the literature.

This chapter is focused on the influence of temperature exposure on the deterioration of microstructure and the consequences on the mechanical and fracture properties of UHPFRC. To this, a comprehensive experimental campaign to determine the mechanical and fracture properties of a UHPFRC reinforced with diverse types of fibres and its corresponding non-reinforced matrix at 300 °C was manufactured. The influence of porous morphology on the mechanical and fracture behaviour was measured through X-ray computed tomography (CT) scan at 300 °C. Additionally, a thermogravimetric analysis of the concrete matrix was conducted from room temperature to 400 °C. Finally, a connection among the results from thermoanalytic techniques, microstructure results and the mechanical and fracture properties at room temperature (from Chapter 3 results) and 300 °C was established.

4.2 Ultra-high-performance concrete mixes

4.2.1 Mix proportions

In this study, the four mixes of ultra-high-performance fibre-reinforced concrete used in Chapter 3 were manufactured (i.e., RC, DS, DL and DSL). All mixes have a concrete matrix with the same components and mix proportions, but with different type of steel fibres as reinforcement. As cementitious materials were used the type I cement of 52.5 R/SR, manufactured by Portland Valderribas company, the silica fume S-92-D from SIKA company and the GGBS provided by Arcelor company. Two quartz aggregates were added to the mixture, the former, find sand, with a maximum particle size of 315 μm and the latter, coarse sand, with 800 μm. The chemical compositions of the components are shown in Table 4.1 The superplasticizer ACE 325 model provided by BASF company with a high-range of water reducing was also incorporated to improve the insufficient flowability due to the low w/b ratio. For more details of mix proportions and mixing process leads to Section 3.2.1.

The mineral composition of plain concrete (i.e., RC) after 28 curing days obtained by X-ray diffraction technique is shown in Fig. 4.1. The main mineral compounds at room temperature were fundamentally quartz, C_3S: Ca_3SiO_5 and Ca_2FeAlO_5. The pozzolanic reaction between the large amount of active SiO_2

Table 4.1 Chemical compositions of the constituents of UHPFRC.

	% mass				
compound	cement[a]	SF	GGBS	FA	CA
CaO	66.07	0.21	51.14	0.09	0.09
Al_2O_3	3.22	0.43	9.12	2.41	2.41
SiO_2	18.96	95.63	28.12	95.60	95.60
Fe_2O_3	4.62	0.10	0.42	0.08	0.08
MgO	1.50	0.39	6.06	0.02	0.02
SO_3	3.00	0.04	1.77	0.00	0.00
K_2O	0.20	0.79	0.54	1.49	1.49
N_2O	0.14	0.00	0.00	0.00	0.00
Na_2O	0.27	0.20	0.19	0.28	0.28
LOI	1.53	1.84	1.47	0.20	0.20

[a] Type I cement 52.5 R/SR

(silica fume) in the high strength admixture and $Ca(OH)_2$ generated during the cement hydration, has formed a lot of C-S-H gel and reducing $Ca(OH)_2$ and CaCO3 content, as it can be seen in Fig. 4.1 [23].

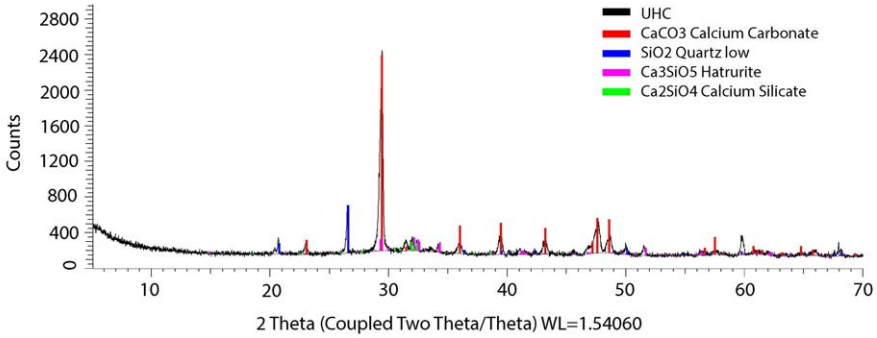

Figure 4.1 Scheme of heating procedure before mechanical and fracture tests .

4.3 Experimental program

The UHPFRC mixes (i.e., RC, DS, DL and DSL) were heated to 300 °C following a heating rate of 10 °C/min and three heat steps (i.e., 100, 200 and 300 °C)

as can be seen in Fig. 4.2. The temperature set point was maintained for 24 hours at each step to ensure the reaching of temperature in the sample core. The heating procedure was designed in three steps to give enough time to evaporated water to be evacuated through open porosity and so diminish the probabilities of spalling failure below 300 °C.

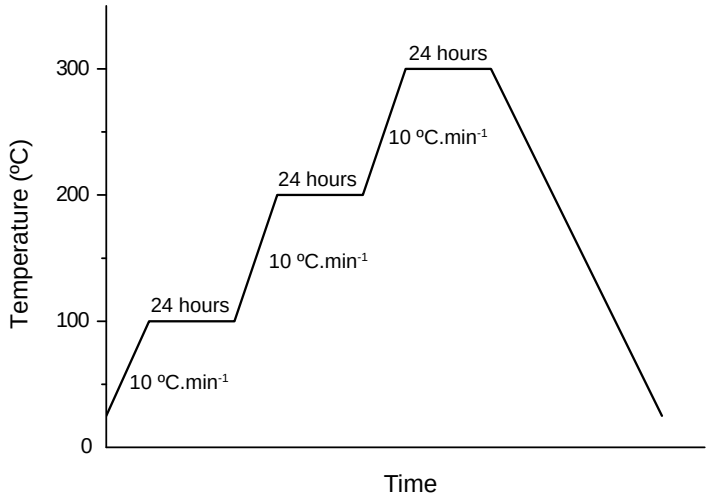

Figure 4.2 Scheme of heating procedure before mechanical and fracture tests .

4.3.1 Thermal tests

The effect of temperature on the concrete was monitored by thermal analysis and variable temperature X-ray powder diffractometry (VTXRD) analysis. VTXRD patterns were recorded at the X-ray laboratory of University of Seville, Spain by a Bruker D8 Advance diffractometer fitted with a high-temperature camera (Anton Paar XRK 900, Austria) and a position-sensitive detector (Bruker Vantec PSD, Germany) in the 25-900 °C temperature range at a heating rate of 10 °C/min (target: Cu, voltage 40 kV; current: 40 mA; $\theta : \theta$ geometry combining divergent Göbel mirror configurations; detector: radial Soller slits; time scans: 5 min).

Thermogravimetric analysis (TA), differential thermal analysis (DTA) and differential scanning calorimetric (DSC) were performed simultaneously at the Functional Characterization Service of the University of Seville using a TA (Q600-SDT model) instrument and alumina as reference material. The samples were put into crucibles in a chamber during the heating period at ambient air. The

heating was performed at a constant rate of 10 °C/min from room temperature to 400 °C.

4.3.2 Mechanical and fracture tests on heated concrete

The compressive strength of all mixes (i.e., RC, DS, DL and DSL) at 300 °C was determined according to EN12390-3:2009 [55] from the cubic specimens of 100 mm of side. The loading rate was established as 0.5 MPa/s and it was used a servo-hydraulic testing machine with a load capacity of 3,000 kN. The Young's modulus of concrete was calculated following the indications of EN12390-13:2014 [54] by gradually compressive loading a cylindrical specimen of 100 mm in diameter and 200 mm in height to approximately one third of its failure load.

Steel fibre-reinforced concrete (DS, DL and DSL mixes)

A distinction must be made in reinforced UHPFRC mixes (i.e., DS, DL and DSL) between its cracking strength (related to the tensile strength of the matrix) and the ultimate tensile strength of the fibre-reinforced composite materia since the addition of fibres influences both strengths. In this study, it was used the inverse analysis method proposed by López et al. [110] to determine the tensile properties of UHPFRC using unnotched four-point bending tests, distinguishing between first-cracking and tensile strength. The procedure followed was described in Chapter 3. For more details of inverse procedure see Subsection 3.3.2. Nevertheless, some modifications had to be cariied out owing to the temperature. The main drawback of high temperature is the impossibility of set the sensors on specimens. The four-point bending tests were done during entire testing within a furnace at 300 °C. The testing equipment of the servo-hydraulic machine used was specifically designed to be settled in a furnace. Notwithstanding the foregoing, only load and actuator position data can be reported due to the transducers cannot bear such high temperatures.

For the estimation of the load-deflection, $P-\delta$, curves from four point bending tests at 300 °C, this procedure was followed:

- It is assumed that the difference between the mid-span deflection and the actuator displacement is due to the machine appliance strain during the loading process.

- From the room temperature tests, it is established a mid-span to deflection-actuator displacement ratio, Ω, for each load applied.

$$\Omega = \frac{X_i^{def}}{X_i^{pos}} \tag{4.1}$$

where X_i^{pos} and X_i^{def} are the actuator displacement and the mid-span deflection at RT respectively.

- At 300 °C tests, it is estimated the mid-span deflection data from the Ω ratio for each load recorded as follows:

$$\Omega = \frac{X_{i_{300}}^{'def}}{X_{i_{300}}^{pos}} \tag{4.2}$$

where the $X_{i_{300}}^{pos}$ and $X_{i_{300}}^{'def}$ are the actuator position and the estimated mid-span deflection at 300 °C respectively.

For the estimation of the stress-strain curves on the Young's modulus tests the same procedure was followed but using LVDT data where the mid-span deflection. A MatLab code to estimate $P-\delta$ curves from $P-position$ following the aforementioned procedure is presented in Appendix C.

Plain concrete (RC mix)

Two different tests were carried out on reference concrete (RC mix). Four-point bending tests were performed on unnotched RC specimens to compare the value of the flexural strength of the plain concrete with that of the fibre-reinforced mixes. In this case, it was not possible to obtain a softening post-peak branch of the $\sigma_{fl}-\delta$ curve; nevertheless, the flexural strength (i.e., modulus of rupture) was determined with the four point-bending tests at 300 °C.

Three-point bending tests were also performed on notched specimens after 300 °C exposure to measure the tensile and fracture properties in accordance to the RILEM work-of-fracture method [146] with the corrections proposed by Guinea et al. [53, 68, 140]. More details about the procedure was described in Subsection 3.3.2.

4.3.3 Microstructure analysis

X-ray computed tomography scan

Four prismatic samples ($100 \times 25 \times 25$ mm^3) of each mix (i.e., RC, DS, DL and DSL) were subjected to X-ray CT scans after 300 °C exposure. The samples were obtained from sawing the $100 \times 100 \times 440$ mm^3 beams used on the four-point bending tests at 300 °C. The extraction process and the part from where the samples were taken are always the same to avoid location effects on the pore structure of matrix. The part from where sawn the samples were the same than the analyses at room temperature in Chapter 3. The X-ray CT data were reconstructed with the commercial software package VGSStudioMax 2.2 from the multiple 2D X-ray scanned radiographs with a scanning resolution of 1024×1024 pixels and the evaluation of pore results was used the software Avizo. For obtain more detail information about the procedure to determine the X-ray CT scan data and microstructure results see Subsection 3.3.3.

4.4 Results and discussion

In this section, the results of the experimental tests for the determination of the phase changes by means of thermogravimetric curves, the pore structure analysis by X-Ray CT scan and the mechanical and fracture properties at room temperature (from Chapter 3) and 300 °C are presented. The average value and the standard deviation are reported for each mixture and property determined.

4.4.1 Thermal analysis

The thermal equipment used to analyse the UHPFRC samples provides the thermogravimetric analysis (TG), the differential scanning calorimetry (DSC) and the differential thermal analysis (DTA) curves simultaneously for each sample. The information about the phase transitions and transformations were determined by the inflection points (i.e., peaks) in DTA diagrams [11][52] (dash-point curve in Fig. 4.3). From the thermal analysis diagrams (Fig. 4.3) different temperature ranges can be defined. The first observed effect is the evaporation of moisture and the water in capillary pores in the range from 20 to 250 °C (4.5% wt of mass loss) [43, 62, 184], which is an endothermic process. The second, in the range of 250 and 400 °C, dehydration of C-S-H gel is observed, with a total mass loss of 2.5% wt [15, 62] and an endothermic process too.

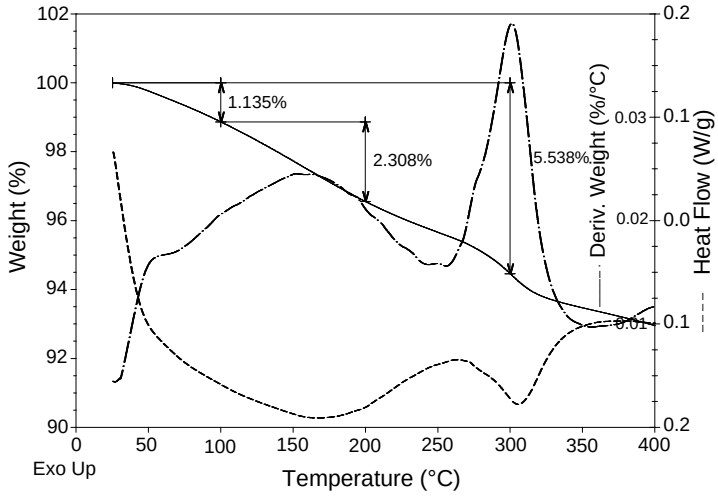

Figure 4.3 Plots of the TG, DTA and DSC curves of reference concrete, RC mix, from room temperature to 400 °C.

4.4.2 Microstructure analysis by X-ray CT scan

Four samples of each mix (i.e., RC, DS, DL and DSL) after 300 °C heating were analysed by X-ray CT scan and an average value of the porosity parameters determined were shown. The samples were sawn from the prismatic specimens ($440\times100\times100$ mm^3) from four-point bending tests. The samples analysed by X-ray CT scan were the same than were analysed at room temperature in Section 3.4. Thus, the differences found by the comparison of porosity parameters measured at room temperature (in Section 3.4) and 300 °C come exclusively from the thermal damage in the pore structure.

Fig. 4.4 shows 3D reconstructions of each mix (i.e., RC, DS, DL and DSL) after 300 °C heating by X-ray CT scan. The spherical shaped volumes represent the pores and the lines represent the steel fibres. The X-ray CT analysis conditions, details of equipment used, a description of the post-processing of X-ray CT images and their treatments has been comprehensibly described in Section 3.4. The interpretation of X-ray CT scan data was conducted by using Avizo software, which is specialized in X-ray CT treatments. The porosity, Φ_{xr}, their average equivalent diameter, $\overline{d_{eq}}$ and the average sphericity, $\overline{\Psi}$, are shown in Table 4.2 at room temperature and 300 °C for each mixture (i.e., RC, DS, DL and DSL mixes). The porosity parameters in Table 4.2 have been determined as display in Section 3.4.

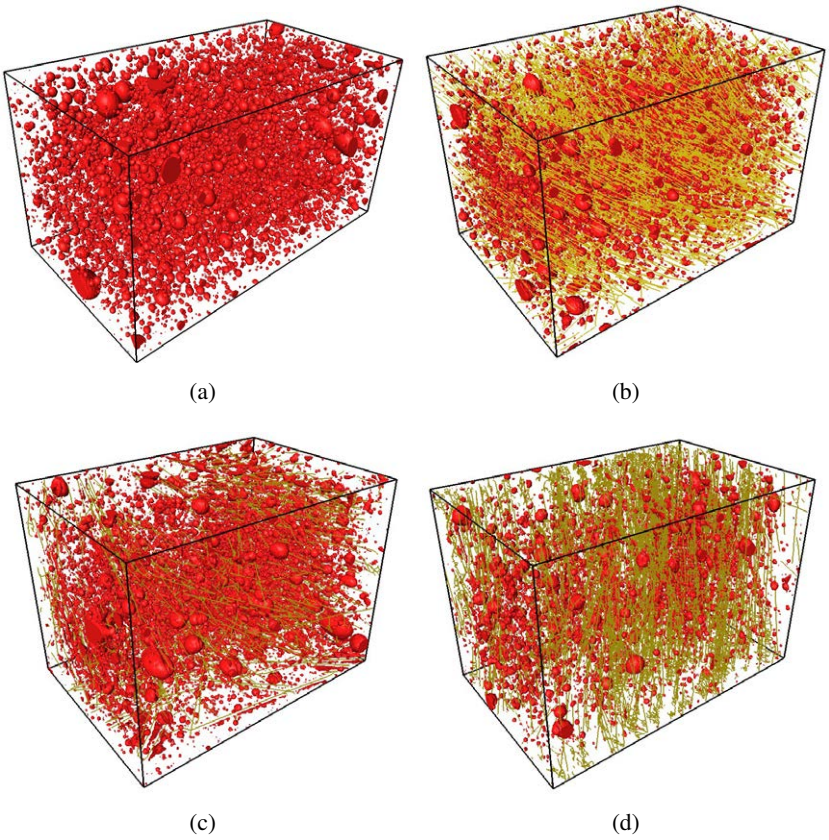

Figure 4.4 X-ray CT reconstruction of the RC (a), DS (b), DL (c) and DSL (d) mixes after 300 °C temperature exposure.

Table 4.2 Porosity parameters from X-ray CT analysis at RT and 300 °C.

	Room temperature (RT)			
Property	RC	DS	DL	DSL
$\overline{d_{eq}}$ (mm)	0.28 ± 0.03	0.33 ± 0.01	0.44 ± 0.03	0.34 ± 0.02
$\overline{\Psi}$	0.93 ± 0.02	0.91 ± 0.01	0.84 ± 0.01	0.88 ± 0.01
$\Phi_{xr}(\%)$	4.0 ± 0.9	1.9 ± 0.3	3.4 ± 0.8	2.2 ± 0.5
	300 °C			
$\overline{d_{eq}}$ (mm)	0.29 ± 0.02	0.21 ± 0.01	0.27 ± 0.01	0.21 ± 0.02
$\overline{\Psi}$	0.96 ± 0.01	0.91 ± 0.01	0.91 ± 0.01	0.92 ± 0.01
$\Phi_{xr}(\%)$	5.0 ± 0.3	3.9 ± 0.3	4.3 ± 0.9	2.6 ± 0.1

From porosity parameters, the cumulative porosity and differential pore size distribution of each pore, in y-axis, and their evolution with regard to the equivalent diameter, in x-axis, are presented in Fig. 4.5 and Fig. 4.6 respectively. Fig. 4.6.a shows the differential pore size distribution of each mix (i.e., RC, DS, DL and DSL) at room temperature and Fig. 4.6.b presents the data after 300 °C heating.

At room temperature, it is observed that the addition of steel fibres (i.e., DS, DL and DSL mixes) significantly reduces the porosity, Φ_{xr} especially in DS and DSL mixes, as it is deduced from Table 4.2 and Fig. 4.5. It is important to emphasize this aspect, since a high concentration of fibres did not produce a negative distortion in the matrix but rather improves its microstructure by reducing the porosity. RC mix had a predominant equivalent diameter in the range of 0.25-1.2 mm (Fig. 4.6.a); the distribution was much more uniform when the different types of steel fibres were used, although the number of larger pores was higher. One of the most relevant effects observed in the analysis was the size of the pores, which increased with the presence of fibres. The average equivalent diameter, $\overline{d_{eq}}$, (Table 4.2) increased with the presence of fibres, particularly in DL mix, reinforced only with the macro-fibres. Most pores were clearly spherical with values between 0.8 and 1 (Table 4.2). However, it was observed that the presence of fibres modified the shape of pores and reduced their sphericity. The greatest influence was produced by macro-fibres (i.e., DL) while micro-fibres (i.e., DS and DSL) showed an intermediate effect.

The heating of the concrete mixes (i.e. RC, DS, DL and DSL) to 300 °C increased the porosity, Φ_{xr}, in all mixes (i.e. RC, DS, DL and DSL) (see Table 4.2) and Fig. 4.5), which implied a thermal damage generated within the material. The heating causes high internal pressure as a result of two endothermic processes: the evaporation of free water, between 20 and 250 °C [62], and dehydration of C-S-H gel [62, 184], between 250 and 400 °C, as additionally was confirmed for these mixes from the results of the thermogravimetric analysis shown in Fig. 4.3 and described in Subsection 4.4.1. These effects in conjunction with the lower porosity of the matrix in ultra-high-performance concrete with respect to ordinary concrete [169, 208], leads to reach high internal stresses that infer into the propagation of thermal damage. If the damage is significantly high, it might lead to an explosive spalling [10, 11, 87, 207].

The temperature effect in the pore structure of the matrix in all mixes (i.e., RC, DS, DL and DSL) affected more strongly to smaller pore-sizes (i.e., equivalent diameter below 2.6 mm) as it is deduced from the results of the differential pore size distribution shown in Fig. 4.6.b. This implies that smaller pore sizes reach

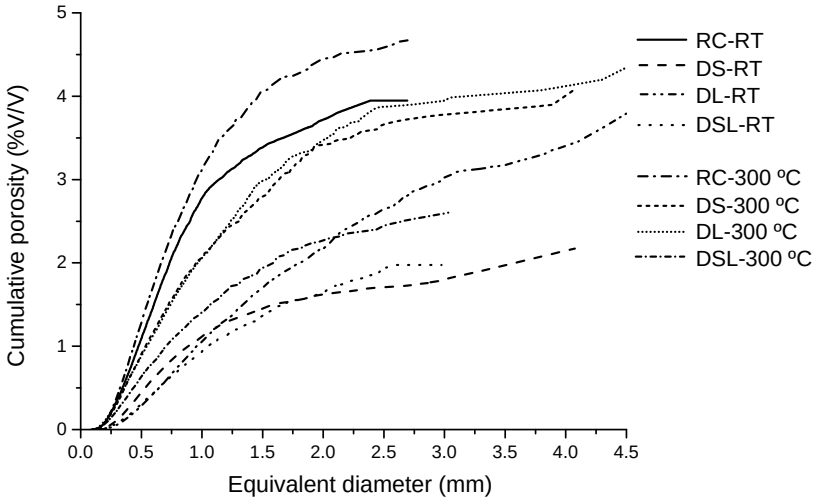

Figure 4.5 Cumulative pore size distributions of mixes determined by X-ray CT scan (a) at room temperature and 300 °C.

higher stresses and consequently, it appears cracks in their border [181] which deteriorate the concrete matrix. The thermal damage in non-reinforced matrix, RC, is focused on the range of pores between 0.25-1.2 mm (Fig. 4.6.b), which was the range of more amount of pores and smaller equivalent diameter. This fact confirms that the thermal damage is especially generated in the smaller pore sizes. In the steel fibre-reinforced mixes (i.e., DS, DL and DSL), the thermal damage affected very uniformly to all mixes (i.e., DS, DL and DSL) to a range of pores between 0.3 and 2.5 mm. It is worth noting as in the mixes with micro-fibres, DS and DSL, the range of pore sizes thermally affected is lightly lower, between 0.2 and 1.4 mm (Fig. 4.6.b) as well as the porosity, Φ_{xr}, (Table 4.2). As shown, the pore shape is clearly spherical in all mixes (i.e., RC, DS, DL and DSL) and the thermal damage increased the average sphericity since thermal damage affected more strongly to smaller pores which have a more spherical shape due to its reduced pore area, A_{pore}, (see Eq. (3.2)). From results, it is observed that the thermal effect at 300 °C provokes a high deterioration of the total porosity of the smallest size of pores. As fibre-reinforced mixes contain less amount of pores with higher equivalent diameter, they are less deteriorated by thermal damage. These modifications of concrete microstructure must be related with changes in the macroscopic behaviour of the mixes, as stated in the following sections.

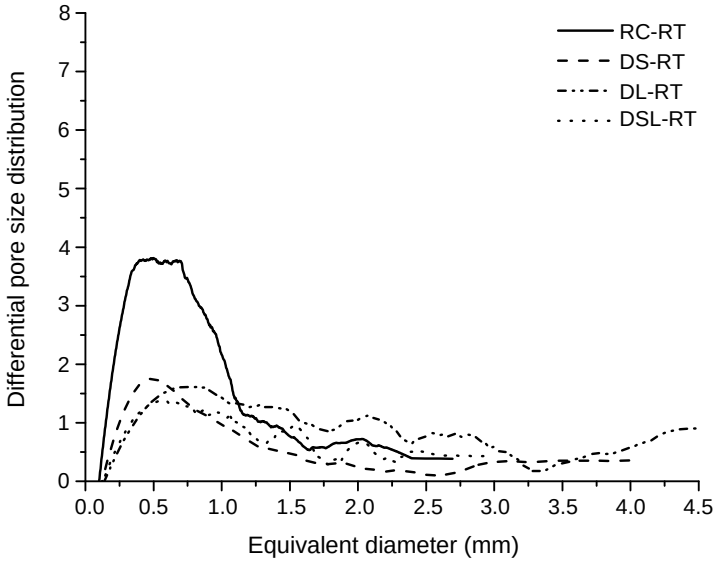

(a)

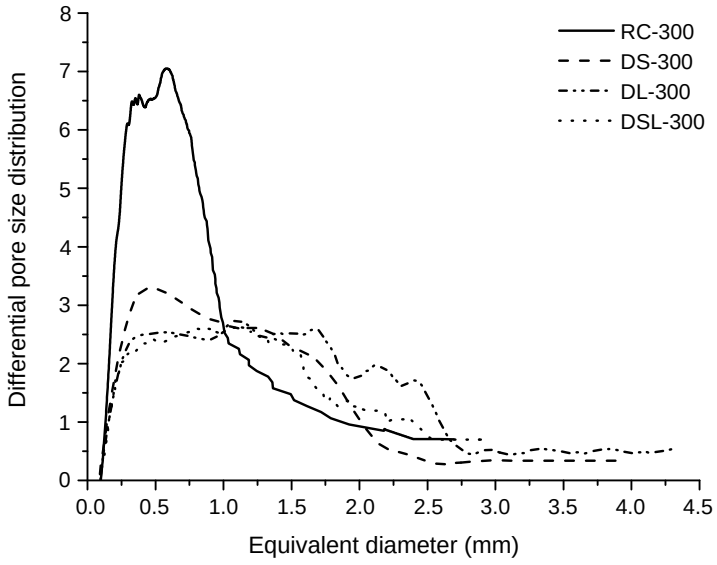

(b)

Figure 4.6 Differential pore size distributions of mixes determined by X-ray CT scan (a) at room temperature and (b) at 300 °C.

4.4.3 Mechanical properties

In this subsection, the mechanical and fracture properties of all mixes (i.e., RC, DS, DL and DSL) are shown. All results correspond to the average of four specimens tested for each mix and temperature (i.e., RT and 300 °C) with indication of the standard deviation.

Compressive strength and Young's modulus on heated concrete

From the mechanical property tests, the compressive strength, f_c, and Young's modulus, E_c, of each mix (i.e., RC, DS, DL and DSL) and temperature (i.e., RT and 300 °C) are shown in Fig. 4.7.a and b, respectively. At room temperature, the addition of steel fibres led to a significant enhancement in the compressive strength (Fig. 4.7.a) with an average increase of 17%, according to results of other authors [185]. As shown, the lower the porosity values the higher the compressive strength (see Table 4.2). Thus, the increase of compressive strength obtained with respect to the non-reinforced mix, RC, is due to the crack bridging effect of fibres but also the reduction of the matrix porosity originated by the fibre addition. Steel fibre might act like tiny shovels helping to mix the concrete during its manufacturing. This effect was previously observed by Ponikiewski et al. [141].

At 300 °C, the compressive strength decreased for all mixes (i.e., RC, DS, DL and DSL) due to the thermal damage generated in the concrete matrix. The RC mix shown the smallest reduction of compressive strength (8.7%) since the thermal damage affected especially in the range of smaller pore sizes (i.e., between 0.25-1.2 mm Fig. 4.6.b). Steel fibre-reinforced mixes (i.e., DS, DL and DSL) followed showing higher compressive strength than non-reinforced, RC, with an average reduction of 15% because of thermal damage. It is worth noting that the mixes more affected by thermal damage were those with lower porosity at RT, i.e. DS and DSL, with a reduction of compressive strength of 16.7% and 17% respectively. It is important to emphasize that the thermal damage inferred is not uniform in the concrete matrix since depends on numerous issues (i.e., thermal conductivity of material, pore distribution, total porosity, components, area of incidence of heat flow) [10, 174] and that provokes a higher dispersion of results at 300 °C (see Fig. 4.7.a).

With regards to the Young's modulus at RT, it is not observed a clear contribution of the presence of steel fibres in this property (Fig. 4.7.b) as occurred to other authors [201]. As it was described in Subsection 3.4.3, this parameter is mainly influenced by the existence of a large number of pores with sizes in the order of nanometers, rather than by the existence of a smaller number of pores

with sizes in the order of millimeters [90]. The addition of fibres essentially affect to the micro pores, as determined in Subsection 3.4.3 so that the Young's modulus results are very similar for any mix (i.e., RC, DS, DL and DSL) at RT (see Fig. 4.7.b).

From the results of Young's modulus at 300 °C, it is observed as the thermal damage significantly decreased very similar for all mixes (i.e., RC, DS, DL and DSL) and no steel fibres influence was observed, as occurred at RT. Thus, the steel fibres has not influence on the Young's modulus since they are not effective on pores of nanometers which are those that significantly affect to Young's modulus results [90]. However, the Young's modulus results confirm that the internal pore pressure (i.e., stresses) generated by thermal gradients in matrix affects more strongly to those pores with smaller sizes.

Flexural strength on heated concrete

The flexural strength at RT presented a clear influence of the steel fibre reinforcement (see Fig. 4.8). Mixes reinforced with micro-fibres (i.e., DS and (DSL) shown the best behaviour, with a similar maximum value above 20 MPa. Despite the fact that macro-fibres present a better alignment, the higher fibre density and better distribution in the matrix, that occurred when using micro-fibres, produced a greater increase in the flexural behaviour of DS and DSL mixes [148, 201]. That shows as the bridging effect of fibres is very significant in flexural strength. The tensile and flexural strength are the greatest weakness of concrete materials and where the steel fibre-reinforcement contribute more significantly and is more effective.

At 300 °C, mixes reinforced with steel fibres (i.e., DS, DL and DSL) suffered a great decrease of flexural strength (an average decrease of 63%) respect to unreinforced mix, RC, (19%). The best behaviour is observed for those mixes reinforced with micro-fibres, as observed at RT for the same property. The reason of so significant decrease for this property is the significant higher number of cracks generated by thermal damage in the matrix, which increased the total porosity (Table 4.2) and the pore size in a wide range between 0.3 and 2.5 mm (Fig. 4.6). Thus, there is a more distributed crack propagation in the matrix and consequently steel fibres are less effective than at RT.

4.4.4 Fracture properties

First-cracking and tensile strength

The tensile stress-strain ($\sigma - \varepsilon$) curves for each of the fibre-reinforced mixes (i.e., DS, DL and DSL) and temperature (i.e., RT and 300 °C), obtained according

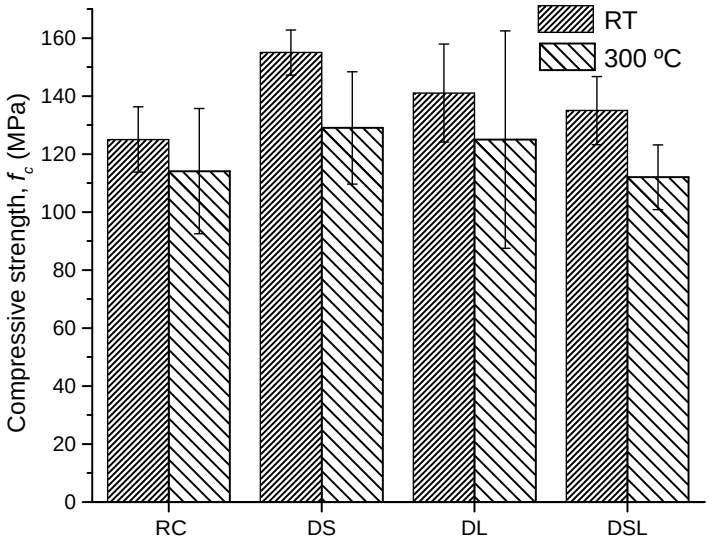

(a)

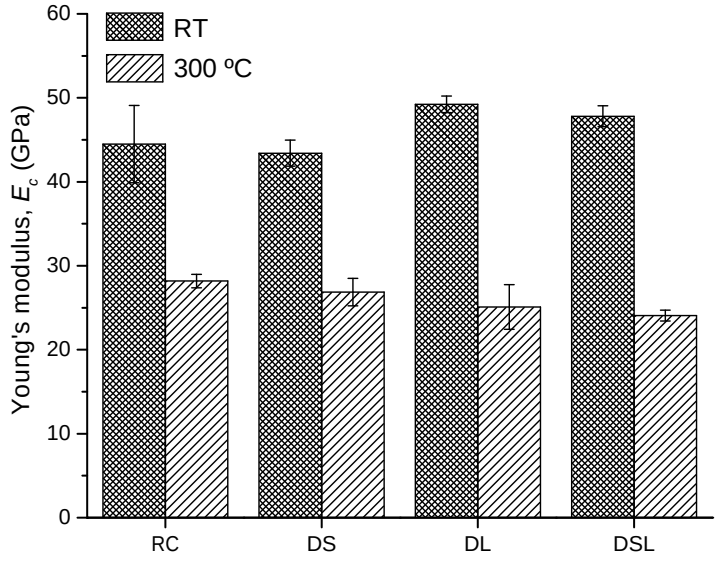

(b)

Figure 4.7 Compressive strength (a) and Young's modulus (b) of mixes at room temperature and 300 °C.

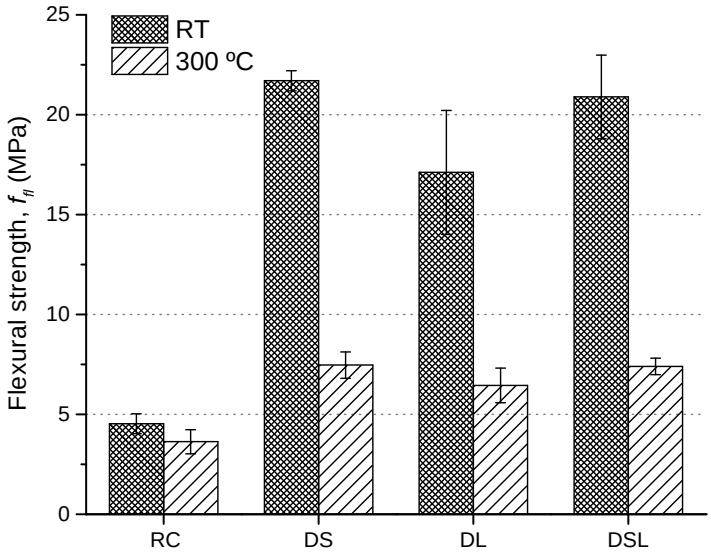

Figure 4.8 Flexural strength of UHPFRC mix at RT and 300 °C.

to the inverse method proposed by López et al. [110], are shown in Fig. 4.9.a. Fig. 4.9.b exhibits the first-cracking strength (f_t) and tensile strength (f_{tu}) values of all mixes (i.e., RC, DS, DL and DSL).

From the results at RT, the tensile strength, f_{tu}, of the fibre-reinforced mixes (i.e., DS, DL and DSL) followed the same trend than flexural strength. The mix reinforced only with micro-fibres, DS, shown the highest tensile strength value. However, DL and DSL presented quite similar values (Fig. 4.9.b). With regards to first-cracking strength, the highest value was obtained again for the DS mix. Nonetheless, the lowest value was obtained for the mix reinforced only with macro-fibres, DL. The DSL mix an intermediate result obtained. The steel fibres improved the first-cracking strength, f_t, of the matrix and the tensile strength, f_{tu}, of the composite structure (cementitious matrix + steel fibres) due to the bridging effect of fibres and the reduction of porosity by the presence of fibres (see Table 4.2 and Fig. 4.6.a).

At 300 °C, the first-cracking strength f_t and the tensile strength, f_{tu}, of the fibre-reinforced mixes (i.e., DS, DL and DSL) suffer a great decrease, in relative terms, that reach values quite similar to unreinforced concrete, RC (see Fig. 4.9.b). The degradation by temperature exposure was so extended in the matrix of those mixes with less initial porosity and smaller pore sizes at RT (i.e., steel fibre-reinforced mixes) that the decrease was enormously higher at 300 °C.

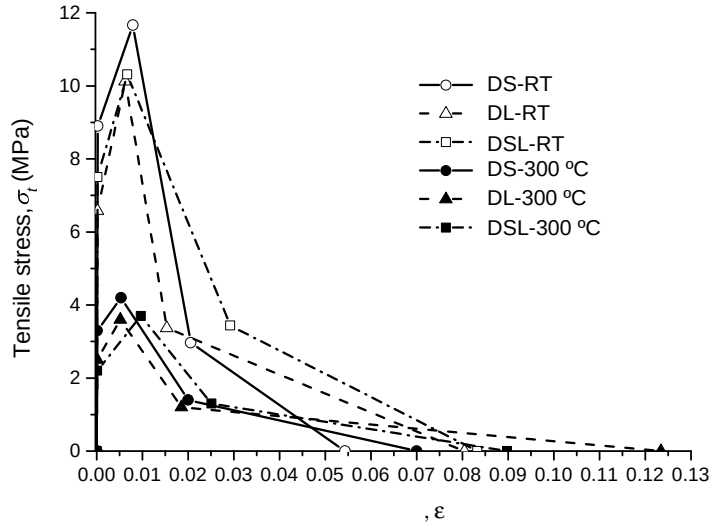

(a)

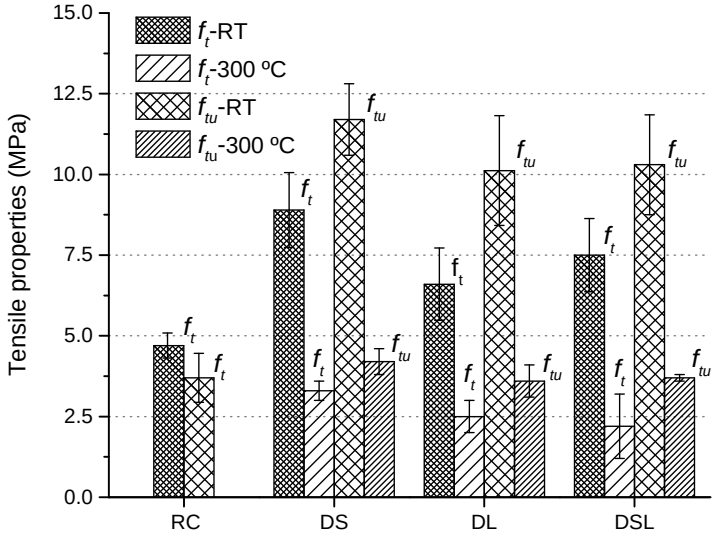

(b)

Figure 4.9 (a) σ-ε constitutive laws obtained at RT [149] and (b) 300°C for fibre-reinforced concrete and tensile properties for f_t and f_{tu} for all mixes.

The multiple cracking generated in the matrix by thermal damage leads to a more extended crack propagation so that the bridging effect of fibres was less effective than at RT. The best tensile strength, f_t, at 300 °C was observed for the mix reinforced only with micro-fibres because the well-distribution of fibres in the matrix leads to a more effective bridging effect of fibres, as occurred at RT. However, the presence of macro-fibres in DL and DSL mixes derived into a bigger distortion of the pore structure and consequently lower values of tensile strength reaching similar values in both cases (i.e., DL and DSL). With regards to first-cracking behaviour, the mix reinforced with only micro-fibres, DS, shown the highest strength because of the positive effect of fibres explained above. The worse cracking behaviour was observed for mixes with macro-fibres, DL and DSL because of the less amount of fibres distributed in the material.

Bilinear softening diagrams and fracture energy

The size-independent fracture energy for unreinforced concrete, RC, was determined according to the RILEM work-of-fracture method and with the corrections proposed by Guinea et al. [53, 68, 140]. The specific fracture energy of the plain concrete mix at RT and 300 °C were determined as follows:

$$G_F = \frac{W_m + W_{nm}}{A_{lig}} \tag{4.3}$$

where W_m is the work-of-fracture after the corrections of the initial part of the $P-\delta$ curve, W_{nm} is the non-measured work-of-fracture, determined by adjusting the tail of the softening branch of the curve and $A_{lig} = B_s(D-a_0)$ is the ligament area.

The bilinear tension softening diagram ($\sigma - w_n$) for the plain concrete, RC, at RT and 300 °C (Fig. 4.10.a) were also obtained according to the hinge model described in [5] and described in Section 3.4. For the steel fibre-reinforced mixes (i.e., DS, DL and DSL), the fracture energy was determined as the area under the cohesive $\sigma - \omega$ laws (Fig. 4.10.b) [88] obtained by the procedure proposed by López et al. [109]. The mechanisms involve in the fracture processes of UHPFRC are not exactly the same as in case of normal plain concrete due to the absence of coarse aggregates and the presence of steel fibres. However, cohesive models are also valid for this kind of concrete 2010 and, although the whole $\sigma - \omega$ diagram is influenced by fibres, the first linear branch of the softening diagram is more related with the microcracking of the matrix [18] while the second linear branch is mainly governed by the pullout of fibres [134].

At room temperature, the crack bridging effect of steel fibres greatly increased the value of G_F (see Fig. 4.10 and Table 4.3) [185]. The lowest value of the

fracture energy was obtained for micro-fibre reinforced mix, DS, because of the lower length and diameter of fibres leads to a lowest interfacial bond with the cementitious matrix [201]. The mix reinforced only with macro-fibres, DL, reached the highest value of the critical opening displacement, $_{max}$, (see Fig. 4.10.b) since a higher adherence of fibres to the matrix is achieved [171]. The mix reinforced with micro and macro-fibres obtained the highest value of fracture energy because it combines the beneficial effects of both types of fibres. On the one hand, the presence of micro-fibres reduces more remarkably the porosity and increased the cracking strength. On the other hand, the presence of macro-fibres provided a greater deformation and increased the energy enclosed by the second branch of the bilinear softening diagram.

At 300 °C, the fracture energy significantly decreased in steel-fibre reinforced mixes (i.e., DS, DL and DSL) because of the damage inferred by temperature. The thermal effect increased the amount of small pores (Fig. 4.6.b) which mainly affected to the first branch of the bilinear softening diagram (Fig. 4.10.b) which is related with the microcracking. However, the higher porosity in the matrix increased the deformation of concrete and higher crack opening displacement values are reached (see Fig. 4.10.b) since the adherence of fibres is reduced. The mix reinforced only with micro-fibres, DS, reached the lowest fracture energy (Table 4.3)) because of the less efficient adherence of fibre with matrix described above for RT tests. However, unlike at room temperature, the highest fracture energy (Table 4.3) was obtained clearly for the mix reinforced only with macro-fibres, DL, due to the best adherence conducts to a higher crack opening displacement values (Fig. 4.6.b) and the quite similar values obtained of tensile strength (Fig. 4.9.b) after thermal degradation of matrix.

Table 4.3 Fracture energy and characteristic length.

	Room temperature		300 °C	
Mix	G_F (N/m)	l_{ch} (mm)	G_F (N/m)	l_{ch} (mm)
RC	64 ± 8%	128	205[b] ± 4.4%	171.5[b]
DS	19201 ± 13%	6093	10167 ± 24%	15440
DL	24614 ± 17%	11832	12711 ± 31%	24858
DSL	32552 ± 15%	14667	10533 ± 7%	18085

[b] Measured on cooled specimens (residual property)

Table 4.3 also shows the values of the characteristic length of each mix at

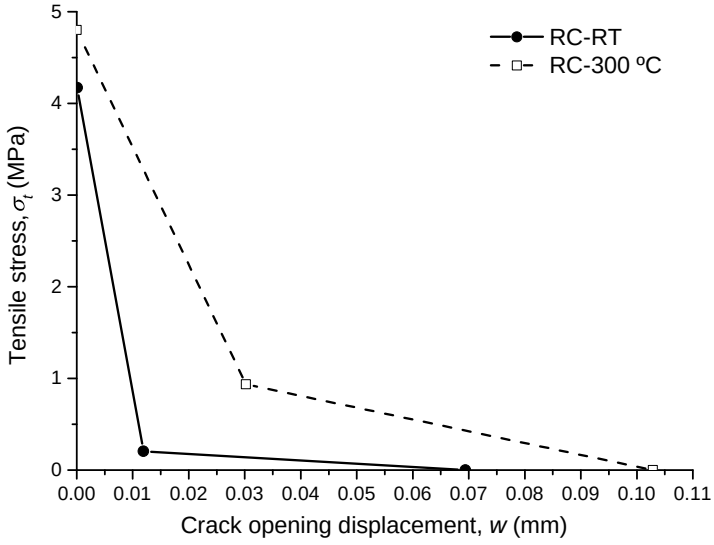

(a)

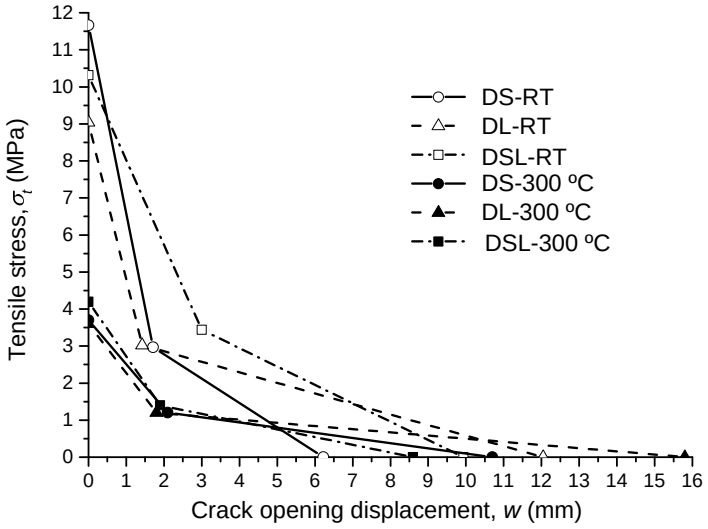

(b)

Figure 4.10 (a) Bilinear tension softening diagram at RT [149] and 300 °C for fibre-reinforced concrete and (b) plain concrete.

RT and 300 °C. As the size of all specimens was the same, a ductility analysis directly based on the results of the characteristic length could be performed [41], so that the greater characteristic length, l_{ch}, the greater the ductility of the mix. From the comparison between the characteristic length at room temperature and 300 °C, it is observed as the increase of porosity in the matrix inferred by the thermal damage led to a more ductile behaviour of material for any mix (i.e., RC, DS, DL and DSL). At 300 °C, the highest ductile behaviour was reached for DL according to the highest fracture energy value. By contrast the most brittle behaviour was shown by unreinforced concrete, RC, as its G_F value was much lower. That trend of higher fracture energy, higher characteristic length was the same observed at RT.

4.5 Concluding remarks

In this chapter, the results of the thermogravimetric analysis and X-ray computed tomography scan have been compared in order to find a direct relationship between thermal effects and the degradation of the pore structure of concrete matrix due to temperature exposure. Furthermore, the work interrelates the mechanical and fracture properties of UHPFRC with the pore structure deterioration due to the thermal damage. This issue has not been dealt with up to the present using UHPFRC and by using the X-ray CT technique. From the results was observed as the reduction of the compressive, tensile strength and fracture energy as a result of thermal damage in each mix (RC, DS, DL and DSL) is, in relative terms, more abrupt in case of UHPFRC due to its lower initial porosity at room temperature, determined by X-ray CT scan, in comparison with unreinforced mix, RC. The internal stresses generated by thermal gradient, evaporation of moisture and dehydration process only affects to smaller pores and the range of pore size affected depends on the type of fibre length and the pore size distribution at room temperature. The best tensile strength at 300 °C was observed for the mix reinforced only with micro-fibres because of the well-distribution of fibres in the matrix leads to a more effective bridging effect. However, the highest fracture energy at 300 °C was for the mix reinforced only with macro-fibres because its adherence with the matrix is more effective and increase the deformation of material. The increase of porosity caused by the thermal damage improved the toughness and ductility of all mixes but especially of fibre-reinforced concrete since they are more affected by thermal damage in relative terms.

5 Fatigue behaviour of plain and fibre-reinforced concrete in flexion

5.1 Probabilistic flexural fatigue of concrete

It is very common for civil infrastructures to be subjected to time-variable loading [172]. Under such circumstances, the strength of concrete materials under compression [29, 38, 76, 93, 135, 138], tension or flexion [14, 69–71, 104, 105, 115, 118, 128, 130, 144, 159, 175, 193] or combined tension-compression [100, 120, 187] is a great concern. In particular, the addition of fibres combined with high strength concrete has improved the tensile or flexural strength of the material, thereby enabling the application of concrete in situations where traditionally, only metallic materials were used. Consequently, the interest in the flexural fatigue strength of concrete has grown significantly, in structures such as bridge slabs, prestressed concrete railroad ties and concrete pavement slabs. However, there is a lack of a systematic analysis of concrete fatigue tests, especially under flexion.

In this chapter has been assessed the adaptability of the probabilistic fatigue model developed by Saucedo et al. [154], validated for compressive fatigue test, to the fatigue of plain and steel fibre-reinforced concrete under bending and, thus,

obtain highly satisfactory results. For this purpose, a new two-step procedure is developed for parameter estimation; meanwhile, abundant literature data (112 series, which amount to 1,350 fatigue tests in total) are collected and analysed. Those tests cover loading frequencies from 1–20 Hz and the fibre volume ratio until 2.0%. Subsequently, the influence of fibre volume and fibre length on model parameters is discussed. From these results, the capability of the model to reorganize the available fatigue test results is highlighted, thereby permitting an easier interpretation from the model parameters of the flexural fatigue of either plain or fibre-reinforced concrete. Thus, this model becomes one of the few (if not the only) models available in the literature for the prediction of flexural fatigue behaviour of plain and fibre-reinforced concrete.

5.2 Description of the probabilistic fatigue model used

The probabilistic fatigue model postulated by Saucedo et al. [154] is briefly presented below. A more detailed description of this model and its derivation can be found in [154].

The model is reflected by the following expressions:

$$P_{fail}(\sigma_{f_0}) = 1 - \exp\left[-\left(\frac{\sigma_{f_0} - \sigma_{min_0}}{\lambda}\right)^k\right], \quad \sigma_{f_0} \geq \sigma_{min_0}, \tag{5.1}$$

$$P_{fail}(N;\sigma_{max},R,f) = 1 - \exp\left\{-\left[\frac{\sigma_{max_0} - \sigma_{min_0}}{\lambda N^{-a(1-R)}}\right]^k\right\}, \tag{5.2}$$

where σ_{f0} is the static strength, either compressive, tensile or flexural (as mentioned, the model was initially assessed for compressive fatigue, but it should also be valid for tensional or flexural since it is probabilistic), with a Weibull distribution, characterised by the scale parameter λ (representative of the static mean strength), the shape parameter k (a smaller value indicates a larger scattering) and the location parameter σmin_0. Within the framework of a fatigue distribution, σmin_0 represents the endurance limit, which is the threshold stress below which no fatigue failure will occur. It should be emphasized that the parameters (λ, k) are considered as material properties. Therefore, they are distinct for different types of concrete (plain or reinforced with fibres). In

contrast, a and α are dependent on both the material type and the loading frequency.

Note that Eq. (5.1) describes the distribution of static properties, whereas Eq. (5.2) represents the probability of failure of a fatigue test under given loading conditions (maximum stress level, loading ratio and loading frequency). Moreover, the equivalent static stress level, σ_{max_0}, is related to its dynamic counterpart, σ_{max}, through the Model Code [1] by means of Eq. (5.3), where σ_c^d and σ_c are the respective dynamic and static strengths and $\dot{\sigma}_d$ and $\dot{\sigma}_0$ are the loading rates of the dynamic and static tests.

$$\frac{\sigma_c^d}{\sigma_c} = \left(\frac{\dot{\sigma}_d}{\dot{\sigma}_0}\right)^{\alpha}, \tag{5.3}$$

When the stress rate, $\dot{\sigma}_d$, is approximated by:

$$\dot{\sigma}_d = 2f\Delta\sigma,, \tag{5.4}$$

the equivalent static stress level can be related to the maximum stress as follows:

$$\sigma_{max_0} = \sigma_{max}\left(\frac{\dot{\sigma}_0}{2f\Delta\sigma}\right)^{\alpha}, \tag{5.5}$$

It needs to be emphasized that even though the exponent α is fitted as a constant equal to 0.014 in the Model Code [1], depending on the available experimental data, it should be adjusted as a function of the loading frequency. Indeed, Saucedo et al. [154] proposed an exponential function to fit with the experimental data of Ruiz et al. [152].

Iso-probability curves for the evolution of the failure stress, σ_f , expressed in Eq. (5.6) were proposed by Saucedo et al. [154] to satisfy the following limit conditions of fatigue strength: (a) the endurance limit is obtained when the fatigue life approaches infinity; (b) the static strength is recovered when the fatigue life is a single cycle or when the stress ratio is equal to one. Operating with Eq. (5.1)-Eq. (5.6) the probabilistic model for compressive fatigue of plain and fibre-reinforced concrete developed by the same authors [154] is acquired as Eq. (5.8).

$$\sigma_f = \sigma_{min_0} + \left(\sigma_{f_0} - \sigma_{min_0}\right) N^{-a(1-R)}, \tag{5.6}$$

$$P_{fail}(N;\sigma_{max},f,R) = 1 - \exp\left\{ - \left[\frac{\sigma_{max}\left(\frac{\delta_0}{2f\Delta\sigma}\right)^{\alpha} - \sigma_{min_0}}{\lambda} N^{a(1-R)} \right]^{k} \right\}, \tag{5.7}$$

5.3 The two-step procedure to estimate model parameters

In order to estimate the model parameters in Eq. (5.1) and Eq. (5.8), the method of maximum-likelihood used by Saucedo et al. [154] was first employed to obtain the parameters λ and k for the static material strength distribution and, secondly, to obtain α and a for the fatigue life distribution. Nonetheless, this procedure is only possible if there are sufficient static strength measurements available to obtain the initial distribution. For most of the fatigue test data in the literature, solely the static mean strength and deviation are given. In this case, we must carry out the parameter estimation using only the data of the fatigue tests.

Assuming that n series of fatigue data are available for different stress levels and/or stress ratios, but with the same loading frequency, the following steps are performed in order to obtain the estimation for (λ, k, α, a). Since the four parameters are for the same material and the same loading frequency, they are enforced to have the same values for all of the series of fatigue tests.

1. For series i of fatigue life data, use Mathematica to get the initial estimate $(\lambda_0^i, k_0^i, a_0^i, \alpha_0^i)$, $i = 1, \ldots, n$.
2. The set $(\lambda_0^i, k_0^i, a_0^i, \alpha_0^i)$ is input to Matlab (or any other optimisation tool) to obtain the best fit $(\lambda^i, k^i, a^i, \alpha^i)$.
3. The final estimate for all n series is calculated as

$$\left(\frac{1}{n}\sum_{i=1}^{n} \lambda^i, \frac{1}{n}\sum_{i=1}^{n} k^i, \frac{1}{n}\sum_{i=1}^{n} a^i, \frac{1}{n}\sum_{i=1}^{n} \alpha^i \right), \tag{5.8}$$

It needs to be highlighted that the endurance limit is preset at 5% of the mean strength to simplify the fitting process and to avoid local maxima.

5.4 Analysis of flexural fatigue data by the probabilistic model

In this section, it is explained the experimental data collected on flexural fatigue of both plain and fibre-reinforced concrete. Brief information on concrete type, fibre content, specimen geometry, fatigue test conditions is summarised herein. Subsequently, the aforementioned procedure is employed to fit the fatigue data with the probabilistic model Eq. (5.8). Among the various tests in the literature [14, 64, 65, 69–71, 84, 104, 105, 115, 118, 128–130, 144, 159, 167, 175, 193, 206], only those with the fatigue life listed in tables are chosen for our analysis. This is based on the fact that nearly all curves for fatigue life are presented in a logarithmic scale. Thus, data extracted from those curves will not be as accurate as tabular ones.

The study is arranged and presented as follows: first, flexural fatigue tests of plain concrete, whereas the second is dedicated to those of steel fibre-reinforced concrete (SFRC). The test configuration (three- or four-point bending), specimen and fibre dimensions and effective span are collected in Table 5.1. The measured static properties and the fitted parameters of Eq. (5.8) for each series of experimental data are listed in Table 5.2, respectively, for plain concrete, whereas those for fibre-reinforced concrete are set forth in Table 5.4 and Table 5.5. It needs to be emphasized that, since the static loading rate, s_0, is rarely given, a reference value of 0.5 MPa/s is adopted to fit the model parameters in Table 5.3 and Table 5.5.

5.4.1 Analysis of the flexural fatigue tests on plain concrete by the probabilistic fatigue model

In this subsection, firstly it has been given a brief introduction on the flexural fatigue tests of plain concrete carried out by Oh [129], Shi et al. [159] and Zhang et al. [206]. Then, the tabular data are extracted to fit the fatigue Eq. (5.8), the corresponding parameters of which are shown in Table 5.3. The feasibility of the probabilistic fatigue model is corroborated by the flexural behaviour of plain concrete.

Table 5.1 Specimen and fibre dimensions (in mm), test configuration (TPB: three-point bending, FPB: four-point bending), employed by Oh [129], Shi et al. [159], Zhang et al. [206] for plain concrete, Johnston & Zemp [84], Singh et al. [167], Mohammadi & Kaushik [118], Goel & Singh [64] for fibre reinforced ones.

Ref.	Test configuration	Specimen dimension (mm)	Span (mm)	L_f (mm)	L_f/D_f
[129]	FPB	$500 \times 100 \times 100$	400	-	-
[159]	TPB	$500 \times 100 \times 100$	450	-	-
[206]	TPB	$500 \times 100 \times 100$	450	-	-
[84]	TPB	$356 \times 102 \times 102$	305	-	47-100
[167]	FPB	$500 \times 100 \times 100$	450	25, 50	20, 40
[118]	TPB	$500 \times 100 \times 100$	450	25, 50	20, 40
[64]	TPB	$500 \times 100 \times 100$	450	30	30

Table 5.2 Measured compressive strength, f_c, and flexural strength, f_{fl}, for the plain concrete tested by Oh [129], Shi et al. [159] and Zhang et al. [206].

Ref.	Age	f_c (MPa)	f_{fl} (MPa)	E_c(GPa)	ν
[129]	60 days	27	4.58	-	-
[159]	28 days	-	5.83	-	-
[206]	28 days	50.7	7.19	-	-
	4 months	57.4	7.88	41.1	0.17

Table 5.3 Fitted model parameters for flexural fatigue tests of plain concrete carried out by Oh [129], Shi et al. [159] and Zhang et al. [206] as well as testing conditions.

Ref.	k	λ (MPa)	a	α	f (Hz)	R
[129]	95.62	4.93	0.055	0.029	4.17	0.00
[159]	37.42	8.75	0.084	0.026	1	0.08
[206]	69.19	7.52	0.0429	0.0167	1	0.20

Table 5.4 Measured flexural strength, f_{fl}, by Johnston & Zemp [84], Singh et al. [167], Mohammadi & Kaushik [118], Goel & Singh [64]. The two-million cycle endurance limit $\sigma_{min_{2m}}$ for the plain and fibre-reinforced SCC, Goel and Singh 2014 [64].

V_f (%)	0.0	0.5	1.0	1.5	2.0	age (days)	Ref.
f_{fl} (MPa)	4.45	6.19	7.24	8.11	-	60	[84]
f_{fl} (MPa)	5.35	-	-	-	-	28	[167]
(65L-35S)	-	-	7.61	9.05	10.05	28	[167]
(50L-50S)	-	-	7.45	8.44	9.15	28	[167]
(35L-55S)	-	-	7.50	7.98	8.44	28	[167]
f_{fl} (MPa)	5.35	-	-	-	-	90	[118]
(50 mm-L)	-	-	7.50	9.44	10.72	90	[118]
(25 mm-S)	-	-	7.16	7.73	8.11	90	[118]
f_{fl} (MPa)	4.85	6.05	7.20	9.00	-	28	[64]
$\sigma_{min_{2m}}$ (MPa)	3.00	4.30	5.50	6.40	-	28	[64]

Experimental results of Oh, 1991 [129]

For the purpose of examining the distributions of fatigue life of concrete at various levels of applied stress, Oh [129] performed four-point flexural fatigue tests at three different values of S_{max} (0.65, 0.75 and 0.85), with zero minimum stress. Prismatic concrete beams of dimension $500 \times 100 \times 100$ mm^3, with an effective span of 400 mm, were tested at a rate of 250 cycles/min (4.17 Hz). The static 60-day compressive strength and flexural strength are given in Table 5.2. Assuming a two-parameter fatigue life distribution, Oh estimated the mean life as 2240, 27,800 and 410,000 cycles (corresponding variations are of 28%, 43% and 49%) for the stress levels of 0.85, 0.75 and 0.65 respectively.

Herein it has been used the same tabular data given by Oh [129] to fit Eq. (5.8), the result in Fig. 5.1.a is obtained with the parameters listed in Table 5.3. The correlation coefficient varies between 0.92 and 0.96. By setting the probability of failure at 50%, Eq. (5.8) can be used to obtain the mean fatigue life as 2871, 31,026 and 485,804 cycles for the stress level at 0.85, 0.75 and 0.65 respectively. It is noteworthy that the obtained mean cycles from Eq. (5.8) vary by only 22%, 10% and 18% from those estimated by Oh [129] using three different Weibull distributions for the three levels of fatigue tests. This is a strong evidence for the feasibility of Eq. (5.8) to predict the flexural fatigue life of plain concrete at different stress levels.

Table 5.5 Model parameters and loading frequency, stress ratio for flexural fatigue tests of SFRC carried out by Johnston & Zemp 1991 [84], Singh et al. 2005 [167], Mohammadi & Kaushik 2005 [118] and Goel & Singh 2014 [64].

Johnston & Zemp [84]	k	λ (MPa)	a	α	f (Hz)	R
$V_f = 0.0\%$	32.63	3.82	0.028	0.023	15	0.1
$V_f = 0.5\%$-SW(75)	40.25	6.23	0.028	0.015	15	0.1
$V_f = 1.0\%$-SW(75)	48.77	7.60	0.029	0.020	15	0.1
$V_f = 1.5\%$-SW(75)	48.24	7.25	0.025	0.027	15	0.1
$V_f = 1.0\%$-SW(50)	37.75	7.12	0.036	0.033	15	0.1
$V_f = 1.0\%$-SW(100)	39.89	7.24	0.028	0.017	15	0.1
$V_f = 1.0\%$-SDW(47)	39.21	7.22	0.037	0.021	15	0.1
$V_f = 1.0\%$-ME(54)	40.04	7.22	0.040	0.021	15	0.1
$V_f = 1.0\%$-SS(71)	42.94	5.72	0.029	0.037	15	0.1
Singh et al. [167]	k	λ (MPa)	a	α	f (Hz)	R
$V_f = 1.0\%$-(65L-35S)	58.90	7.24	0.030	0.018	20	0.0
$V_f = 1.5\%$-(65L-35S)	39.27	7.25	0.036	0.042	20	0.0
$V_f = 2.0\%$-(65L-35S)	41.13	7.24	0.034	0.041	20	0.0
$V_f = 1.0\%$-(50L-50S)	60.38	7.19	0.031	0.019	20	0.0
$V_f = 1.5\%$-(50L-50S)	40.54	7.25	0.034	0.027	20	0.0
$V_f = 2.0\%$-(50L-50S)	39.89	7.24	0.028	0.017	20	0.0
$V_f = 1.0\%$-(35L-65S)	57.46	7.25	0.028	0.016	20	0.0
$V_f = 1.5\%$-(35L-65S)	38.33	7.22	0.038	0.030	20	0.0
$V_f = 2.0\%$-(35L-65S)	43.19	7.25	0.030	0.021	20	0.0
Moh. & Kaushik [118]	k	λ (MPa)	a	α	f (Hz)	R
$V_f = 0.0\%$	67.90	5.03	0.060	0.040	20	0.1
$V_f = 1.0\%$-L	51.72	7.81	0.046	0.018	20	0.1
$V_f = 1.5\%$-L	37.15	9.01	0.048	0.016	20	0.1
$V_f = 2.0\%$-L	29.48	9.14	0.050	0.018	20	0.1
$V_f = 1.0\%$-S	41.32	6.82	0.037	0.025	20	0.1
$V_f = 1.5\%$-S	37.87	6.86	0.038	0.026	20	0.1
$V_f = 2.0\%$-S	38.18	7.27	0.039	0.020	20	0.1
Goel & Singh [64]	k	λ (MPa)	a	α	f (Hz)	R
$V_f = 0.0\%$	58.22	4.63	0.060	0.051	10	0.1
$V_f = 0.5\%$	45.71	5.84	0.052	0.043	10	0.1
$V_f = 1.0\%$	32.87	7.45	0.054	0.046	10	0.1
$V_f = 1.5\%$	40.58	8.03	0.044	0.031	10	0.1

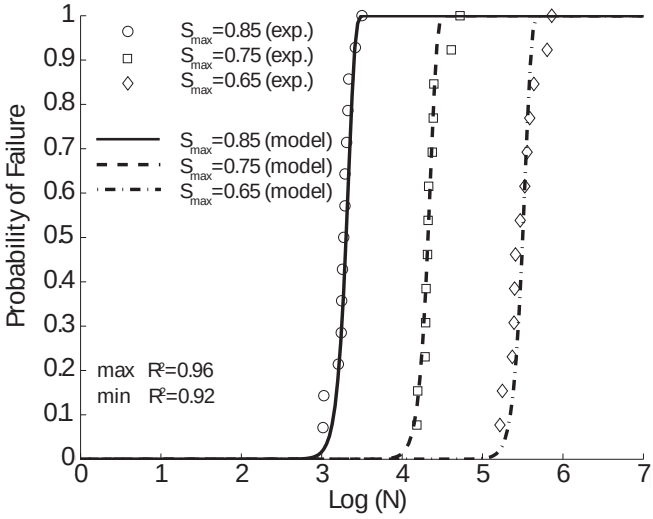
Probability of Failure
Log (N)
S_max=0.85 (exp.)
S_max=0.75 (exp.)
S_max=0.65 (exp.)
S_max=0.85 (model)
S_max=0.75 (model)
S_max=0.65 (model)
max R²=0.96
min R²=0.92

(a)

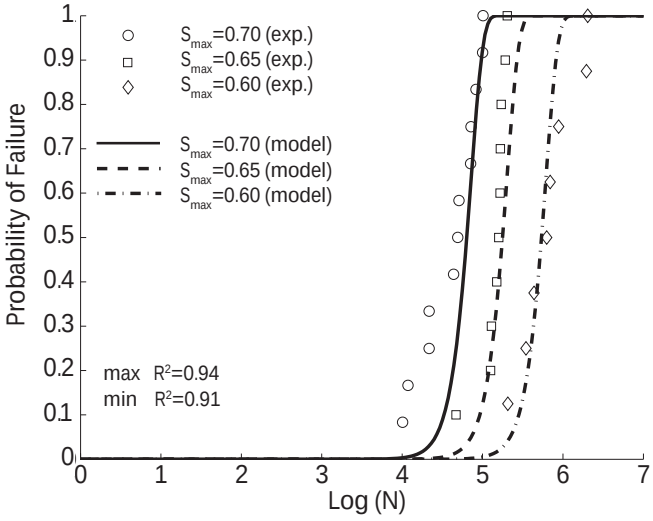
Probability of Failure
Log (N)
S_max=0.70 (exp.)
S_max=0.65 (exp.)
S_max=0.60 (exp.)
S_max=0.70 (model)
S_max=0.65 (model)
S_max=0.60 (model)
max R²=0.94
min R²=0.91

(b)

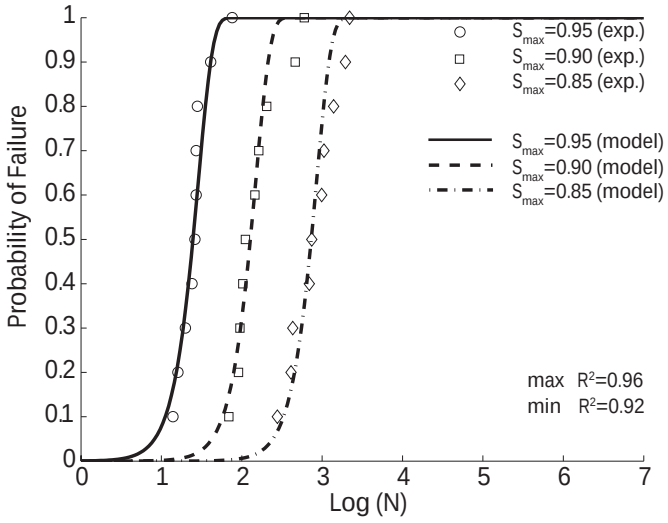

(c)

Figure 5.1 Comparison of flexural fatigue data for concrete by (a) Oh [129]; (b) Shi et al. [159] and (c) Zhang et al [206], where R^2 is the Pearson's coefficient of correlation.

Experimental results of Shi et al., 1994 [159]

Shi et al. [159] introduced a concept of equivalent fatigue life, defined as $N^{(1-R)}$, in the derivation of an expression to describe the flexural fatigue strength of plain concrete. They carried out flexural fatigue tests on 78 plain concrete beams under three-point bending loading. Those beams had a dimension of $500 \times 100 \times 100$ mm^3, with an effective span of 450 mm. Three different stress ratios (0.08, 0.2 and 0.5) and nine values of stress levels (S_{max} varied from 0.50 to 0.90, with an increment of 0.05) were examined. It was select only those tests with enough number of repetitions, i.e., those with a stress ratio of 0.08, stress levels of 0.60, 0.65 and 0.70, all at a loading frequency of 1 Hz, to fit Eq. (5.8). The corresponding results are demonstrated in Fig. 5.1.b, with the statistical correlation values exceeding 0.91.

It should be emphasis that Oh [129] claimed that the shapes of the probabilistic fatigue-life distributions were dependent on the level of applied stress, from Eq. (5.8), it has observed that this dependency is expressed as the equivalent relation between the static and dynamic stresses. Indeed, the good correlation of the test data of Shi et al. [159] shown in Fig. 5.1.b further verifies this statement.

Furthermore, the concept of equivalent fatigue life, is enhanced to in order to take into consideration the influence of loading frequency on parameter a in Eq. (5.8).

Experimental results of Zhang et al., 1996 [206]

In order to investigate the effects of loading frequency and stress reversal on fatigue properties of plain concrete, Zhang et al. [206] carried out both static and cyclic flexural tests on 171 plain concrete beams under three-point bending configuration. Those beams were of $500 \times 100 \times 100$ mm^3 in size, 450 mm in effective span. The measured static properties at 28 days and 4 months are listed in Table 5.2. Fatigue tests at different stress levels, stress ratios and loading frequencies were carried out. From their own experimental data and those from the literature, Zhang et al. [206] established a fatigue equation to account for the effect of loading frequency and stress reversal. It has been only considered those with enough number of samples to fit with Eq. (5.8). The obtained results are illustrated in Fig. 5.1.c for a constant stress ratio, R,(0.2). Note that the coefficient of correlation, R^2, surpasses 0.92 for all three stress levels.

5.4.2 Analysis of the flexural fatigue tests on SFRC by the probabilistic fatigue model

In this subsection, it first summarise the flexural fatigue tests carried out by Johnston & Zemp [84], Singh et al. [167], Mohammadi & Kaushik [118] and Goel & Singh [64] for fibre-reinforced concrete. The static strength data are extracted and shown in Table 5.4. Then, Eq. (5.8) is used to fit with that data. The corresponding parameters are shown in Table 5.5. The feasibility and predictive nature of the probabilistic fatigue model given by Eq. (5.8) are demonstrated for SFRC.

Flexural fatigue tests of SFRC by Johnston and Zemp [84]

In the early 1990s, Johnston and Zemp [84] studied the performance of steel fibre reinforced concrete under flexural fatigue loading in terms of fibre content (0.5%, 1.0% and 1.5% in volume fraction), fibre aspect ratio, L_f/D_f (47 to 100), and fibre type. Specifically, eight fibre-reinforced mixtures and one control concrete were cast; five types of straight fibres of uniform cross-section were employed: smooth hard drawn wire (SW), slit sheet (SS), hooked-end wire (HW), crimped hard-drawn wire (CW), surface-deformed wire (SDW). In total, 194 fatigue tests and 135 complementary static tests on prismatic beams under three-point bending configuration were conducted. The beams were of $356 \times 102 \times 102$ mm^3 in size, 305 mm in effective span. Both the first crack strength

and the ultimate strength were recorded at the age of 60 days, see Table 5.4. The fatigue tests were performed at a loading frequency of 15 Hz up to 0.5 million cycles, and the stress ratio was kept at 0.1. A minimum of six specimens were tested at each stress level from 0.75 to 0.98. The authors stated that since the static first-crack and ultimate strengths vary with an insignificant amount, the $S-N$ relationships can be established based on stress level as a percentage of either strength, based on actual applied stress versus number of loading cycles. Fibre content is the primary governing factor, whereas aspect ratio and fibre type are of secondary importance. The best performance was obtained with 1.5% in volume ratio and 70 in aspect ratio cold drawn wires. The two-million endurance limit varied from 66 to 82 percent of the static first-crack strength.

It first fit these experimental fatigue data with Eq. (5.8) for the same type of fibre (smooth hard drawn wires, 75 in aspect ratio), volume ratio of 0.5%, 1.0% and 1.5%, the corresponding results are presented in Fig. 5.2 for each concrete with the model parameters listed in Table 5.5.

Secondly, without distinguishing between the fibre type or the aspect ratio, the fitted results are shown in Fig. 5.4 for the same fibre volume ratio (1.0%) using the same set of model parameters listed in Table 5.5. It is noteworthy that the correlation coefficients surpasses 0.90 for the same type of fibres. This coefficient decreases significantly when the fibres are distinct. This indicates that for the same amount of fibre content, even though the flexural strength may not greatly vary, the fatigue life may vary significantly depending on the type of steel fibres.

Flexural fatigue data for SFRC by Singh et al. 2005 [167]

In order to determine the influences of fibre length and fibre volume fraction, Singh et al. [167] conducted on fatigue tests for SFRC reinforced with long and short fibres (50 mm and 25 mm in length), 0.6 mm in width and 0.2 mm in thickness. Nine types of concretes, with three fibre proportions, 65%L-35%S, 50%L-50%S, 35%L-65%S (where L and S stand for long and short fibres respectively) and three fibre volume ratios, 1.0%, 1.5%, 2.0% were designed. Prismatic specimens with a size of $500 \times 100 \times 100$ mm^3 were cast and tested. In particular, 269 fatigue tests (20 Hz in loading frequency, stress ratio if zero), 108 complimentary static ones were carried out under four-point bending configurations. The average compressive and flexural strength of the nine mixes at the age of 28 days are shown in Table 5.4.

The experimental fatigue data obtained and the fit model curves for each series of tests are shown from Fig. 5.5 to Fig. 5.7 for fibre proportions of 65%L-35%S, 50%L-50%S, 35%L-65%S respectively. It should be emphasis that Singh et al.

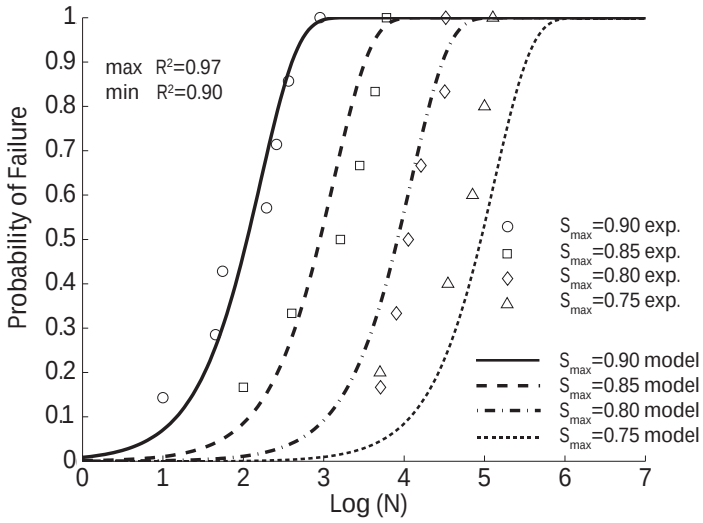

(a)

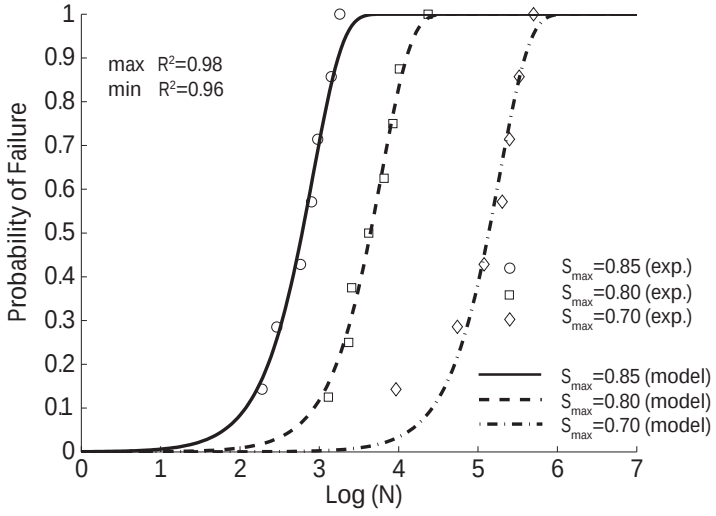

(b)

[167] concluded that the statistical distribution of equivalent SFRC fatigue-life at a given stress level approximately follows a two-parameter Weibull distribution. From Fig. 5.5 to Fig. 5.7, it is observed that the same set of parameters for Eq. (5.8) produces an excellent correlation for three different of stress levels.

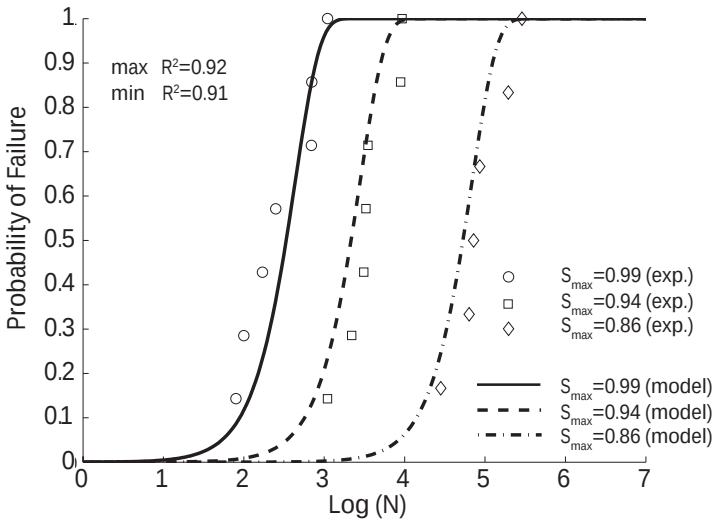

(c)

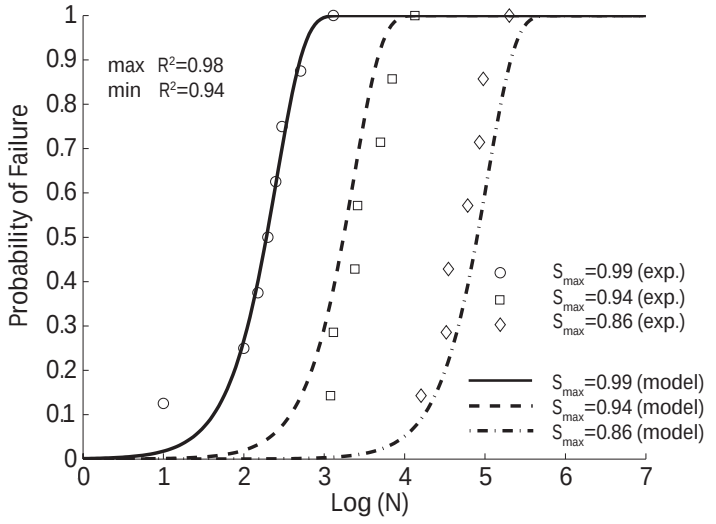

(d)

Figure 5.2 Comparison of flexural fatigue data of Johnston and Zemp [84] with the fitted probabilistic model Eq. (5.8) for concrete reinforced with smooth hard drawn fibres, 75 in aspect ratio, (a) 0.0%; (b) 0.5%; (c) 1.0%; and (d) 1.5% in volume ratio.

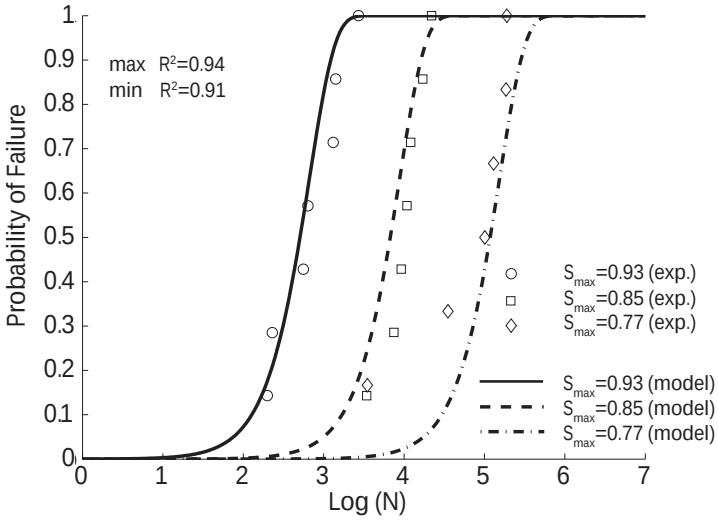

(a)

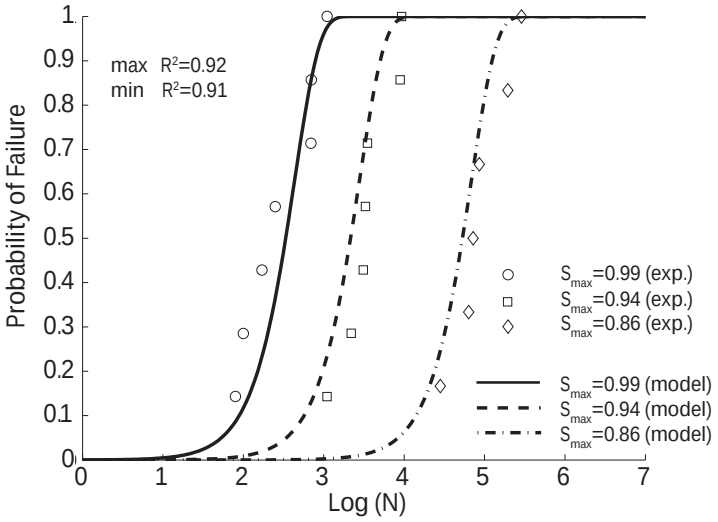

(b)

This further indicates the validity of Eq. (5.8) in predicting the SFRC fatigue life. This is further demonstrated in Table 5.6, where the estimated mean fatigue life cycles by Singh et al. [167] and by inverting Eq. (5.8) in the current study. In order to determine the effect of fibre content, only the common stress

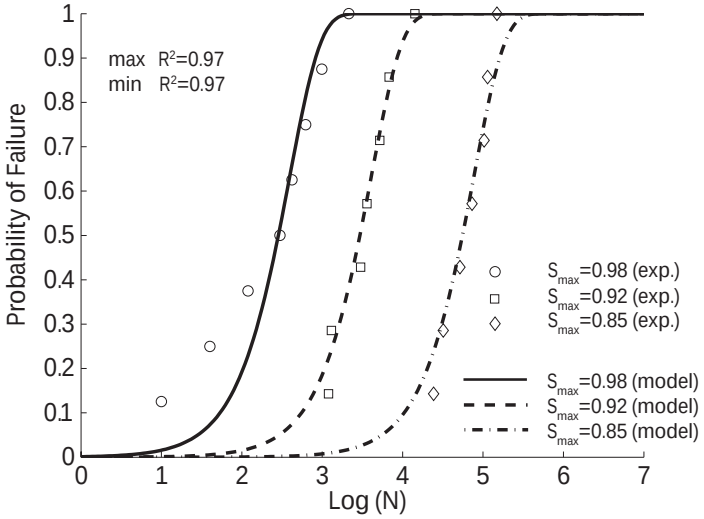

Figure 5.3 Comparison of flexural fatigue data of Johnston and Zemp [84] with the fitted probabilisitic model Eq. (5.8) for concrete reinforced with smooth hard drawn steel fibres 1.0% in volume ratio, (a) 50; (b) 75; and (c) 100 in aspect ratio..

level 80% is selected for this comparison. It is noteworthy that the fatigue life decreases with the increase of the fibre content for the same stress level, σ_{max}/f_{fl}. Nevertheless, when the maximum stress, σ_{max}, is maintained, the mean fatigue life is shown to significantly increase with the fibre volume ratio.

Flexural fatigue data for SFRC by Mohammadi & Kaushik, 2005 [118]

Mohammadi & Kaushik [118] studied the fatigue life of plain and steel fibre reinforced concrete with different volume fractions (0.0%, 1.0%, 1.5%, 2.0%) and fibre lengths (50 mm and 25 mm) for various levels of the applied fatigue stress. All the fibres were of the same width (2 mm) and thickness (0.2 mm). Extensive experimental research was planned in which 210 flexural fatigue tests and 84 complementary static ones were conducted on prismatic plain concrete and fibre-reinforced concrete specimens of $500 \times 100 \times 100$ mm^3 in size under three-point loading (450 mm in span). The static properties for seven types of concrete (all sharing the same matrix) at the age of 90 days were measured and listed in Table 5.4.

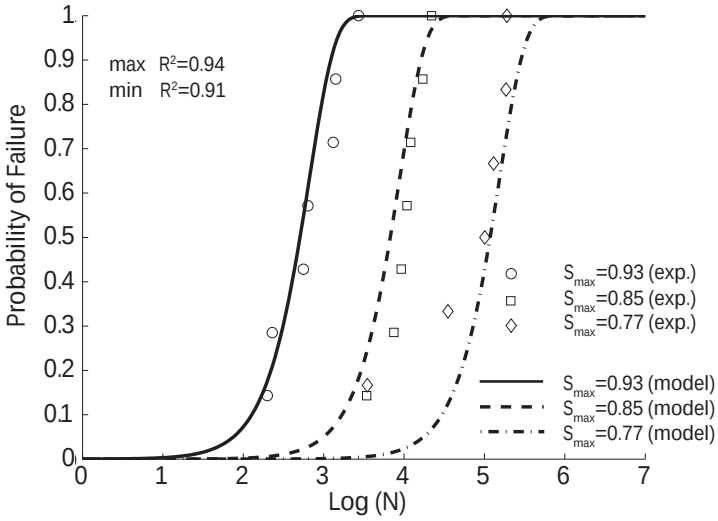

(a)

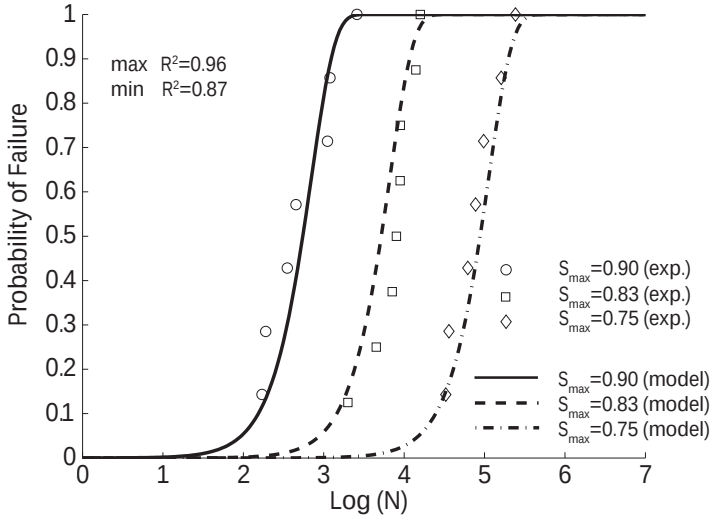

(b)

The fatigue tests were performed at a loading frequency of 20 Hz. Three stress levels, all with the same stress ratio of 0.1, were employed for each concrete. The authors fitted their fatigue data with a two-parameter Weibull model for each stress level with correlation coefficients exceeding 0.90. It is adopted Eq. (5.8)

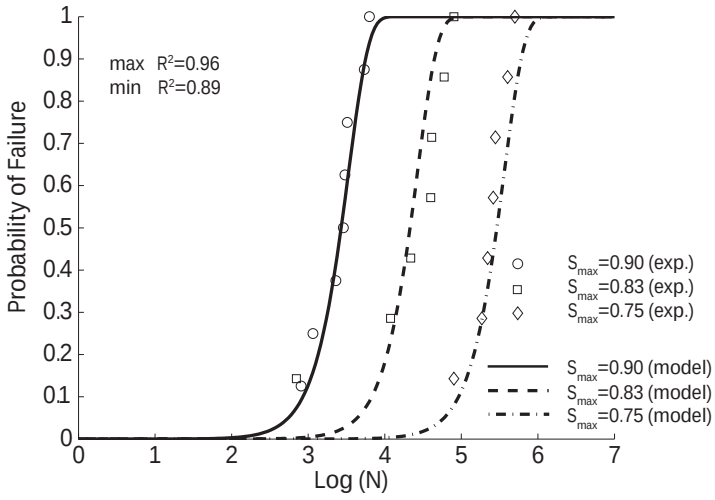

(c)

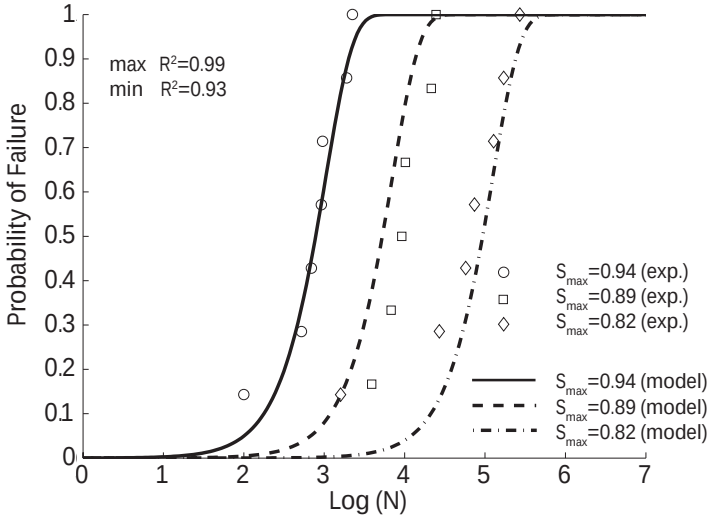

(d)

Figure 5.4 Comparison of flexural fatigue data of Johnston and Zemp [84] with the fitted probabilistic model Eq. (5.8) for concrete reinforced with 1.0% steel fibres of (a) SW(50); (b) SDW(47); (c) ME(54); (d) SS(71) in fibre type (aspect ratio).

Table 5.6 Comparison of the mean fatigue life cycles given by Singh et al. [167] and those predicted by inverting Eq. (5.8) for the tests of Singh et al. [167] at stress level of 80%. N_f is the predicted mean fatigue life when σ_{max} is set at the static strength of the plain concrete.

Fibre volume ratio-(mix proportion)	N_{f_1} (cycles)	N_{f_2} (cycles)	N_f (10^6 cycles)
$V_f = 1.0\%$-(65L-35S)	220,736	120,147	11.6
$V_f = 1.5\%$-(65L-35S)	14,193	14,283	104
$V_f = 2.0\%$-(65L-35S)	1,313	1,046	365
$V_f = 1.0\%$-(50L-50S)	146,313	160,597	6.4
$V_f = 1.5\%$-(50L-50S)	13,070	8,841	12.6
$V_f = 2.0\%$-(50L-50S)	3,174	307	49.2
$V_f = 1.0\%$-(35L-65S)	276,571	300,055	23.2
$V_f = 1.5\%$-(35L-65S)	73,675	21,410	2.9
$V_f = 2.0\%$-(35L-65S)	11,236	7,787	30.0

herein to get a single fitting for the fatigue tests conducted on three different stress levels, the corresponding results of which are given in Fig. 5.8 and Fig. 5.9 for long (50 mm) and short (25 mm) fibres respectively. Taking into the account the fact that, the model parameters for the same material has to be the same, the correlation is satisfactory.

In Table 5.7, it is compared the mean fatigue life cycles obtained by Mohammadi and Kaushik and by inverting Eq. (5.8) for the stress level of 80%. As expected, the comparison is very strong. The mean fatigue life is observed to decrease as the fibre content increases. Also shown in Table 5.7 is the predicted mean fatigue life, N_f, when the maximum stress is set as the flexural strength (5.35 MPa) of the reference plain concrete. Note that the mean fatigue life increases with the fibre content, and this improvement is more pronounced for short fibres.

Flexural fatigue data for SFRC by Goel and Singh, 2014 [64]

Recently, Goel and Singh carried out a study on the fatigue performance of plain and steel-fibre reinforced self-compacting concrete (SCC). The experimental campaign consisted in 250 flexural fatigue tests and 195 complementary static flexural tests on four-point-bending beams with dimensions of $500 \times 100 \times 100$ mm^3 and a span of 450 mm. Four types of concrete, with the same matrix (the control concrete), the same type of steel fibre (30 mm in length and 1 mm in diameter), and different fibre volume ratios – 0%, 0.5%, 1% and 1.5% –, were

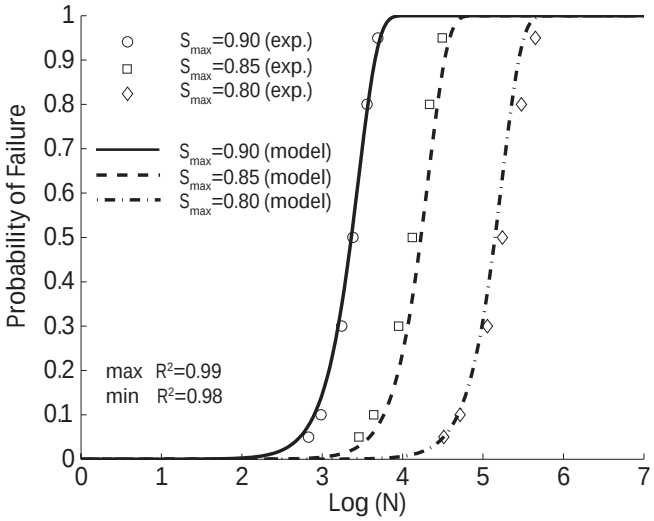

(a)

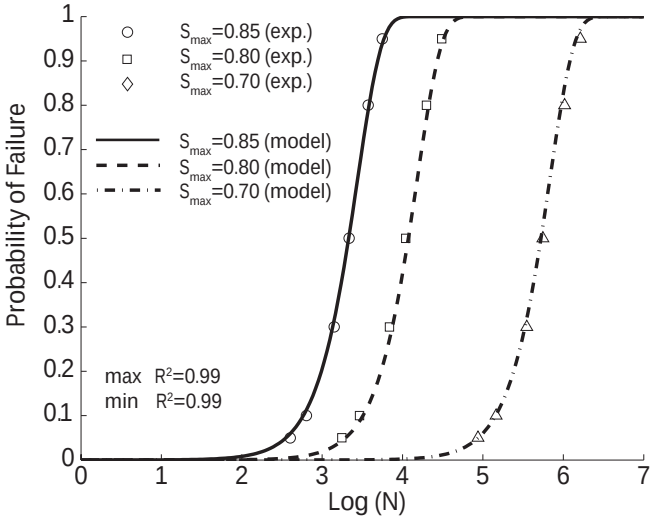

(b)

studied. The fatigue test were performed at a loading frequency of 10 Hz, the stress ratio was kept at 0.1, the stress level, S, varied from 0.65 to 0.85. The authors used a two-parameter Weibull model to fit the fatigue life distribution for the obtained test data. The shape parameter and characteristic life (or the

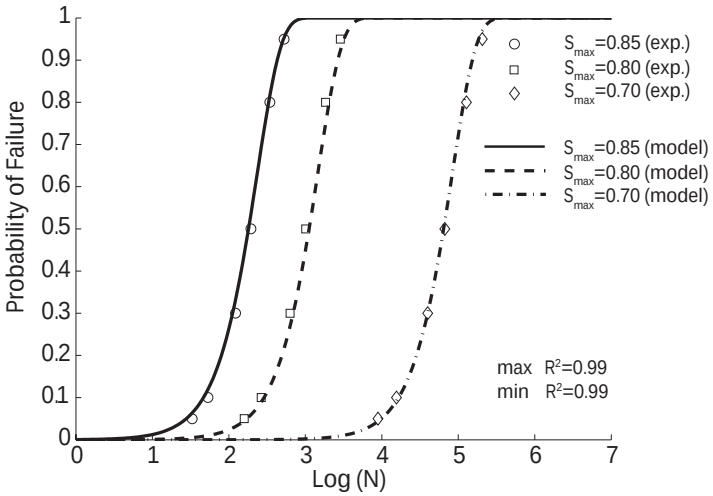

(c)

Figure 5.5 Comparison of flexural fatigue data of Singh et al. [167] with the fitted probabilisitic model Eq. (5.8) for SFRC of volume ratio of (a) 1.0%; (b) 1.5%; and (c) 2.0%, with 65% of long fibres and 35% of short fibres.

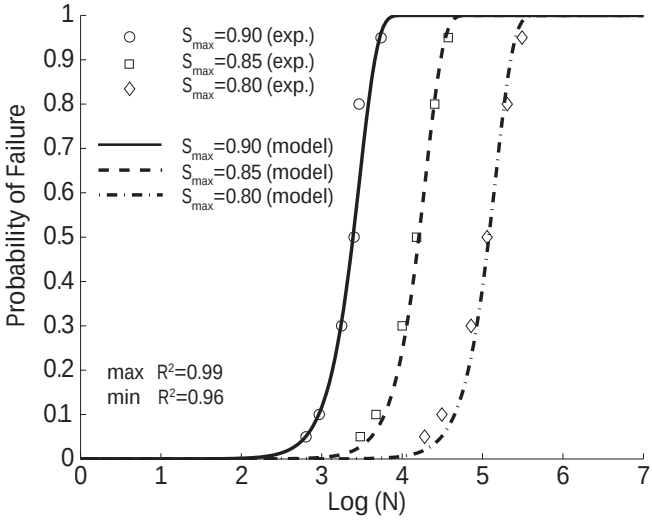

(a)

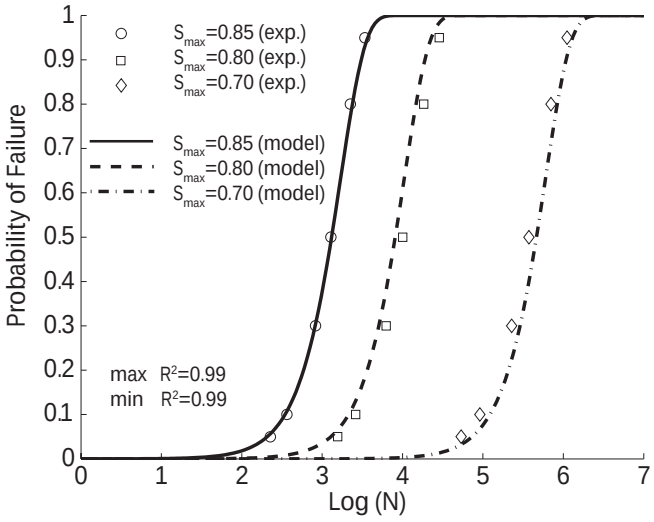

(b)

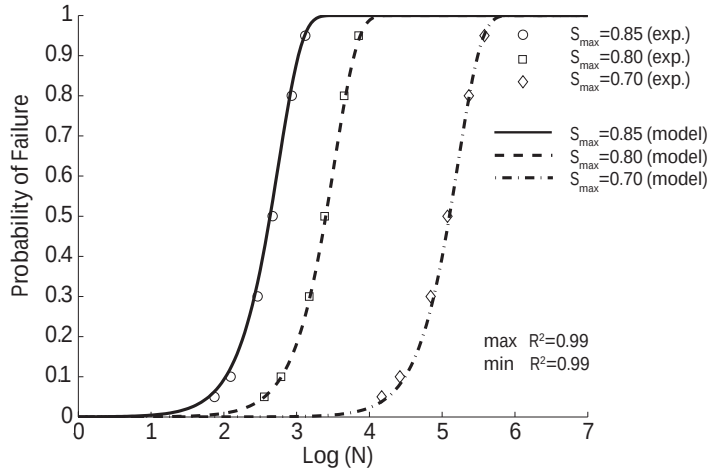

(c)

Figure 5.6 Comparison of flexural fatigue data of Singh et al. [167] with the fitted probabilisitic model Eq. (5.8) for SFRC of volume ratio of (a) 1.0%; (b) 1.5%; and (c) 2.0%, with equal proportions of long and short fibres.

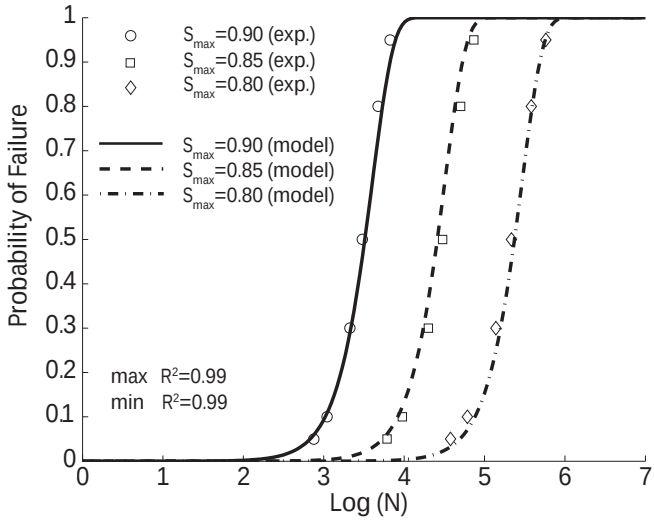

(a)

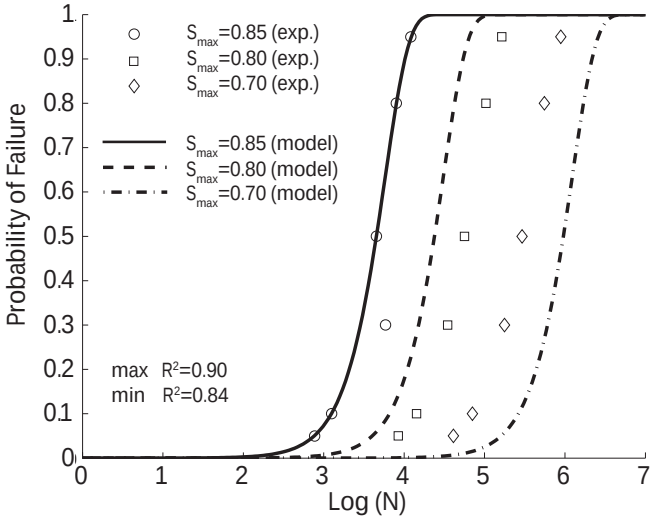

(b)

scale parameter) were determined from $S-N$ relationships. The measured static compressive strength, f_c, the flexural strength, f_{fl} at 28 days and the two-million cycle endurance limit, $\sigma_{min_{2m}}$, are shown in Table 5.4.

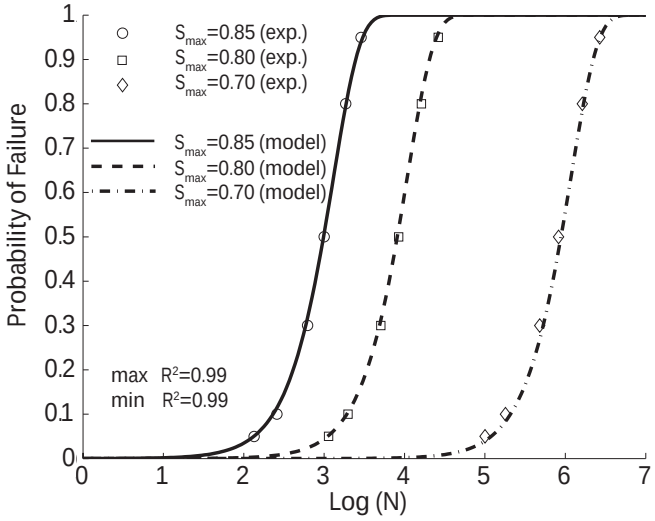

(c)

Figure 5.7 Comparison of flexural fatigue data of Singh et al. [167] with the fitted probabilisitic model Eq. (5.8) for SFRC for volume ratio of (a) 1.0%; (b) 1.5%; and (c) 2.0%, with 35% of long fibres and 65% of short fibres.

Table 5.7 Comparison of the mean fatigue life cycles given by Mohammadi and Kaushik [118], N_{f_1}, and those predicted by inverting Eq. (5.8), N_{f_2}, for the tests in [118] at stress level of 80%. N_f is the predicted mean fatigue life when σ_{max} is set at the static strength of the plain concrete.

Concrete type	N_{f_1} (cycles)	N_{f_2} (cycles)	N_f (10^6 cycles)
$V_f = 0.0\%$	9,229	7,195	-
$V_f = 1.0\%$-L	84,177	46,488	0.74
$V_f = 1.5\%$-L	2,284	3,609	1.33
$V_f = 2.0\%$-L	375	230	1.68
$V_f = 1.0\%$-S	199,315	135,374	1.11
$V_f = 1.5\%$-S	36,333	17,268	1.38
$V_f = 2.0\%$-S	9,149	6,380	1.79

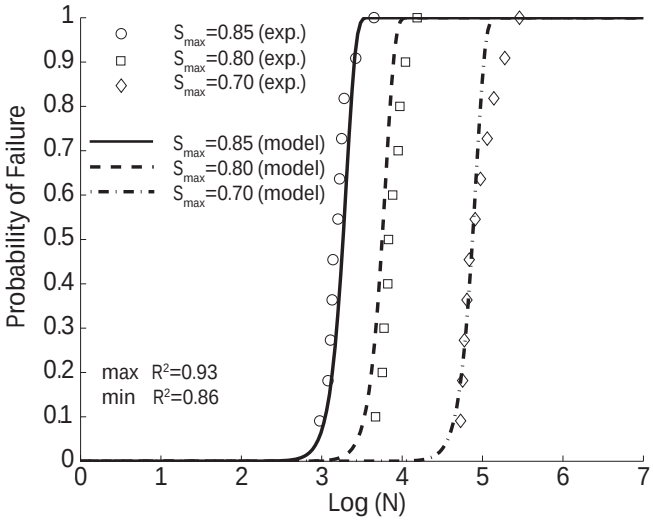

(a)

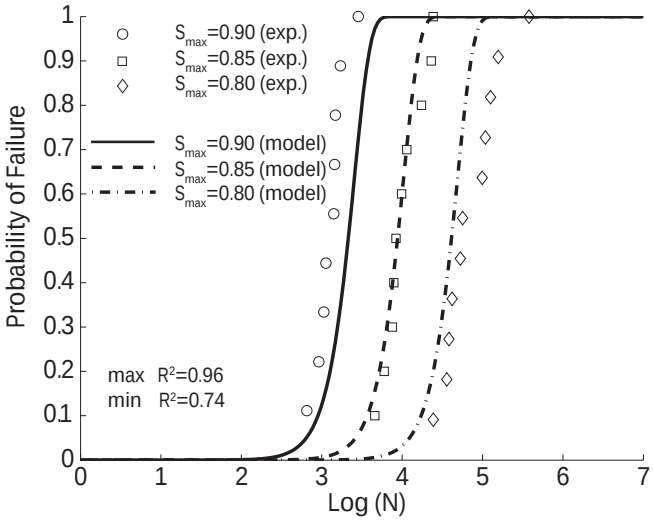

(b)

The experimental fatigue life data and their corresponding fit with the probabilistic model Eq. (5.8) are demonstrated in Fig. 5.10. Note that the Pearson's coefficient of correlation, R^2, varied from 0.81 to 0.98 for the plain concrete, from 0.79 to 0.96 for the concrete with a V_f of 1.5%, whereas for V_f of 0.5% and

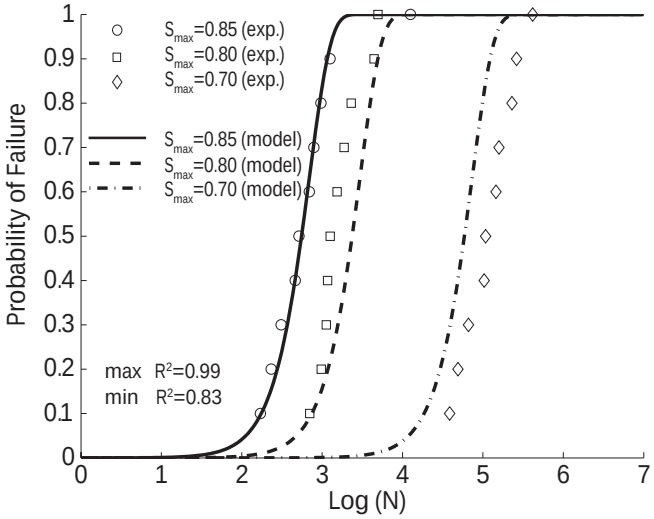

(c)

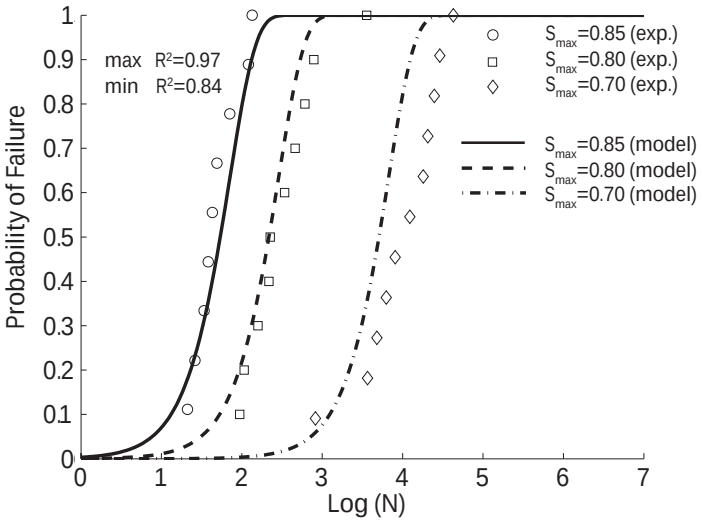

(d)

Figure 5.8 Comparison of flexural fatigue data of Mohammadi and Kaushik [118] with the fitted probabilisitic model Eq. (5.8) for concrete reinforced with fibres of 50 mm in length, volume ratio of (a) 0.0%; (b) 1.0%; (c) 1.5%; and (d) 2.0%.

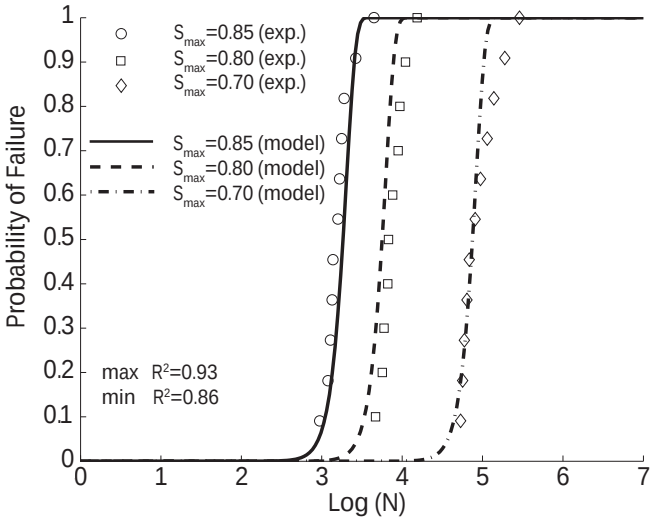

(a)

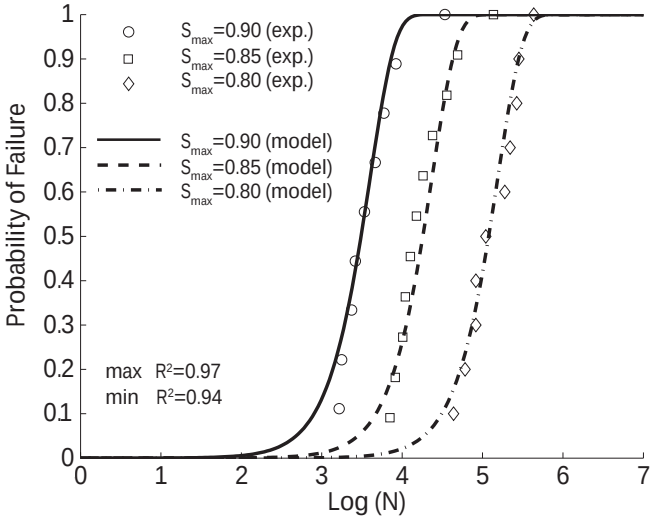

(b)

1.0%, better correlations were reached (R^2 is more than 0.96%). This means that by adding an adequate amount of fibres, on the one hand, there can be a reduction of the dispersion in fatigue life and an enhancement in the fatigue performance under flexion; on the other hand, when V_f surpasses a certain

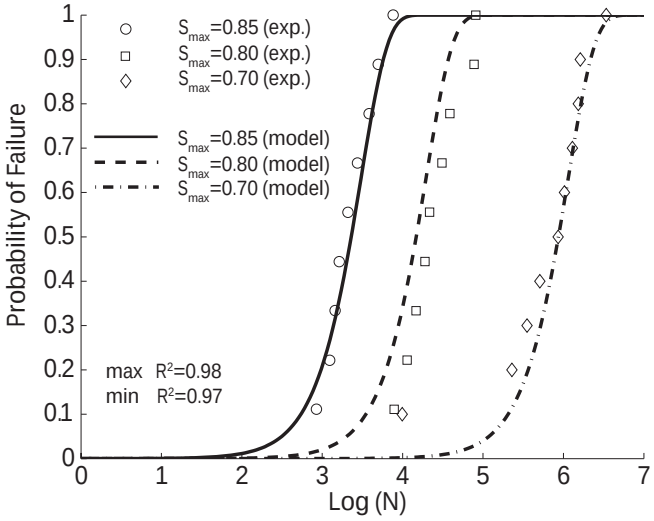

(c)

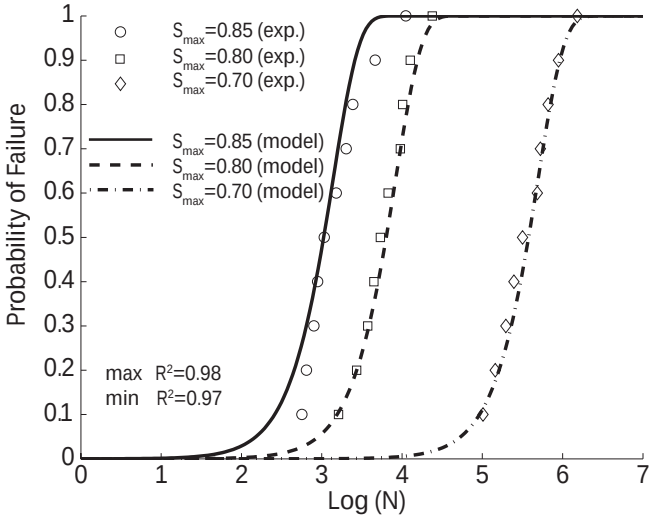

(d)

Figure 5.9 Comparison of flexural fatigue data of Mohammadi and Kaushik [118] with the fitted probabilisitic model Eq. (5.8) for concrete reinforced with fibres of 25 mm in length, volume ratio of (a) 0.0%; (b) 1.0%; (c) 1.5%; and (d) 2.0%.

value, the benefits of fibres may decrease for the same stress level (mainly due to the fact that high fibre content distorts the matrix and produces pores and imperfections in the material that favors the initiation of cracks [142]. This is different from that of static properties as shown in Table 5.4, where both the compressive and flexural strengths as well as the two-million endurance limit increased with the fibre volume ratio. This is further demonstrated in Section 5.4.

In Table 5.8, it is compared the mean fatigue life cycles obtained by Goel and Singh [64] and by inverting Eq. (5.8) for the stress level of 80%. As expected, the comparison is very satisfactory. The mean fatigue life is observed to increase as the fibre content increases until 1.5% for the same stress level. This trend is different from that of Mohammadi and Kaushik [118]. This may be attributed to the different fibre and the lower loading frequency.

Additionally, the predicted mean fatigue life, N_f, is shown in Table 5.8, when the maximum stress is set as the flexural strength (4.85 MPa) of the reference plain concrete. Note that the mean fatigue life increases with the fibre content, and this improvement is more pronounced when V_f is higher.

Table 5.8 Comparison of the mean fatigue life cycles given by Goel and Singh, 2014 [64], N_{f_1}, and those predicted by inverting Eq. (5.8), N_{f_2}, for the tests in [64] at stress level of 80%. N_f is the predicted mean fatigue life when σ_{max} is set at the static strength of the plain concrete (4.85 MPa).

Fibre volume ratio	N_{f_1} (cycles)	N_{f_2} (cycles)	N_f (10^6 cycles)
$V_f = 0.0\%$	11,808	11,769	-
$V_f = 0.5\%$	51,163	30,307	0.03
$V_f = 1.0\%$	237,492	136,822	5.51
$V_f = 1.5\%$	83,418	6,809	282

5.5 Discussion

As mentioned above, among the four parameters, (k,λ,a,α), a lower k represents a larger scattering, a larger λ corresponds to stronger material strength (in the case of bending, λ is approximately 95% of the flexural resistance, f_{fl}). The exponent α represents the dynamic amplification of the material strength, whereas

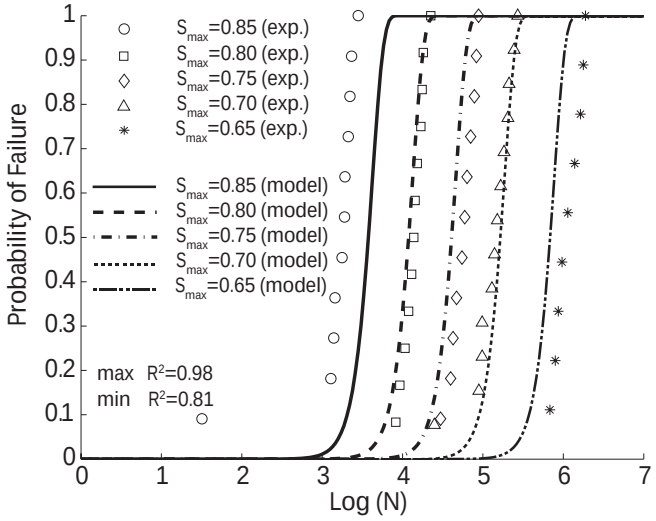

(a)

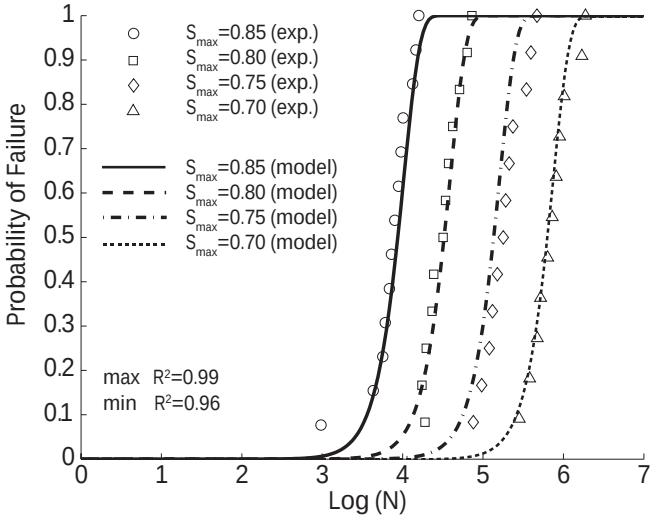

(b)

a reflects the influence of loading frequency, when the others do not change. In other words, both λ and α can be considered material properties, whereas *k* indicates the static properties are distributive in a more or less extension. In this Section, it is analysed the results obtained in Section 5.4, specifically, it is paid

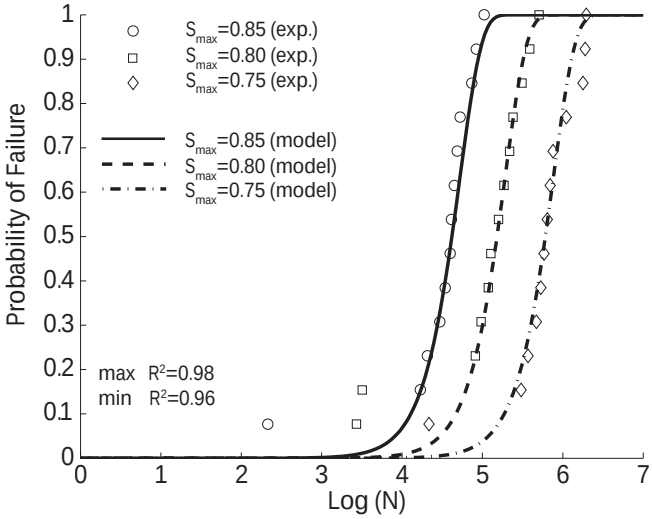

(c)

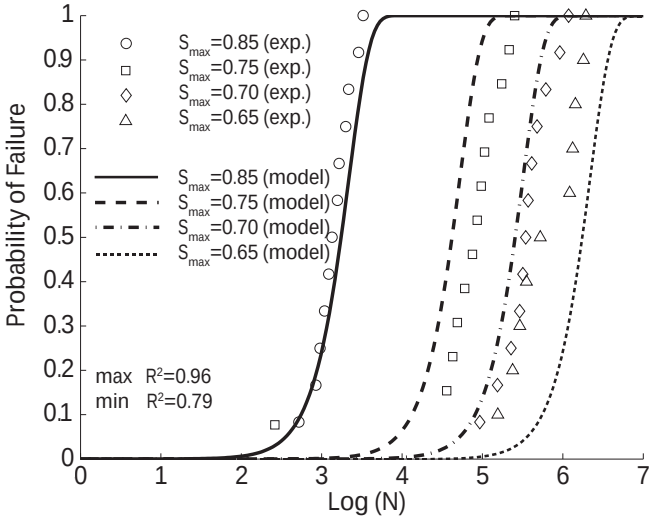

(d)

Figure 5.10 Comparison of experimental data of Goel and Singh [64] with the fitted probabilistic model Eq. (5.8) for concrete reinforced with steel fibres, (a) 0.0%; (b) 0.5%; (c) 1.0% and (d) 1.5% in volume ratio.

attention to the influences of fibre volume ratio V_f, fibre length, L_f and loading frequency, f.

5.5.1 The influence of the fibre volume fraction

Among the four references described in Subsection 5.4.2, three of them [64, 118, 167] explored the influence of the fibre volume ratio by maintaining the fibre length and concrete matrix.

Furthermore, except for Mohammadi and Kaushik [118], the complementary tests for plain concrete were also included, which further highlighted the effect of fibre addition. The work of Mohammadi and Kaushik [118] is the only one that considered the mixed proportion of both short and long fibres. From Fig. 5.11 to Fig. 5.14, the variations of the parameters (k, λ, a, α) with respect to the fibre volume ratio, V_f, are presented.

It is observed in Fig. 5.11 that, k is the highest for plain concrete. For the concrete reinforced with steel fibres of 50 mm long, 2×0.2 mm^2 in cross section, k decreases with the volume ratio V_f for the four values (0.5%, 1.0%, 1.5% and 2.0%) studied by Mohammadi and Kaushik [118]. For the one reinforced with fibres of 25 mm long, 2×0.2 mm^2 in cross section, or fibres of 30 mm in length, 1 mm in diameter, tested by Goel and Singh [64], the minimum k was reached at 1.0% of V_f. For the case of hybrid combination of long and short fibres, k hardly differ with the mix proportion, slight variation is observed when for volume ratios of 1.5% and 2.0%. This indicates that, fibre addition contributes to the further scattering of fatigue resistance, which is usually attributed to the additional voids created around the fibres.

Regarding the scale parameter, λ, it is observed in Fig. 5.12 that, the minimum is obtained for plain concrete, even though an ascending trend is noticed as V_f increases. Only a slight enhancement is perceived when V_f increased from 1.0% to 1.5% and 2.0%. In the case of hybrid fibres of different length, λ does not vary with either the volume fraction or the mix proportion.

Fig. 5.13 shows that the parameter a is the highest for plain concrete. It decreases with the addition of steel fibres, but no remarkable variation is observed for volume fraction of 0.5%, 1.5% and 2.0%. Notwithstanding, this reduction of a was more significant when the fatigue tests were carried out at 20 Hz than those of 10 Hz. This indicates that the effect of fibre addition is stronger when the loading frequency is at 20 Hz.

A trend similar to that of a is appreciated for parameter α in Fig. 5.14. Explicitly, the maximum α is reached for plain concrete. The addition of fibres reduces the value of α, but this reduction is not clearly proportional with the

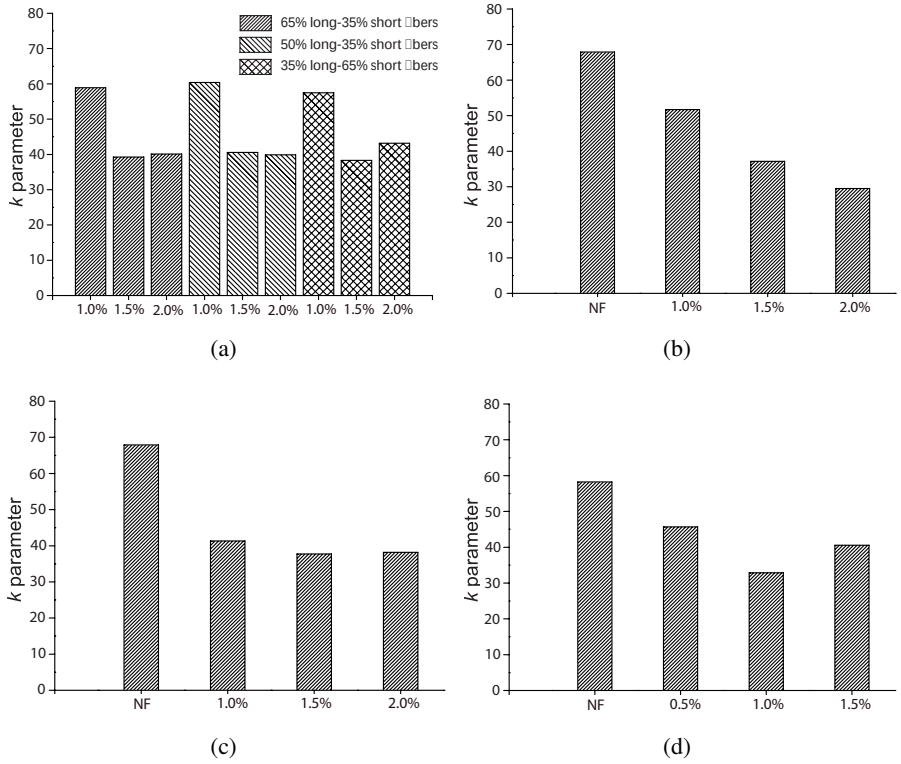

Figure 5.11 Influence of fibre volume fraction on the shape parameter, k: (a) Singh et al. [167]; (b) Mohammadi and Kaushik [118], 50 mm in fibre length; (c) Mohammadi and Kaushik [118], 25 mm in fibre length; (d) Goel and Singh [64].

amplitude of V_f but rather to a higher loading frequency. In other words, the dynamic effect is stronger when the loading frequency is higher, which is as expected.

In Fig. 5.15 are plotted all the data points exposed in Table 5.3 and Table 5.5 for the four parameters together with their density distribution. Note that there is a clear ascending trend for λ, which corresponds to the fact that the flexural strength increases with the fibre amount.

5.5.2 The influence of the fibre length

The influence of fibre length L_f was only studied by Mohammadi and Kaushik [118] for fibres of 50 mm and 25 mm in length, 2 mm in width and 0.2 mm in

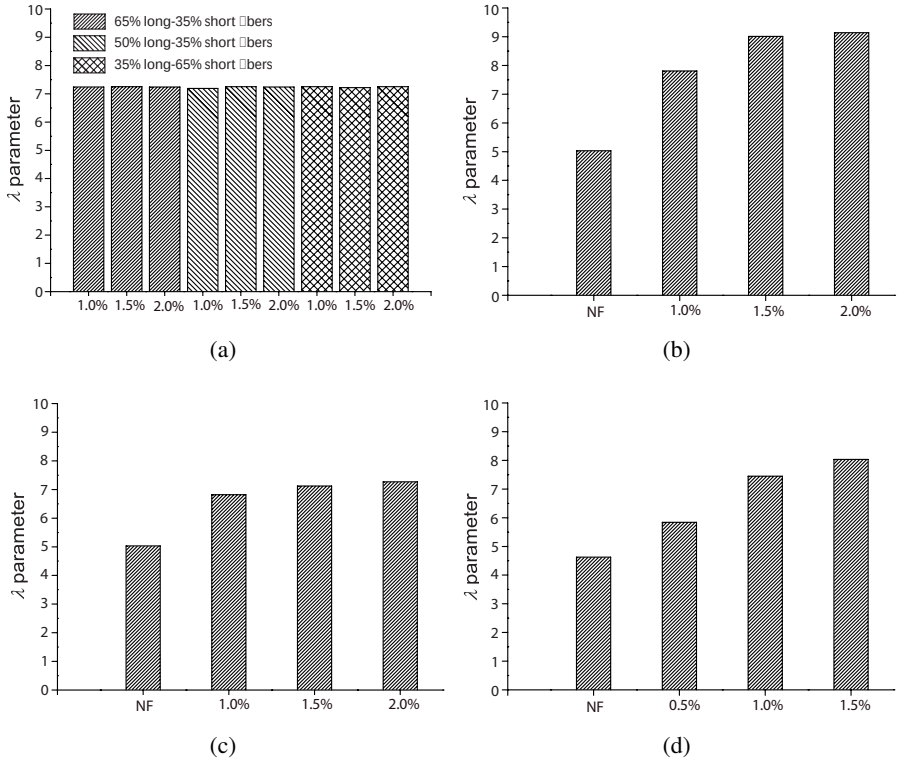

Figure 5.12 Influence of fibre volume fraction on the scale parameter, λ: (a) Singh et al. [167]; (b) Mohammadi and Kaushik [118], 50 mm in fibre length; (c) Mohammadi and Kaushik [118], 25 mm in fibre length; (d) Goel and Singh [64].

thickness. The fitted parameters (k, λ, a, α) for their fatigue tests are plotted in Fig. 5.16 with respect to the fibre volume ratio, V_f.

As mentioned before, the shape parameter, k, is higher for the control concrete due to the fact that the addition of fibres may modify the concrete matrix by creating more voids around the fibres (as observed in Chapter 3 by X-ray CT analysis on UHPFRC) and consequently, the scatter on the fatigue life is increased. This effect leads to lower k values when the fibres are added. In Fig. 5.16.a, it may be observed that the reduction of k due to fibre addition has a stronger correlation with V_f for long fibres and a weaker for short ones. This can be attributed to the easier workability of short fibres. Thus, a more uniform fibre distribution during the mixing process is reached with the addition of short

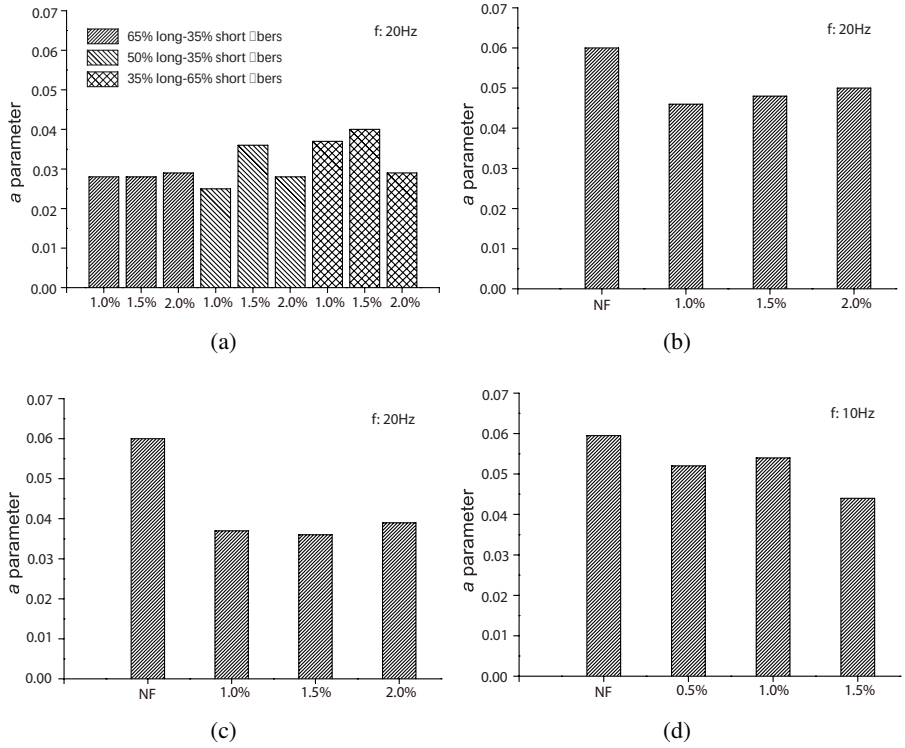

Figure 5.13 Influence of fibre volume fraction on *a* parameter: (a) Singh et al. [167]; (b) Mohammadi and Kaushik [118], 50 mm in fibre length; (c) Mohammadi and Kaushik [118], 25 mm in fibre length; (d) Goel and Singh [64].

fibres.

Fig. 5.16.b shows the influence of L_f on the scale parameter, λ, which is proportional to the flexural strength as far as flexural fatigue tests are concerned. As observed, both long and short fibres improve the material strength by more than 40%. However, this enhancement is more significant for longer fibres. Moreover, with a further increase of V_f beyond 1.0% (1.5%) for short (long) fibres, strength enhancement may be hardly distinguished.

Fig. 5.16.c illustrates that the parameter, a, decreases upon fibre addition. This diminution is more remarkable for short fibres. Particularly, for 1.0% of the volume fraction of short fibres, a is 43% less than that of plain concrete; for 1.0% of long fibres, a is 20% than that of of the control concrete.

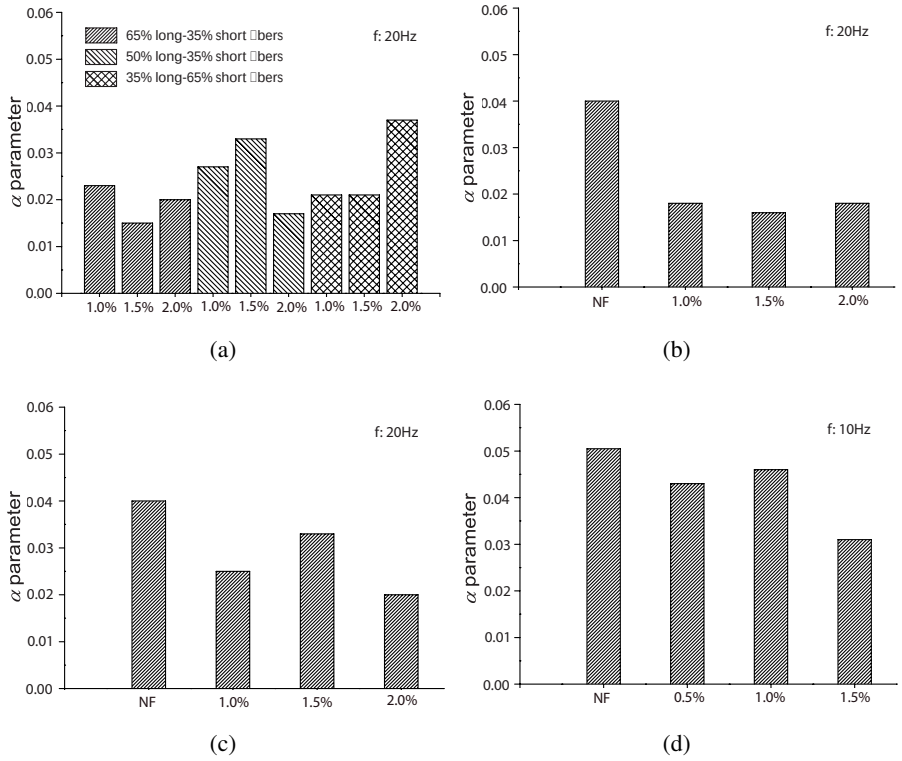

Figure 5.14 Influence of fibre volume fraction on α parameter: (a) Singh et al. [167]; (b) Mohammadi and Kaushik [118], 50 mm fibres, (c) Mohammadi and Kaushik [118], 25 mm fibres; (d) Goel and Singh [64].

Regarding to α, in Fig. 5.16.d, it is appreciated that the highest value is reached for plain concrete, more than 50%, and a reduction of 50% is obtained for long fibres regardless of volume fraction. Less of a decrease of α is obtained for short fibres. This indicates that, the dynamic strength of the SFRC is more sensitive when longer fibres were employed, see Eq. (5.3).

5.5.3 The influence of loading frequency, f

The influence of loading frequency on the compressive fatigue life of plain and reinforced concrete at low loading rates has been demonstrated by the experimental work of Ruiz et al. [152] and Medeiros et al. [116]. This influence is accounted for through the a and α parameters in Eq. (5.8) by Saucedo et

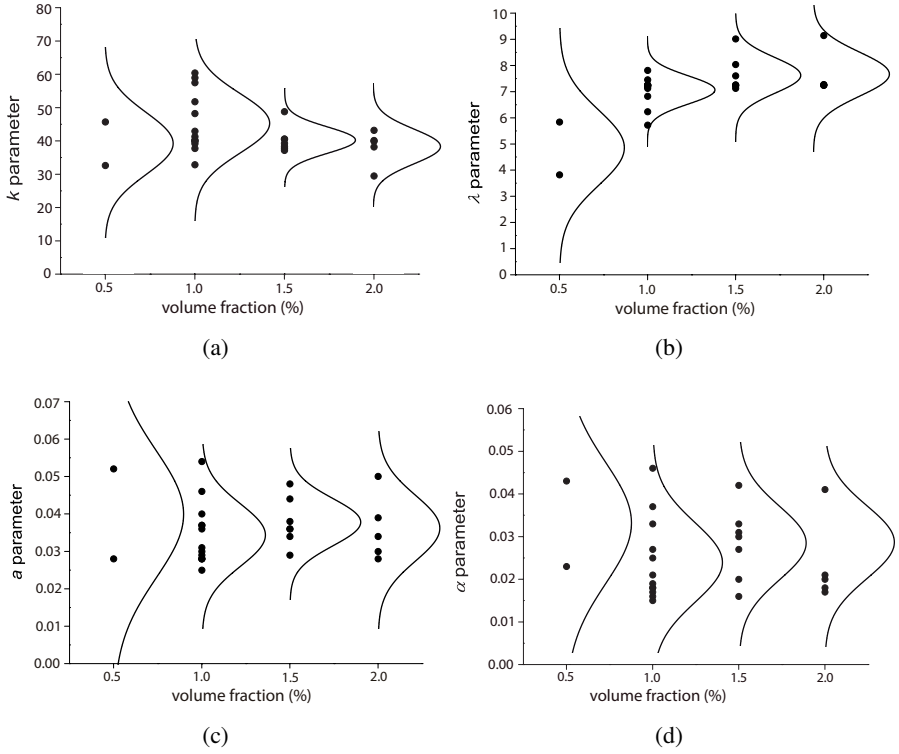

Figure 5.15 The influence of fibre volume fraction: a global perspective.

al. [154]. Fig. 5.17 presents the values for these two parameters for flexural fatigue tests carried out at difference loading frequency for both plain and fibre reinforced concrete. Note that there is a descending trend for a until 15 Hz. For α, similar trend is observed for loading frequencies between 10 and 15 Hz. Since very few data are available for lower loading frequencies, it is difficult to achieve at a definite statement.

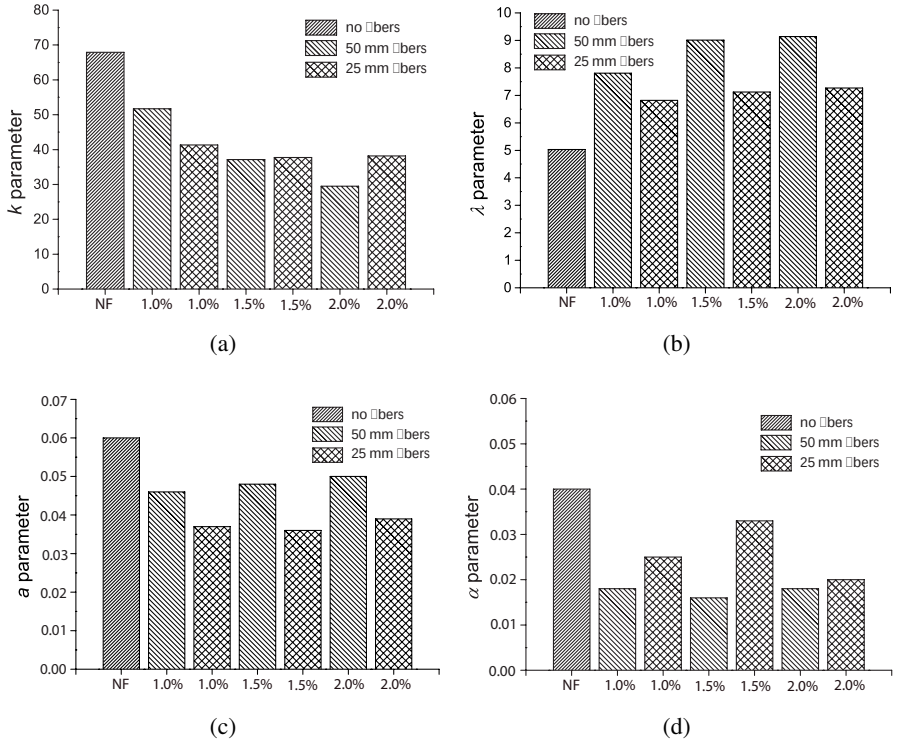

Figure 5.16 Influence of fibre length on model parameters: (a) k; (b) λ; (c) a; and (d) α, by fitting the flexural fatigue tests by Mohammadi and Kaushik [118].

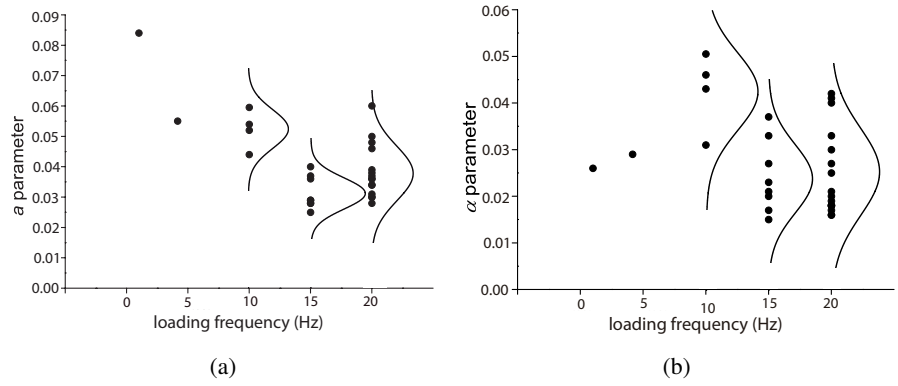

Figure 5.17 The variations of (a) a; and (b) α with respect to the loading frequency.

5.6 Concluding remarks

A new two-step procedure in order to estimate the parameters of the model of Saucedo et al. [154] has been developed based only on the fatigue tests and to demonstrate that this probabilistic fatigue model is also valid for predicting fatigue damage under flexion. With only four parameters, the model captures the fatigue damage of plain and fibre-reinforced concrete very well under bending, thereby allowing the analysis of its fatigue behaviour through the model parameters. The obtained results conform with well-established conclusions of the fatigue behaviour of plain and fibre-reinforced concrete, which further confirms the reliability of the model.

It is concluded that the flexural strength of SFRC, which is directly related to the scale parameter λ, is improved by the addition of fibres. Nonetheless, this improvement is less pronounced when the fibre volume fraction surpasses 1.0‰. Moreover, longer fibres are more effective in enhancing the flexural strength. The scattering of flexural fatigue data, measured by the shape parameter k, increases with fibre addition. This can be attributed to the additional voids created around fibres. This scattering is more significant for larger volume ratios of longer fibres, but hardly varies with V_f for short fibres. Both a and α are sensitive with the loading frequency, f. Particularly, a decreasing trend is observed for a when f is less than 15 Hz. Nevertheless, due to the lack of experimental data in the low loading rate range, no specific conclusions can be drawn. Fibre aspect ratio plays a role on the flexural strength, but there are not sufficient experimental data to draw definite conclusions. For the same stress level, σ_{max}/f_{fl}, the mean fatigue life may decrease or increase with the fibre content. However, when the maximum stress, σ_{max}, is kept the same, the mean fatigue life increases significantly with fibre volume ratio. In addition, at the same volume ratio, short fibres offer more enhancement in fatigue life than longer fibres.

6 Thermal effect on flexural fatigue behaviour of UHPFRC

6.1 Fatigue failure of UHPFRC

The researches carried out focused on fatigue behaviour of UHPFRC are scarce so far despite on the increasingly interest in this concrete and its great application possibilities in which cyclic loads are predominant (e.g., offshore structures, slenderer bridge decks and piers, airport pavements, machine foundations, wind turbine towers) [12, 111]. Most of research has been focused essentially on the determination of the fatigue strength (i.e., endurance limit) in flexion [16, 111] and in uniaxial tension [111, 112] due to the high improvement of tensile strength in this concrete. Moreover, few of researches deal with the influence of fibres on the fatigue life in UHPFRC [12, 60]. In fact, despite the important role of concrete matrix (i.e., components, amount and fibre distribution, and inherent flaws) in fatigue behaviour of concrete under cyclic loading [12], there are few studies focused on establishing a relationship among the matrix pore structure and degradation by thermal damage, with the contribution of the fibre reinforcement, in the mechanical properties and the fatigue performance of UHPFRC at different temperatures.

A comprehensive experimental campaign has been carried out in this chapter to analyse the fatigue behaviour of UHPFRC, reinforced with steel and

polypropylene fibres, by the determination of the S-N field at room temperature, 100, 200 and 300 °C. A probabilistic fatigue model based on Weibull distribution functions developed by Castillo and Canteli [33, 61] has been used to determine the S-N field. Previously, static three-point bending tests were performed to determine the mechanical properties of concrete under static loading at the different temperatures tested. The influence of the addition of fibres and the temperatures in the concrete microstructure and their consequences, in the mechanical properties and fatigue behaviour was determined through X-ray computed tomography (CT) scan. Finally, it was established a connection among the results from X-ray CT scan, thermoanalytic analysis performed, the mechanical properties and fatigue behaviour at the diverse temperatures tested.

6.2 Ultra-high-performance concrete mixes

6.2.1 Mix proportions and specimen preparation

Three ultra-high-performance fibre-reinforced concrete mixes were manufactured in this study. All of them were exactly prepared with the same constituents of the matrix and only differed in the type of fibres added as reinforcement. The constituents of matrix were the same used in Chapter 3 and Chapter 4 for the study of fracture behaviour under monotonic loads. The mixes were designed in accordance with the recommendations given in [47]. The binder was formed by the CEM I 52.5 R/SR provided by Portland Valderribas; the silica fume was the S-92-D model produced by SIKA and the ground granulated blast furnace slag (GGBS) was provided by Arcelor. Two types of quartz sand were used as aggregate. The finest aggregate had a maximum particle size of 0.315 mm and the coarsest one was 0.800 mm. The superplasticizer ACE 325 model of BASF company was used as reducing of water.

From the results obtained in Chapter 3 and Chapter 4 was decided used DSL and RC mixes for this study and a new variant with polypropylene fibres designed as DSLPP to improve the thermal performance of DSL. The mix proportions of each sort of mixes are shown in Table 6.1. The former concrete, labelled as DSL, was reinforced with two types of steel fibres exclusively. The steel fibres used were the OL 13/0.2 model and the C80/30BP model provided by Bekaert company and designated as micro- and macro-fibres in our study. The micro-fibres had straight shape, 13 mm in length, 0.2 mm in diameter and yield strength of 2750 MPa. The macro-fibres had hooked-end shape, 30 mm in length, 0.38 mm in diameter and yield strength of 3070 MPa. The fibre

Table 6.1 Constituents and mix proportions of mixes.

	Mixes (kg/m^3)		
Constituents	RC	DSL	DSLPP
cement (c)	544	544	544
silica fume	214	214	214
GGBS	312	312	312
fine sand (< 315 μm)	470	470	470
coarse sand (< 800 μm)	470	470	470
water (w)	188	188	188
superplasticizer (SP)	42	42	42
steel micro-fibres	-	98	98
steel macro-fibres	-	98	98
PP fibres	-	-	1.2
w/c	0.34	0.34	0.34
w/binder	0.17	0.17	0.17

content was of 2.5% in volume fraction and both types of fibres (micro- and macro-fibres) combined at 50% (i.e., 98 kg/m^{3}of micro-fibres and 98 kg/m^3 of macro-fibres). The second concrete, labelled as DSLPP, contained the same types and proportions of steel fibres as DSL but also polypropylene fibres were included. The polypropylene fibres were provided by Geotexan. The Geocem model was used with 24 mm in length and 8.9 dtex in diameter. A plain concrete with the same matrix as constituents of matrix was manufactured to be used as reference concrete (RC mix).

All specimens were manufactured following the same procedure. First, all dry constituents were poured into the mixer and rotated for 5 min. Next, the solution water-superplasticizer was added and rotating for 15 min until a fluid and homogeneous mix was observed. Finally, fibres were poured into the mixer and rotated for 10 min until were efficiently dispersed. The specimens were immediately cast, subsequently unmolded, and after 24 h cured immerse in a water bath at 20 °C for 28 days.

6.3 Experimental program

6.3.1 Mechanical and fracture tests

Cubic specimens with 100 mm of side, cylinders of 100 mm in diameter and 200 mm of height and prismatic specimens of $100 \times 100 \times 440$ mm^3 were casted in order to determine the mechanical and fracture properties. The RC and DSL concrete were tested at room temperature, 100, 200 and 300 °C; and the DSLPP at room temperature and 300 °C.

Testing on room temperature specimens

The compressive strength was determined on four cubic specimens for each mix (i.e., RC, DSL and DSLPP) according to the EN 12390-3 standard [55]. The Young's modulus was measured on four cylinders for every mix in accordance with the EN 12390-13 standard [54]. This test was gradually loading until a third of its failure load and recording the relative strain by two linear variable differential transformer (LVDT) sensors of 25 mm in length, one in front of the other, surrounding the cylinder. Three-point bending tests on four notched prismatic specimens for every mix were performed to measure the work-of-fracture in accordance with the RILEM method [146] and determine the fracture energy following the corrections proposed by Guinea et al. [53, 68, 140]. All specimens had a notch to depth ratio of one sixth. The mid-span deflection was measured by means of a LVDT of 25 mm mounted on a rigid frame to avoid torsional effects and a clip gage on the bottom of specimen to measure the crack mouth opening displacement (CMOD).

Testing on heated specimens

The specimens were heated on a 10 °C/min rate and the objective temperature was maintained at least for 24 hours to ensure a homogeneous temperature in the material. The type of tests and the number of specimens tested were the same as at room temperature. However, the temperature leads to the impossibility of using the sensors on these tests. The three-point bending tests were carried out within a furnace at each temperature (i.e., 100, 200 and 300 °C) for every mix due to the actuator and supporting framework can be entered inside the furnace. Only load and actuator position data can be recorded due to temperatures. For the estimation of the load-deflection curves from three-point bending tests at various temperatures (100, 200 and 300 °C) was followed the procedure explained in Subsection 4.3.2. The thermal analysis of matrix used in this chapter was that carried out in Subsection 4.4.1 since the same matrix has been used.

6.3.2 Fatigue tests

Fourteen prismatic specimens of $100\times100\times440$ mm^3 for each fatigue test (i.e., mixes and temperatures) were manufactured in order to determine the fatigue life. Three-point bending fatigue tests on notched prismatic specimens were performed with a depth ratio of one sixth. Fatigue tests were conducted in a servo-hydraulic machine with maximum loading capacity of 150 kN. All tests were carried out with the same stress ratio, R=0.2 and loading frequency, f=4 Hz and varying the maximum load applied. The reference concrete, RC, and steel fibre-reinforced concrete, DSL, were heated to room temperature, 100, 200 and 300 °C; and the steel-PP fibre-reinforced concrete, DSLPP, at room temperature and 300 °C. All fatigue tests were carried out over heated specimens inside furnace at the target temperature. From experimental fatigue data, the probabilistic fatigue model developed by Castillo and Fernández-Canteli [33] was used to estimate the S-N field. The fatigue model, based on Weibull distribution functions, defines the S-N field by means of different hyperbolic curves that represents the same probability of failure (different percentiles). The model can be applied to any general fatigue reference parameter that defines a crack initiation criterion (i.e., stress, strain, energetic parameters, etc.). The probability of failure is calculated as follows:

$$P_{fail} = 1 - exp\left[-\left(\frac{V-\nu}{\lambda}\right)^{k}\right], \tag{6.1}$$

in which

$$V = (logGP - C)\,(N_{ini} - B), \tag{6.2}$$

where GP is the damage generalized parameter, N_{ini} is the lifetime and ν, k and λ are, respectively, the location, shape and scale parameters, of the Weibull distribution and V is the normalized parameter. In this work, the damage generalized parameter used was the stress level, S, defined as f_r/f_{fl}, where f_r is the flexural stress applied and f_{fl} is the monotonic flexural strength from notch three-point bending tests. The location parameter represents the smallest value of V at which the failure probably occurs. Both scale, λ, and shape, k, parameters are related to the scatter of the experimental results. The former is related to the specimen size and the latter with the fracture mechanism. For

more detail information about the probabilistic fatigue model used see [33].

6.3.3 Microstructural analysis by X-ray CT scan

The X-ray computed tomography technique was used to determine the pore structure in the concrete matrix at room temperature due to air entrapped during mixing process and fibre effect as well as the influence of temperature on microstructure at 300 °C. The X-ray inspection equipment, Y. Cougar SMT model of the YXLON company, sited in the Characterization Service of the University of Seville, was used. The equipment contains a multi-focus tube and wolfram target which allows the inspection in the range between 25-160 kV and 0.01-1 mA intensity. It allows generate images with a maximum geometric magnification of 2,000x. The X-ray graphs are reconstructed and treated by using the VGStudio MAX 2.2.3 software. The samples specimens used on the X-ray analysis were sawn and extracted from the core of the prismatic specimens ($100\times100\times440$ mm^3) to avoid boundary effects. The dimensions of samples were approximately $25\times25\times100$ mm^3. Four samples of each mix (i.e., RC, DSL and DSLPP) and the most extreme temperatures (RT and 300 °C) were analysed exclusively. The sample were scanned at RT and after being subjected at 300 °C. Only the extreme temperatures (RT and 300 °C) were scanned because intermediate behaviour were assumed at 100 and 200 °C. The 2D X-ray radiographs had a resolution of 1024×1024 pixels. These images are digitally reconstructed into 3D absorption contrast image of the sample providing 3D information about different density areas. A final resolution of 40 μm in the three cartesian directions were obtained for these samples and mixes. The X-ray CT scan results of DSLPP were determined for this study. However, the X-ray CT scan results of RC and DSL mix at RT and 300 °C were those obtained in Chapter 3 and Chapter 4 respectively. To obtain more detail about the analysis procedure by X-ray CT scan see Subsection 3.3.3.

6.4 Results and discussion

In this section, the experimental results from the microstructural analysis at different temperatures and the thermal analysis of concrete matrix (RC) -carried out in Chapter 4- is established a connection with the macroscopic behaviour of mixes (i.e., RC, DSL and DSL): mechanical and fracture properties as well as the fatigue behaviour of UHPFRC studied (i.e., RC, DSL, and DSLPP).

6.4.1 Microstructural analysis by X-ray CT scan

An average value of porosity parameters measured from four samples of each mix (i.e., RC, DSL and DSLPP) and temperature (i.e., RT and 300 °C) were shown in Table 6.2. The porosity, Φ_{xr}, their average equivalent diameter, $\overline{d_{eq}}$, and the average sphericity, $\overline{\Psi}$, are presented. The evolution of the cumulative porosity and differential pore size distribution, in y-axis, with regard to the equivalent diameter size, in x-axis, are shown in Fig. 6.1.a and b respectively. The samples analysed at RT and 300 °C were the same to ensure that differences in microstructure come exclusively from the temperature effect.

With regards to microstrcuture at room temperature, it is observed that the presence of fibres in the matrix reduced the porosity from 4.0% for the reference concrete, RC, (plain concrete) to 2.2% and 3.7% (Table 6.2 and Fig. 6.1.a) on the DSL and DSLPP respectively, according to the results obtained by other authors [141, 188]. The reduction of porosity was due to the steel fibres smash the air entrapped bubbles (pores above 10 μm) in the concrete paste during the mixing process [188] when the amount of fibres is high (e.g., 2.5% in volume fraction) according to the results obtained by Ponikiewski et al. [141] and the results obtained in Fig. 6.1.b. RC mix shown a predominant amount of pores in the range of 0.25-1.2 mm. However, the pore size distribution was more uniform for fibre-reinforced mixes (i.e., DSL and DSLPP). It is worth noting as the presence of fibres induced pore concentration [81] which conducted to the amount of larger pores increased, as observed in Fig. 6.1.b (i.e., DSL and DSLPP) and deduced from higher average equivalent diameter results in Table

Table 6.2 Porosity parameters of each mixture from X-ray CT analysis.

	Room temperature		
Property	RC	DSL	DSLPP
$\overline{d_{eq}}$ (mm)	0.28 ± 0.03	0.34 ± 0.02	0.31 ± 0.03
$\overline{\Psi}$	0.93 ± 0.02	0.88 ± 0.01	0.92 ± 0.01
$\Phi_{xr}(\%)$	4.0 ± 0.9	2.2 ± 0.5	3.7 ± 0.4
	300 °C		
$\overline{d_{eq}}$ (mm)	0.29 ± 0.02	0.27 ± 0.01	0.32 ± 0.03
$\overline{\Psi}$	0.96 ± 0.01	0.92 ± 0.01	0.93 ± 0.01
$\Phi_{xr}(\%)$	5.0 ± 0.3	2.6 ± 0.1	4.1 ± 0.6

Results of the porosity of all mixes (i.e., RC, DSL and DSLPP) at 300 °C exhibited an increase in comparison with those at room temperature (Table

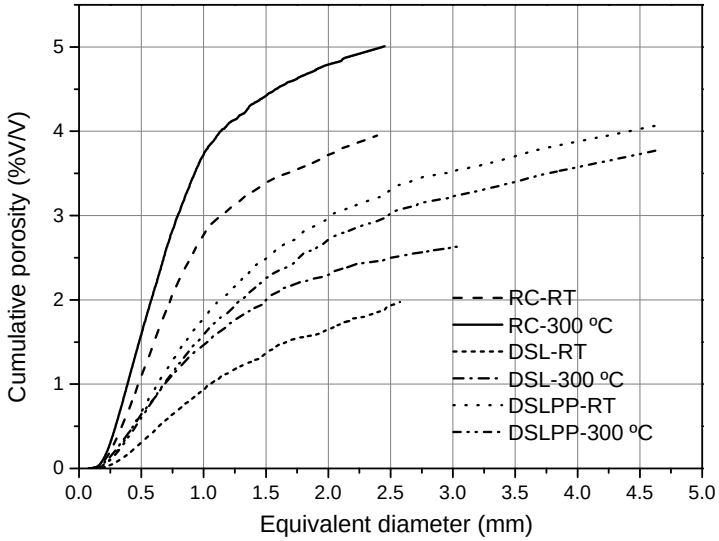

(a)

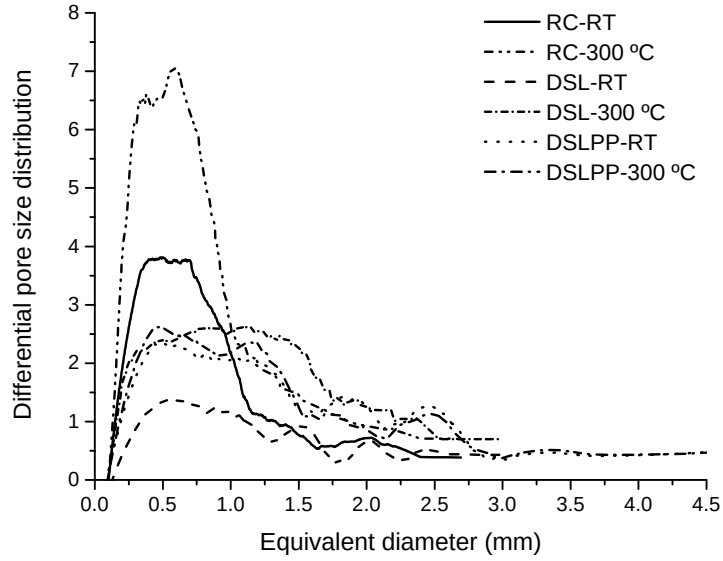

(b)

Figure 6.1 Cumulative pore size distributions (a) and differential pore size distributions (b) of mixes at RT and 300 °C.

6.4.2 Mechanical and fracture properties

The mechanical and fracture properties of each mix (i.e., RC, DSL and DSLPP) and temperature tested (i.e., RT, 100, 200 and 300 °C) are presented in this subsection. As mentioned above, the PP fibre-reinforced mixes (DSLPP) were exclusively tested at room temperature and 300 °C. Fracture energy, G_F, of the reference concrete (RC) could not be determined at 100, 200 and 300 °C because the testing control by CMOD clip could not be set on heating tests.

Compressive strength and Young's modulus

From the results at room temperature, fibre-reinforced mixes (i.e., DSL and DSLPP) exhibited a remarkable enhancement on the compressive strength, f_c, in comparison with RC (plain concrete) with an average increase of 31% in the DSL and 33% in the DSLPP. This improvement was essentially due to the positive sewing effect of the steel fibres against the tensile strains generated during the compression tests in the concrete [123]. Additionally, the total porosity is considerably lower than RC (Table 6.2) and more uniformly pore size distributed (Fig. 6.1.b). As observed, the presence of PP fibres in concrete matrix resulted in a higher total porosity (Table 6.2). However, it did not show a clear influence on the compressive strength, according to results obtained by other authors [145, 147]. At 100 °C, the compressive strength decreased for RC (21%) and DSL (2.6%) due to high pore pressure inferred by the evaporation of moisture. When stresses reach tensile strength, microcracks are generated in the concrete matrix which results in strength loss [42,147,205]. The decrease is more significant for RC because of pore pressure is more harmful on small pore size and the porosity of RC mix are essentially characterised by having the smallest pore size (Fig. 6.1.b). At 200 °C, two simultaneous and contradictory effects took place, the temperature on the cement paste improved its hydration [15, 147] and the high vapour pressure damaged the concrete matrix. The first one, inferred into the highest compressive strength, was reached, with an average value of 172 MPa (i.e., an increase of 20%), for the fibre-reinforced concrete (DSL) and an increase of 15.6% for RC mix. At 300 °C, the matrix showed considerable damage due to dehydration of C-S-H gel (see Subsection 4.4.1). In fact, some samples, even those reinforced exclusively with steel fibres (DSL), presented an explosive failure in furnace during the heating process. Nonetheless, spalling failure was not observed on PP fibre-reinforced concrete (DSL) since PP fibres were melted [43,147] and generated a network of channels through which vapour could be evacuated more efficiently, mitigating the harmful effect of heating in the concrete matrix. It is worth noting as that the scatter of results increased

with the increment of temperature showing as that thermal gradient does not infer a uniform harmful in the concrete matrix (Fig. 6.3).

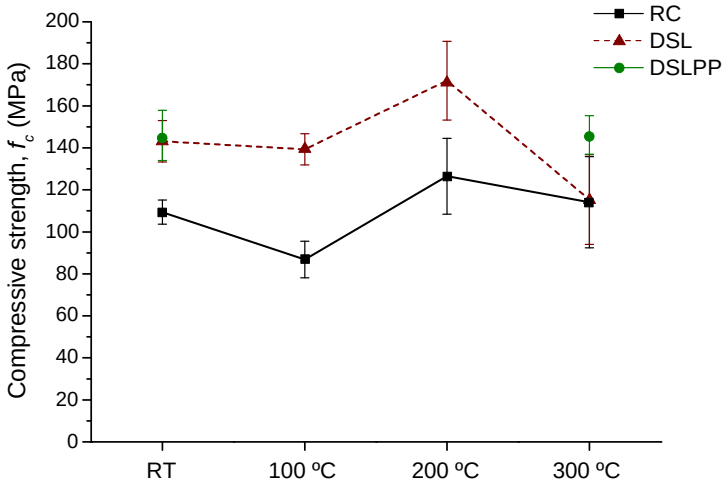

Figure 6.2 Compressive strength of mixes at RT, 100, 200 and 300 °C.

With regards to Young's modulus at room temperature, although a slight increase is appreciated for fibre-reinforced concrete (i.e., DSL and DSLPP), it cannot be concluded that the addition of fibres, (on the rates used), have a clear influence, as observed by other authors [4, 147]. At 100°C, a 10% decrease was observed on RC (plain concrete) due to that damage inferred by the vapour pressure by moisture evaporation. However, that harmful effect is not appreciated on Young's modulus when the matrix is reinforced with steel fibres (DSL), as concluded by results (Fig. 6.3). At 200°C, a 20% and 19% decrease took place on RC and DSL respectively. Note that, both mixes (RC and DSL) reached a similar decrease on Young's modulus. Thus, steel fibre-reinforcement does not show a clear influence on this property. At 300 °C, a 38%, 36% and 31% decrease is observed on RC, DSL and DSLPP respectively. The mitigating effect of PP fibres on the heating damage was observed reaching the best Young's modulus results at 300 °C.

Flexural strength

At room temperature, the flexural strength, f_{fl}, exhibited a remarkable enhancement of fibre-reinforced mixes, 5 times in the DSL and 4 times in the DSLPP mix (Fig. 6.4). The improvement on the flexural strength was due to the crack bridging effect of steel fibres and the decrease of air entrapped by the presence

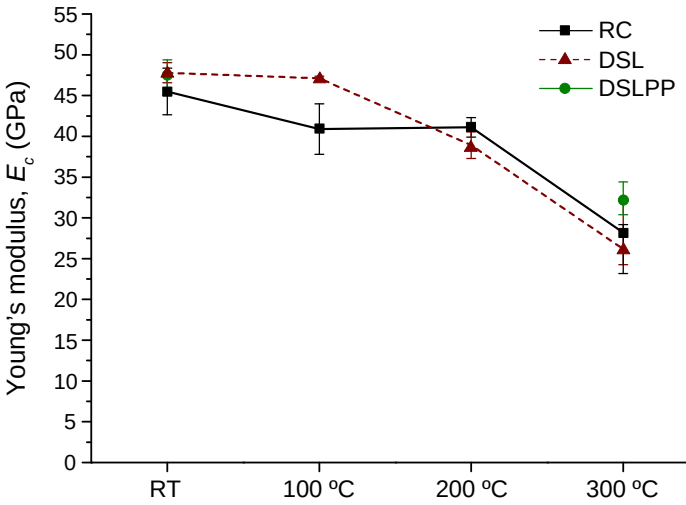

Figure 6.3 Young's modulus of mixes at RT, 100, 200 and 300 °C.

of steel fibres in the concrete matrix (see). At 100 °C, the flexural strength decreases 11% on RC and 21% DSL due to similar effects described on compressive strength. Note that, the harmful effect of heating affects more strongly to fibre-reinforced concrete. In this mix, the evacuation of vapour pressure is less effective because of the lower porosity (Fig. 6.1.a). With regards to 200 °C and 300 °C tests, the heating process conducted on spalling failure on some samples of plain concrete (RC) and tests were carried out on those samples no apparently affected by spalling. As observed, no significant changes are appreciated on the average values of flexural strength on plain concrete (RC) but the standard deviation is strongly higher. A slight decrease was observed at 200 and 300 °C on DSL showing that the strongest damage by heating on this property occurs below 200 °C. Note that, spalling failure occurred on DSL at 300 °C and thus, the standard deviation does significantly rise. The PP fibre-reinforced concrete (DSLPP) presented an 8% decrease at 300 °C and a non-remarkable increase of standard deviation since spalling failure was not inferred.

Fracture energy by three-point bending tests

Fracture energy average values of all mixes and temperature tested are shown in Table 6.3. At room temperature, fracture energy significantly enhanced mainly due to the bridging effect of steel fibres greatly increases the energy absorption capacity of fibre-reinforced concrete [21]. The highest average value was reached for exclusively steel fibre-reinforced concrete (DSL) because the lower porosity

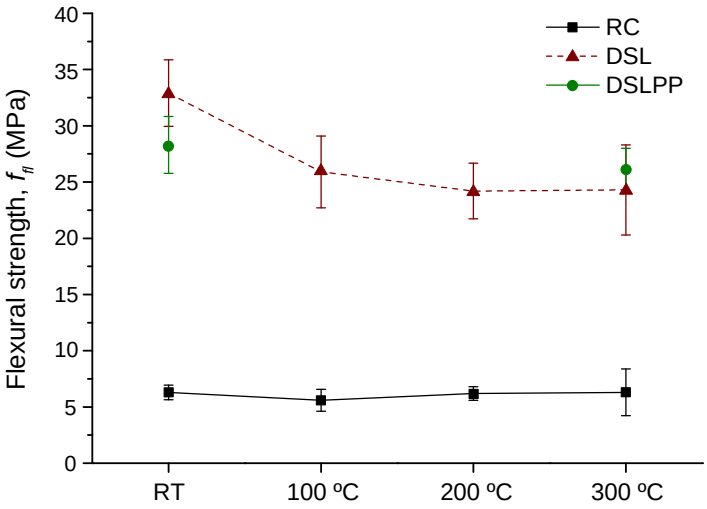

Figure 6.4 Flexural strength of mixes at RT, 100, 200 and 300 °C.

(Fig. 6.1.b) led to reach higher work-of-fracture in accordance with higher flexural strength values in Fig. 6.4. When the temperature is increasing (100, 200 and 300 °C), the vapour pressure and the dehydration generated internal damage that increased the number of pores, especially between 0.20-1.2 mm pore size (Fig. 6.1.b) and decreased the fracture energy. Note that the fracture energy value at 300 °C, is higher and with less deviation for the PP fibre-reinforced concrete (DSLPP) because although PP fibres are melted and that reduces the strength, as explained above, thermal damage by moisture evaporation and dehydration is mitigated and consequently enhanced results are obtained.

Table 6.3 Fracture energy of RC, DSL and DSLPP.

	G_F (N/m)		
Temperature	D0	DSL	DSLPP
RT	61 ± 3	47171 ± 5	42056 ± 6
100 °C	-	32695 ± 9	-
200 °C	-	28662 ± 18	-
300 °C	-	24842[a]	28462 ± 12

[a] Spalling effect observed in some samples during heating

6.4.3 Fatigue behaviour

In this section, the experimental data obtained from the flexural fatigue tests of each mix (i.e., RC, DSL and DSLP) are exposed. At least ten fatigue tests corresponding to diverse stress levels were taken into account on the evaluation by the probabilistic fatigue model [33]. Table 6.4 presents the results of the fatigue tests of reference concrete, RC, (i.e., plain concrete) for diverse stress levels at room temperature, RT, and 100 °C. Premature failure by spalling was observed during the heating process inside furnace in some heated RC specimens at 200 and 300 °C. Thus, not enough number of fatigue tests became available for the application of the probabilistic fatigue model [61] and consequently, they are not shown in Table 6.4 by not being evaluated in the study. Results exhibit an important variation in the fatigue data, commonly accepted of 2 order-of-magnitude on fatigue life [181], even at a particular stress level. This is essentially due to the heterogeneous composition (i.e., cement paste, aggregates, fibres) and statistical nature of fatigue phenomenon [64].

Table 6.4 Stress level and fatigue life data of reference concrete, RC mix.

Temp.	Stress level S (%)	Fatigue life N (cycles)	Temp.	Stress level S (%)	Fatigue life N (cycles)
RT	90	6	100 °C	90	32
	85	19		85	913
	75	16108		80	18
	70	1225		75	18943
	70	99		77.5	6
	65	43000		70	9931
	60	94		60	62337
	57.5	1065		55	228219
	55	93700		50	228635
	52.5	1105		45	669156
	50	2000000[a]		39	2000000[a]
				35	670925
				30	2000000[a]

[a] Run-out

The fatigue results on steel fibre-reinforced concrete mixes (i.e., DSL) are presented in Table 6.5. The tests were carried out for diverse stress levels at

room temperature, 100 and 200 °C. At 300 °C, some of specimens prematurely exploded by spalling and not enough number of data became available for the S-N field determination.

Table 6.5 Stress level and fatigue life data of reference concrete, DSL mix.

Temp.	Stress level S (%)	Fatigue life N (cycles)	Temp.	Stress level S (%)	Fatigue life N (cycles)
RT	90	79	100 °C	90	394
	85	2150		85	64
	80	631		85	2597
	77.5	33		80	4513
	75	3998		80	230
	72.5	15836		77.5	2120
	70	5030		75	2000000[a]
	67.5	16911		75	7
	65	83875		72.5	228635
	62.5	33790		72.5	2000000[a]
	60	256282		70	272
	55	423098		67	7649
	50	2000000		62	7807
Temp.	Stress level S (%)	Fatigue life N (cycles)	Temp.	Stress level S (%)	Fatigue life N (cycles)
200 °C	90	126			
	85	5914			
	82.5	34155			
	80	20			
	80	18396			
	77.5	2000000[a]			
	75	46977			
	72.5	16656			
	71	2000000[a]			
	70	44			
	65	2688			
	60	2000000[a]			
	55	2000000[a]			

[a] Run-out

Table 6.6 exhibits the fatigue results for the steel and polypropylene fibre-reinforced concrete mixes (i.e., DSLPP). This mix was only tested at room temperature and 300 °C. Not spalling effects were observed in these mixes during the heating process since the addition of PP fibres reduced the thermal damage by high pore pressure and dehydration in the matrix, as mentioned in Subsection 6.4.1.

Table 6.6 Stress level and fatigue life data of reference concrete, DSLPP mix.

Temp.	Stress level S (%)	Fatigue life N (cycles)	Temp.	Stress level S (%)	Fatigue life N (cycles)
RT	90	101	300 °C	90	3252
	85.5	26552		87.5	2339
	85	23746		85	45560
	82.5	15		85	11135
	81.1	28		82.5	13780
	80	71921		80	2595
	77.5	38209		77.5	14623
	73.8	40791		75	66212
	72.5	64		70	139
	67.5	2299		68.7	67319
	65	1617740		67.5	58000
	62.5	2000000[a]		65	2000000[a]
	55	2000000[a]		60	161699

[a] Run-out

Table 6.7 shows the model parameters fitted from the experimental fatigue tests according to the probabilistic fatigue model developed by Castillo and Fernández-Canteli [61]. As already mentioned, B is the vertical asymptote, and C is the horizontal asymptote which represents the endurance limit and k and λ are, respectively, the shape and scale parameters of the Weibull distribution. Finally, ν is the location parameter that defines the position of the zero-percentile curve of the S-N field estimated.

Influence of the fibres on the fatigue life

For the purpose of examining the influence of fibre addition on the fatigue behaviour of the diverse mixes manufactured (i.e. RC, DSL and DSLPP), the S-N field has been determined through the application of the a probabilistic fatigue model developed by Castillo and Fernández-Canteli [33]. From the

Table 6.7 Model parameters fitted according to the probabilistic fatigue model [33].

	k	B	C	λ	ν
RC-RT	1.01	4.5	3.85	0.99	0.01
RC-100 °C	7.32	0	2.62	15.68	0
DSL-RT	6.67	0	3.69	5.08	0
DSL-100 °C	1.39	2.97	3.71	3.76	0
DSL-200 °C	1.34	2.02	3.70	1.24	1.53
DSLPP-RT	1.24	3.3	3.97	1.8	0
DSL-300 °C	1.95	4.89	3.79	2.71	0

S-N field, only the 0.5 and 0.95 percentile curves for each mix (i.e., RC, DSL and DSLPP) and temperature tested (i.e., RT, 100, 200 and 300 °C) have been plotted for more clarity.

Fig. 6.5 represents the 0.5 and 0.95 percentile curves of reference concrete, RC, DSL, DSLPP at room temperature. From the results in Fig. 6.5 is observed that the addition of steel fibres (i.e., DSL) does not significantly enhanced the fatigue limit at room temperature (from 48% on RC to 46% on DSL). The addition of steel fibres is positive for the monotonic flexural strength, as seen in Fig. 6.4, essentially due to the bridging effect of steel fibres which avoid the free crack propagation in the matrix and the reduction of porosity (Table 6.2 and Fig. 6.1). However, that factor does not avoid the propagation of the existent defects by repeated loading following the path of minimum energy through matrix resulting in a similar endurance limit. By contrast, whether the fibre distribution is uniform in the matrix, the fatigue life is improved for stress levels above endurance limit and the scatter, represented by the separation between 0.5 and 0.95 percentile curves, is reduced [12]. For steel-PP fibre-reinforced concrete mix (i.e., DSLPP), the presence of PP fibres infers larger pores (Fig. 6.1.b). Larger pores conduct to more stress concentration and less monotonic flexural strength (Fig. 6.4). The random distribution of porosity leads to a more dispersed fatigue life, as observed from the separation of 0.5 and 0.95 percentile curves in Fig. 6.5. By having larger pores leads to non-uniform distribution of them and propagation of microcracks from some pores to others, may become more difficult so that only the harmful ones are prone to grow. Additionally, PP fibres contribute to microcracks propagation [147] like similar way than steel fibres. Thus, fatigue limit becomes lightly higher for DSLPP mix at room temperature compared to the other mixes (Fig. 6.5).

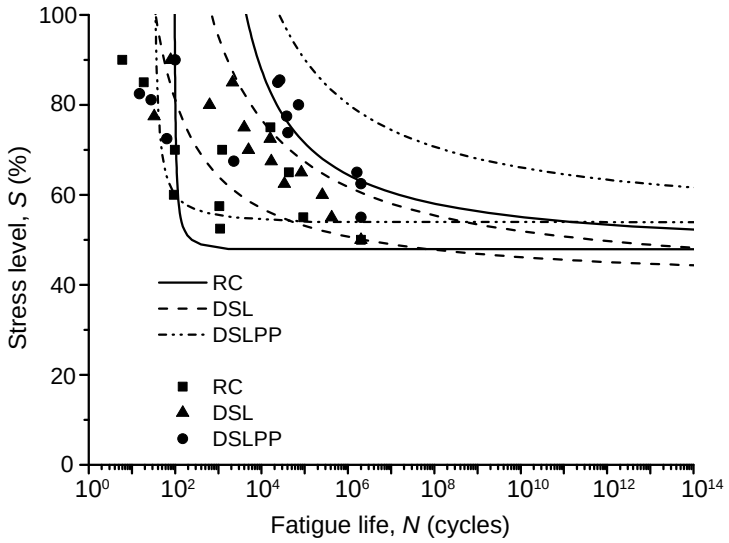

Figure 6.5 S-N field of each mix at room temperature.

From the results at 100 °C shown in Fig. 6.6, the endurance limit of steel fibre-reinforced concrete, DSL, was significantly higher than for the reference concrete, RC, (45% versus 22%). The heating process to 100 °C conducted to favours the generation of microcracks in the concrete matrix inferred by the high pore pressure because of capillary pressure and partial dehydration. This led to a decrease of monotonic flexural strength (Fig. 6.4). The fatigue limit of reference concrete, RC, strongly decreased because it did not have any type of reinforcement to avoid the growing of microcracks by temperature and repeated loading. For steel fibre-reinforced concrete, DSL, the effectiveness of the large number of steel fibres to avoid the microcrack growing in matrix through the path of minimum energy led to a no significant decrease of fatigue life (45% at 100 °C). However, the non-uniform thermal gradients generation derived into promotes a no-uniform thermal damage in the matrix which significantly increased the scatter of S-N curves for DSL mix (see Fig. 6.6).

Influence of the temperature on the fatigue life

Fig. 6.7 represents the influence of temperature on reference concrete S-N field (RC) exposed to room temperature and 100 °C (Fig. 6.7). As failure by spalling was observed in some heated RC specimens at 200 and 300 °C, not enough number of fatigue tests became available for the application of the probabilistic fatigue model [61]. Hence, only S-N curves of RC mix at room temperature and

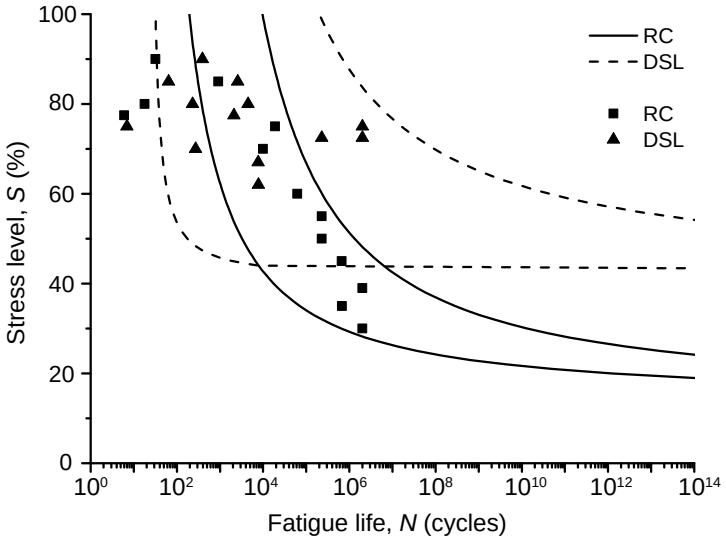

Figure 6.6 S-N field of each mix at 100 °C.

100 °C are presented in Fig. 6.7. At room temperature, the endurance limit is reached on the 47% of stress level, S (Fig. 6.7). The heating to 100 °C conducted to the generation of microcracks in the concrete matrix inferred by the high pore pressure because of capillary pressure and partial dehydration resulting in a more cracked matrix which derived into a significant decrease of endurance limit from 47 to 14% (Fig. 6.7). The repeated loading under maximum monotonic strength leads to birth and growth of micro-defects (i.e., pores, microcracks) following the path of minimal energy conducting to a progressive degeneration of the internal structure which derives into the decrease of material strength, as observed in monotonic flexural results (Fig. 6.4). Due to Since at 100 °C the matrix is initially more deteriorated degraded by thermal damage, the harmful propagation by fatigue loading is more effective and conducts to a significant lower endurance limit (Fig. 6.7).

In steel fibre-reinforced concrete mix (i.e., DSL) at room temperature (Fig. 6.8), the endurance limit reached for the 0.50 percentile curve corresponds to a stress level, S, of 46% and a small scatter shown from the narrow separation between 0.5 and 0.95. Despite the internal degradation of the concrete matrix by thermal damage (i.e., high pore pressure and dehydration) at 100 °C and more strongly at 200 °C, the values of fatigue limit achieved on both temperatures (i.e., 100 and 200 °C) are very similar to that at room temperature (i.e., 45% and 44% of stress level, S, respectively). This demonstrates that the sewing effect of

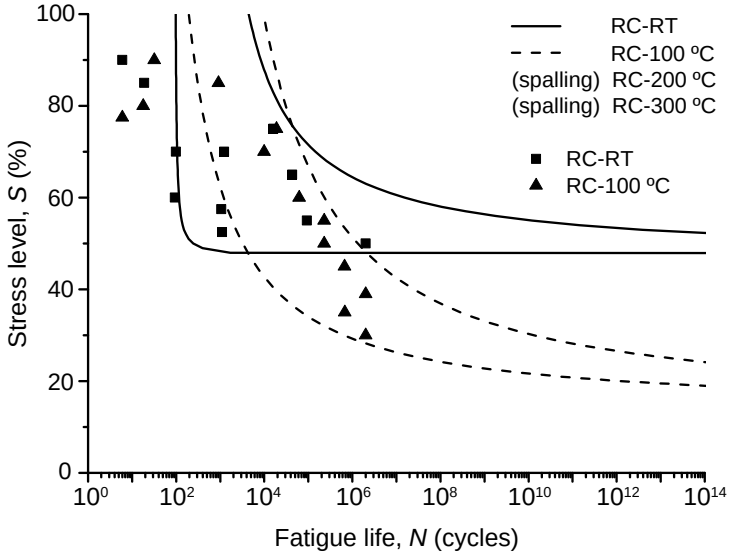

Figure 6.7 S-N curves of reference concrete (RC) at different temperatures.

this large number of steel fibres is essentially providing the fatigue strength of concrete by means of avoiding the crack propagation following the path of minimum energy [181] although the microdefects by thermal damage in concrete matrix is initially higher at 100 and 200 °C. Nevertheless, as thermal gradients is randomly distributed, the defects inferred by thermal damage are also randomly distributed in the matrix [181] resulting in a bigger scatter in the flexural strength (Fig. 6.4) and the fatigue behaviour (Fig. 6.8). The separation between 0.5 and 0.95 percentile curves of DSL-100 °C and DSL-200 °C (Fig. 6.8) is larger representing the bigger scatter among the fatigue life results (Table 6.5).

For steel and polypropylene fibre-reinforced concrete mix (i.e., DSLPP) at room temperature (Fig. 6.9), the endurance limit was a stress level, S, of 56%. The addition of PP fibres increased the total porosity of matrix with a more uniform pore size distribution and a wider range of pore sizes (Fig. 6.1.b) which promote less proportion of microdefects distributed in the matrix and enhanced fatigue behaviour. At 300 °C, this mix (DSLPP) was the only one that not failed by spalling during the heating process inside furnace. The most easily and efficiently evacuation of high pore pressure by capillary pressure and dehydration due to the generation of a network of channels with outside by the melting of PP fibres around 160 °C [147] led to obtain a less harmful matrix. In Fig. 6.1.b is observed that the lower range of pore size distribution at 300 °C almost is

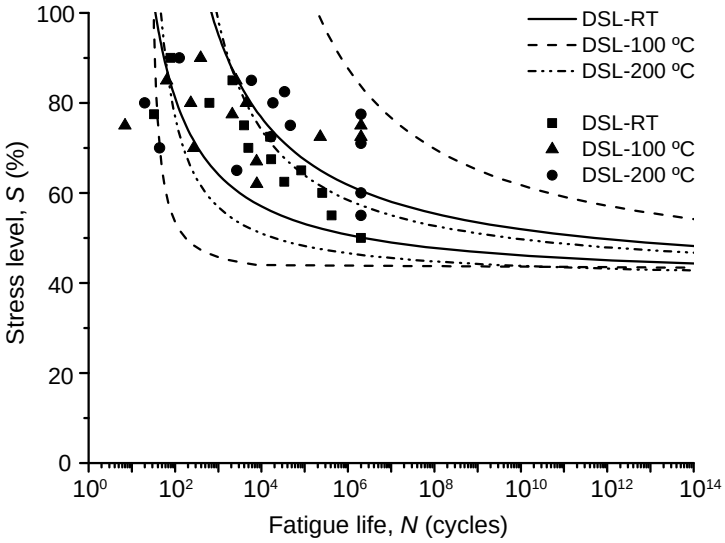

Figure 6.8 S-N field of steel fibre-reinforced concrete (DSL) at different temperatures.

invariant in accordance with the same matrix at room temperature. Thus, the endurance limit at 300 °C decreased to 48% of stress level, *S*, being above any other mix studied at lower temperatures. That improvement on the fatigue limit at 300 °C is in accordance with the results of flexural strength obtained for monotonic tests at room temperature and 300 °C in Fig. 6.4.

6.5 Concluding remarks

In this chapter has been established a relationship among the effect of temperature and fibre addition on the microstructure of UHPFRC with the mechanical and fracture behaviour under monotonic loads as well as the fatigue behaviour. This issue has not been dealt with up to present using UHPFRC and X-ray CT technique. A reduction of total porosity of smaller pore sizes due to the addition of fibres was observed since fibres act like tiny shovels which help during the mixing. The reduction of porosity combined with the bridging effect, essentially of steel fibres, leads to an increase of compressive and flexural strength as well as the fracture energy. Nevertheless, the presence of fibres induced a pore concentration around fibre-matrix interface that derives to larger pore sizes. The presence of PP fibres increase the porosity, especially in the range of larger pore

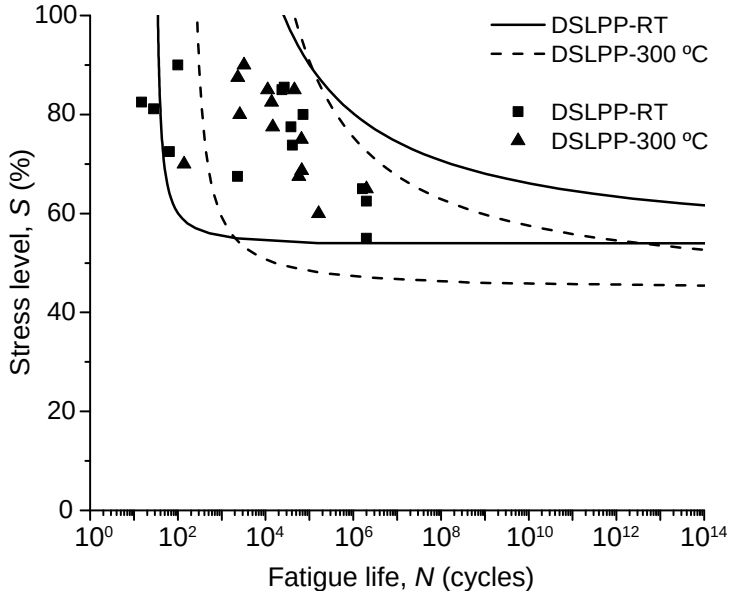

Figure 6.9 S-N curves of PP and steel fibre-reinforced concrete (DSLPP) at different temperatures.

sizes which conduct to light reduction of mechanical and fracture properties. The thermal damage affected more significantly to smaller pores so DSLPP was the least deteriorated mix since had a higher porosity and more uniformly distributed extended to wider range of pore sizes. This effect combined with the melting of PP fibres in those cases over 160 °C helped to evacuate more easily the pore pressure and reduce the thermal degradation. The presence of pores on microstructure are a source of defects which produces crack growth and propagation under cycling loading. Thus, the steel fibre-reinforcement of mixes improves the fatigue behaviour at RT since the presence of steel fibres in proper amount conducts to the significant reduction of pore structure of matrix and a more uniform pore sizes. Nevertheless, the fatigue behaviour of fibre-reinforced mixes is more scattering due to the presence of fibres induces pore concentration around fibres (i.e., steel or PP fibres) so that the pore distribution depends on the well-dispersion of fibres in the matrix. Thus, the combination of PP with steel fibres, DSLPP, lightly reduces the endurance limit. The thermal damage generates a higher porosity very concentrated in the range of smaller pores, especially on the reference concrete, RC, (i.e., between 0.2-1.2 mm) which derives into a strong decrease of endurance limit. In the fibre-reinforced mixes,

DSL and DSLPP, a thermal damage more uniformly distributed in the range of pore sizes between 0.2-1.6 mm is generated which combined with the bridging effect of fibres leads to a higher endurance limit at temperatures. The DSLPP mix reaches the highest endurance limit at 300 °C since the thermal damage in the microstructure comparison with the RT pore size distribution is quite similar.

7 Conclusions and future research

7.1 Conclusions

New requirements in construction materials combined with the progress of the construction technologies have led to the development of the ultra-high-performance fibre-reinforced concrete. The improvement of mechanical and fracture properties, the manufacturing of more durable elements and the reduction of the costs of fabrication have conducted to a new framework in which concrete is used in singular and special applications. The high thermal property of concrete and its improved durability joined to the reduced manufacturing costs, among other benefits, have led to the application of UHPFRC in situations where it is necessary bearing mechanical and thermal loads, e.g. the energy storage systems in solid medium. The multiscale analysis from the micro-level, i.e. microstructure of matrix, to the macro-level, i.e. mechanical, fracture properties and the fatigue behaviour, has not been addressed yet in the literature.

In this thesis, it has been analysed the mechanical and fracture behaviour of high-strength concrete reinforced with polypropylene fibres of different lengths and subjected to several high-temperatures (i.e., room temperature, 100, 300, 500 and 700 °C) for long periods of time. Complementary, a thermogravimetric analysis of the matrix at that range of temperatures combined with mineral composition were used to establish a relationship between the response of the material in the macro-level (i.e., mechanical and fracture properties) with the degradation of its microstructure (i.e., micro-level) caused by the temperature

exposition. The effect of temperature on high-strength concrete led to an irreversible and increasing process of weight loss with increasing temperatures due to the dehydration of residual water at low temperatures, dehydration of chemically bound water at medium-high temperatures and decarbonation of calcium carbonate at higher temperatures. The polypropylene fibres melted at 160 °C so that the presence of these fibres led to the creation of a network of channels in the matrix which evacuated the internal pressure by dehydration processes and reduced the thermal damage generated. Nonetheless, the presence of polypropylene fibres in matrix lightly reduces the material strength at room temperature due to the high number of pores generated around fibre-matrix interface. Polypropylene fibres presented a light bridge effect on the crack front that stitches any eventual microcracking. It was observed as longer fibres reduced the effects of spalling more efficiently than shorter fibres. However, they also increased the number of voids in the matrix, which conducted to lower mechanical properties and a softening of material. The cooling process of concrete derived to an additional microcracking that was more significant from medium-high temperatures where the thermal gradient is more abrupt and fibres are partially melted. It was observed as exposure time had no effect when the temperature is uniformly reached in the entire matrix.

The second type of concrete analysed in this thesis has been an advanced ultra-high-performance fibre-reinforced concrete. In this case a comprehensive study was carried out analysing the effect of large amount of steel fibres with different length and dosages on the microstructure and their consequences in the mechanical and fracture properties at room temperature and 300 °C. The addition of fibres alters the microstructure of the matrix and modifies the thermal conductivity of concrete, which infers on the thermal gradient and consequently on the thermal damage generated in the matrix and is related with the properties in the macro-scale (i.e., mechanical and fracture properties).

The presence of steel fibres in the 2.5% in volume fraction inferred a reduction in the porosity of the microstructure. Steel fibres acted as tiny shovels that help to the mixing process and reduced the porosity specially the smaller pore sizes. Micro-fibres (13/.2) were more effective in this process and were better distributed inside the matrix. The reduction of small pore sizes and the well-distribution of fibres led to an increase of the first-cracking strength f_t, of the reinforced concrete mixes, especially in DS mix, reinforced only with micro-fibres. The tensile strength of the mixes, f_{tu}, was quite similar regardless of whether the fibres used are macro-fibres (35/.55) or micro-fibres. Macro-fibres had an improved adherence to the matrix and increased the deformations before

the debonding of the fibres so that the ductile behaviour of material was enhanced. From a mechanical point of view, the best behaviour was obtained by the mix only reinforced with micro-fibres. However, the higher price of this type of fibres can make interesting to use a hybrid reinforced mix since shows a better behaviour than only reinforced with macro-fibres.

The effect of temperature on UHPFRC at 300 °C derived to a weight of loss by two endothermic processes: the dehydration of free water between 20-250 °C and dehydration of chemically bound water of C-S-H gel from 250-400 °C. When the high pressure reached the tensile strength of material, it generated cracks on the border of pores and its later propagation following the minimal energy way. The range of pore size affected depended on the type of fibre length and the pore size distribution at room temperature. Smaller pore sizes, between 0.2-1.2 mm, were affected for the unreinforced mix. However, a wider range of pore size and a more uniform distribution was affected on fibre-reinforced concrete, 0.2-2.6 mm. Smaller pore sizes were more affected by this process. The unreinforced matrix of the ultra-high-performance concretes had a lower total porosity and a non-uniform distribution of pore sizes, very concentrated in smaller pore sizes (0.25-1.2 mm). That effect combined with the absence of reinforcement led to low mechanical and fracture properties. Nevertheless, the reduction of compressive, tensile strength and fracture energy as a result of thermal damage was, in relative terms, more abrupt in steel fibre-reinforced concretes due to its initial low porosity at room temperature. The highest tensile strength at 300 °C was obtained for the mix reinforced only with micro-fibres, being the mix less thermal damaged and with better distributions of fibres, which leads to a more effective bridging effect. Nonetheless, the highest fracture energy at 300 °C was for the mix reinforced only with macro-fibres because of the adherence fibre-matrix was more effective. The increase of porosity caused by the thermal damage increased the toughness and ductility of all mixes but especially of fibre-reinforced mixes.

The enhancement in concrete strength (e.g., high-strength concrete or ultra-high-performance fibre-reinforced concrete) has made possible to use concrete in some structural applications with new limiting conditions. The use of slenderer elements have led them to be more sensitive to fatigue failure than conventional concrete. Additionally, cycling loading leads to a fatigue damage which is influenced by the microstructure of material and the crack growth and propagation. This effect combined with the influence of fibres and temperature on the microstructure in some applications entails to the necessity of the multiscale analysis of the fatigue behaviour. The probabilistic fatigue models are predomi-

nant to assess this type of concerns although there is a lack of systematic process to carried out a difference with respect to metallic materials.

A new two-step procedure in order to estimate the parameters of the probabilistic fatigue model of Saucedo et al. has been developed, based only on the fatigue tests available in the literature and to demonstrate that this probabilistic fatigue model is also valid for predicting fatigue behaviour under flexion. With only four parameters, the model captures very well the fatigue damage of plain and fibre-reinforced concrete under flexion. The flexural fatigue strength improvement of fibre-reinforced concrete was less pronounced when the fibre volume fraction surpasses 1.0%. Longer fibres were more effective in enhancing the flexural strength. The scattering of flexural fatigue data, measured by the shape parameter k, increased with fibre addition since fibres generated additional voids in the microstructure. This scattering was more significant for larger volume ratios of longer fibres, but hardly varies with V_f for short fibres. Both a and α were sensitive with the loading frequency, f. Fibre aspect ratio plays a role on the flexural strength, but there are not sufficient experimental data to draw definite conclusions. In addition, at the same volume ratio, short fibres offer more enhancement in fatigue life than longer fibres.

The pore structure of concrete matrix has a strong influence on the fatigue behaviour since the pores are a source of defects which conducts to the growth and propagation of cracks, especially affected by cyclic loading. The addition of steel fibres improved the endurance limit, essentially due to the presence of steel fibres in the proper dosage reduced the total porosity of the concrete matrix. Nonetheless, the scattering of fatigue life increased because there was a pore concentration around fibres so that the fatigue life depends strongly on the fibre distribution. The combination of steel and polypropylene fibres led to higher porosity which reduced the endurance limit at room temperature. When concrete were subjected to temperature, the worst fatigue behaviour was for the plain concrete because it did not have fibre that acted like barriers of crack propagation and had a large number of small pore sizes, which were mainly affected by thermal damage. The best endurance limit was reached for the mix reinforced with both steel and polypropylene fibres since the deterioration of matrix by thermal effect, in relative terms, was very reduced in comparison with only steel fibre-reinforced mix.

7.2 Future developments

Different topics have been covered in this thesis on the basis of a microstructural analysis of ultra-high-performance concrete and its consequences on the macroscopic scale related to mechanical, fracture and fatigue behaviour. However, more challenges and researches might be carried out. In this section some of these future developments are briefly presented:

- One of the most important factors affecting on the behaviour of UHPFRC in the macro-scale (i.e., mechanical, fracture and fatigue behaviour) is the pore size and the fracture mechanisms. Therefore, it will be very useful to measure accurately the pore size distribution in the range of capillary pores in a more extended experimental campaign and at different temperatures.
- It would be advisable to extend the mix proportions by employing various volume fractions and types of fibres since the effect of fibres like tiny shovels must be more or less effective depending on the number and type of fibres used.
- An important factor on the concrete performance subjected to temperatures is the heating rates. It would be interesting to use different heating rate over the same UHPFRC and additionally to measure the internal pressure in pores during the process and determine the thermal damage by X-ray compute tomography and mercury intrusion porosimetry.
- It will be worthwhile to study the influence of an abrupt cooling on the mechanical and fracture behaviour of UHPFRC when they are subjected to medium-high temperatures and to obtain whether the UHPFRC might be suitable to bear loads after the abrupt cooling.
- It would be very interesting to study the performance of UHPFRC subjected to thermal-fatigue loading at medium-high temperatures since this type of concrete might be used in some applications where must be capable of bear thermal cyclic of loads.
- There is no doubt that the reduction of pores in the microstructure have a benefit on the fracture behaviour and thermal conductivity of concrete. The addition of a very strength material and with high thermal conductivity, like graphene oxide, might improved the fracture and thermal performance of concrete. Thus, it will be quite useful to investigate the

behaviour of UHPFRC reinforced with graphene oxide nanosheets when the material is subjected to different temperatures.

- From the extensive experimental works on UHPFRC where it has been characterised the mechanical, fracture and fatigue behaviour at different temperatures might be carried out finite element models of applications of the UHPFRC (e.g. energy storage systems, steam containment vessel, etc.)

References

[1] *Model Code 2010, Final Draft*, vol. 1-2. International Federation for Structural Concrete (fib), 2012.

[2] 215R-74:. *Considerations for design of concrete structures subjected to fatigue loading*. American Concrete Institute, 1992.

[3] 446.1R-91:. *Fracture Mechanics of Concrete: Concepts, Models and Determination of Material Properties*. American Concrete Institute, 1991.

[4] 544.1R-96:. *Report on Fiber Reinforced Concrete*. American Concrete Institute, 1996.

[5] Abdalla, H. M., and Karihaloo, B. L. A method for constructing the bilinear tension softening diagram of concrete corresponding to its true fracture energy. *Magazine of Concrete Research 56*, 10 (2004), 597–604. doi.org/10.1680/macr.2004.56.10.597.

[6] Abrams, M. S. Compressive strength of concrete at temperatures to 1600F. *ACI Special Pubication 25* (1971), 33–58.

[7] Abrishambaf, A., Pimentel, M., and Nunes, S. Influence of fibre orientation on the tensile behaviour of ultra-high performance fibre reinforced cementitious composites. *Cement and Concrete Research 97* (2017), 28–40. doi.org/10.1016/j.cemconres.2017.03.007.

[8] Akca, A. H., and Özyurt, N. Deterioration and recovery of FRC after high temperature exposure. *Cement and Concrete Composites 93* (2018), 260–273. doi.org/10.1016/j.cemconcomp.2018.07.020.

[9] Akca, A. H., and Özyurt, N. Effects of re-curing on microstructure of concrete after high temperature exposure. *Construction and Building Materials 168* (2018), 431–441. doi.org/10.1016/j.conbuildmat.2018.02.122.

[10] Akca, A. H., and Özyurt, N. Effects of re-curing on residual mechanical properties of concrete after high temperature exposure. *Construction and Building Materials 159* (2018), 540–552. doi.org/10.1016/j.conbuildmat.2017.11.005.

[11] Akca, A. H., and Özyurt Zihnioglu, N. High performance concrete under elevated temperatures. *Construction and Building Materials 44* (2013), 317–328. doi.org/10.1016/j.conbuildmat.2013.03.005.

[12] Al-Azzawi, B. S., and Karihaloo, B. L. Flexural fatigue behavior of a self-compacting ultrahigh performance fiber-reinforced concrete. *Journal of Materials in Civil Engineering 29*, 11 (2017). doi.org/10.1061/(ASCE)MT.1943-5533.0002051.

[13] Alarcon-Ruiz, L., Platret, G., Massieu, E., and Ehrlacher, A. The use of thermal analysis in assessing the effect of temperature on a cement paste. *Cement and Concrete Research 35*, 3 (2005), 609–613. doi.org/10.1016/j.cemconres.2004.06.015.

[14] Alliche, A., and Frangois, D. Damage of concrete in fatigue. *Journal of Engineering Mechanics 118*, 11 (1992), 2176–2190. doi.org/10.1061/(ASCE)0733-9399(1992)118:11(2176).

[15] Alonso, M. C., and Fernandez, L. Dehydration and rehydration processes of cement paste exposed to high temperature environments. *Journal of Materials Science 39*, 9 (2004), 3015–3024. doi.org/10.1023/B:JMSC.0000025827.65956.18.

[16] Alonso, M. C., Vera-Agullo, J., Guerreiro, L., Flor-Laguna, V., Sanchez, M., and Collares-Pereira, M. Calcium aluminate based cement for concrete to be used as thermal energy storage in solar thermal electricity plants. *Cement and Concrete Research 82* (2016), 74–86. doi.org/10.1016/j.cemconres.2015.12.013.

[17] Alotto, P., Guarnieri, M., and Moro, F. Redox flow batteries for the storage of renewable energy: A review. *Renewable and Sustainable Energy Reviews 29* (2014), 325–335. doi.org/10.1016/j.rser.2013.08.001.

[18] Alyhya, W. S., Dhaheer, M. S. A., Al-Rubaye, M. M., and Karihaloo, B. L. Influence of mix composition and strength on the fracture properties of self-compacting concrete. *Construction and Building Materials 110* (2016), 312–322. doi.org/10.1016/j.conbuildmat.2016.02.037.

[19] Balázs, G. L., Czoboly, O., Lublóy, E., Kapitány, K., and Barsi, A. Observation of steel fibres in concrete with Computed Tomography. *Construction and Building Materials 140* (2017), 534–541. doi.org/10.1016/j.conbuildmat.2017.02.114.

[20] Banjara, N. K., and Ramanjaneyulu, K. Experimental investigations and numerical simulations on the flexural fatigue behavior of plain and fiber-reinforced concrete. *Journal of Materials in Civil Engineering 30*, 8 (2018), 1–15. doi.org/10.1061/(ASCE)MT.1943-5533.0002351.

[21] Barros, J. A. O., and Cruz, J. S. Fracture energy of steel fiber-reinforced concrete. *Mechanics of Composite Materials and Structures 8*, 1 (2001), 29–45. doi.org/10.1080/10759410119428.

[22] Bazant, Z. P., and Planas, J. *Fracture and size effect in concrete and other quasi brittle materials*. Boca Raton, FL: CRC Press, 1998.

[23] Bei, S., and Zhixiang, L. Investigation on spalling resistance of ultra-high-strength concrete under rapid heating and rapid cooling. *Case Studies in Construction Materials 4* (2016), 146–153. doi.org/10.1016/j.cscm.2016.04.001.

[24] Bilodeau, A., Kodur, V. K. R., and Hoff, G. C. Optimization of the type and amount of polypropylene fibres for preventing the spalling of lightweight concrete subjected to hydrocarbon fire. *Cement and Concrete Composites 26*, 2 (2004), 163–174. doi.org/10.1016/S0958-9465(03)00085-4.

[25] Blasón, S., Poveda, E., Ruiz, G., Cifuentes, H., and Fernández-Canteli, A. Twofold normalization of the cycle creep curve of plain and steel-fibre reinforced concrete and its applicactions to predict fatigue failure. *International Journal of Fatigue 120* (2019), 215–227. doi.org/10.1016/j.ijfatigue.2018.11.021.

[26] Bordelon, A. C., and Roesler, J. R. Spatial distribution of synthetic fibers in concrete with X-ray computed tomography. *Cement and Concrete Composites 53* (2014), 35–43. doi.org/10.1016/j.cemconcomp.2014.04.007.

[27] Bouziadi, F., Boulekbache, B., and Hamrat, M. The effects of fibres on the shrinkage of high-strength concrete under various curing temperatures. *Construction and Building Materials 114* (2016), 40–48. doi.org/10.1016/j.conbuildmat.2016.03.164.

[28] Bower, A. F., and Ortiz, M. The influence of grain size on the toughness of monolithic ceramics. *Journal of Engineering Materials and Technology 115*, 3 (1993), 228–236. doi.org/10.1115/1.2904212.

[29] Cachim, P. B., Figueiras, J. A., and Pereira, P. A. A. Fatigue behavior of fiber-reinforced concrete in compression. *Cement and Concrete Composites 24*, 2 (2002), 211–217. doi.org/10.1016/S0958-9465(01)00019-1.

[30] Carpinteri, A., Lacidogna, G., Corrado, M., and Di-Battista, E. Cracking and crackling in concrete-like materials: A dynamic energy balance. *Engineering Fracture Mechanics 155*, 1 (2016), 130–144. doi.org/10.1016/j.engfracmech.2016.01.013.

[31] Casas, J. R. A probabilistic fatigue strength model for brick masonry under compression. *Construction and Building Materials 23*, 8 (2009), 2964–2972. doi.org/10.1016/j.conbuildmat.2009.02.043.

[32] Castillo, C., and Durranil, A. J. Effect of transient high temperature on high strength concrete. *ACI Materials Journal 87*, 1 (1987), 47–53. doi.org/10.14359/2356.

[33] Castillo, E., and Fernández-Canteli, A. *A unified statistical methodology for modeling fatigue damage*. Springer Science, 2009. ISBN:978-1-4020-9181-0.

[34] Castillo, E., Ramos, A., Koller, R., López-Aenlle, M., and Fernández-Canteli, A. A critical comparison of two models for assessment of fatigue data. *International Journal of Fatigue 30*, 1 (2008), 45–57. doi.org/10.1016/j.ijfatigue.2007.02.014.

[35] Chan, S. Y. N., Peng, G., and Chan, J. K. W. Comparison between high strength concrete and normal strength concrete subjected

to high temperature. *Materials and Structures 29*, 194 (1996), 616–619. doi.org/10.1007/BF02485969.

[36] Chandra, S., Berntsson, L., and Anderberg, Y. Some effects of polymer addition on the fire resistance of concrete. *Cement and Concrete Research 10*, 3 (1980), 367–375. doi.org/10.1016/0008-8846(80)90112-X.

[37] Chasanov, M. G., and Staahl, G. E. High temperature sodium-concrete interactions. *Journal of Nuclear Materials 66*, 1-2 (1977), 217–220.

[38] Chen, Y., Ni, J., Zheng, P., Azzam, R., Zhou, Y., and Shao, W. Experimental research on the behaviour of high frequency fatigue in concrete. *Engineering Failure Analysis 18*, 7 (2011), 1848–1857. doi.org/10.1016/j.engfailanal.2011.06.012.

[39] Cheng, F., Kodur, V. K. R., and Wang, T. Stress-strain curves for high strength concrete at elevated temperatures. *Journal of Materials and Civil Engineering 16*, 1 (2004). doi.org/10.1061/(ASCE)0899-1561(2004)16:1(84).

[40] Cifuentes, H., García, F., Maeso, O., and Medina, F. Influence of the properties of polypropylene fibres on the fracture behaviour of low-, normal- and high-strength FRC. *Construction and Building Materials 45* (2013), 130–137. doi.org/10.1016/j.conbuildmat.2013.03.098.

[41] Cifuentes, H., and Karihaloo, B. L. Determination of size-independent specific fracture energy of normal- and high-strength self-compacting concrete from wedge splitting tests. *Construction and Building Materials 48* (2013), 548–553. doi.org/10.1016/j.conbuildmat.2013.07.062.

[42] Cifuentes, H., Leiva, C., Fernandez-Pereira, C., and Medina, F. Effects of fibers and rice husk ash on properties of heated high-strength concrete. *Magazine of Concrete Research 64*, 5 (2012), 457–470. doi.org/10.1680/macr.11.00087.

[43] Cifuentes, H., Leiva, C., Medina, F., and Fernández-Pereira, C. Effects of fibres and rice husk ash on properties of heated HSC. *Magazine of Concrete Research 64*, 5 (2012), 457–470. doi.org/10.1680/macr.11.00087.

[44] Cifuentes, H., Lozano, M., Holušová, T., Medina, F., Seitl, S., and Fernández-Canteli, A. Modified disk-shaped compact tension test for measuring concrete fracture properties. *International Journal of Concrete Structures and Materials 11*, 2 (2017), 215–228. doi.org/10.1007/s40069-017-0189-4.

[45] Cifuentes, H., Rios, J. D., and Gomez, E. J. Effect of mix design on the size-independent fracture energy of normal- and high-strength self-compacting concrete. *Materiales de Construccion 68*, 329 (2018). doi.org/10.3989/mc.2018.00717.

[46] Correia, J. A. F. O. *An integral probabilistic approach for fatigue lifetime prediction of mechanical and structural components.* PhD thesis, School of Engineering. University of Porto, 2014.

[47] Deeb, R., and Karihaloo, B. L. Mix proportioning of self-compacting normal and high-strength concretes. *Magazine of Concrete Research 65*, 9 (2013), 546–556. doi.org/10.1680/macr.12.00164.

[48] Deng, F., Ding, X., Chi, Y., Xu, L., and Wang, L. The pull-out behavior of straight and hooked-end steel fiber from hybrid fiber reinforced cementitious composite: Experimental study and analytical modelling. *Composite Structures 206* (2018), 693–712. doi.org/10.1016/j.compstruct.2018.08.066.

[49] Ding, Y., Azevedo, C., Aguiar, J. B., and Jalali, S. Study on residual behaviour and flexural toughness of fibre cocktail reinforced self compacting high performance concrete after exposure to high temperature. *Construction and Building Materials 26*, 1 (2012), 21–31. doi.org/10.1016/j.conbuildmat.2011.04.058.

[50] du Plessis, A., Olawuyi, B. J., Boshoff, W. P., and le Roux, S. G. Simple and fast porosity analysis of concrete using X-ray computed tomography. *Materials and Structures 49*, 1–2 (2016), 553–562. doi.org/10.1617/s11527-014-0519-9.

[51] EFNARC-2005. *The European guidelines for self-compacting concrete, specification, production and use*. 2005.

[52] El-Hawary, M. M., Ragab, A. M., El-Azim, A. A., and Elibiari, S. Effect of fire on flexural behaviour of RC beams. *Construction*

and Building Materials) 10, 2 (1996), 147–150. doi.org/10.1016/0950-0618(95)00041-0.

[53] Elices, M., Guinea, G. V., and Planas, J. Measurement of the fracture energy using three-point bend tests: Part 3 - Influence of cutting the P-δ tail. *Materials and Structures 25*, 6 (1992), 327–334. doi.org/10.1007/BF02472591.

[54] EN-12390-13:2014. *Testing hardened concrete Part 13: Determination of secant modulus of elasticity in compression*. AENOR, 2014.

[55] EN-12390-3:2009. *Testing hardened concrete Part 3: Compressive strength of test specimens*. AENOR, 2009.

[56] EN-12390-6:2009. *Testing hardened concrete Part 6: Tensile splitting strength of test specimens*. AENOR, 2009.

[57] EN-197-1:2000/A3:2008. *Cement. Part 1: Composition, specifications nad conrmity creiteria from common cements*. AENOR, 2000.

[58] EN-1992-1-1:1992. *Eurocode 2: Design of concrete structures-Part 1-1: General rules and rules for buildings*. 1992.

[59] Evans, L. M., Margetts, L., Casalegno, V., Leonard, F., Lowe, T., Lee, P. D., Schmidt, M., and Mummery, P. M. Thermal characterisation of ceramic/metal joining techniques for fusion applications using X-ray tomography. *Fusion Engineering and Design 89*, 6 (2014), 826–836. doi.org/10.1016/j.fusengdes.2014.05.002.

[60] Farhat, F. A., Nicolaides, D., Kanellopoulos, A., and Karihaloo, B. L. High performance fibre-reinforced cementitious composite (CARDIFRC)—performance and application to retrofitting. *Engineering Fracture Mechanics 74*, 1-2 (2007), 151–167. doi.org/10.1016/j.engfracmech.2006.01.023.

[61] Fernández-Canteli, A., Przybilla, C., Nogal, M., Aenlle, M. L., and Castillo, E. Profatigue: A software program for probabilistic assessment of experimental fatigue data sets. *Procedia Engineering 74*, 1 (2014), 236–241. doi.org/10.1016/j.proeng.2014.06.255.

[62] Garcia, I. G. *Carbonatación del hormigón: combinación de CO_2 con las fases hidratadas del cemento y frente de cambio de pH*. PhD thesis, School of Engineering. Universidad Politecnica de Madrid, 2011.

[63] Gencel, O., Ozel, C., Brostow, W., and Martínez-Barrera, G. Mechanical properties of self-compacting concrete reinforced with polypropylene fibres. *Materials Research Innovations 15*, 3 (2011), 216–225. doi.org/10.1179/143307511X13018917925900.

[64] Goel, S., and Singh, S. P. Fatigue performance of plain and steel fibre reinforced self compacting concrete using S–N relationship. *Engineering Structures 74* (2014), 65–73. doi.org/10.1016/j.engstruct.2014.05.010.

[65] Goel, S., Singh, S. P., and Singh, P. Fatigue analysis of plain and fiber-reinforced self-consolidating concrete. *ACI Materials Journal 109*, 5 (2012), 573–582. doi.org/10.14359/51684089.

[66] Graybeal, B. A. Compressive behavior of ultra-high-performance fiber-reinforced concrete. *ACI Materials Journal 104*, 2 (2007), 146–152. doi.org/10.14359/18577.

[67] Guan, J., Hu, X., and Li, Q. In-depth analysis of notched 3-p-b concrete fracture. *Engineering Fracture Mechanics 165* (2016), 57–71. doi.org/10.1016/j.engfracmech.2016.08.020.

[68] Guinea, G. V., Planas, J., and Elices, M. Measurement of the fracture energy using three-point bend tests: Part 1 - Influence of experimental procedures. *Materials and Structures 25*, 4 (1992), 212–218. doi.org/10.1007/BF02473065.

[69] Guo, L. P., Carpinteri, A., Spagnoli, A., and Sun, W. Experimental and numerical investigations on fatigue damage propagation and life prediction of high-performance concrete containing reactive mineral admixtures. *International Journal of Fatigue 32*, 2 (2010), 227–237. doi.org/10.1016/j.ijfatigue.2009.05.009.

[70] Guo, L. P., Sun, W., Carpinteri, A., Chen, B., and He, X. Y. Real-time detection and analysis of damage in high-performance concrete under cyclic bending. *Experimental Mechanics 50*, 3 (2010), 413–428. doi.org/10.1007/s11340-009-9227-8.

[71] Guo, L. P., Sun, W., Zheng, K. R., Chen, H. J., and Liu, B. Study on the flexural fatigue performance and fractal mechanism of concrete with high proportions of ground granulated blast-furnace slag. *Cement and Concrete Research 37*, 2 (2007), 242–250. doi.org/10.1016/j.cemconres.2006.11.009.

[72] Gustaferro, A. H., and Lin, T. D. Rational design of reinforced concrete members for fire resistance. *Fire Safety Journal) 11*, 1-2 (1986), 85–98. doi.org/10.1016/0379-7112(86)90054-8.

[73] Harmathy, T. Z. Determining the temperature history of concrete constructions following fire exposure. *ACI Journal Proceedings 65*, 959–964.

[74] Herrmann, H., Pastorelli, E., Kallonen, A., and Suuronen, J.-P. Methods for fibre orientation analysis of X-ray tomography images of steel fibre reinforced concrete (SFRC). *Journal of Materials Science 51*, 8 (2016), 3772–3783. doi.org/10.1007/s10853-015-9695-4.

[75] Hillerborg, A., Modéer, M., and Petersson, P.-E. Analysis of crack formation and crack growth in concrete by means of fracture mechanics and finite elements. *Cement and Concrete Research 6*, 6 (1976), 773–781. doi.org/10.1016/0008-8846(76)90007-7.

[76] Hop, T. Fatigue of high strength concrete. *Building Science 3*, 2 (1968), 65–80. doi.org/10.1016/0007-3628(68)90017-0.

[77] Hu, X., Guan, J., Wang, Y., Keating, A., and Yang, S. Comparison of boundary and size effect models based on new developments. *Engineering Fracture Mechanics 175* (2017), 146–167. doi.org/10.1016/j.engfracmech.2017.02.005.

[78] Huang, B.-T., Li, Q.-H., and Xu, S.-L. Fatigue Deformation Model of Plain and Fiber-Reinforced Concrete Based on Weibull Function. *Journal of Structural Engineering 145*, 1 (2019), 04018234. doi.org/10.1061/(ASCE)ST.1943-541X.0002237.

[79] Huang, B.-T., Li, Q.-H., Xu, S.-L., and Zhou, B.-M. Tensile fatigue behavior of fiber-reinforced cementitious material with high ductility: Experimental study and novel P-S-N model. *Construction and Building Materials 178* (2018), 349–359. doi.org/10.1016/j.conbuildmat.2018.05.166.

[80] Huining, X., Yiqiu, T., and Xingao, Y. X-ray computed tomography in hydraulics of asphalt mixtures: Procedure, accuracy, and application. *Construction and Building Materials 108* (2016), 10–21. doi.org/10.1016/j.conbuildmat.2016.01.032.

[81] Hwang, J. P., Kim, M., and Ann, K. Y. Porosity generation arising from steel fibre in concrete. *Construction and Building Materials 94* (2015), 433 – 436. doi.org/10.1016/j.conbuildmat.2015.07.044.

[82] Isojeh, B., El-Zeghayar, M., Vecchio, F. J., and Eng, P. Fatigue behaviour of steel fiber concrete in direct tension. *Journal of Materials in Civil Engineering 29*, 9 (2017). doi.org/10.1061/(ASCE)MT.1943-5533.0001949.

[83] John, E., Hale, M., and Selvam, P. Concrete as a thermal energy storage medium for thermocline solar energy storage systems. *Solar Energy 96* (2013), 194–204. doi.org/10.1016/j.solener.2013.06.033.

[84] Johnston, C. D., and Zemp, R. W. Flexural fatigue performance of steel fibre reinforced concrete - influence of fibre content, Aspect Ratio and Type. *ACI Materials Journal 88*, 4 (1991), 374–383. doi.org/10.14359/1875.

[85] Kahanji, C., Ali, F., and Nadjai, A. Explosive spalling of ultra-high performance fibre reinforced concrete beams under fire. *Journal of Structural Fire Engineering 7*, 4 (2016), 328–348. doi.org/10.1108/JSFE-12-2016-023.

[86] Kahanji, C., Ali, F., Nadjai, A., and Alam, N. Effect of curing temperature on the behaviour of UHPFRC at elevated temperatures. *Construction and Building Materials 182* (2018), 670–681. doi.org/10.1016/j.conbuildmat.2018.06.163.

[87] Kalifa, P., Menneteau, F.-D., and Quenard, D. Spalling and pore pressure in HPC at high temperatures. *Cement and Concrete Research 30*, 12 (2000), 1915–1927. doi.org/10.1016/S0008-8846(00)00384-7.

[88] Karihaloo, B. L. *Fracture Mechanics and Structural Concrete*. Longman, 1995.

[89] Karihaloo, B. L., Abdalla, H. M., and Imjai, T. A simple method for determining the true specific fracture energy of concrete. *Magazine of Concrete Research 55*, 5 (2003), 471–481. doi.org/10.1680/macr.2003.55.5.471.

[90] Kendall, K., Howard, A. J., Birchall, J. D., Pratt, P. L., Proctor, B. A., and Jefferis, S. A. The relation between porosity, microstructure and strength, and the approach to advanced cement-based materials. *Philosophical Transactions of the Royal Society of London. Series A, Mathematical and Physical Sciences 310*, 1511 (1983), 139–153. doi.org/10.1098/rsta.1983.0073.

[91] Kerckhofs, G., Schrooten, J., Cleynenbreugel, T. V., Lomov, S. V., and Wevers, M. Validation of X-ray microfocus computed tomography as an imaging tool for porous structures. *Review of Scientific Instruments 79*, 1 (2008). doi.org/10.1063/1.2838584.

[92] Khosravani, M. R., Silani, M., and Weinberg, K. Fracture studies of Ultra-High Performance Concrete using dynamic Brazilian tests. *Theoretical and Applied Fracture Mechanics 93* (2018), 302–310. doi.org/10.1016/j.tafmec.2017.10.001.

[93] Kim, J.-K., and Kim, Y.-Y. Experimental study of the fatigue behavior of high strength concrete. *Cement and Concrete Research 26*, 10 (1996), 1513–1523. doi.org/10.1016/0008-8846(96)00151-2.

[94] Kim, M.-J., Kim, S., Lee, S.-K., Kim, J.-H., Lee, K., and Yoo, D.-Y. Mechanical properties of ultra-high-performance fiber-reinforced concrete at cryogenic temperatures. *Construction and Building Materials 157* (2017), 498–508. doi.org/10.1016/j.conbuildmat.2017.09.099.

[95] Kim, M.-J., Yoo, D.-Y., Kim, S., Shin, M., and Banthia, N. Effects of fiber geometry and cryogenic condition on mechanical properties of ultra-high-performance fiber-reinforced concrete. *Cement and Concrete Research 107*, October 2017 (2018), 30–40. doi.org/10.1016/j.cemconres.2018.02.003.

[96] Kim, S., Kim, M.-J., Yoon, H., and Yoo, D.-Y. Effect of cryogenic temperature on the flexural and cracking behaviors of ultra-high-performance fiber-reinforced concrete. *Cryogenics 93*, May (2018), 75–85. doi.org/10.1016/j.cryogenics.2018.06.002.

[97] Kodur, V. K. R., Bhatt, P. P., Soroushian, P., and Arablouei, A. Temperature and stress development in ultra-high performance concrete during curing. *Construction and Building Materials 122* (2016), 63–71. doi.org/10.1016/j.conbuildmat.2016.06.052.

[98] Kodur, V. K. R., and Sultan, M. A. Structural behaviour of high strength concrete columns exposed to fire. *Conference Paper: International Symposium on High Performance and Reactive Powder Concrete, Sherbrooke, Quebec* (1998), 217–232.

[99] Kumar, R., and Bhattacharjee, B. Porosity, pore size distribution and in situ strength of concrete. *Cement and Concrete Research 33*, 1 (2003), 155–164. doi.org/10.1016/S0008-8846(02)00942-0.

[100] Lü, P., Li, Q., and Song, Y. Damage constitutive of concrete under uniaxial alternate tension–compression fatigue loading based on double bounding surfaces. *International Journal of Solids and Structures 41*, 11-12 (2004), 3151–3166. doi.org/10.1016/j.ijsolstr.2004.01.026.

[101] Lankard, D. R., Birkimer, D. L., Fondriest, F. F., and Snyder, M. J. Effects of moisture content on the structural properties of Portland cement concrete exposed to temperatures up to 500F. *ACI Special Pubication 25* (1971), 59–102.

[102] Lappa, E. S. *High strength fiber reinforcement concrete. Static and fatigue behaviour in bending*. PhD thesis, University of Delf, 2007.

[103] Lau, A., and Anson, M. Effect of high temperatures on high performance steel fibre reinforced concrete. *Cement and Concrete Research 36*, 9 (2006), 1698–1707. doi.org/10.1016/j.cemconres.2006.03.024.

[104] Leung, C. K. Y., Cheung, Y. N., and Zhang, J. Fatigue enhancement of concrete beam with ECC layer. *Cement and Concrete Research 37*, 5 (2007), 743–750. doi.org/10.1016/j.cemconres.2007.01.015.

[105] Li, H., Zhang, M.-H., and Ou, J.-P. Flexural fatigue performance of concrete containing nano-particles for pavement. *International Journal of Fatigue 29*, 7 (2007), 1292–1301. doi.org/10.1016/j.ijfatigue.2006.10.004.

[106] Li, V. C., Stang, H., and Krenchel, H. Micromechanics of crack bridging in fibre-reinforced concrete. *Materials and Structures 26*, 8 (1993), 486–494. doi.org/10.1007/BF02472808.

[107] Liang, X., Wu, C., Su, Y., Chen, Z., and Li, Z. Development of ultra-high performance concrete with high fire resistance. *Construction and Building Materials 179* (2018), 400–412. doi.org/10.1016/j.conbuildmat.2018.05.241.

[108] Liu, X., G.Ye, Schutter, G. D., Yuan, Y., and Taerwe, L. On the mechanism of polypropylene fibres in preventing fire spalling in self-compacting and high-performance cement paste. *Cement and Concrete Research 38*, 4 (2008), 487–499. doi.org/10.1016/j.cemconres.2007.11.010.

[109] López, J. A., Serna, P., Navarro-Gregori, J., and Camacho, E. An inverse analysis method based on deflection to curvature transformation to determine the tensile properties of UHPFRC. *Materials and Structures 48* (2015), 3703–3718. doi.org/10.1617/s11527-014-0434-0.

[110] López, J. A., Serna, P., Navarro-Gregori, J., and Coll, H. A simplified five-point inverse analysis method to determine the tensile properties of UHPFRC from unnotched four-point bending tests. *Composites Part B 91* (2016), 189–204. doi.org/10.1016/j.compositesb.2016.01.026.

[111] Makita, T., and Brühwiler, E. Tensile fatigue behaviour of ultra-high performance fibre reinforced concrete (UHPFRC), journal=Materials and Structures, publisher = , volume = 47, number=3, pages=475-491, note=doi.org/10.1617/s11527-013-0073-x, year = 2014.

[112] Makita, T., and Brühwiler, E. Tensile fatigue behaviour of ultra-high performance fibre reinforced concrete combined with steel rebars (R-UHPFRC). *International Jounral of Fatigue 59* (2014), 145–152. doi.org/10.1016/j.ijfatigue.2013.09.004.

[113] Makita, T., and Brühwiler, E. Damage models for UHPFRC and R-UHPFRC tensile fatigue behaviour. *Engineering Structures 90* (2015), 61–70. doi.org/10.1016/j.engstruct.2015.01.049.

[114] Marrow, T. J., Babout, L., Jivkov, A. P., Wood, P., Engelberg, D., Stevens, N., Withers, P. J., and Newman, R. C. Three dimensional observations and modelling of intergranular stress corrosion cracking in austenitic stainless steel. *Journal of Nuclear Materials 352*, 1-3 (2006), 62–74. doi.org/10.1016/j.jnucmat.2006.02.042.

[115] Matsumoto, T., and Li, V. C. Fatigue life analysis of fiber reinforced concrete with a fracture mechanics based model. *Cement and Concrete Composites 21*, 4 (1999), 249–261. doi.org/10.1016/S0958-9465(99)00004-9.

[116] Medeiros, A., Zhang, X., Ruiz, G., Yu, R. C., and Velasco, M. S. L. Effect of the loading requency on the compressive fatigue behaviour of plain and fiber reinforced concrete. *International Journal of Fatigue 70* (2015), 342–350. doi.org/10.1016/j.ijfatigue.2014.08.005.

[117] Minguez, J., Gonzalez, D. C., and Vicente, M. A. Fiber geometrical parameters of fiber-reinforced high strength concrete

and their influence on the residual post-peak flexural tensile strength. *Construction and Building Materials 168* (2018), 906–922. doi.org/10.1016/j.conbuildmat.2018.02.095.

[118] Mohammadi, Y., and Kaushik, S. K. Flexural fatigue-life distributions of plain and fibrous concrete at various stress levels. *Journal of Materials in Civil Engineering 17*, 6 (2005), 650–658. doi.org/10.1061/(ASCE)0899-1561(2005)17:6(650).

[119] Montero-Chacón, F. *Multiscale analysis for the design of fiber-reinforced cementitious composites*. PhD thesis, School of Engineering. University of Seville, 2013.

[120] Morris, A. D., and Garrett, G. G. A comparative study of the static and fatigue behaviour of plain and steel fibre reinforced mortar in compression and direct tension. *International Journal of Cement Composites and Lightweight Concrete 3*, 2 (1981), 73–91. doi.org/10.1016/0262-5075(81)90002-6.

[121] Mousa, M. I. Effect of elevated temperature on the properties of silica fume and recycled rubber-filled high strength concretes (RHSC). *HBRC Journal 13*, 1 (2017), 1–7. doi.org/10.1016/j.hbrcj.2015.03.002.

[122] Murthy, A. R., Karihaloo, B. L., Rani, P. V., and Priya, D. S. Fatigue behaviour of damaged RC beams strengthened with ultra high performance fibre reinforced concrete. *International Journal of Fatigue 116* (2018), 659–668. doi.org/10.1016/j.ijfatigue.2018.06.046.

[123] Neville, A. *Properties of concrete*, 5th ed. Pearson Education Limited, England, 2011.

[124] Nicolaides, D. *Fracture and fatigue of CARDIFRC*. PhD thesis, School of Engineering. Cardiff University, 2004.

[125] Nicolaides, D., Kanellopoulos, A., and Karihaloo, B. L. Fatigue life and self-induced volumetric changes of CARDIFRC. *Magazine of Concrete Research 62*, 9 (2010), 679–683. doi.org/10.1680/macr.9.00149.

[126] Nielsen, C. V., and Bicanic, N. Residual fracture energy of high-performance and normal concrete subject to high temperatures. *Materials and Structures 36*, 262 (2003), 515–521. doi.org/10.1007/BF02480828.

[127] Noumowé, A., Carré, H., Daoud, A., and Toutanji, H. High-Strength Self-Compacting Concrete Exposed to Fire Test. *Journal of Materials in Civil Engineering 18*, 6 (2006), 754–758. doi.org/10.1061/(ASCE)0899-1561(2006)18:6(754).

[128] Oh, B. Fatigue analysis of plain concrete in flexure. *Journal of Structural Engineering 112*, 2 (1986), 273–278. doi.org/10.1061/(ASCE)0733-9445(1986)112:2(273).

[129] Oh, B. H. Fatigue life distributions of concrete for various stress levels. *ACI Materials Journal 88*, 2 (1991), 122–128. doi.org/10.14359/1870.

[130] Ohlsson, U., Daerga, P. A., and Elfgren, L. Fracture energy and fatigue strength of unreinforced concrete beams at normal and low temperatures. *Engineering Fracture Mechanics 35*, 1-3 (1990), 195–203. doi.org/10.1016/0013-7944(90)90197-O.

[131] Oneschkow, N. Fatigue behaviour of high-strength concrete with respect to strain and stiffness. *International Journal of Fatigue 87* (2016), 38–49. doi.org/10.1016/j.ijfatigue.2016.01.008.

[132] Oró, E., Gil, A., de Gracia, A., Boer, D., and Cabeza, L. F. Comparative life cycle assessment of thermal energy storage systems for solar power plants. *Renewable Energy 44* (2012), 166–173. doi.org/10.1016/j.renene.2012.01.008.

[133] Ortega, J. J., Ruiz, G., Yu, R. C., Afanador-García, N., Tarifa, M., Poveda, E., Zhang, X., and Evangelista Jr, F. Number of tests and corresponding error in concrete fatigue. *International Journal of Fatigue 116* (2018), 210–219. doi.org/10.1016/j.ijfatigue.2018.06.022.

[134] Park, K., Paulino, G. H., and Roesler, J. Cohesive fracture model for functionally graded fiber reinforced concrete. *Cement and Concrete Research 40*, 6 (2010), 956–965. doi.org/10.1016/j.cemconres.2010.02.004.

[135] Paskova, T., and Meyer, C. Low-cycle fatigue of plain and fiber-reinforced concrete. *ACI Materials Journal 94*, 4 (1997), 273–286. doi.org/10.14359/309.

[136] Peng, G.-F., Niu, X.-J., Shang, Y.-J., Zhang, D.-P., Chen, X.-W., and Ding, H. Combined curing as a novel approach to improve resistance of

ultra-high performance concrete to explosive spalling under high temperature and its mechanical properties. *Cement and Concrete Research*, 109 (2018), 147–158. doi.org/10.1016/j.cemconres.2018.04.011.

[137] Phan, L. T. Pore pressure and explosive spalling in concrete. *Materials and Structures 41*, 10 (2008), 1623–1632. doi.org/10.1617/s11527-008-9353-2.

[138] Pindado, M. A., Aguado, A., and Josa, A. Fatigue behavior of polymer-modified porous concretes. *Cement and Concrete Research 29*, 7 (1999), 1077–1083. doi.org/10.1016/S0008-8846(99)00095-2.

[139] Planas, J. *Experimental determination of the stress-crack opening curve for concrete in tension*. RILEM Rep. No. 39. Bagneux. France:RILEM, 2007.

[140] Planas, J., Elices, M., and Guinea, G. V. Measurement of the fracture energy using three-point bend tests: Part 2 - influence of bulk energy dissipation. *Materials and Structures 25*, 5 (1992), 305–312. doi.org/10.1007/BF02472671.

[141] Ponikiewski, T., Katzer, J., Budgol, M., and Rudzki, M. Determination of 3D porosity in steel fibre reinforced SCC beams using X-ray computed tomography. *Construction and Building Materials 68* (2014), 333–340. doi.org/10.1016/j.conbuildmat.2014.06.064.

[142] Poveda, E., Ruiz, G., Cifuentes, H., Yu, R. C., and Zhang, X. Influence of the fiber content on the compressive low-cycle fatigue behavior of self-compacting SFRC. *International Journal of Fatigue 101*, 9–17.

[143] Qsymah, A., Sharma, R., Yang, Z., Margetts, L., and Mummery, P. Micro X-ray computed tomography image-based two-scale homogenisation of ultra high performance fibre reinforced concrete. *Construction and Building Materials 130* (2017), 230–240. doi.org/10.1016/j.conbuildmat.2016.09.020.

[144] Raithby, K. D. Flexural fatigue behaviour of plain concrete. *Fatigue and Fracture of Engineering Materials and Structures 2*, 3 (1979), 269–278. doi.org/10.1111/j.1460-2695.1979.tb01085.x.

[145] Ramezanianpour, A. A., Esmaeili, M., Ghahari, S. A., and Najafi, M. H. Laboratory study on the effect of polypropylene fiber on durability,

and physical and mechanical characteristic of concrete for application in sleepers. *Construction and Building Materials 44* (2013), 411–418. doi.org/10.1016/j.conbuildmat.2013.02.076.

[146] RILEM-TCM85. Determination of the fracture energy of mortar and concrete by means of three-point bend tests on notched beams. *Materials and Structures 18*, 4 (1985), 287–290. doi.org/10.1007/BF02472918.

[147] Rios, J. D., Cifuentes, H., Leiva, C., García, C., and Alba, M. Behavior of high-strength polypropylene fiber-reinforced self-compacting concrete exposed to high temperatures. *Journal of Material and Civil Engineering 30*, 11 (2017). doi.org/10.1061/(ASCE)MT.1943-5533.0002491.

[148] Rios, J. D., Cifuentes, H., Yu, R. C., and Ruiz, G. Probabilistic flexural fatigue in plain and fiber-reinforced concrete. *Materials 10*, 7 (2017). doi.org/10.3390/ma10070767.

[149] Rios, J. D., Leiva, C., Ariza, M. P., Seitl, S., and Cifuentes, H. Analysis of the tensile fracture properties of ultra-high-strength fiber-reinforced concrete with different types of steel fibers by X-ray tomography. *Materials and Design 165* (2019). doi.org/10.1016/j.matdes.2019.107582.

[150] Romualdi, J. P., and Batson, G. B. Mechanics of crack arrest in concrete. *Journal of the Engineering Mechanics Division 89*, 3 (1963), 147–168.

[151] Rosselló, C., Elices, M., and Guinea, G. V. Fracture of model concrete: 2. Fracture energy and characteristic length. *Cement and Concrete Research 36*, 7 (2006), 1345–1353. doi.org/10.1016/j.cemconres.2005.04.016.

[152] Ruiz, G., Medeiros, A., and Zhang, X. Experimental study of loading frequency effect on compressive fatigue. *Anales de Mecánica de la Fractura 29* (2011), 535–540.

[153] Sanjayan, G., and Stocks, L. J. Spalling of high-strength silica fume concrete in fire. *ACI Materials Journal 90*, 2 (1993), 170–173. doi.org/10.14359/4015.

[154] Saucedo, L., Yu, R. C., Medeiros, A., Zhang, X., and Ruiz, G. A probabilistic fatigue model based on the initial distribution to consider frequency effect in plain and fiber reinforced concrete. *International Journal of Fatigue*, 48 (2013), 308–318. doi.org/10.1016/j.ijfatigue.2012.11.013.

[155] Schilling, P. J., Karedla, B. R., Tatiparthi, A. K., Verges, M. A., and Herrington, P. D. X-ray computed microtomography of internal damage in fiber reinforced polymer matrix composites. *Composites Science and Technology 65*, 14 (2005), 2071–2078.

[156] Shafieifar, M., Farzad, M., and Azizinamini, A. Experimental and numerical study on mechanical properties of Ultra High Performance Concrete (UHPC). *Construction and Building Materials 156* (2017), 402–411. doi.org/10.1016/j.conbuildmat.2017.08.170.

[157] Shah, S. P. Determination of fracture parameters (KIc-s and CTODc) of plain concrete using three-point bend tests. *Materials and Structures 23*, 6 (1990), 457–460. doi.org/10.1007/BF02472029.

[158] Shen, P., Lu, L., He, Y., Rao, M., Fu, Z., Wang, F., and Hu, S. Experimental investigation on the autogenous shrinkage of steam cured ultra-high performance concrete. *Construction and Building Materials 162* (2018), 512–522. doi.org/10.1016/j.conbuildmat.2017.11.172.

[159] Shi, X. P., Fwa, T. F., and Tan, S. A. Flexural fatigue strength of plain concrete. *ACI Materials Journal 90*, 5 (1993), 435–440. doi.org/10.14359/3872.

[160] Sideris, K. K., and Manita, P. Residual mechanical characteristics and spalling resistance of fiber reinforced self-compacting concretes exposed to elevated temperatures. *Construction and Building Materials 41* (2013), 296–302. doi.org/10.1016/j.conbuildmat.2012.11.093.

[161] Sideris, K. K., Manita, P., and Chaniotakis, E. Performance of thermally damaged fibre reinforced concretes. *Construction and Building Materials 23*, 3 (2009), 1232–1239. doi.org/10.1016/j.conbuildmat.2008.08.009.

[162] Simões, T., Octávio, C., Valença, J., Costa, H., da Costa, D. D., and Júlio, E. Influence of concrete strength and steel fibre geometry on the fibre/matrix interface. *Composites Part B: Engineering 122* (2017), 156–164. doi.org/10.1016/j.compositesb.2017.04.010.

[163] Simoes, T., Costa, H., da Costa, D. D., and Júlio, E. Influence of fibres on the mechanical behaviour of fibre reinforced concrete matrixes. *Construction and Building Materials 137* (2017), 548–556. doi.org/10.1016/j.conbuildmat.2017.01.104.

[164] Singh, S. P., and Kaushik, S. K. Flexural fatigue life distributions and failure probability of steel fibrous concrete. *ACI Materials Journal 97*, 6 (2000), 658–667. doi.org/10.14359/9979.

[165] Singh, S. P., and Kaushik, S. K. Flexural fatigue analysis of steel fiber-reinforced concrete. *ACI Materials Journal 98*, 4 (2001), 306–312. doi.org/10.14359/10399.

[166] Singh, S. P., and Kaushik, S. K. Fatigue strength of steel fibre reinforced concrete in flexure. *Cement and Concrete Composites 25*, 7 (2003), 779–786. doi.org/10.1016/S0958-9465(02)00102-6.

[167] Singh, S. P., Mohammadi, Y., and Kaushik, S. K. Flexural fatigue analysis of steel fibrous concrete containing mixed fibers. *ACI Materials Journal 102*, 2 (2005), 438–444. doi.org/10.14359/14807.

[168] Sohel, K. M. A., Al-Jabria, K., Zhang, M. H., and Richard Liew, J. Y. Flexural fatigue behavior of ultra-lightweight cement composite and high strength lightweight aggregate concrete. *Construction and Building Materials 173* (2018), 90–100. doi.org/10.1016/j.conbuildmat.2018.03.276.

[169] Song, Q., Yu, R., Wang, X., Rao, S., and Shui, Z. A novel self-compacting ultra-high performance fibre reinforced concrete (SCUHPFRC) derived from compounded high-active powders. *Construction and Building Materials 158* (2018), 883–893. doi.org/10.1016/j.conbuildmat.2017.10.059.

[170] Sovják, R., Máca, P., and Imlauf, T. Effect of fibre length on the fracture energy of UHPFRC. *Procedia Engineering 193* (2017), 74–79. doi.org/10.1016/j.proeng.2017.06.188.

[171] Su, Y., Li, J., Wu, C., Wu, P., Tao, M., and Li, X. Mesoscale study of steel fibre-reinforced ultra-high performance concrete under static and dynamic loads. *Materials and Design 116* (2017), 340–351. doi.org/10.1016/j.matdes.2016.12.027.

[172] Susmel, L. A unifying methodology to design un-notched plain and short-fibre/particle reinforced concretes against fatigue. *International Journal of Fatigue 61*, 61 (2014), 226–243. doi.org/10.1016/j.ijfatigue.2013.11.006.

[173] Suuronen, J.-P., Kallonen, A., Eik, M., Puttonen, J., Serimaa, R., and Herrmann, H. Analysis of short fibres orientation in steel fibre-reinforced concrete (SFRC) by X-ray tomography. *Journal of Materials Science 48*, 3 (2013), 1358–1367. doi.org/10.1007/s10853-012-6882-4.

[174] Tanyildizi, H. Post-fire behavior of structural lightweight concrete designed by Taguchi method. *Construction and Building Materials 68* (2014), 565–571. doi.org/10.1016/j.conbuildmat.2014.07.021.

[175] Tepfers, R. Tensile fatigue strength of plain concrete. *ACI Journal Proceedings 76*, 8 (1979), 919–934. doi.org/10.14359/6969.

[176] Tran, N. T., Tran, T. K., Jeon, J. K., Park, J. K., and Kim, D. J. Fracture energy of ultra-high-performance fiber-reinforced concrete at high strain rates. *Cement and Concrete Research 79* (2015), 169–184. doi.org/10.1016/j.cemconres.2015.09.011.

[177] Tufail, M., Shahzada, K., Gencturk, B., and Wei, J. Effect of elevated temperature on mechanical properties of limestone, quartzite and granite concrete. *International Journal of Concrete Structures and Materials 11*, 1 (2017), 17–28. doi.org/10.1007/s40069-016-0175-2.

[178] Türkel, S., and Alabas, V. The effect of excessive steam curing on Portland composite cement concrete. *Cement and Concrete Research 35*, 2 (2005), 405–411. doi.org/10.1016/j.cemconres.2004.07.038.

[179] Varona, F. B., Baeza, F. J., and Bru, D. Experimental analysis of the loss of bond between rebars and concrete exposed to high temperatures. *Dyna (Spain) 90*, 1 (2015), 78–86. doi.org/10.6036/7184.

[180] Varona, F. B., Baeza, F. J., Bru, D., and Ivorra, S. Influence of high temperature on the mechanical properties of hybrid fibre reinforced normal and high strength concrete. *Construction and Building Materials 159* (2018), 73–82. doi.org/10.1016/j.conbuildmat.2017.10.129.

[181] Vicente, M. A., González, D. C., Mínguez, J., Tarifa, M., Ruiz, G., and Hindi, R. Influence of the pore morphology of high strength concrete on its fatigue life. *International Journal of Fatigue 112* (2018), 106–116. doi.org/10.1016/j.ijfatigue.2018.03.006.

[182] Vigneshwari, M., Arunachalam, K., and Angayarkanni, a. Replacement of silica fume with thermally treated rice husk ash in Reactive

Powder Concrete. *Journal of Cleaner Production 188* (2018), 264–277. doi.org/10.1016/j.jclepro.2018.04.008.

[183] Vilches, L. F., Leiva, C., Vale, J., and Fernández-Pereira, C. Insulating capacity of fly ash pastes used for passive protection against fire. *Cement and Concrete Composites 27*, 7-8 (2005), 776–781. doi.org/10.1016/j.cemconcomp.2005.03.001.

[184] Villain, G., Thiery, M., and Platret, G. Measurement methods of carbonation profiles in concrete: Thermogravimetry, chemical analysis and gammadensimetry. *Cement and Concrete Research 37*, 8 (2007), 1182–1192. doi.org/10.1016/j.cemconres.2007.04.015.

[185] Voit, K., and Kirnbauer, J. Tensile characteristics and fracture energy of fiber reinforced and non-reinforced ultra high performance concrete (UHPC). *International Journal of Fracture 188*, 2 (2014), 147–157. doi.org/10.1007/s10704-014-9951-7.

[186] Wan-Wendner, L., Wan-Wendner, R., and Cusatis, G. Age-dependent size effect and fracture characteristics of ultra-high performance concrete. *Cement and Concrete Composites 85* (2018), 67–82. doi.org/10.1016/j.cemconcomp.2017.09.010.

[187] Wang, H. L., and Song, Y. P. Fatigue capacity of plain concrete under fatigue loading with constant confined stress. *Materials and Structures 44*, 1 (2011), 253–262. doi.org/10.1617/s11527-010-9624-6.

[188] Wang, R., Gao, X., Zhang, J., and Han, G. Spatial distribution of steel fibers and air bubbles in UHPC cylinder determined by X-ray CT method. *Construction and Building Materials 160* (2018), 39–47. doi.org/10.1016/j.conbuildmat.2017.11.030.

[189] Wang, Y., Hu, X., Liang, L., and Zhu, W. Determination of tensile strength and fracture toughness of concrete using notched 3-p-b specimens. *Engineering Fracture Mechanics 160* (2016), 67–77. doi.org/10.1016/j.engfracmech.2016.03.036.

[190] Wille, K., Naaman, A. E., and Parra-Montesinos, G. J. Ultra high performance concrete with compressive strength exceeding 150 MPa (22 ksi): A simpler way. *ACI Materials Journal 108*, 1 (2011), 46–54. doi.org/10.14359/51664215.

[191] Wright, P., Fu, X., Sinclair, I., and Spearing, S. Ultra high resolution computed tomography of damage in notched carbon fiber-epoxy composites. *Journal of Composite Materials 42*, 19 (2008), 1993–2002. doi.org/10.1177/0021998308092211.

[192] Wuest, J., Denarié, E., Brühwiler, E., Tamarit, L., Kocher, M., and Gallucci, E. Tomography analysis of fiber distribution and orientation in ultra high–performance fiber-reinforced composites with high-fiber dosages. *Experimental Techniques 33*, 5 (2009), 50–55. doi.org/10.1111/j.1747-1567.2008.00420.x.

[193] Xiao, J., Li, H., and Yang, Z. Fatigue behavior of recycled aggregate concrete under compression and bending cyclic loadings. *Construction and Building Materials 38* (2013), 681–688. doi.org/10.1016/j.conbuildmat.2012.09.024.

[194] Xu, B., Han, J., Kumar, A., Li, P., and Yang, Y. Thermal storage using sand saturated by thermal-conductive fluid and comparison with the use of concrete. *Journal of Energy Storage 13* (2017), 85–95. doi.org/10.1016/j.est.2017.06.010.

[195] Yang, H. T. Y. A finite element stress analysis of the vertical buttresses of a nuclear containment vessel. *Nuclear Engineering and Design 11*, 2 (1970), 255–268. doi.org/10.1016/0029-5493(70)90150-0.

[196] Yang, Z., Ren, W., Sharma, R., McDonald, S., Mostafavi, M., Vertyagina, Y., and Marrow, T. J. In-situ X-ray computed tomography characterisation of 3D fracture evolution and image-based numerical homogenisation of concrete. *Cement and Concrete Composites 75* (2017), 74–83. doi.org/10.1016/j.cemconcomp.2016.10.001.

[197] Yoo, D.-Y., and Banthia, N. Mechanical properties of ultra-high-performance fiber-reinforced concrete: A review. *Cement and Concrete Composites 73* (2016), 267–280. doi.org/10.1016/j.cemconcomp.2016.08.001.

[198] Yoo, D.-Y., Banthia, N., and Yoon, Y.-S. Effectiveness of shrinkage-reducing admixture in reducing autogenous shrinkage stress of ultra-high-performance fi ber-reinforced concrete. *Cement and Concrete Composites 64* (2015), 27–36. doi.org/10.1016/j.cemconcomp.2015.09.005.

[199] Yoo, D.-Y., Kang, S.-T., and Yoon, Y.-S. Enhancing the flexural performance of ultra-high-performance concrete using long steel fibers. *Composite Structures 147* (2016), 220–230. doi.org/10.1016/j.compstruct.2016.03.032.

[200] Yoo, D.-Y., Kim, S., Park, G.-J., Park, J.-J., and Kim, S.-W. Effects of fiber shape, aspect ratio, and volume fraction on flexural behavior of ultra-high-performance fiber-reinforced cement composites. *Composite Structures 174* (2017), 375–388. doi.org/10.1016/j.compstruct.2017.04.069.

[201] Yoo, D.-Y., Shin, H.-O., Yang, J.-M., and Yoon, Y.-S. Material and bond properties of ultra high performance fiber reinforced concrete with micro steel fibers. *Composites: Part B 58* (2014), 122–133. doi.org/10.1016/j.compositesb.2013.10.081.

[202] Yousefieh, N., Joshaghani, A., Hajibandeh, E., and Shekarchi, M. Influence of fibers on drying shrinkage in restrained concrete. *Construction and Building Materials 148* (2017), 833–845. doi.org/10.1016/j.conbuildmat.2017.05.093.

[203] Yu, R., Spiesz, P., and Brouwers, H. J. H. Mix design and properties assessment of ultra-high performance fibre reinforced concrete (UHPFRC). *Cement and Concrete Research 56* (2014), 29–39. doi.org/10.1016/j.cemconres.2013.11.002.

[204] Zanuy, C., de la Fuente, P., and Albajar, L. Effect of fatigue degradation of the compression zone of concrete in reinforced concrete sections. *Engineering Structures 29*, 11 (2007), 2908–2920. doi.org/10.1016/j.engstruct.2007.01.030.

[205] Zhang, B., and Bicanic, N. Fracture energy of high-performance concrete at high temperatures up to 450°C: the effects of heating temperatures and testing conditions (hot and cold). *Magazine of Concrete Research 58*, 5 (2006), 277–288. doi.org/10.1680/macr.2006.58.5.277.

[206] Zhang, B., Phillips, D. V., and Wu, K. Effect of loading frequency and stress reversal on fatigue life of plain concrete. *Magazine of Concrete Research 48*, 177 (1996), 361–375. doi.org/10.1680/macr.1996.48.177.361.

[207] Zhang, W., Min, H., Gu, X., Xi, Y., and Xing, Y. Mesoscale model for thermal conductivity of concrete. *Construction and Building Material 98* (2015), 8–16. doi.org/10.1016/j.conbuildmat.2015.08.106.

[208] Zhao, J., Zheng, J.-J., Peng, G.-F., and van Breugel, K. Numerical analysis of heating rate effect on spalling of high-performance concrete under high temperature conditions. *Construction and Building Materials 152* (2017), 456–466. doi.org/10.1016/j.conbuildmat.2017.07.023.

[209] Zhou, B., and Uchida, Y. Influence of flowability, casting time and formwork geometry on fiber orientation and mechanical properties of UHPFRC. *Construction and Building Materials 95* (2017), 164–177. doi.org/10.1016/j.cemconres.2017.02.017.

[210] Zīle, E., and Zīle, O. Effect of the fiber geometry on the pullout response of mechanically deformed steel fibers. *Cement and Concrete Research 44* (2013), 18–24. doi.org/10.1016/j.cemconres.2012.10.014.

[211] Özrahat, E., and Ünalan, S. Thermal performance of a concrete column as a sensible thermal energy storage medium and a heater. *Renewable Energy 111* (2017), 561–579. doi.org/10.1016/j.renene.2017.04.046.

Appendix A
Load-deflection curves of high-strength PP fibre-reinforced SCC

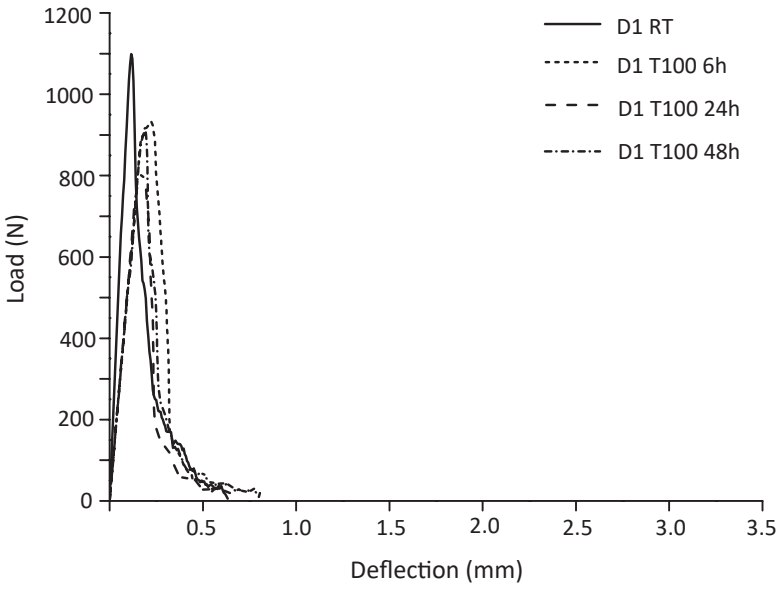

Figure A.1 Load-deflection curves in D1 hot tests at 100 °C.

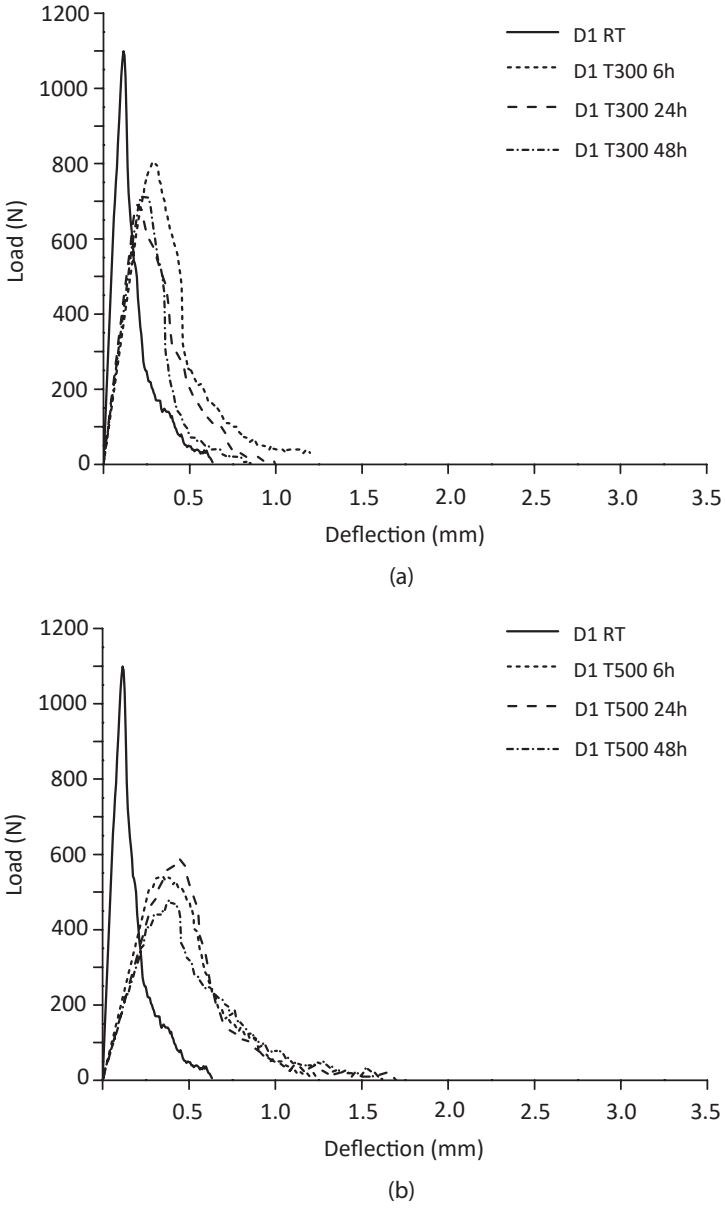

Figure A.2 Load-deflection curves in D1 hot tests: (a) 300 °C and (b) 500 °C.

APENDICE B

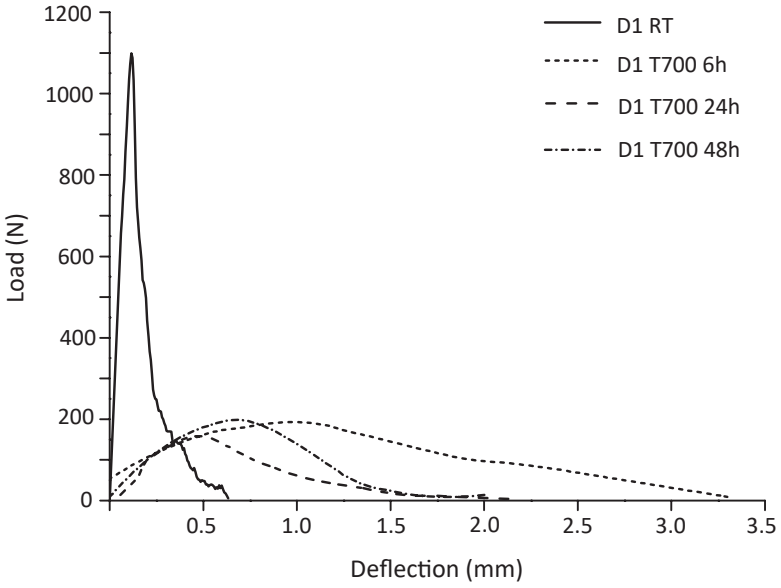

Figure A.3 Load-deflection curves in D1 hot tests at 700 °C.

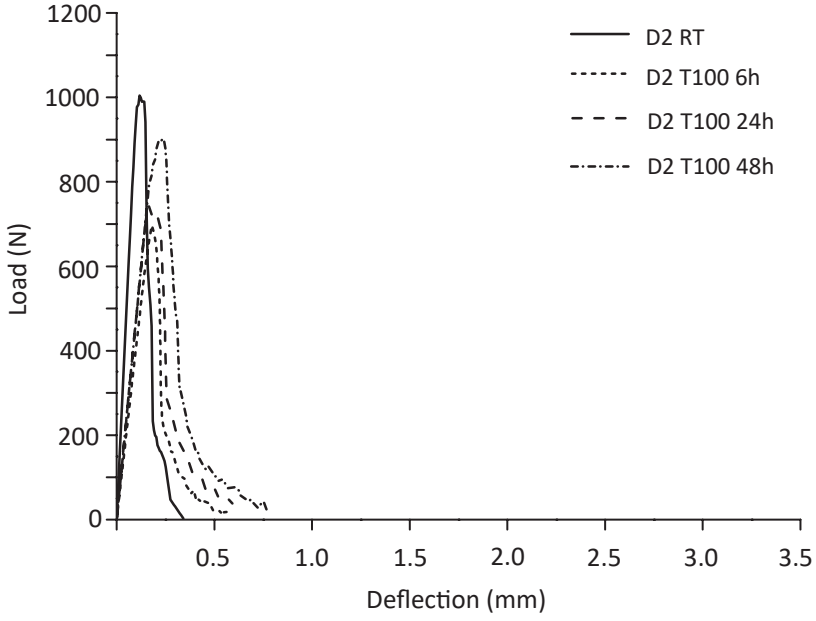

(a)

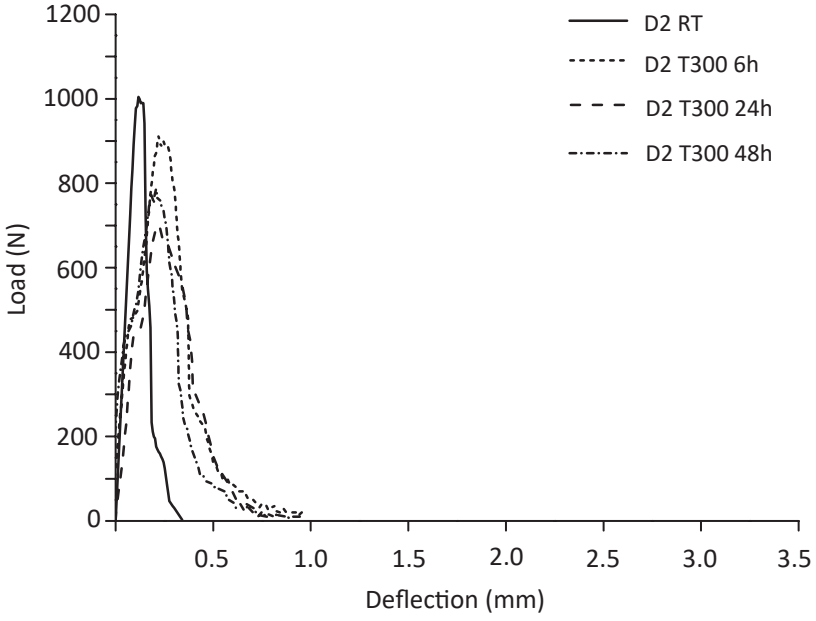

(b)

Figure A.4 Load-deflection curves in D2 hot tests: (a) 100 °C and (b) 300 °C.

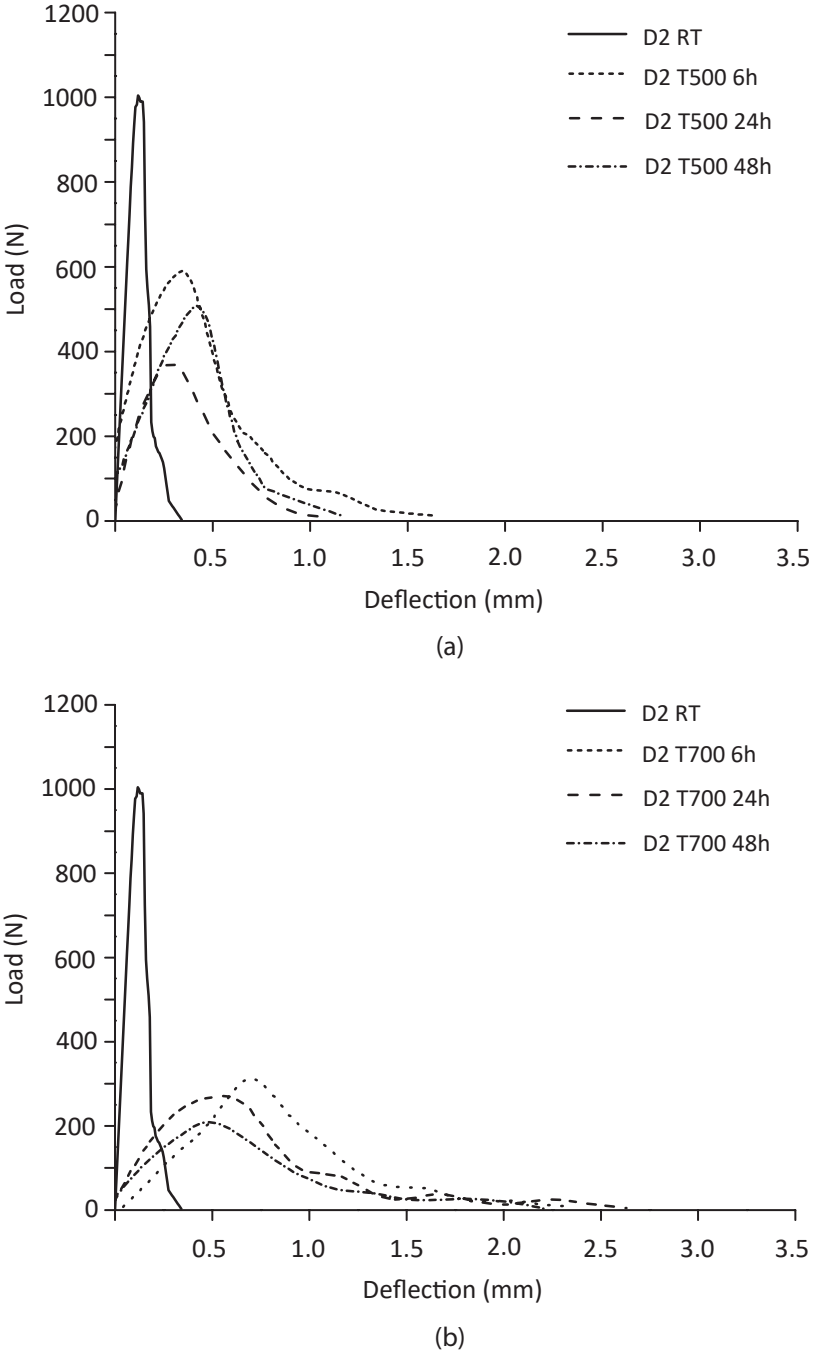

Figure A.5 Load-deflection curves in D2 hot tests: (a) 500 °C and (b) 700 °C.

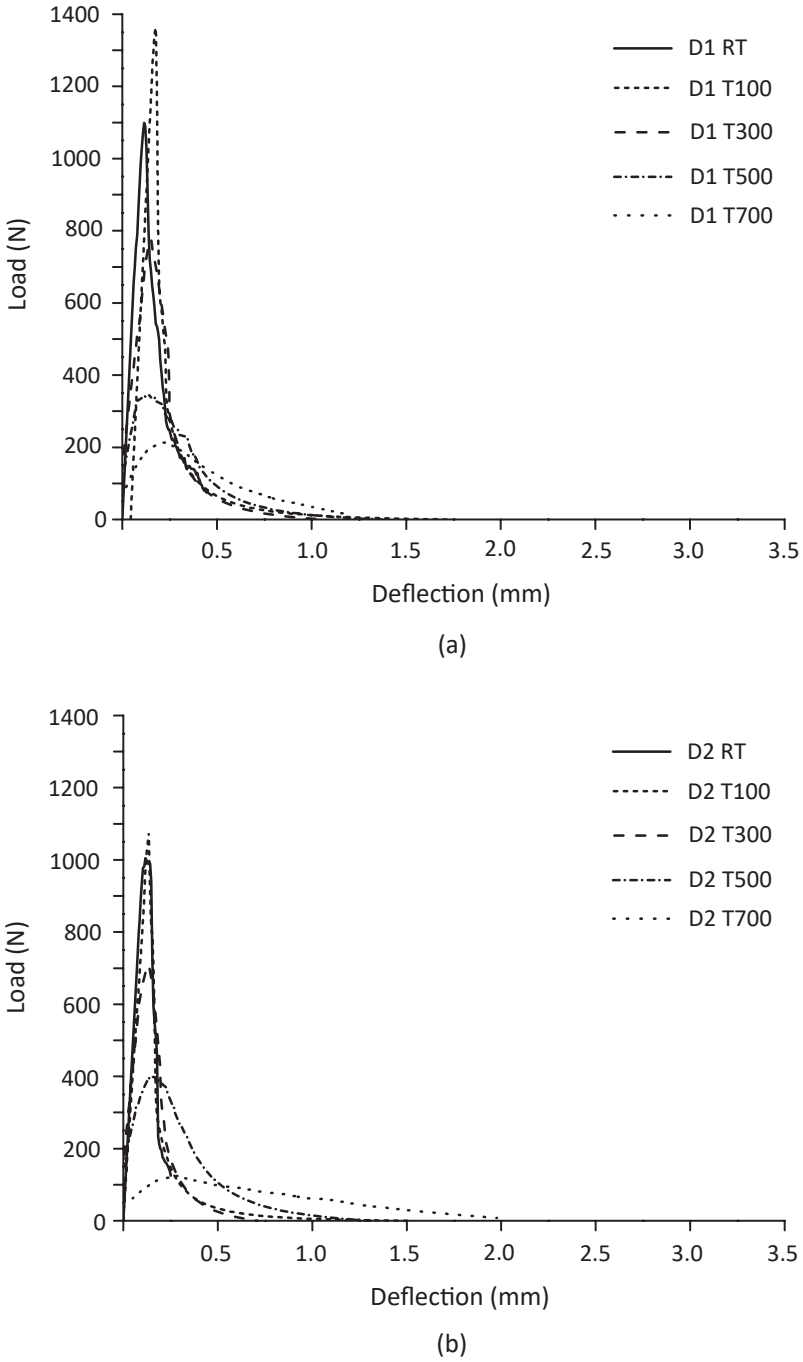

Figure A.6 Load-deflection curves in cold tests: (a) D1 and (b) D2 mixes.

Appendix B
MatLab-code, stress-strain curves from FPB

"Program to Determine the Tensile properties of UHPFRC from Unnotched Four-point Bending Tests" according to the inverse method developed by López et al. [110].

Written and copyrighted (2019) of MatLab code by
M.Sc. Ph.D. Student Jose D. Rios
Department of Continuum Mechanics and Structural Analysis.
Camino de los descubrimientos s/n, 41092
Sevilla, Spain
Email: jdrios@us.es

This program determines the stress-strain relationship of UHPFRC from the five key points extracted from flexural stress-deflection experimental curves obtained from unnotched four-point bending tests according to López et al.[1].

The program is freeware. The author takes no responsibility for any use of the program and the user is encouraged to validate the results by other means.

```
function out=ft4PBTinterpol(h,pend,dfis)
close all
```

```
%======= Determination sigma 40%m =======
A=textread('DL4pbt3.dat');

m=pend; % initial slope of "input".
d=dfis; % crack displacement from the mid point of spec-
imen, (mm).
L=400; % specimen span, (mm).
w0=0; % crack opening at peak, (mm).
E=25000; % Young's modulus, (MPa).

% h, specimen height (mm)
% input, [stress (MPa), deflection (mm)].
% pend, initial slope of "input".

%======= Determination sigma 75%m =======
sigma75est=0.75.*m.*A(:,2)
error=abs(A(:,1)-sigma75est)
sigma75est;
[a,b]=min(error);
sigma75=A(b,1);
delta75=A(b,2);

%======= Determination sigma 40%m =======

sigma40est=0.40*m.*A(:,2);
error=abs(A(:,1)-sigma40est);
[a,b]=min(error);
sigma40=A(b,1);
delta40=A(b,2);

%======= Determination sigma loc =======

[sigmamax,posmax]=max(A(:,1));
sigmaloc=0.97*sigmamax;
errorloc=abs(A(1:posmax,1)-sigmaloc);
[a,b]=min(errorloc);
sigmaloc=A(b,1);
```

```
deltaloc=A(b,2);

tam=size(A);
curva=A(b:1:tam,1:1:2);

%======= Determination sigma 80%sigmaloc =======

sigmaloc80=0.8*sigmaloc;
error80loc=abs(curva(:,1)-sigmaloc80);
[a,b]=min(error80loc);
sigmaloc80=curva(b,1);
deltaloc80=curva(b,2);

%======= Determination sigma 30%sigmaloc =======

sigmaloc30=0.3*sigmaloc;
error30loc=abs(curva(:,1)-sigmaloc30);
[a,b]=min(error30loc);
sigmaloc30=curva(b,1);
deltaloc30=curva(b,2);

%crack position correction from mid point of specimen

k1=1+(0.6/L)*d;
k2=1+(2.1/L)*d;

% stress-strain relationship for L/h=4.5 [110]

ft45=(sigma75/1.59)*((sigma75/sigma40)^0.21);

eptu45=(ft45/E)*((6.65*(deltaloc/delta75))-9.40);

eptel45=ft45/E;

alpha=eptu45/eptel45;
ftu45=(alpha^(-0.17))*(2.24*(sigmaloc/sigma75)-1.55)*ft45;
```

```
gamma=ftu45/ft45;
eptd45=(gamma^(-0.38))*(alpha^0.89)*(2.82*(deltaloc80*k1/deltaloc)-
1.68)*(ft45/E);

beta=eptd45/eptel45;
eptmax45=2.17*(beta^(-0.76))*(gamma^(-0.26))*(alpha^1.48)*
(((deltaloc30*k2)/deltaloc)^1.86)*(ft45/E);

wd45=w0+(eptd45-eptu45+((2*ftu45)/(3*E)))*(L/3)
%wd45=w0+(eptd45-eptu45)*(L/3);

wmax45=w0+(eptmax45-eptu45+(ftu45/E))*(L/3)
%wmax45=w0+(eptmax45-eptu45)*(L/3);

%======= Stress-strain relationship for L/h=4.5 [110]========

ft3=(sigma75/1.63)*((sigma75/sigma40)^0.19);

eptu3=(ft3/E)*((7.65*(deltaloc/delta75))-10.53);

eptel3=ft3/E;

alpha=eptu3/eptel3;
ftu3=(alpha^(-0.18))*(2.46*(sigmaloc/sigma75)-1.76)*ft3;

gamma=ftu3/ft3;
eptd3=(gamma^-0.37)*(alpha^0.88)*(3*(deltaloc80*k1/deltaloc)-
1.80)*(f3/E);

beta=eptd3/eptel3;
eptmax3=2.81*(beta^(-0.76))*(gamma^(-0.19))*(alpha^1.42)*
(((deltaloc30*k2)/deltaloc)^1.85)*(ft3/E);

wd3=w0+(eptd3-eptu3+((2*ftu3)/(3*E)))*(L/3);
%wd3=w0+(eptd3-eptu3)*(L/3);
```

```
wmax3=w0+(eptmax3-eptu3+(ftu3/E))*(L/3);
%wmax3=w0+(eptmax3-eptu3)*(L/3);

% ============ interpolation to L/h=4 ===============

ft4=(ft45-ft3)*(2/3)+ft3;
eptu4=(eptu45-eptu3)*(2/3)+eptu3;
eptel4=(eptel45-eptel3)*(2/3)+eptel3;
ftu4=(ftu45-ftu3)*(2/3)+ftu3;
eptd4=(eptd45-eptd3)*(2/3)+eptd3;
eptmax4=(eptmax45-eptmax3)*(2/3)+eptmax3;
wd4=(wd45-wd3)*(2/3)+wd3;
wmax4=(wmax45-wmax3)*(2/3)+wmax3;

%======= save results from L/h=4.5 ========

ptos=[sigma75,delta75,sigma40,delta40,sigmaloc,deltaloc,
sigmaloc80,deltaloc80,sigmaloc30,deltaloc30,alpha,gamma,
beta,0];

save puntocurva.dat ptos -ascii

out=[E,ftu45,ft45,eptu45,eptel45,eptd45,eptmax45]
save salida45.dat out -ascii

out2=[0,0
eptel45,ft45
eptu45,ftu45
eptd45,ftu45/3
eptmax45,0]
save stress-straincurve45.dat out2 -ascii

out3=[0,ftu45
wd45,ftu45/3
wmax45,0]
save stress-wcurve45.dat out3 -ascii
```

```
%======= save results from L/h=3 ========

out=[E,ftu3,ft3,eptu3,eptel3,eptd3,eptmax3]
save salida3.dat out -ascii

out2=[0,0
eptel3,ft3
eptu3,ftu3
eptd3,ftu3/3
eptmax3,0]
save stress-straincurve3.dat out2 -ascii

out3=[0,ftu3
wd3,ftu3/3
wmax3,0]
save stress-wcurve3.dat out3 -ascii

%======= save results from L/h=4 =========

out=[E,ftu4,ft4,eptu4,eptel4,eptd4,eptmax4]
save salida4.dat out -ascii

out2=[0,0
eptel4,ft4
eptu4,ftu4
eptd4,ftu4/3
eptmax4,0]
save stress-straincurve4.dat out2 -ascii

out3=[0,ftu4
wd4,ftu4/3
wmax4,0]
save stress-wcurve4.dat out3 -ascii

figure(1)
plot(A(:,2),A(:,1))
hold on
plot(delta75,sigma75,'ro')
```

```
hold on
plot(delta40,sigma40,'bo')
hold on
plot(deltaloc,sigmaloc,'go')
hold on
plot(deltaloc80,sigmaloc80,'yo')
hold on
plot(deltaloc30,sigmaloc30,'ro')
% hold on
% plot(input(:,2),0.75.*m.*A(:,2),'red')
% hold on
% plot(input(:,2),0.40.*m.*A(:,2),'red')

clear all
```

Appendix C
MatLab-code, $P-\delta$ curves estimation at temperature

"Code to estimate the deflection values of concrete from position values at room temperature of the same material"

Written and copyrighted (2019) of MatLab code by
M.Sc. Ph.D. Student Jose D. Rios
Department of Continuum Mechanics and Structural Analysis.
Camino de los descubrimientos s/n, 41092
Sevilla, Spain
Email: jdrios@us.es

This program estimates the P-deflection curves of concrete from the P-position curves at room temperature.

The program is freeware. The author takes no responsibility for any use of the program and the user is encouraged to validate the results by other means.

```
clear all
clc

Pos_RT=textread('position_DSL.dat'); % machine position at RT
Def_RT=textread('deflection_DSL.dat'); % deflection at RT
Load_RT=textread('load_DSL.dat'); % load at RT
```

```
Pos_temp=textread('pos_300.dat'); % machine position at any temperature
Load_temp=textread('load_300.dat'); % load at any temperature

%================= Estimation P-delta curve ===============
size(Pos_RT)
size(Def_RT)
size(Load_RT)

[a,g]=max(Load_RT);
Load_adim=Load_RT./a;
ratio=Def_RT./Pos_RT;
size_ratio=size(ratio);

[b,h]=max(Load_temp);
Load_adim_temp=Load_temp./b;
c=size(Load_adim_temp);
d=size(Load_adim);

for i=1:h
for m=1:g
if Load_adim(m,1)-0.01<Load_adim_temp(i,1) || Load_adim_temp(i,1)>Load_-
adim(m,1)+0.01;
Def_temp(i,1)=ratio(m,1)*Pos_temp(i,1);
end
end
end

for i=h:1:c(1,1)
for m=g:1:d(1,1)
if Load_adim(m,1)-0.01<Load_adim_temp(i,1) || Load_adim_temp(i,1)>Load_-
adim(m,1)+0.01;
Def_temp(i,1)=ratio(m,1)*Pos_temp(i,1);
end
end
end

%=================== Save solution ====================
```

```
out=[Def_temp];
save Deflection_300.dat out -ascii

size(Def_temp)
size(Load_temp)

   %=================== Plotting ===================
figure(1)
plot(Def_temp(:,1),Load_temp(:,1))
hold on
plot(Pos_temp(:,1),Load_temp(:,1),'red')
```

List of Figures

List of Tables

Curriculum Vitae
José D. Ríos

José D. Ríos
PhD. Student
jdrios@us.es
(+34) 637 354 811

Researcher ID: Y-5741-2018
ORCID: 0000-0002-2079-5133
ScopusID: 57192652633
Research Gate profile: https://www.researchgate.net/profile/Jose_Rios18

Professional Address
Departamento de Mecánica de Medios Continuos y Teoría de Estructuras
Escuela Técnica Superior de Ingenería
Camino de los Descubrimientos s/n
Sevilla, 41092
Spain

Education

2014, Master of Science in Mechanical Engineering
School of Engineering. Universidad de Sevilla, Spain.

Master of Science final project concluded with first class honours, titled "Numerical study of the steel concrete shear bond behaviour of composite slabs".

2015-present, PhD. Student
Pre-doctoral student on the international doctoral program titled "Mechanical

Engineering and Industrial Organization". Research line "Application of numerical methods to the study of static and dynamic of solids and structures". Universidad de Sevilla, Spain.

Current Position

2015 - present, Research Internship
School of Engineering. Department of Continuum Mechanics and Structural Analysis. Universidad de Sevilla, Spain.

Research Interest

Fracture mechanics of concrete; fibre-reinforced concrete; ultra-high performance concrete; fatigue of concrete. Composite structures: steel-concrete. Reinforced concrete structures. Advanced cement based materials. Pre-stressed concrete structures. Experimental analysis. Non-linear numerical models of materials and structures.

Funded Research Projects

2014 - 2016, Participation: Pre-doctoral researcher
Fracture behaviour and thermo-mechanical fatigue of high-strength posttensioned concrete elements under tension-compression loading cycles. BIA2013-48352-P.

2016 - present, Participation: Pre-doctoral researcher
Fracture and thermo-mechanical fatigue on ultra-high-performance fiber-reinforced concrete: Analyses of thermal-shock damage. BIA2016-75431-R.

Funded Teaching Projects

2018 - present, Participation: Pre-doctoral teacher
Coordinated projects of teaching innovation in engineering of ETS Ingeniería of Sevilla.

Publications

Journal Articles

- Ríos, José D.; Leiva, Carlos; Ariza, M. Pilar; Seitl, Stanislav; Cifuentes, Héctor. (2019) "Analysis of the tensile fracture properties of ultra-high-strength fiber-reinforced concrete with different types of steel fibers by X-ray tomography". *Materials and Design*. Vol. 165.

10.1016/j.matdes.2019.107582.

- Ríos, José D.; Cifuentes, Héctor; Leiva, Carlos; García, Celia; Alba, Maria D. (2018) "Behavior of high-strength polypropylene fiber-reinforced self-compacting concrete exposed to high temperatures". *Journal of Materials in Civil Engineering. ASCE*. Vol. 30. No. 11. 10.1061/(ASCE) MT.1943-5533.0002491.

- Cifuentes, Héctor; Ríos, José D.; Gómez, Emilio (2018) "Effect of mix design on the size-independent fracture energy of normal- and high-strength self-compacting concrete". *Materiales de Construccion*. Vol. 68. No. 329. 10.3989/mc.2018.00717.

- Ríos, José D.; Cifuentes, Héctor; Yu, Rena C.; Ruiz, Gonzalo (2017), " Probabilistic flexural fatigue in plain and fiber-reinforced concrete". *Materials*. Vol. 10. No. 7-767. Pag. 1-25. 10.3390/ma10070767.

- Ríos, José D.; Cifuentes, Héctor; Martínez de la Concha, Antonio; Medina-Reguera, Fernando (2017), "Numerical modelling of the shear-bond behaviour of composite slabs in four and six-point bending tests". *Engineering Structures*. 2017. Vol. 133. Pag. 91-104. 10.1016/j.engstruct.2016.12.025.

- Seitl, Stanislav; Ríos, José D.; Cifuentes, Héctor, (2017)" Comparison of fracture toughness values of normal and high strength concrete determined by three point bend and modified disk-shaped compact tension specimens". *Frattura ed Integrita Strutturale*. Vol. 42. Pag. 67-76. 10.3221/Igf-Esis.42.08.

- Seitl, Stanislav; Ríos, José D.; Cifuentes, Héctor; Veselý, Václav, (2017), " Effect of the Load Eccentricity on Fracture Behaviour of Cementitous Materials Subjected to the Modified Compact Tension Test". *Solid State Phenomena*. Vol. 258. Pag. 518-521. 10.4028/www.scientific.net/SSP.258.518

- Leiva, Carlos; Garcia, Celia; Cifuentes, Héctor; Vilches, Luis; Ríos, José D. (2017), "Radiological, Leaching, and Mechanical Properties of Co-combustion Fly Ash in Cements". *Journal of Hazardous, Toxic, and Radioactive Waste*. Vol. 21. No. 4. 10.1061/(ASCE)HZ.2153-5515.0000362.

Conference Proceedings

- Ríos, José D.; Cifuentes, Héctor (2018), "Probabilistic fatigue analysis of ultra-high-performance fibre-reinforced concrete under thermal effects". *12th International Fatigue Conference Proceedings*.

- Ríos, José D.; Cifuentes, Héctor (2018), "Análisis del comportamiento en fractura de un hormigón de muy alta resistencia sometido a temperaturas de 300 °C mediante tomografía computarizada". *Anales de Mecánica de la Fractura*. Vol. 35. Pag. 134-139.

- Ríos, José. D.; Cifuentes, Héctor; Medina, Fernando (2018), "Determinación de las curvas de Wöhler en fatiga a flexotracción de un hormigón de muy alta resistencia sometido a temperatura elevada". *Libro de publicaciones del IV congreso HAC2018*. Vol. 5. No. 1. Pag. 629-638. 10.4995/HAC2018.2018.8274.

- Cifuentes, Héctor; Ríos, José D., Gómez, Emilio (2017), "Influencia de la adición de humo de sílice en el comportamiento en fractura y ductilidad de los hormigones autocompactantes". *Anales de Mecánica de la Fractura*. Vol. 34. Pag. 286-293.

- Ríos, José. D.; Cifuentes, Héctor (2017)," Comportamiento en fractura de un hormigón de muy altas prestaciones frente a la adición de fibras metálicas".*Anales de Mecánica de la Fractura*. Vol. 34. Pag. 212-219.

- Ríos, José. D.; Cifuentes, Héctor; Medina, Fernando (2016), " Analisis del efecto de la adición de fibras de acero sobre el comportamiento de hormigones sometidos a cargas de flexotracción". *Libro de artículos XXI Congreso Nacional de Ingeniería Mecánica*. Vol. 1. No. 1. Pag.

1328-1335.

- Ríos, José. D.; Cifuentes, Héctor (2016)," Aplicación de un Modelo Probabilístico al Comportamiento en Fatiga por Flexotracción de Hormigones Reforzados con Fibras de Acero". *Anales de Mecánica de la Fractura*. Vol. 1. No. 33. Pag. 206-211.

- Ríos, José. D.; Martinez de la Concha, Antonio; Cifuentes, Héctor (2015), "A simple model to analyse the shear-bond behaviour in steel deck composite slabs". *X Congresso de Construçao Metálica e Mista*. Vol. 1. Pag. 303-312.

- Cifuentes, Héctor; Ríos, José D.; Leiva, Carlos; Medina, Fernando (2016)," Influencia del Tiempo de Exposición a Altas Temperaturas en el Comportamiento en Fractura de Hormigones Autocompactantes Reforzados con Fibras. *Anales de Mecánica de la Fractura*. Vol. 33. Pag. 297-302.

Conferences

- Ríos, José D.; Cifuentes, Héctor,"Probabilistic fatigue analysis of ultra-high-performance fibre-reinforced concrete under thermal effects". *12th International Conference of Fatigue Congress*. July 2018, Poitiers, France.

- Ríos, José D.; Cifuentes, Héctor; Ariza,M.P.,"Learning focused on structural projects adapted to the University teaching mission". *IV International Conference on Structural Engineering Education*. June 2018, Madrid, Spain.

- Ríos, José D.; Cifuentes, Héctor,"Aprendizaje centrado en el proyecto de estructuras adaptados a la enseñanza universitaria. Comunicación en congreso". *XXVI Congreso Universitario de Innovación en las Enseñanzas Técnicas*. June 2018, Gijón, Spain.

- Ríos, José D.; Cifuentes, Héctor; Medina, Fernando,"Determinación de las curvas de Wöhler en fatiga a flexotracción de un hormigón de muy alta resistencia sometido a temperatura elevada". *V Iberoamerican Congress of Self-Compacting and Special Concretes*. March 2018, Valencia, Spain.

- Ríos, José D.; Cifuentes, Héctor,"Análisis del comportamiento en fractura de un hormigón de muy alta resistencia sometido a temperaturas de 300 °C mediante tomografía computarizada". *35th Encuentro del Grupo Español de Fractura*. March 2018, Málaga, Spain.

- Ríos, José D.; Cifuentes, Héctor; Gómez, Emilio; Ariza, Pilar,"Influence of fibres on the tensile fracture behaviour of the matrix of ultra-high strength fibre-reinforced concrete"*14th International Conference on Fracture*. June 2017, Rhodes, Greece.

- Ríos, José D.; Cifuentes, Héctor; Medina, Fernando."Fatigue mechanical properties of ultra-high performance concrete by using three-point bend tests". *VII International Congress of Structures ACHE*. June 2017, La Coruña, Spain.

- Ríos, José D.; Cifuentes, Héctor; Leiva, Carlos; Medina, Fernando, "Influence of exposure time of temperatures on fracture behaviour of self-compacting concrete reinforced with PP fibres". *VII International Congress of Structures ACHE*. June 2017, La Coruña, Spain.

- Cifuentes, Héctor; Ríos, José D.; Gomez, Emilio, "Influencia de la adicion de humo de silice en el comportamiento en fractura y ductilidad de los hormigones autocompactantes. Ponencia en Congreso". *34th Encuentro del Grupo Español de Fractura*. March 2017, Santander, Spain.

- Ríos, José D.; Cifuentes, Héctor, "Comportamiento en fractura de un hormigón de muy altas prestaciones frente a la adición de fibras metálicas". *34th Encuentro del Grupo Español de Fractura*. March 2017, Santander, Spain.

- Cifuentes, Héctor; Ríos, José D.;Leiva, Carlos; Medina, Fernando, "Influencia del Tiempo de Exposición a Altas Temperaturas en el Comportamiento en Fractura de Hormigones Autocompactantes Reforzados con Fibras". *33th Congreso del Grupo Español de Fractura*. March 2016, San Sebastian, Spain.

- Ríos, José D.; Cifuentes, Héctor;, C. Yu, Rena, Ruiz, Gonzalo, "Aplicación de un Modelo Probabilístico al Comportamiento en Fatiga Por Flexotracción de Hormigones Reforzados con Fibras de Acero". *33th Congreso del Grupo Español de Fractura*. March 2016, San Sebastian, Spain.

- Seitl, Stanislav; Ríos,José D.; Cifuentes, Héctor; Veselý, Václav, "Effect of the Load Eccentricity on Fracture Behaviour of Cementitous Materials Subjected to the Modified Compact Tension Test". *8th International Conference on Materials Structure Micromechanics of Fracture*. June 2016, Brno, Czech Republic.

- Ríos, José D.; Martínez de la Concha, Antonio; Cifuentes, Héctor; Medina, Fernando (2015),"A simple numerical model to analyse the shear-bond behaviour in steel deck composite slabs". *X Congresso de Construçao Metálica e Mista*.

Participation in books

- Redaction and working committee member of the ACHE recommendations on Ultra-High Performance Fiber-Reinforced Concrete, 2016-2017. In press.

Pre-doctoral research stays

September 2018 - December 2018, Evanston (Illinois), United States of America

McCormick School of Engineering and Applied Science. Northwestern University. Department of Civil and Environmental Engineering. Preliminary experimental campaign to analyse the influence of temperature in the microstructure

and fracture properties of ultra-high-performance concrete matrix reinforced with graphene oxide.

July 2017 - September 2017, Gijón, Spain
School of Engineering. Universidad de Oviedo. Department of Construction and Manufacturing Engineering. Application of a probabilistic Weibull fatigue model, developed by the Professor Fernández-Canteli from the Universidad de Oviedo, in the determination of the probabilistic S-N fields from the experimental fatigue data of ultra-high performance fibre-reinforced concrete designed and tested in the Universidad de Sevilla.

July 2016 - September 2016, Brno, Czech Republic
Institute of Physics of Materials. High Cycle Fatigue Group. Comparison of fracture toughness values of normal and high-strength concrete determined by three-point bend and modified disk-shaped compact tension specimens. The experimental campaign was previously performed in the Universidad de Sevilla.

Teaching Activities

Teacher Training Course

- Participation on the "Preliminary phase of the teacher training and innovation program 2018". *Imparted: Universidad de Sevilla.*

Lessons

- (2018-2019). "Reinforced Concrete Structures". 3rd course. B.S. Industrial Engineering. School of Engineering. Universidad de Sevilla, Spain.

- (2018-2019). "Concrete Structures I". 3rd course. B.S. Civil Engineering.School of Engineering. Universidad de Sevilla, Spain.

- (2018-2019). "Concrete Structures II". 4th course. B.S. Civil Engineering. School of Engineering. University of Seville, Spain.

- (2018-2019). "Metallic Structures II". 4th course. B.S. Civil Engineering. School of Engineering. Universidad de Sevilla, Spain.

- (2018-2019). "Airport Structures II". 4th course. B.S. Aerospace Engineering. School of Engineering. Universidad de Sevilla, Spain.

- (2017-2018). "Reinforced Concrete Structures". 3rd course. B.S. Industrial Engineering. School of Engineering. Universidad de Sevilla, Spain.

- (2017-2018). "Concrete Structures I". 3rd course. B.S. Civil Engineering. School of Engineering. Universidad de Sevilla, Spain.

- (2017-2018). "Airport Structures II". 4th course. B.S. Aerospace Engineering. School of Engineering. Universidad de Sevilla, Spain.

- (2016-2017). "Reinforced Concrete Structures". 3rd course. B.S. Industrial Engineering. School of Engineering. Universidad de Sevilla, Spain.

- (2016-2017). "Concrete Structures I". 3rd course. B.S. Civil Engineering. School of Engineering. Universidad de Sevilla, Spain.

- (2016-2017). "Airport Structures II". 4th course. B.S. Aerospace Engineering. School of Engineering. Universidad de Sevilla, Spain.

- (2015-2016). "Reinforced Concrete Structures". 3rd course. B.S. Industrial Engineering. School of Engineering. Universidad de Sevilla, Spain.

Students Advised

- Afán Torrijos, Alicia. Project submitted for the degree B.S Civil Engineering (2018), "Análisis experimental del comportamiento de hormigones de ultra-altas prestaciones a temperatura elevada". Advisors: Cifuentes, Héctor; Ríos, José D.

- Gómez Casado, Alejandro. Project submitted for the degree B.S Civil Engineering (2017), "Estudio analítico y experimental de elementos flectados de hormigón de ultra-altas prestaciones armado y pretensado". Advisors: Cifuentes, Héctor; Ríos, José D.

Seminar Imparted

- "Influence of steel fibre length on the behaviour of ultra-high performance concrete subjected to flexural loading".
  July 2016, Brno, Czech Republic.

Others

- "Member of the local organizing committee of the *"First Colloquium of the Spanish Theoretical and Applied Mechanics Society"*. STAMS 2019. Madrid, Spain. 28-29th March 2019.

- "Member of the local organizing committee of the colloquium *"Micromechanics of Defects in Crystalline Solids and Metals"*. European Mechanics Society (EUROMECH). Seville, Spain. 11-15th June 2018.